Synthesis of optimized cathode materials for all-solid-state lithium batteries

Von der Fakultät für Ingenieurwissenschaften,
Abteilung Maschinenbau und Verfahrenstechnik der
Universität Duisburg-Essen

zur Erlangung des akademischen Grades eines

Doktors der Naturwissenschaften

Dr. rer. nat.

genehmigte Dissertation

von

Christoph Roitzheim

aus Bonn, Deutschland.

Gutachter: Univ.-Prof. Dr. Dina Fattakhova-Rohlfing
Univ.-Prof. Dr. Olivier Guillon

Tag der mündlichen Prüfung: 14.11.2022

DOI: 10.17185/duepublico/78166
URN: urn:nbn:de:hbz:465-20230412-084836-4

„Verstehen kann man das Leben rückwärts; leben muß man es aber vorwärts.“

(Søren Kierkegaard, dänischer Schriftsteller, Theologe und Philosoph)

Acknowledgements

First and foremost, I would like to thank my PhD supervisor, Prof. Dr. Dina Fattakhova-Rohlfing, for giving me the opportunity to do my PhD thesis in the exciting field of battery research in the department Electrochemical Storage at the Institute of Energy and Climate Research-Materials Synthesis and Processing (IEK-1). I am grateful for her mentoring during the past three years and the intense, scientific discussions about my work. Additionally, I like to thank her for giving me the freedom to realize my own ideas and the chance to present my results on international conferences. Finally, I am thankful for her assistance with manuscript writing as well as for reviewing this thesis.

I would also like to thank Prof. Dr. Olivier Guillon (director of IEK-1) for his approval to be my second reviewer. I am very grateful to him for providing the excellent infrastructure at IEK-1. Additionally, I thank him for his helpful ideas and remarks during the presentations of my work reports.

I like to express my gratitude to my scientific advisor and team leader, Dr. Martin Finsterbusch, for the comfortable working atmosphere in his team. I thank him for the numerous discussions, the guidance in manuscript and presentation preparation as well as for revising a lot of slides, abstracts, and manuscripts. I am grateful to him for organizing the funding for of all the new equipment we bought during the last three years.

My special thanks go to all colleagues from IEK-1 who contributed to the success of this thesis. These include Andrea Hilgers (PSD), Sigrid Schwartz-Lückge (BET surface area and density), Marie-Theres Gerhards (DTA/TG/MS), Beatrix Göths (FIB-SEM), Dr. Sahir Naqash (TOF-SIMS), Dr. Markus Mann (Rietveld refinements and EIS), and Volker Bader (heat treatments). Especially, I like to thank Dr. Doris Sebold for analyzing more than 60 NCM powders and serval additional samples by SEM and EDS. Furthermore, I am very grateful to Dr. Yoo Jung Sohn for performing the HT-XRD experiments and the Rietveld refinements. Finally, I would also like to thank Dr. Sören Möller for characterizing my samples by ion beam analysis, especially, for this great job in detecting the light element boron.

Additionally, I would like to thank Dr. Liang-Yin Kuo and Dr. Payam Kaghazchi, from the IEK-1 modeling team, for the interesting discussions about doped cathode materials and for performing the theoretical calculations for this thesis.
I also like to thank our partners form RWTH Aachen University (GFE), Dr. Maria Meledina and Helen Valencia, for characterizing my samples by TEM and delivering great images with atomic resolution.

I am also grateful for the support by the colleagues from ZEA-3, Dr. Volker Nischwitz (ICP-OES), Dr. Uwe Breuer (TOF-SIMS), and Dr. Heinrich Hartmann (XPS) who have made a special contribution to this thesis.

My special thanks go to my friends and office mates Grit Häuschen, Philipp Hecker, and Ruijie Ye. I like to thank you for the comfortable working atmosphere and for a lot of nice conversations. I am grateful to Philipp for his always good advice, for ordering, and for his daily support in the laboratory. I would especially like to thank my colleague and friend, Grit, for supplying me with LLZO powders, for her daily support in the laboratory, and for lots of funny but also serious conversations and discussions.

Finally, I like to thank my family for their great and unconditional support especially on the way towards the completion of this PhD thesis.

Abstract

Batteries are already and will continue to be the most important energy storage systems for operating portable electronic devices and electric vehicles as well as for stationary energy storage in power grids. Lithium-ion batteries (LIBs), which dominate the market for portable devices and electric vehicles, have been optimized for higher energy density over the past 30 years. However, the physicochemical limit of LIBs based on the state-of-the-art $Li[Ni_xCo_yMn_{1-x-y}]O_2$ (NCM)/carbon chemistry has almost been reached, requiring the development of new battery technologies. To meet the future requirements, a further battery improvement is needed in terms of a higher energy density, a longer cycle life, and higher safety levels. All-solid-state batteries (ASBs), including ceramic ASBs with garnet electrolytes, are considered as one of the promising next generation battery technologies, so the further development and optimization of the garnet-type ASBs is the focus of this thesis. Unlike conventional LIBs, garnet-based ASBs use $Li_{6.45}Al_{0.05}La_3Zr_{1.6}Ta_{0.4}O_{12}$ (LLZO:Ta) garnet as separator and solid-state electrolyte (SSE). Due to the ceramic nature of the SSE, the garnet-based SSEs are nonflammable and offer a higher safety than LIBs based on liquid, organic electrolytes. In addition to nonflammability, the compatibility of LLZO:Ta with metallic lithium makes it very attractive for the development of ASBs with Li metal anodes, which can increase the energy density. Although Li metal anodes are an important prerequisite for a higher energy density, achieving this goal also requires the development of composites cathodes containing an SSE with a high ionic conductivity and a cathode active material (CAM) with a high gravimetric and volumetric capacity and high areal loadings. Since ceramic composite cathodes are typically manufactured via co-sintering, the elevated temperatures required for this process pose challenges for material compatibility. High-capacity cathode active materials like NCM exhibit insufficient material compatibility with LLZO:Ta during co-sintering, leading to the formation of highly resistive interphases. Therefore, to enable high capacity garnet-based composite cathodes, the thermodynamic stability of NCM with LLZO:Ta at elevated temperatures must be improved. It is well known that the electrochemical properties of NCM in conventional LIBs with liquid electrolytes strongly depend on the nature and composition of the transition metals (TM) in the host structure, as well as on the doping of the NCM structure with various elements. Due to its versatility, doping has been intensively studied as a means to improve the electrochemical performance of NCMs in conventional LIBs with liquid electrolytes, where it has already proven to be an effective strategy for a performance

optimization. It is expected that doping can also improve the material compatibility of NCM with solid electrolytes, but no research has been done in this area.

Due to the importance of NCM cathode materials for the further development of lithium batteries with both conventional, liquid electrolytes and emerging solid-state electrolytes, this thesis addresses the performance optimization of NCM through structural doping as well as the integration of NCM powders into garnet-based composite cathodes. Two NCM compositions, namely, $Li[Ni_{1/3}Co_{1/3}Mn_{1/3}]O_2$ (NCM111) and Ni-rich $Li[Ni_{0.8}Co_{0.1}Mn_{0.1}]O_2$ (NCM811), as well as doping of the NCM host structure with boron and ruthenium were investigated. Pristine NCM111, pristine NCM811, B-doped NCM111, B-doped NCM811 and Ru-doped NCM811 were synthesized in a laboratory scale batch process via a hydroxide co-precipitation route. In addition to this batch synthesis in a glass flask, the use of a Couette-Taylor-Flow-Reactor (CTFR) for a continuous co-precipitation was demonstrated. The synthesis conditions thus optimized lead to an optimized NCM morphology with greatly improved electrochemical performance. All CAM compositions were characterized in detail to investigate the incorporation and distribution of the dopants in the NCM lattice. The effects of NCM composition, B, and Ru doping on the morphology and electrochemical performance were investigated in cells with a liquid electrolyte. Based on density functional theory (DFT) calculation, it was found that boron can be located in the Ni- and/or O-layers of the NCM lattice, depending on the concentration, and exhibits tetrahedral or trigonal planar coordination with oxygen, respectively. Therefore, B doping of NCM811 affects the crystal structure and cation disorder, leading to a change in the size and shape of the primary particles. To experimentally prove that the observations are caused by boron incorporated into the NCM lattice, boron was detected, quantified, and localized in B-doped NCM811 by ion beam analysis (IBA) and time-of-flight secondary ion mass spectrometry (TOF-SIMS). A boron enrichment was detected at the agglomerate surface, but also, more importantly, a significantly high and constant boron concentration was found inside the primary particles near the surface, confirming experimentally that boron is incorporated into the NCM811 lattice. B doping of NCM811 was shown to enhance capacity retention during long-term galvanostatic cycling, which could be an effect of the boron enrichment on the secondary particle surface, where it likely forms a protective surface coating.

Comparative analysis of NCM811 and NCM111 showed that the TM composition affects the shape of the primary particles. While cuboidal primary particles were obtained for Ni-rich NCM811, NCM111 shows thin flake-shaped primary particles. The 2 mol% B doping of NCM111 leads to increased lattice parameters, slightly enhanced cation disorder, and shows

interesting effects on the morphology, namely, harder and larger agglomerates, resulting in a strongly reduced BET surface area compared to pristine NCM111. In contrast to NCM811, B-doping of NCM111 did not result in improved electrochemical performance during long-term cycling, as NCM111 itself already showed excellent capacity retention of 93 % after 100 charge-discharge cycles.

In addition to boron, ruthenium was also investigated as a dopant of NCM811. Ruthenium was successfully incorporated into the NCM811 lattice and preferentially occupies octahedral Ni positions in the mixed Mn/Ni planes, as found by DFT calculation. Ru doping increases the NCM lattice parameters and leads to higher cation disorder and larger amount of Li vacancies due to its high oxidation state (Ru^{5+}). In addition, Ru doping decreases the size of the cuboidal primary particles. Ruthenium was successfully detected and localized in Ru-doped NCM811 by transmission electron microscopy/energy dispersive X-ray spectroscopy (TEM/EDS), IBA, and TOF-SIMS. The main difference of Ru doping compared to B doping is the homogenous distribution of ruthenium on the agglomerate surface and inside the primary particles, as no enrichment was observed. However, despite the successful incorporation into NCM lattice and contrary to previous studies on other cathode materials, Ru doping did not show any advantage compared to parent NCM structure, as the Ru-doped NCM811 exhibited an increased cell resistance and lower specific charge/discharge capacities compared to pristine NCM811 and B-doped NCM811.

The CAMs compositions studied in this thesis were also mixed with LLZO:Ta to investigate the material compatibility during co-sintering at elevated temperatures. Differential thermal analysis/thermogravimetry coupled with a mass spectrometer (DTA/TG/MS), *in-situ* high temperature X-ray diffraction (HT-XRD), scanning electron microscopy (SEM), and EDS were used to monitor the phase evolution during sintering. Although DTA/TG/MS analysis did not reveal any endo- or exothermic processes indicative of a decomposition reaction, the *in-situ* HT-XRD analysis detected two secondary phases, namely, $LaCo_{1-x}Mn_xO_3$ and $La_2(Ni_{0.5}Li_{0.5})O_4$ during co-sintering of NCM and LLZO:Ta. Their formation onset temperature and amount were found to be strongly dependent on the NCM composition and doping. The B doping of NCM111 enhances the formation of the secondary phases, while the B doping of NCM811 has no effect on the thermodynamic stability. The Ru doping was shown to even slightly reduce the amount of secondary phases. The experimental work was supported by simulation studies with DFT calculation, which clearly show that Mn is the most favorable TM in NCM to undergo interchange with Zr from LLZO:Ta. Therefore, the Mn-rich NCM111 shows enhanced formation of secondary phases. Surprisingly, the Ni-rich NCM811 formed only small amounts

of $La_2(Ni_{0.5}Li_{0.5})O_4$ in contact with LLZO:Ta. This phase formed self-constrained and thus, it is proving Ni-rich NCM811 to be the most promising active material for the combination with garnet-type LLZO:Ta. Moreover, the B doping of NCM811 does not deteriorate its thermal stability toward LLZO:Ta, which also validates the use of Li_3BO_3 (LBO) as a sintering additive. Thus, the use of LBO enables the fabrication of fully inorganic ceramic lithium batteries by conventional sintering. The resulting ASBs have a Li metal anode, a LLZO:Ta separator and a composite cathode consisting of LLZO:Ta, LBO, and NCM811. The use of LBO as a sintering additive significantly lowers the sintering temperature and enables the fabrication of a dense composite cathode as low as 750 °C. The reaction between LBO and Li_2CO_3 enables the formation of a $Li_{2+y}C_{1-y}B_yO_3$ (LCBO) interphase with the desired Li-ion conductivity. The fully inorganic ASB demonstrated in this thesis operated without polymeric interlayers and delivered a high specific areal discharge capacity of 0.7 mAh cm^{-2} in the first cycle, which is one of the highest performances obtained for garnet-based ASBs.

Kurzfassung

Bereits heute sind Batterien wichtige Energiespeichersysteme für den Betrieb von tragbaren elektronischen Geräten und Elektrofahrzeugen sowie für stationäre, netzgebundene Energiespeicher und werden hier, auch zukünftig, eine bedeutende Rolle einnehmen. Die heute weit verbreiteten Lithium-Ionen-Batterien (LIB), wurden innerhalb der letzten 30 Jahren hin zu immer höheren Energiedichten weiterentwickelt und optimiert. Damit LIB auch die zukünftigen Anforderungen erfüllen können, ist eine weitere Optimierung zu noch höher Energiedichte, länger Lebensdauer und höherer Sicherheit notwendig. Allerdings ist die physikalisch-chemische Leistungsgrenze der LIB, basierend auf der aktuellen $Li[Ni_xCo_yMn_{1-x-y}]O_2$ (NCM)/Kohlenstoff Chemie, fast erreicht, weshalb die Entwicklung neuer Batterietechnologien notwendig ist. Die Festkörperbatterie, ist eine der möglichen Batterietechnologien der nächsten Generation. Daher sind die Weiterentwicklung und Optimierung granatartiger Festkörperbatterien das Thema dieser Dissertation. Im Gegensatz zu konventionellen LIB, nutzen granatartige Festkörperbatterien $Li_{6.45}Al_{0.05}La_3Zr_{1.6}Ta_{0.4}O_{12}$ (LLZO:Ta) als Separator und Festkörperelektrolyt. Auf Grund des keramischen Festkörperelektrolyten, sind granatartige Festkörperbatterien nicht brennbar und deutlich sicherer als LIB basieren auf flüssigen, organischen Elektrolyten. Zusätzlich ist LLZO:Ta stabil gegenüber metallischem Lithium, sodass die Verwendung einer Lithiummetallanode ermöglicht wird und somit Festkörperbatterien mit deutliche höheren Energiedichten entwickelt werden können. Allerdings ist für eine solche Festkörperbatterie mit hoher Energiedichte, neben einer Lithiummetallanode, auch die Entwicklung einer Mischkathode, bestehend aus einem Festkörperelektrolyten mit guter ionischer Leitfähigkeit und einem Aktivmaterial mit hoher gravimetrischer und volumetrischer Kapazität sowie hoher flächenbezogener Aktivmaterialbeladung, notwendig. Keramische Mischkathoden werden üblicherweise durch Co-Sintern der beiden Komponenten gefertigt, wobei die hierzu benötigten hohen Temperaturen zu einer herausfordernden Materialkompatibilität führen. Kathodenmaterialien mit hoher Kapazität, wie NCM, weisen eine unzureichende Kompatibilität gegenüber LLZO:Ta während des Co-Sinterns auf, welche zur Ausbildung von unerwünschten Zwischenphasen mit hohen Widerständen führt. Daher muss die thermodynamische Stabilität von NCM gegenüber LLZO:Ta erhöhten werden, um granatbasierte Mischkathoden mit hoher Kapazität realisiert zu können. Es ist bereits bekannt, dass die Übergangsmetallzusammensetzung die elektrochemischen und thermischen Eigenschaften des NCM, in konventionellen Zellen basierend auf flüssigem, organischem Elektrolyten, beeinflusst. Dotierungen der NCM

Gerüststruktur mit verschiedenen Elementen haben sich bereits als effektive Strategie zur Optimierung von NCM für die Anwendung in konventionellen LIB herausgestellt. Es wird erwartet, dass eine Dotierung auch die Materialkompatibilität von NCM mit Festelektrolyten verbessern kann, aber in diesem Bereich wurde bisher noch keine Forschung betrieben.

Aufgrund der Bedeutung von NCM als Kathodenmaterial für die weitere Entwicklung von Lithiumbatterien, sowohl mit konventionellen Flüssigelektrolyten als auch mit neuartigen Festkörperelektrolyten, befasst sich diese Arbeit mit der Optimierung von NCM durch Dotierung sowie mit der Integration von NCM-Pulvern in Mischkathoden basierend auf LLZO:Ta. Zwei NCM Zusammensetzungen, $Li[Ni_{1/3}Co_{1/3}Mn_{1/3}]O_2$ (NCM111) und Ni-reiches $Li[Ni_{0.8}Co_{0.1}Mn_{0.1}]O_2$ (NCM811), sowie Dotierungen mit Bor und Ruthenium wurden untersucht. Dazu wurden reines NCM111, reines NCM811, B-dotiertes NCM111, B-dotiertes NCM811 und Ru-dotiertes NCM811 batchweise über eine Co-Fällung im Labormaßstab hergestellt. Zusätzlich zu dieser Batchsynthese im Glaskolben, wurde ein Couette-Taylor-Flow-Reaktor (CTFR) zur kontinuierlichen Synthese eingesetzt. Die dadurch optimierten Synthesebedingungen, resultieren in NCM mit optimaler Morphologie sowie deutlich verbesserten Lade- und Entladekapazitäten. Alle Kathodenaktivmaterialien wurden eingehend charakterisiert, um die erfolgreiche Dotierung des NCM Gitters nachzuweisen. Zusätzlich wurde der Einfluss der NCM Zusammensetzung und der Dotierungen auf die Morphologie und die elektrochemische Aktivität, in Zellen basierend auf flüssigem Elektrolyten, analysiert. Dichtefunktionaltheorie (DFT)-Berechnungen haben gezeigt, dass Bor, in Abhängigkeit seiner Konzentration, in den Ni und/oder O Schichten des NCM-Gitters sitzt und eine tetraedrische, beziehungsweise, trigonal planare Koordination mit Sauerstoff eingeht. Daher beeinflusst die B-Dotierung von NCM811 dessen Kristallstruktur, führt zu Kationenmischung sowie einer Veränderung der Primärpartikelform und -größe. Zum experimentellen Nachweis, dass diese Beobachtungen wirklich durch den Einbau von Bor in das NCM-Gitter hervorgerufen werden, wurde Bor über Ionenstrahlanalytik und Flugzeit-Sekundärionen-Massenspektrometrie (TOF-SIMS) detektiert, quantifiziert und lokalisiert. Die Ergebnisse zeigen, dass sich Bor auf der Oberfläche der Agglomerate anreichert, aber auch eine signifikant hohe Konzentration im inneren der Primärpartikel zu finden ist. Somit wurde der experimentelle Nachweis für den erfolgreichen Einbau von Bor in das NCM-Gitter erbracht. Letztendlich führt die B-dotierung von NCM811 zu einem verbesserten Kapazitätserhalt während des galvanostatischen Zyklierens der Zelle, welcher möglicherweise durch die Anreicherung von Bor auf der Sekundärpartikeloberfläche, unter Ausbildung einer Schutzschicht, erklärt werden kann.

Die vergleichende Analyse von NCM811 und NCM111 zeigte, dass die Übergangsmetallzusammensetzung einen Einfluss auf die Primärpartikelform hat. Während für das Ni-reiche NCM811 würfelförmige Primärpartikel erhalten wurden, zeigt NCM111 dünne flockenartige Primärpartikel. Eine Dotierung mit 2 mol% Bor führte zu größeren Gitterparametern und leicht erhöhter Kationenmischung. Zudem zeigt sie interessante Auswirkungen auf die Morphologie, nämlich härtere und größere Agglomerate, welche zu einer stark reduzierten BET Oberfläche, im Vergleich zum reinen NCM111, führen. Im Gegensatz zu NCM811, bewirkte die B-Dotierung von NCM111 keine verbesserte elektrochemische Leistung während Langzeitzelltests. NCM111 zeigte bereits einen sehr guten Kapazitätserhalt von 93 % nach 100 Lade- und Entladezyklen, welcher im Rahmen dieser Arbeit nicht weiter steigerbar war.

Neben Bor wurde auch Ruthenium als Dotierstoff in NCM811 untersucht. Ruthenium wurde erfolgreich in das NCM811 Gitter eingebaut und besetzt dabei, wie durch DFT-Berechnungen belegt wurde, vorzugsweise Ni-Positionen in den gemischten Mn/Ni Schichten. Die Ru-Dotierung vergrößert die Gitterparameter des NCM811 und führt, bedingt durch den hohen Oxidationszustand (Ru^{5+}), zu einer stark erhöhten Kationenmischung und der Ausbildung von Lithiumleerstellen. Des Weiteren führt die Ru-Dotierung zu einer deutlichen Verkleinerung der Primärpartikel. Ruthenium wurde erfolgreich über Transmissionselektronenmikroskopie (TEM)/Energiedispersive Röntgenspektroskopie (EDS), Ionenstrahlanalytik und TOF-SIMS nachgewiesen und quantifiziert. Im Vergleich zur B-Dotierung, führt eine Ru-Dotierung nicht zur Anreicherung von Ruthenium auf Sekundärpartikeloberfläche. Es zeigt sich eine gelichmäßige Verteilung von Ruthenium auf der Oberfläche sowohl als auch im inneren der Primärpartikel. Während der elektrochemischen Charakterisierung zeigten sich, im Vergleich zu NCM811 und B-dotiertem NCM811, höhere Widerstände und deutlich geringere Lade- und Entladekapazitäten.

Die verschiedenen Kathodenmaterialien, welche im Rahmen dieser Dissertation synthetisiert wurden, wurden auch mit LLZO:Ta gemischt, um die Materialkompatibilität während des Co-Sinterns zu untersuchen. Differenz-Thermoanalyse/Thermogravimetrie gekoppelt mit einem Massenspektrometer (DTA/TG/MS), *in-situ* Hochtemperaturröntgenbeugung (HT-XRD), Rasterelektronenmikroskopie (SEM) und EDS wurden benutzt, um die Nebenphasenbildung während des Co-Sinterns zu beobachten. Die DTA/TG/MS Analyse zeigte keine endo- oder exothermen Prozesse, die auf eine Zersetzungsreaktion hindeuten würden. Dennoch zeigte die *in-situ* HT-XRD Analyse, dass sich zwei Nebenphasen, nämlich $LaCo_{1-x}Mn_xO_3$ und $La_2(Ni_{0.5}Li_{0.5})O_4$, während des Co-Sinterns von NCM und LLZO:Ta bilden. Die Temperatur

bei der die Nebenphasenbildung beginnt sowie deren Menge hängt stark von der NCM Zusammensetzung und der Dotierung ab. Die B-Dotierung von NCM111 führte zu einer Verstärkung der Nebenphasenbildung. Im Gegensatz dazu, zeigte die B-Dotierung von NCM811 keinen Einfluss auf die thermodynamische Stabilität und die Ru-Dotierung resultierte sogar in einer leicht reduzierten Nebenphasenbildung. Die experimentellen Untersuchungen wurden durch DFT-Berechnungen unterstützt, welche belegen, dass Mn das bevorzugte Übergangsmetall in NCM ist, das einen Austausch mit Zr vom LLZO:Ta eingeht und es deshalb besonders beim Mn-reichen NCM111 zu verstärkter Nebenphasenbildung kommt. Erstaunlicherweise bildet Ni-reiches NCM811 im Kontakt mit LLZO:Ta nur eine, sich selbstbeschränkende, Menge an $La_2(Ni_{0.5}Li_{0.5})O_4$ aus und stellt sich damit als vielversprechendstes Aktivmaterial für die Kombination mit granatartigem LLZO:Ta heraus. Des Weiteren beeinträchtigt die B-Dotierung von NCM811 die thermische Stabilität gegenüber LLZO:Ta nicht, sodass die Verwendung von Li_3BO_3 (LBO) als Sinteradditiv problemlos möglich ist. Dies ermöglicht die Herstellung einer vollständig anorganischen Festkörperbatterie mit einer Lithiummetallanode, einem LLZO:Ta Separator und einer Mischkathode bestehend aus LLZO:Ta, LBO und NCM811. Die Verwendung des Sinteradditives ermöglicht die Herstellung einer dichten Mischkathode bereits bei 750 °C. Zusätzlich wird durch die Reaktion zwischen LBO und Li_2CO_3 die Ausbildung einer $Li_{2+y}C_{1-y}B_yO_3$ (LCBO) Zwischenphase, mit Lithiumionenleitfähigkeit, ermöglicht. Die im Rahmen dieser Arbeit hergestellte anorganische Festkörperbatterie funktionierte ohne Polymerzwischenschichten und lieferte eine besonders hohe spezifische flächenbezogene Entladekapazität von 0.7 mAh cm^{-2} im ersten Zyklus, welche eine der höchsten Leistungen ist, die bisher für granatartige Festkörperbatterien erreicht wurden.

Table of contents

Acknowledgements iv
Abstract vi
Kurzfassung x
Table of contents xiv
1. Introduction 16
1.1. Motivation – energy storage 16
1.2. Batteries for electrochemical energy storage 17
1.3. The cathode active material NCM: state of the art 24
1.3.1. Synthesis of NCM 24
1.3.2. Properties and drawbacks of NCM 31
1.3.3. NCM with core–shell and concentration gradient structure 35
1.3.4. Coating of NCM particles 39
1.3.5. Doped NCM 41
1.4. All-solid-state lithium batteries as future energy storage system 45
1.4.1. Anodes, separators, and composite positive electrodes for ASBs 46
1.4.2. Compatibility between solid-state electrolytes and cathode active materials 51
1.4.3. State of the art garnet-type ASBs 53
1.5. Objective of this thesis 59
2. Material characterization – theory and application 61
2.1. X-ray diffraction 61
2.2. Inductively coupled plasma – optical emission spectrometry 63
2.3. Electron microscopy 64
2.3.1. Scanning electron microscopy 64
2.3.2. Transmission electron microscopy 66
2.4. X-ray photoelectron spectroscopy 68
2.5. Ion beam analysis 69
2.6. Time-of-flight secondary ion mass spectrometry 73
2.7. Thermal analysis 75
2.8. Specific surface area by nitrogen adsorption 76
2.9. Powder density determination 78

2.10. Particle size distribution 79
2.11. Electrochemical characterization 79
2.11.1. Cyclic voltammetry 80
2.11.2. Galvanostatic charge/discharge technique 82
2.11.3. Electrochemical impedance spectroscopy 84
2.12. DFT calculation 88
2.12.1. Simulation of atomistic structure 88
2.12.2. Simulation of interdiffusion processes 89
3. Material synthesis, compatibility tests and cell fabrication: experimental part 91
3.1. Synthesis of cathode active materials 91
3.2. Synthesis of solid-state electrolytes 93
3.3. Fabrication of conventional cathodes and assembly of coin cells 94
3.4. Compatibility tests between NCM and LLZO:Ta 95
3.5. Fabrication of all-solid-state batteries 96
4. Detection and localization of boron in B-doped $Li[Ni_{0.8}Co_{0.1}Mn_{0.1}]O_2$ 98
5. Impact of $Li[Ni_{1-x-y}Co_xMn_y]O_2$ composition and doping on microstructural and electrochemical properties 116
5.1. B-doped $Li[Ni_{1/3}Co_{1/3}Mn_{1/3}]O_2$ 116
5.2. Ru-doped $Li[Ni_{0.8}Co_{0.1}Mn_{0.1}]O_2$ 124
6. The effects of a continuous co-precipitation in a Couette-Taylor-Flow-Reactor on the properties of NCM 137
7. Material compatibility of LLZO:Ta and NCM during co-sintering 145
8. Garnet-type all-solid-state battery with a NCM811 based composite cathode 156
9. Conclusions and outlook 162
List of abbreviations 167
References 170
Appendix 193
Publications and presentations 218
Curriculum vitae 220

1. Introduction

1.1. Motivation – energy storage

The availability of fossil energy sources for electricity generation is strongly limited and the consequences of global warming, caused by an increased man-made carbon dioxide emission (greenhouse effect), become more and more obvious by affecting our daily life. This reveals the importance of a transition from fossil to renewable energy sources. This increasing imperative of an energy transition, which is also promoted by the governments, requires a modification of the energy infrastructure to ensure a stable and climate friendly energy supply. During the last decade the share of renewable energies in gross electricity generation increased continuously, so that renewable energies already covered 44.5 % of the total amount of electricity generated in Germany in 2020 (Figure 1). In comparison, the share of renewable energies was only 33 % in 2017 [1, 2].

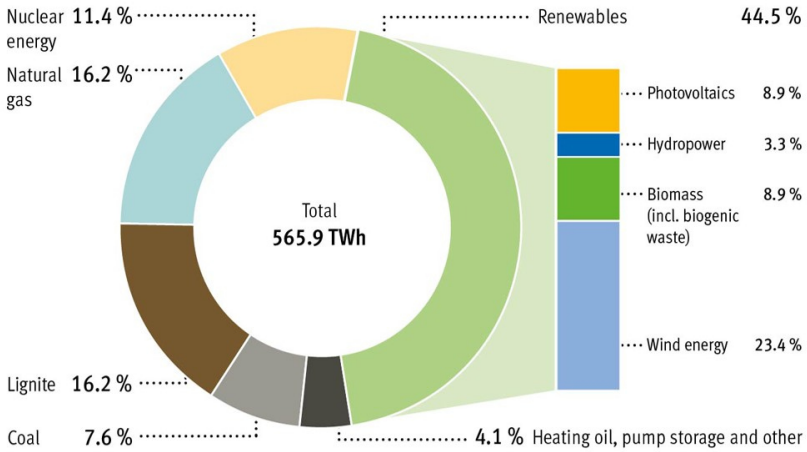

Figure 1: Gross electricity generation 2020 in Germany. Reproduced from ref. [2], Copyright 2021 Fachagentur Nachwachsende Rohstoffe e.V. (FNR).

Figure 1 clearly shows that the renewable energies are mainly based on wind power, biomass, and photovoltaics. Wind power and photovoltaics in particular are dependent on local and seasonal conditions, making them less flexible in use. Compared to a coal power plant, which can adapt to the demand of the grid, renewable energy sources are not predictable and continuously available. The excess energy generated during peak times must be stored when the generated energy cannot be fed into the electric grid. Therefore, the development of advanced energy storage systems with high specific energies is the focus of research. Compact electrochemical energy storage systems, such as batteries, that store energy with high efficiency (round trip efficiencies of up to 95 %), minimal environmental impact and a high level of safety are candidates for the energy storage system of the future. In particular, lithium-ion batteries

(LIBs) can be combined with the electric grid and can support the integration of a high share of photovoltaic and wind energy into the power mix. To achieve CO_2 neutral mobility soon, an electricity mix based on renewables and an excellent storage possibility in high-energy density batteries are the basis for the widespread introduction of electric vehicles (EVs) [3-10].

1.2. Batteries for electrochemical energy storage

Electrochemical energy storage systems, which include supercapacitors and fuel cells in addition to batteries, are preferred because of its desirable characteristics such as pollution free operation, long cycle life, and minimal maintenance. Batteries in particular have preferred energy characteristics, such as a direct response when spontaneous injection into the grid is required. They can bridge the gap between storage times of seconds or minutes (supercapacitors) and weeks or months (H_2 generation). In addition, batteries can be tiny (miniaturized) or large in terms of cell dimensions and capacity, enabling flexible use and opening up a wide range of applications. In this respect, batteries are excellent energy storage systems for the integration of renewable energy sources, portable electronics, and electric vehicles [3, 10-12].

The development of advanced energy storage systems is one of the most important issues of the 21st century. However, one of the first batteries – the voltaic pile – was already introduced in 1800 by Alexander Volta [13]. A battery is a series or parallel combination of several electrochemical cells. These cells convert chemical energy directly into electric energy through an electrochemical redox reaction. Compared to combustion processes, electrochemical conversion results in a high energy conversion efficiency. Battery cells consist of three main components, namely, a negative electrode (anode), which is oxidized and gives up electrons during the electrochemical reaction, a positive electrode (cathode), where reduction takes place by accepting electrons, and an electrolyte, which serves as an ionic conductor between the anode and the cathode. By convention, the terms anode and cathode are defined for the discharge process. The anode and the cathode need to be mechanically separated by a permeable separator to prevent short circuiting but enable ionic conduction between the electrodes. A liquid electrolyte is usually used to wet the separator and permeate the electrodes. The key features and basic construction of a battery cell are shown in Figure 2.

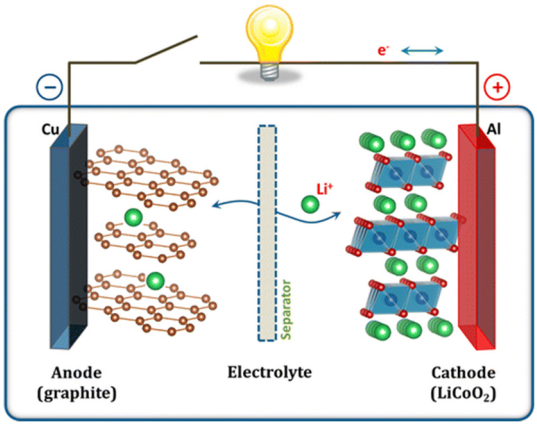

Figure 2: Schematic representation of a conventional Li-ion battery. Reprinted with permission from ref. [14], Copyright 2013 American Chemical Society.

The driving force for the redox reaction is a change in the systems standard free Gibbs energy ΔG^0. The relation between the cell potential and the free Gibbs energy is shown in equation (1):

$$\Delta G^0 = -nFE^0 \tag{1}$$

where F is the Faraday constant (F = 96487 C mol^{-1}), n the number of involved electrons, and E^0 (V) the standard potential. The standard cell potential is determined by the reduction potentials of the electrode materials E^0 under standard conditions (equation (2)).

$$E^0 = E^0_{\text{Cathode}} - E^0_{\text{Anode}} \tag{2}$$

If the cell is not working under standard conditions, the cell voltage is given by the Nernst-equation:

$$E = E^0 - \frac{RT}{nF} \ln\left(\frac{a^{\nu}_{\text{ox}}}{a^{\nu}_{\text{red}}}\right) \tag{3}$$

where R is the ideal gas constant (R = 8.31447 J mol^{-1} K^{-1}), T is the absolute temperature (K), and ν the stoichiometric coefficient. a_{ox} and a_{red} are the activities of the oxidized and reduced species, respectively.

As shown in equation (1), the change in the free Gibbs energy ΔG^0 defines the maximum electric energy that can be delivered by an electrochemical cell employing specific electrode materials. It is desired to convert the whole amount of this energy into useful electric energy during the discharge process. However, the current flow during the electrochemical reaction caused losses due to polarization. These polarization effects include activation and concentration polarization, which consume a part of the theoretical available energy. The activation polarization directs and limits the electrochemical surface reactions. Concentration polarization originates from the concentration gradient of reactants and products in the electrolyte between the electrode surface and the bulk. Another energy limiting factor is the

Ohmic drop (or IR drop), which originates from the internal cell resistance and results in a cell voltage drop. The influence of the polarization effects and the IR drop is shown in Figure 3.

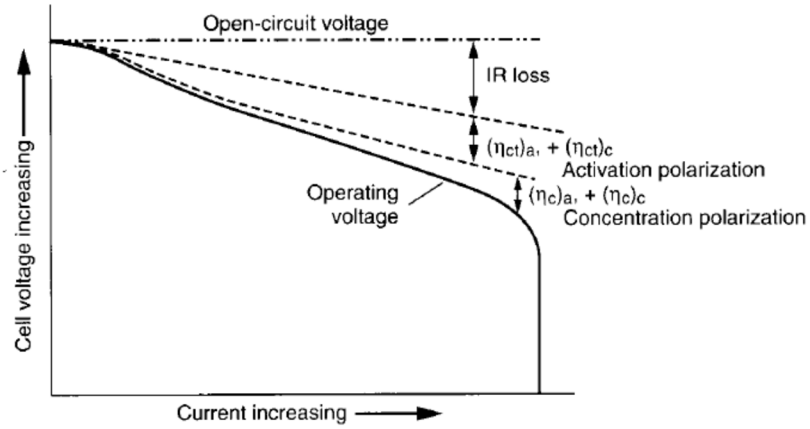

Figure 3: Theoretical cell voltage profile. The influence of polarization, discharge current, and cell impedance on the cell voltage are shown. Reproduced with permission from ref. [15], Copyright 2002 The McGraw-Hill Companies, Inc.

The influence of polarization and IR drop is small at low discharge currents, but at higher currents the Ohmic drop and the polarization cause a sharp drop in the operating voltage and available electrical energy. The definition of the specific electric energy is shown in equation (4).

$$\text{Specific Energy} = \int_0^{\Delta t} \frac{E(t) \cdot I \cdot dt}{m} \tag{4}$$

The gravimetric discharge energy density (Wh kg^{-1}) is calculated by the integration of the discharge voltage E (V) and discharge current I (A) divided by the active material loading m (kg) over the discharge period Δt (h). Of interest for portable batteries is also the volumetric energy density (Wh L^{-1}), which is obtained by dividing the gravimetric energy density by the cell volume (L).

The definition of the specific capacity is given in equation (5).

$$\text{Specific Capacity} = \int_0^{\Delta t} \frac{I \cdot dt}{m} \tag{5}$$

The specific gravimetric (Ah kg^{-1}) and specific areal (Ah cm^{-2}) discharge capacities are obtained by the integration of the discharge current I (A) over the discharge period Δt (h) divided by the active material loading m (kg) and electrode area (cm^2), respectively. In other words, the capacity is determined by the total amount of charge transferred by the current I. Thus, the capacity depends on I because the ion transfer rate across the electrolyte/electrode interface becomes diffusion limited at high currents causing a reversible capacity loss. Additionally, irreversible capacity losses occur due to changes in electrode volume, electrode-

electrolyte chemical reactions, and electrolyte decomposition. In rechargeable batteries, irreversible capacity loss occurs during the first charge due to the formation of a passivating solid electrolyte interphase (SEI) on an electrode, which is independent of the irreversible capacity fading during prolonged cycling (charge/discharge). The available energy of a battery depends on the electrochemical reactions at the anode and cathode, but there are other factors, such as the chemical stability of the battery components, the conductivity of the electrolyte, and the electrode materials themselves, that can decrease the usable energy and should be considered in battery design [14, 15].

Various battery systems have been developed over the last 200 years. Depending on their recharge capability, batteries are defined as primary (non-rechargeable) or secondary (rechargeable). Primary batteries are generally inexpensive and have been used primarily to power portable electronic devices, lighting, and toys. They cannot be easily recharged electrically and are therefore usually discarded after use [15]. The most common representatives are alkaline, zinc-carbon, and lithium batteries, but also metal–air batteries, such as Si–air batteries, which are still in the development stage [11, 16, 17]. Typical representatives of secondary batteries are lead-acid, Li–S, Li–ion, Al–ion, Ni–MH, Ni–Cd, and Ni–Zn batteries. Rechargeable batteries for large-scale/grid-scale energy storage include vanadium-based redox flow and Na–S batteries [11, 18]. On the one hand, secondary batteries are used as energy-storage devices that deliver energy one demand. Applications include motor vehicles (lead-acid batteries), emergency power units, and hybrid electric vehicles. In contrast to the primary batteries, the secondary battery can be recharged after the stored energy has been consumed [15].

Primary lithium batteries, developed since 1960, are based on a lithium metal anode and offer outstanding features such as high voltage, high specific energy density, and long shelf life. However, they are inferior because of major safety concerns due to the high reactivity of Li metal in contact with air and moisture, which produces hydrogen gas. Therefore, lithium batteries should not be confused with today's secondary lithium-ion batteries (LIBs) [11, 15]. Rechargeable LIBs, which offer a higher level of safety, high reliability, high energy density and good cycling stability, are the focus of research and are considered as one of the most promising energy storage devices. They are considered to play an important role in promoting the development of electric vehicles, as well as a power source for small electronic devices, portable electronics, power tools, medical devices, and renewable power supply systems that can be grid-connected or off-grid (e.g., solar home systems) [10, 18].

One of the first LIBs was demonstrated in 1976 by M. S. Whittingham[19], who was employed by Exxon at that time. This battery was based on the layered TiS_2 intercalation cathode, Li metal anode, and lithium perchlorate in dioxolane as electrolyte. However, the establishment was not successful because the metallic Li anode combined with the liquid, organic electrolyte led to shortcomings due to dendrite growth, resulting in short circuits and explosion hazards during prolonged cycling. The discovery of graphite with layered structure as a reversible Li^+ intercalation anode by J. O. Besenhard as well as the proposal of layered $LiCoO_2$ (LCO) as a high energy and high voltage cathode active material by J. B. Goodenough in 1981 led to a breakthrough in LIB development. In 1987, A. Yoshino filled a patent and built the first cell with air stable materials, namely, a carbonaceous anode and discharged LCO cathode [20, 21]. J. B. Goodenough, M. S. Whittingham and A. Yoshino were deservedly honoured with the 2019 Nobel Prize in Chemistry for their pioneering work in the development of LIBs [22].

This first-generation of lithium-ion batteries, commercialized by Sony in 1991, was based on a graphite anode, a lithium ion-conducting liquid, organic electrolyte ($LiPF_6$ in propylene carbonate and diethyl carbonate (PC:DEC, 1:1)), and a $LiCoO_2$ (LCO) cathode [20, 23]. The setup and the electrochemical half-cell reactions of the first commercialized LIB are shown in Figure 2 and Scheme 1, respectively. During battery discharge, the deintercalation of Li ions from the anode material takes place (oxidation). The Li ions diffuse through the electrolyte to the cathode, where intercalation of Li ions into the cathode material takes place (reduction). This process is reversed when the battery is charged. The generated electrons are transferred through an external electric circuit via a consumer load between the anode and the cathode. This early battery delivered a cell voltage of 3.6 V and a specific discharge energy of around 98 Wh kg^{-1} [6, 15, 24].

$$Li_{1-x}CoO_2 + x\,Li^+ + x\,e^- \underset{\text{charge}}{\overset{\text{discharge}}{\rightleftharpoons}} LiCoO_2$$

$$LiC_6 \underset{\text{charge}}{\overset{\text{discharge}}{\rightleftharpoons}} Li_{1-x}C_6 + x\,Li^+ + x\,e^-$$

Scheme 1: Electrochemical half-cell reactions during charging and discharging [6].

Following the commercialization of Li-ion batteries in the 1990s, they quickly conquered the market and can now be found in a wide range of applications, with new applications still emerging. The growing interest in powering various portable electronic devices, power tools and electric vehicles drove rapid development of the electrode materials and improved battery pack designs aimed at higher energy and power density. However, this led to new challenges

such as range, lifetime, cost, safety, dimensions, and weight of the batteries. These challenges have been addressed through the development of battery systems, including anode and cathode materials that meet the necessary requirements to overcome the drawbacks of the early battery systems.

In addition to the development and optimization of cell/ battery-pack designs [25, 26] and anode materials [27], most attention has been paid to the adaptation of cathode active materials (CAMs) for lower cost, higher capacities, and energy densities. Various CAMs have been developed for rechargeable LIBs because they are an important component determining the battery's storage capacity (Figure 4).

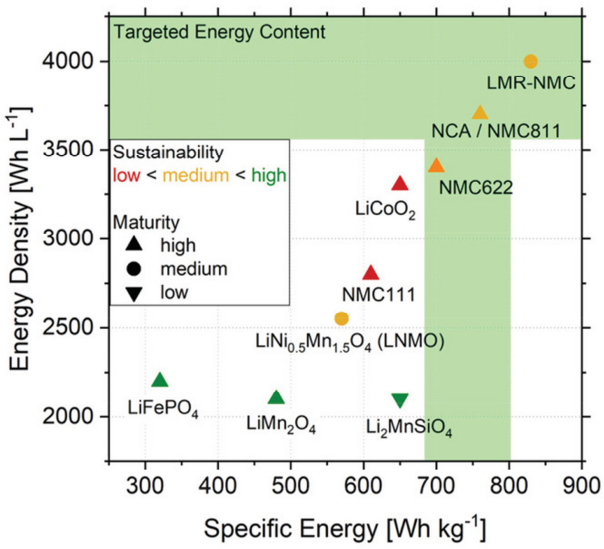

Figure 4: Energy density versus specific energy at the material level of selected cathode materials for LIBs. Their sustainability and technological maturity are visualized. Reproduced from ref. [28], Copyright 2020 The Authors.

A suitable cathode material for a LIB must contain an easily reducible/oxidizable cation, for example a transition metal cation (M^{m+}) and should react rapidly and reversibly with lithium at a high free energy of reaction. A high capacity (at least one Li atom per transition metal) and a high voltage of around 4 V are preferred, resulting in a high energy density. In addition, the cathode material should be a good electronic conductor to enable the electrochemical reaction at all contact points between active material and electrolyte and to minimize the need for conductive additives. In addition, structural stability with low volume change during charge/discharge is required to minimize the mechanical degradation. Furthermore, the CAM should be cost effective and environmentally friendly [29]. The CAMs which are widely used in commercial LIBs include $LiCoO_2$ (LCO), $LiMn_2O_4$ (LMO), $Li[Ni_{1-x-y}Co_xMn_y]O_2$ (NCM), $Li[Ni_{0.8}Co_{0.15}Al_{0.05}]O_2$ (NCA), and $LiFePO_4$ (LFP) [30]. Table 1 provides an overview of these cathode materials, their potentials, and specific practical capacities.

Table 1: Overview of common cathode active materials for LIBs [15, 31].

Cathode material	Structure type	Potential vs. Li/Li^+ [V]	Capacity [mAh g^{-1}]
LCO	layered	3.9	140 – 145
NCM	layered	3.8	160 – 170
NCA	layered	3.8	180 – 200
LFP	olivine	3.5	150 – 170
LMO	spinel	4.1	100 – 120

The layered structured cathode material LCO was introduced by J. B. Goodenough *et al*.[32] and is still popular today due to its high energy density, high operating voltage, excellent cycle stability, easy synthesis and stability under ambient atmosphere. LCO exhibits very high compacted density and is therefore the most commonly used cathode material in LIBs for small portable electronic devices [4, 30]. Other layer structured cathode materials have been obtained by substituting Co in LCO with elements such as Ni, Mn, and Al. As shown in Table 1, due to lower Co and higher Ni content, these CAMs provide better specific capacity and are less toxic and expensive. Since increasing the Ni content leads to higher capacity, many of today's electric vehicles (BMW i3, VW e-Golf, etc.) have incorporated LIBs based on layered Ni-rich NCM as a cathode material [10, 33]. Of the CAMs listed in Table 1, NCA delivers the highest specific capacity and is the cathode material used in Tesla's electric vehicle batteries. Lithium iron phosphate (LFP) with olivine structure, discovered in 1997 by A. Padhi *et al*.[34], delivers only a moderate capacity up to 170 mAh g^{-1}, but has many advantageous properties such environmental benign, high safety, non-toxicity, low cost and high electrochemical stability. LFP is considered as the most promising cathode material for next generation lithium-ion batteries [4, 5, 10, 24]. The LIBs based on LFP are successfully used in e-bikes [10]. LMO spinel cathodes show the highest potential versus Li/Li^+ of the above CAMs. Unlike the layered structure, the spinel structure exhibits three-dimensional Li-ion diffusion paths, resulting in a low internal resistance and thus a relatively high specific power can be obtained. In addition, LMO is cobalt free and based on abundant and environmentally friendly materials, but its drawback is its low energy density. LIBs with LMO as cathode material are mainly used in e-bikes, power tools, and medical devices [10].

Due to the outstanding high capacities, but also the limited stability of Ni-rich NCM [33], the NCM class of CAMs is in the focus of this work and will be discussed in more detail in the following chapter.

1.3. The cathode active material NCM: state of the art

This chapter focuses on the synthesis of layered lithium-nickel-cobalt-manganese-oxide ($Li[Ni_{1-x-y}Co_xMn_y]O_2$, NCM) and its properties and drawbacks as a cathode material in LIBs. Furthermore, possible options to improve the electrochemical performance of Ni-rich NCM are discussed.

1.3.1. Synthesis of NCM

A suitable synthesis strategy is the crucial step to develop promising cathode materials. Sol–gel[35], Pechini[36], spray-pyrolysis[37] and co-precipitation[38, 39] are the main methods for the synthesis of NCM cathode material powders for LIBs. Among these routes, the co-precipitation is preferred because it offers a unique growth mechanism to spherical particles, high tap density, and the possibility of industrial large-scale production. A high tap density is advantageous to obtain cathode materials with high volumetric energy density, and the unique growth mechanism of spherical precursors particles is particularly important when synthesis of core–shell and concentration gradient structures is desired. The synthesis of NCM by co-precipitation is easily scalable and typically carried out in a continuous stirred tank reactor (CSTR) with volumes of up to 170 L (Figure 5a) [40-43].

Regarding the chemical nature of the precipitant, the co-precipitation is classified into three routes, namely, hydroxide[38], carbonate[44], and oxalate[45]. In the following, the discussion is limited to hydroxide co-precipitation, which was used to synthesize NCM in this thesis. Figure 5b shows a schematic representation of the hydroxide co-precipitation route based on the optimized synthesis conditions for $LiNi_{1/3}Co_{1/3}Mn_{1/3}O_2$ (NCM111) found by M. H. Lee *et al*.[38]. The route to obtain NCM mainly consists of two steps, the co-precipitation of the hydroxide precursor and subsequent solid-state reaction (calcination) in the presence of a lithium source (Figure 5b) [40]. For the synthesis of the NCM hydroxide precursor ($Ni_{1-x-y}Co_xMn_y(OH)_2$), an aqueous solution containing the transition metals Ni, Co, and Mn with a desired concentration and ratio is needed. Already in this solution, other elements, such as dopants, can be easily introduced to optimize the cathode material (the importance of doping is explained in Chapter 1.3.5). In addition, two aqueous, alkaline solutions containing NaOH and NH_4OH as chelating agents with desired concentrations are required. The transition metal and NH_4OH solutions are fed in a dropwise manner into a reactor under stirring, and the pH is precisely controlled by adding the NaOH solution. The co-precipitation is performed at medium temperatures of up to 60 °C.

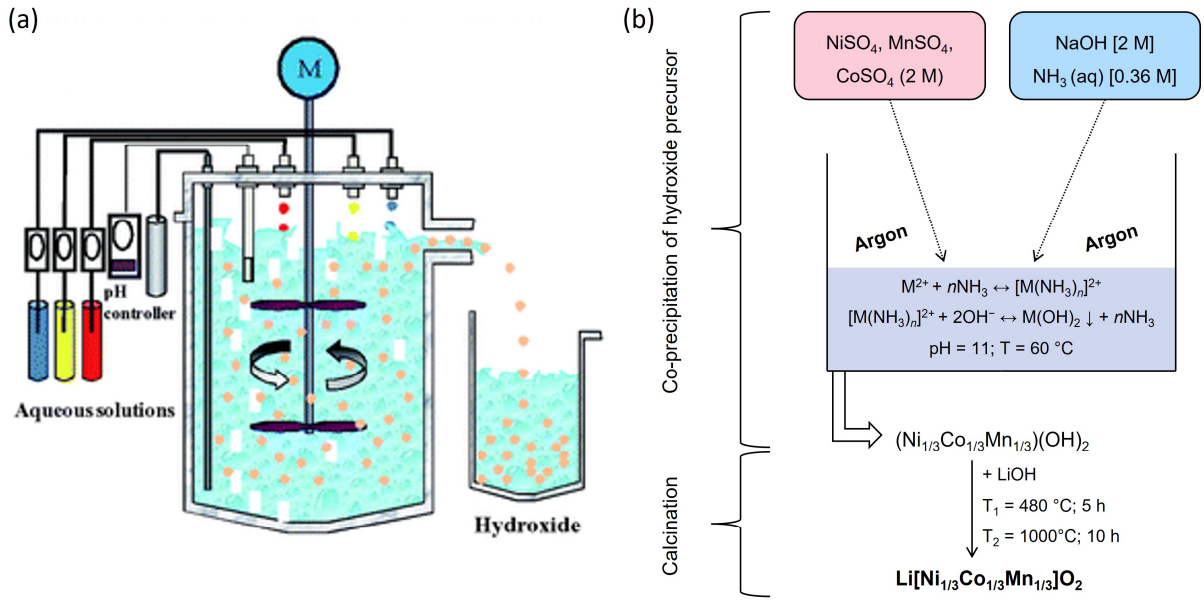

Figure 5: (a) Schematic representation of a CSTR used for the continuous co-precipitation of NCM precursors. Reproduced (adapted) with permission from ref. [46], Copyright 2010 The Royal Society of Chemistry. (b) Schematic display of NCM111 synthesis via co-precipitation based on the optimized conditions found by M. H. Lee *et al*. [38].

The precipitation of the hydroxide starts with the addition of the alkaline solution. Since the solubility product constant (K_{sp}) of $Mn(OH)_2$ ($K_{sp} = -12.7$) is significant higher than that for $Ni(OH)_2$ ($K_{sp} = -15.2$) and $Co(OH)_2$ ($K_{sp} = -14.9$), ammonium hydroxide is necessary as a chelating agent to achieve a homogenous, atomic distribution of nickel, cobalt, and manganese. In the presence of aqueous ammonia, an alternative growth mechanism for spherical hydroxides is proposed, where particle growth takes place due to the equilibrium between metal hydroxide particles and aqueous ammonia solution [24, 38, 40, 42, 47]. The mechanism is shown in Scheme 2.

$$M^{2+} + n NH_3 \leftrightarrow [M(NH_3)_n]^{2+}$$

$$[M(NH_3)_n]^{2+} + 2OH^- \leftrightarrow M(OH)_2 \downarrow + n NH_3$$

Scheme 2: Mechanism of metal hydroxide precipitation in the presence of aqueous ammonia (M = Ni, Co, Mn) [40, 42].

Co-precipitations with ammonia as chelating agent starts with the formation of a metal-ammonia complex. The transition metal (TM) ions are coordinated simultaneously with ammonia ligands. The ammonia anions are slowly replaced by hydroxide anions via an anion-exchange reaction. In this mechanism, the metal hydroxide has an increased solubility in the presence of aqueous ammonia. The strength of dissolution of the metal hydroxide depends on the pH, which varies depending on the metal. The growth of micrometer-sized, monodisperse,

spherical hydroxide particles is believed to be due to the self-assembly of nano-sized primary particles in response to coalescence and the Ostwald-ripening mechanisms, in which small particles (crystal nuclei) are progressively consumed in favor of the formation of larger particles. The driving force is the minimization of the surface free energy via a dissolution–recrystallization mechanism. Accordingly, spherical particles are obtained due to a lower free energy compared to other morphologies [40, 42].

To prevent the oxidation of $Ni_{1-x-y}Co_xMn_yO_2(OH)_2$, the co-precipitation reaction takes place under an inert gas atmosphere (nitrogen or argon), and degassed water is used as starting medium and for preparation of the TM and alkaline solutions. Nevertheless, oxidation of the hydroxide occurs when it is exposed to air after synthesis, especially at elevated temperatures. During oxidation, in the case of NCM111, the color of the precursor changes from light pink to dark brown. The color change can be explained by the formation of an oxyhydroxide side phase ($Ni_{1-x-y}Co_xMn_y(OOH)$). The spherical NCM hydroxide precursor particles (Figure 6a) are finally obtained after filtration, washing, and drying at 80 °C in vacuum. Subsequently, lithiation to the final $Li[Ni_{1-x-y}Co_xMn_y]O_2$ is carried out by a two-step calcination. The precursor powder is mixed with 3 – 10 wt% excess of a Li source (e.g., LiOH) and heat threated at elevated temperatures under an oxygen containing atmosphere. The first step is performed at 480 °C for 5 h, and the calcination temperature of the second step depends strongly on the composition of TM in the NCM. Usually, temperatures between 750 °C and 1000 °C for 10 h are chosen [24, 38, 47, 48].

For the synthesis of NCM precursors with core–shell structure or concentration-gradient, the same co-precipitation route as described before can be used. To realize a core–shell structure, the NCM core should be pre-synthesized by adding the core solution (aqueous transition metal solution with the desired core composition) into the reactor. Afterwards, a transition metal solution with desired NCM shell composition is added into the reactor containing the pre-synthesized spherical core particles. The shell precipitates on the core. In order to obtain concentration-gradient layered oxides, the core solution is partially dripped into the reactor to form the core. Then the shell solution is gradually added to the residual core solution to form the concentration gradient solution, which is meanwhile also injected into the reactor. Finally, the core is encapsulated by a concentration-gradient layer. It is well known that calcination temperatures of 850 °C and higher can lead to a partial cross-diffusion of cations between the core and shell, which should be taken into account when calcining NCM with core–shell structure [40]. The concepts of core–shell and concentration-gradient structures are presented in detail in Chapter 1.3.3.

The concentrations of transition metal, NaOH and NH_4OH solutions, the adjusted pH, the precipitation temperature, the stirring speed as well as the reaction time are important factors to be controlled. However, they vary from publication to publication and depend on the composition of NCM and the targeted morphology. The effects of these important parameters are described below for the synthesis of NCM111 in a CSTR (capacity 4 L) [38]. The concentration of chelating agent NH_4OH affects the particle morphology and particle size distribution (PSD). Increasing the NH_4OH concentration results in more uniform and more spherical particles with narrower PSD and higher tap density. The presence of NH_4OH prevents phase separation of $Ni(OH)_2$, $Co(OH)_2$, and $Mn(OH)_2$ by leading to a heterogeneous precipitation of the metal hydroxides, so that a homogenous hydroxide precursor is obtained. The control of the pH is important because it determines particle size and morphology. Increasing the pH leads to a decrease in secondary particle size, but high pH values should be avoided in the presence of oxygen, as they facilitate the formation of manganese dioxide. In the case of NCM111, pH = 11 was chosen as this leads to ideally spherical secondary particles with an average diameter of 10 µm (Figure 6a) and high tap density. The stirring speed during co-precipitation also affects the particle size and shape. At high stirring speeds, the secondary particles become smaller, denser, and more spherical. The highest tap density of 2.39 g cm^{-3} and the highest specific gravimetric and volumetric capacity were obtained at 1000 rpm. During calcination, the shape of acicular primary particle of the precursor changes to a square shape (cuboidal) with a diameter of 0.5 – 1 µm, while a similar size and shape of secondary particles is observed (Figure6 b) [38].

The calcination temperature has a strong influence on the morphology of the NCM cathode powder, which ultimately affects the electrochemical performance. In the case of NCM111, calcination at 850 °C and 900 °C results in flake-shaped primary particles (Figure 6c), while cuboidal primary particles are obtained after calcination at 950 °C and 1000 °C (Figure 6d). The size of primary particles increases with increasing the calcination temperature, while the BET surface area decreases. The electronic conductivity measured by dielectric spectroscopy is affected by the calcination temperature, so it was one order of magnitude higher for NCM111 calcined at 850 °C than after calcination at 1000 °C. This indicates that the flake-shaped primary particles facilitate electronic motion on all length scales and that the charge-transfer limitations are not electronic but result from the contribution of material interface to the electrochemical process. For the NCM111 with cuboidal primary particles, diffusion is the rate limiting step because dense agglomerates dictate the electrochemical process and opening the intra-agglomerate porosity can strongly increase the power performance [49].

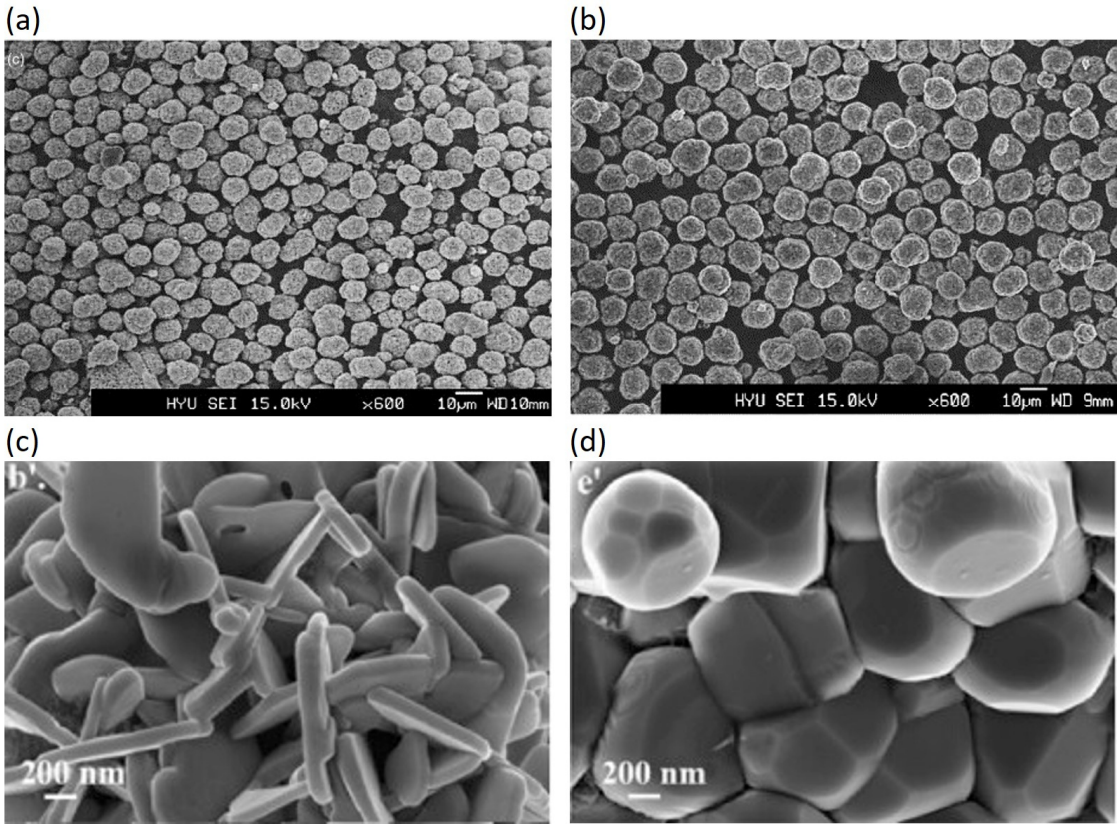

Figure 6: SEM image of (a) NCM111 precursor and (b) NCM111 calcined at 1000 °C. Reproduced (adapted) with permission from ref. [38], Copyright 2004 Elsevier Ltd. Magnified SEM images of NCM111 calcined at (c) 850 °C showing flake-shaped primary particles and at (d) 1000 °C showing cuboidal primary particles. Reproduced (adapted) with permission from ref. [47], Copyright 2017 Elsevier B.V.

As mentioned above, the synthesis of $Li[Ni_{1-x-y}Co_xMn_y]O_2$ is usually performed in a large scale continuous co-precipitation process in a CSTR with a volume of 4 – 170 L to obtain high performance NCM with optimized morphology. The particles produced in this way are characterized by an ideal spherical shape and narrow PSD (Figure 6a,b), which is difficult to achieve with other synthesis methods, reactor types, and production scales. The uniform particle growth within such a CSTR enables the synthesis of particles with core-shell structure[40] and concentration gradients [50, 51]. In addition, the ideal spherical shape of the particles opens the possibility of applying homogenous surface coatings to the NCM particles [52-54]. The necessity of such modifications will be discussed in the following chapters.

In addition to a CSTR, the so-called Couette-Taylor-Flow-Reactor (CTFR) is well known and highly appreciated for the continuous NCM precursor synthesis [55-59]. A schematic representation a CTFR is shown in Figure 7a,b.

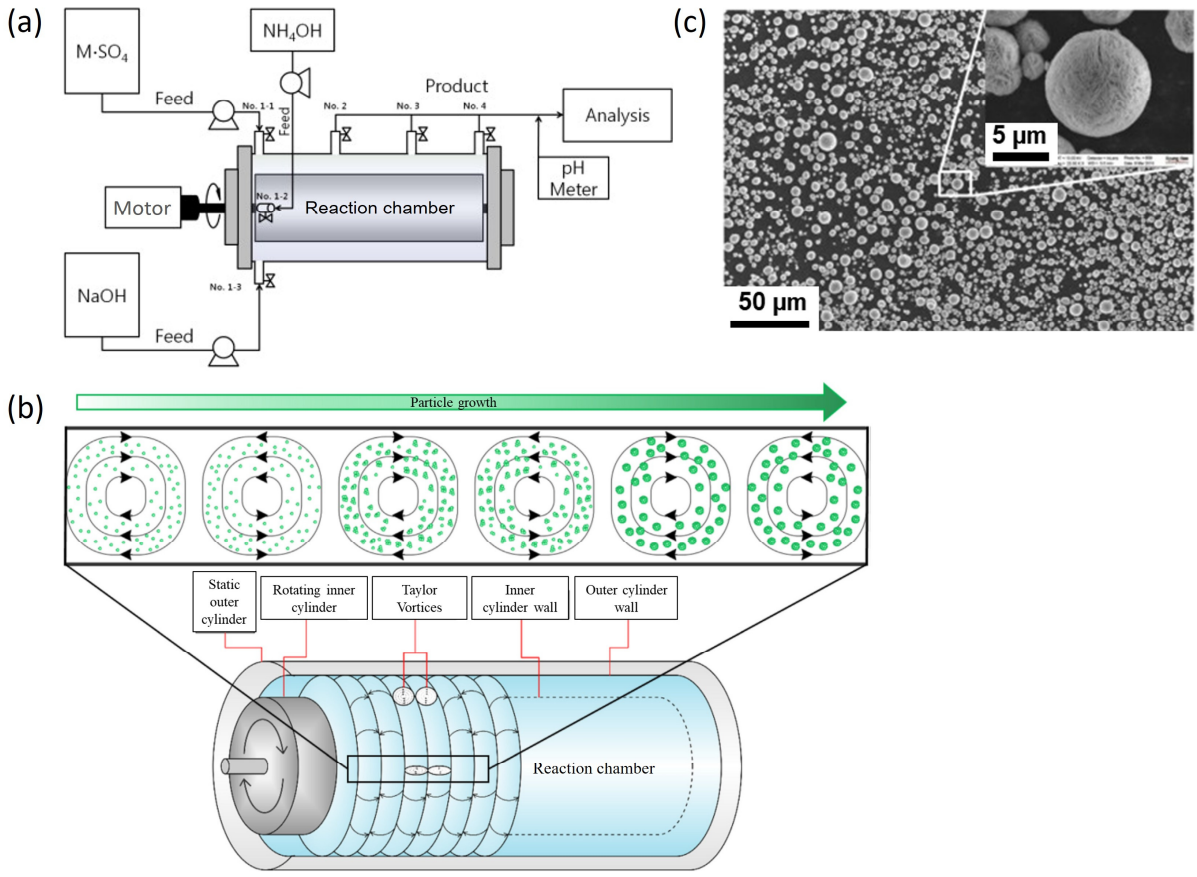

Figure 7: (a) Schematic drawing of a Couette-Taylor-Flow-Reactor (CTFR). Reproduced (adapted) with permission from ref. [58], Copyright 2011 Elsevier B.V. (b) Reaction chamber of a CTFR showing the formation of Taylor vortexes and the particle growth along the length scale of the reaction chamber. Reproduced (adapted) with permission from ref. [60], Copyright 2020 Elsevier B.V. (c) SEM images of the resulting NCM hydroxide precursor secondary particles. Reproduced (adapted) with permission from ref. [58], Copyright 2011 Elsevier B.V.

The main reactor consists of two co-axially arranged stainless steel cylinders with different diameters (Figure 7b). The stainless steel can be coated with Teflon to avoid corrosion and to increase the lifetime. For example, the diameters of the inner and outer cylinders are 76 mm and 84 mm, respectively, and have a length of 250 mm. The space between the two cylinders forms the reaction chamber. The reactors are available with working volumes between 0.1 and 1000 L. A motor rotates the inner cylinder so that the solution starts moving and then forms a stream in the direction of rotation, but centrifugal and Coriolis forces act on the fluid so that it moves toward the outer cylinder. When the rotation speed is high enough, the fluid flow gradually becomes unstable and the transition region between laminar and turbulent flow, the Taylor flow, is reached. In the solution between the two cylinders, Taylor vortexes of a ring pair array are formed. They rotate regularly in the counter directions along the axial direction (Figure 7b). These Taylor vortexes result in an intense and homogeneous radial mixing with low axial dispersion. In this way, high mass and heat transfer can be realized and dead zones

are avoided, leading to an overall improvement of purity, morphology, and crystallinity. Unlike stirred tank reactors and CSTR, in which macro-mixing occurs, micro-mixing is realized in a CTFR. The Taylor vortexes generate periodic toroidal flow motions, which have been shown to be more effective for the continuous co-precipitation of the NCM precursors than the random turbulent vortexes of other reactors [57, 59, 61, 62]. The design of the Taylor-flow reactor enables automatic and simultaneous dosing of up to three reactants into the reaction chamber. The transition metal solution (Ni, Co, and Mn) and the NH_4OH solution are fed into the reactor at defined flow rates, while the pH is controlled and automatically adjusted by dosing of the NaOH solution. After a defined residence time, which is determined by the substrates volume flow, the product is collected on the opposite side of the reaction chamber. Ideally, spherical particles with a narrow particle size distribution can be obtained by precise selection of the rotation speed and residence time (Figure 7c) [58]. As demonstrated by J.-E. Kim *et al*.[57] and J. Helbig *et al*.[63], it is also possible to synthesize NCM particles with core-shell structure using a CTFR. A transfer of this approach to the production of NCM particles with concentration gradients is also possible.

In general, a Couette-Taylor-Flow-Reactor offers the same possibilities for synthesis of NCM precursors as a CSTR. However, the major advantages of the CTFR are the three times higher mass transfer velocity, the seven times higher agitation strength, and the micro mixing, which positively affects the homogeneity and morphology towards ideally spherical secondary particles with narrow PSD. Furthermore, the CTFR is available as a compact device and includes the main reaction chamber as well as the controlling units. The CTFR enables the automated, continuous NCM precursor synthesis at laboratory scale without compromising morphology and electrochemical performance [62, 64]. The application of a CTFR is not limited to the synthesis of precursors for cathode active material. It also enables the continuous synthesis of the precursors for, $Li_7La_3Zr_2O_{12}$ (LLZO) solid-state electrolyte (SSE) via co-precipitation with non-negligible advantages compared to a batchwise synthesis. In the case of Ga-doped LLZO (LLZO:Ga), the ionic conductivity could be increased from $3.9 \cdot 10^{-4}$ S cm^{-1} (batch synthesis) to $1.2 – 1.75 \cdot 10^{-3}$ S cm^{-1} by a continuous synthesis using a CTFR [61]. Moreover, composites of active material (NCM) and SSE (LLZO) precursors can be synthesized in a one-step process using a CTFR [65].

Based on these previous publications, the use of a Couette-Taylor-Flow-Reactor for the continuous synthesis of NCM and LLZO by co-precipitation proves to be a suitable method to obtain active materials, as well as solid-state electrolytes with optimized performance.

1.3.2. Properties and drawbacks of NCM

$Li[Ni_{1-x-y}Co_xMn_y]O_2$ (NCM) is considered as one of the most promising cathode materials to replace the expensive and toxic $LiCoO_2$ (LCO) in lithium-ion batteries (LIBs) while increasing their energy density. Basically, NCM is obtained by substituting cobalt in LCO with nickel and manganese. Both NCM and LCO belong to the intercalation cathode materials. An intercalation cathode is a solid host framework that can reversibly store guest ions like Li ions. Li ions are de-intercalated or intercalated while charging or discharging a LIB, respectively. NCM has a layered structure and crystallizes in the α-$NaFeO_2$ structure with the space group $R\bar{3}m$ (No. 166), as shown in Figure 8 [24, 66].

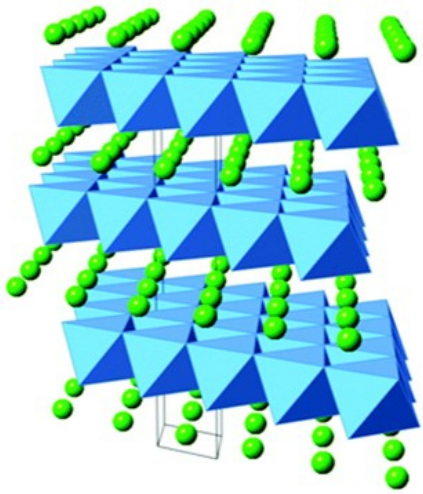

Figure 8: Crystal structure of layered NCM. Li ions are shown as green spheres and MO_6 octahedron are depicted in blue. Reproduced (adapted) from ref. [67], Copyright 2014 The Royal Society of Chemistry (https://creativecommons.org/licenses/by/3.0/).

The transition metal ions and Li ions occupy the octahedral coordinated positions in a cubic closed packed oxygen-grid. In the [111] direction of the cubic structure, the Li ions are located between the MO_2-layers (layered structure). The diffusion of Li ions takes place two-dimensionally between the lattice space in the *a*- and *b*-directions, resulting in a high Li-ion mobility.

Layered $Li[Ni_{1/3}Co_{1/3}Mn_{1/3}]O_2$ (NCM111) was first reported in 2001 by O. Tsutomu *et al.*[68] who demonstrated that it can delivered a capacity of 150 mAh g^{-1} when operated between 3.5 V and 4.2 V. Compared to $Li_{1-x}CoO_2$, whose structure becomes instable at lithium extraction degrees below x(Li) = 0.5, NCM can be charged to higher cut-off potentials because the redox couples Ni^{2+}/Ni^{3+} and Ni^{3+}/Ni^{4+} allow higher Li extraction without direct structural deterioration. Thus, Ni in NCM provides the high capacity, while Co is responsible for an increased electronic conductivity, leading to a good rate capability, and the electrochemically inactive Mn stabilizes the hexagonal NCM structure at high lithium extraction degrees,

providing excellent cycle life and safety during cycling [24, 40, 68, 69]. Therefore, the intrinsic properties of NCM cathodes are strongly dependent on the individual Ni/Co/Mn ratios. The phase diagram shown in Figure 9 illustrates the compositions of common NCM materials.

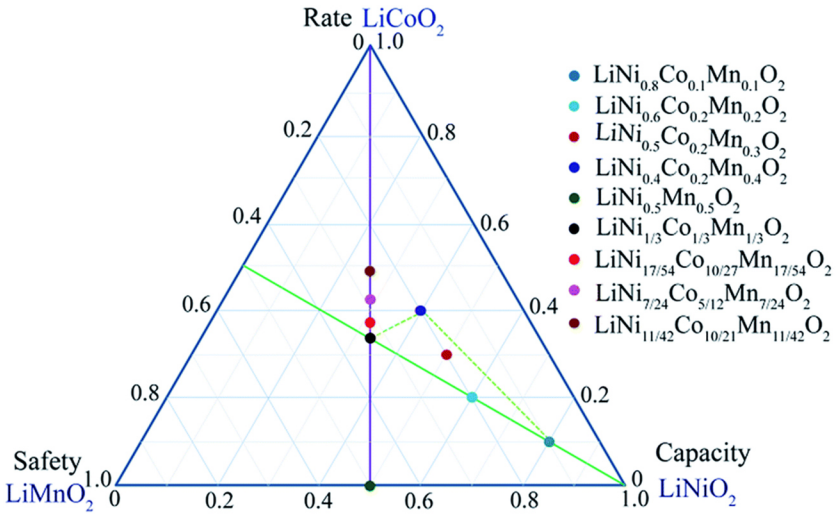

Figure 9: Triangular phase diagram of $LiNiO_2$–$LiCoO_2$–$LiMnO_2$ and the corresponding NCM compositions located in this phase diagram. Reprinted with permission from ref. [40], Copyright 2017 The Royal Society of Chemistry.

As shown in Figure 10a, the initial specific discharge capacity increases significantly with increasing the Ni content from 160 mAh g^{-1},for standard NCM111, to 206 mAh g^{-1} for Ni-rich $Li[Ni_{0.85}Co_{0.075}Mn_{0.075}]O_2$ (NCM85) [24]. For the highly Ni-rich $Li[Ni_{0.95}Co_{0.025}Mn_{0.025}]O_2$ (NCM95), even 235 mAh g^{-1} were reported by H.-H. Ryu *et al.* [70]. In addition to the capacity, also the electronic conductivity increases nearly linearly with the nickel content from $5.2 \cdot 10^{-8}$ S cm^{-1}, for NCM111, to $2.8 \cdot 10^{-5}$ S cm^{-1} for NCM85. This can be explained by the mixed valence of Ni^{2+}/Ni^{3+} in NCM, which leads to an increasing Ni^{3+} concentration when the Ni-content increases. Moreover, the Li^+ chemical diffusivity increases with increasing Ni content from around 10^{-11} cm^2 s^{-1}, for NCM111, to 10^{-8} cm^2 s^{-1} for NCM811. Thus, the rate capability of NCM is affected by the NCM composition as it directly depends on the electronic conductivity and Li^+ chemical diffusivity [24].

Modification of the NCM compositions toward higher Ni contents can greatly increase the energy density of a LIB. However, the composition of transition metals in the NCM structure also affects the structural, cycling, and thermal stability of the cathode active material (Figure 10a). In addition to the advantageous high capacities, the Ni-rich NCM cathodes have disadvantages such as fast capacity fading during cycling, poor thermal stability, cation disorder, and dramatic heat release in the highly delithiated state. These properties are problematic for the practical application of Ni-rich NCM in LIBs. The electrochemical properties and safety of CAMs depend on the microstructure and the physicochemical

properties, such as Li^+ diffusivity, electronic conductivity, volume expansion, chemical stability, and Li excess. While the Ni-deficient NCM111 with its stable composition and high structural stability exhibits high Li^+ interaction stability during cycling and thus, a capacity retention of more 92 % after 100 cycles, the Ni-rich $Li[Ni_{0.8}Co_{0.1}Mn_{0.1}]O_2$ (NCM811) shows capacity retention of only 70 %. This poor Li^+ intercalation stability can be explained by the formation of a more stable spinel or $Li_xNi_{1-x}O$ phase on the surface of NCM811 after prolonged cycling, while NCM111 retains the original layered structure. This structural degradation leads to an increasing interfacial resistance and therefore to capacity loss during long-term cycling. The structural stability of NCM is affected by the primary particle size, which decreases significantly when the Ni content in NCM is increased. Due to the strain associated with the phase transformation, a structural transformation becomes easier with the smaller particles of Ni-rich NCM [24].

Differential capacity plots and cyclic voltammetry (CV) during charging of Ni-rich NCM811show multiple phase transitions from hexagonal (H1) to monoclinic (M), from monoclinic to hexagonal (H2), and from hexagonal to hexagonal (H3), which were not observed for NCM with lower Ni-contents (e.g., NCM622 or NCM111). The structural transformation from H2 to H3 is accompanied by a rapid volume contraction in *c*-direction, which underlines the structural instability of Ni-rich NCM [24, 70]. In general, an anisotropic volume contraction of the $Li_x[Ni_{1-y-z}Co_yMn_z]O_2$ lattice is observed during delithiation (charging). The negative changes in lattice parameter *a* during charging are rather small, but affect the cell volume to the second power, so that the overall cell volume shrinks, although the lattice parameter *c* increases. However, above $x(Li) = 0.5$, the variations in lattice parameter *a* are less significant, but the lattice parameter *c* exhibits significant negative changes, leading to further volume contraction [71]. As depicted in Figure 10b, the volume contraction appears to be small during charging up to up to $x(Li) = 0.6$, but thereafter the volume shrinks much more rapidly, with the most pronounced changes occurring above 4.0 V. For NCM, the volume contraction during charging strongly depends on the Ni content and is around 1.2 and 5.1 % for NCM111 and NCM811, respectively (Figure 10b). In contrast to NCM, the unit cell volume of LCO increases by about 2 % upon delithiation to $Li_{0.5}CoO_2$, while a further delithiation leads to less repulsion of the oxygen layers and a decrease in Li slab width, so that the unit cell volume decreases again (Figure 10b). In general, the cell volume contraction or expansion during the cycling of a battery due to the oxidation and reduction of the transition metal ions, which effects the TM–O bond lengths. The volume changes are more severe for Ni-rich compounds because nickel undergoes the largest change in ionic radius upon transition metal oxidation/reduction and, in addition, the

higher Ni content allows for a higher degree of delithiation. These periodic volume changes lead to intrinsic mechanical degradation of NCM materials, which can be observed by micro cracking or intergranular fractures of NCM particles in cross sectional scanning electron microscopy (SEM) images. In summary, the significant anisotropic lattice changes observed during cycling of Ni-rich NCM are possible explanations for the enhanced capacity fading accompanied by increasing cell resistance [69-72].

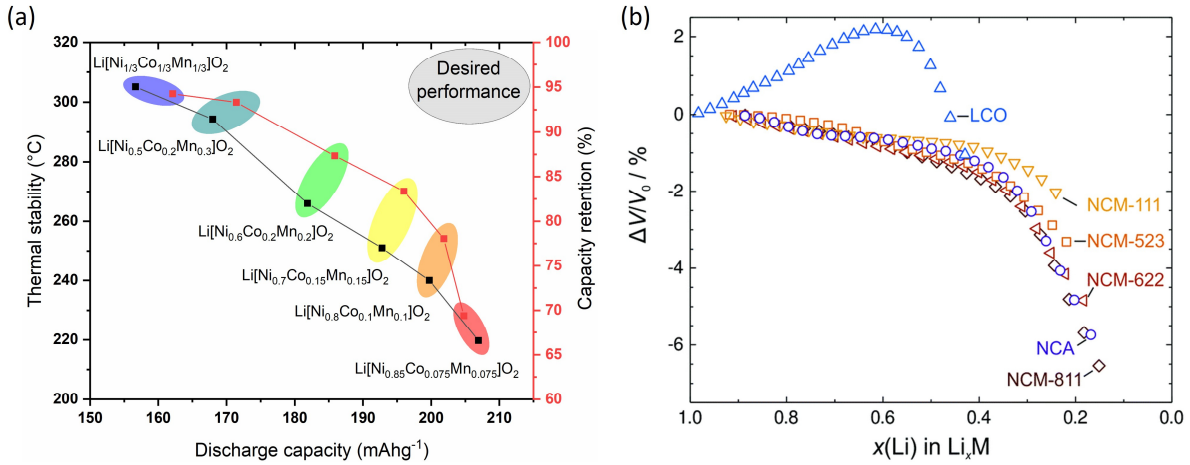

Figure 10: (a) Overview of the relationship between discharge capacity, thermal stability, and capacity retention for NCM with different compositions. Idea and data adapted from Noh *et al.* [24]. (b) The unit cell volume determined from crystallographic data versus the state of lithiation of different cathode materials. Reproduced with permission from ref. [72], Copyright 2018 The Royal Society of Chemistry.

Most important are the safety characteristics of a cathode active material, which in the case of NCM are strongly influenced by the TM composition. NCM111 is characterized by particularly high safety, so that it has already been commercialized for automotive applications. However, the high-capacity, Ni-rich NCM suffers from a poor thermal stability and inferior safety characteristics (Figure 10a). In all NCM compositions, oxygen loss occurs in their delithiated state at elevated temperatures due to several phase transitions from the layered phase to the spinel phase, to another spinel phase, and finally to the rock salt phase. In the case of NCM85, the phase transition starts at 145 °C and leads to an oxygen release of 52 %. In contrast, an oxygen release of 18 % was observed for NCM111 at a higher temperature of 295 °C. The phase transition temperature shifts towards lower temperatures with increasing Ni content and greater oxygen releases because Ni-rich NCM in the delithiated state contains more of the unstable and reactive Ni^{4+} species, which is reduced to more stable Ni^{2+} under oxygen release. Moreover, the peak temperature of the exothermic reaction of a charged cathode also shifts to lower temperatures, which is associated with higher heat generation when the Ni content in NCM is increased. In the case of NCM111, a heat generation of 513 Jg^{-1} was observed at

306 °C, while for NCM85, 972 Jg^{-1} was already released at 225 °C. Overall, the thermal stability of Ni-poor cathode materials is significant higher due to an increased Mn^{4+} and a reduced reactive Ni^{4+} content [24].

In summary, NCM111 has the best capacity retention and thermal stability (highest safety), but its discharge capacity is rather low. However, the capacity and energy density can be greatly increased by tailoring the transition metal composition to a higher Ni content. Ni-rich NCM, however, suffers from severe capacity fading due to larger volume changes during cycling and surface structural degradation. In addition, the increased reactivity of the Ni-rich compounds with the liquid, organic electrolyte results in drastically reduced thermal stability and difficult safety characteristics, which hinder the commercialization of high-capacity Ni-rich NCM. Unfortunately, it is not possible to synthesize active materials that have both high specific capacity and sufficiently high safety. Considering the trade-off, a modification of the Ni-rich cathode materials is required to achieve an optimal performance of layer structured Ni-rich NCM. Possible concepts for such an optimization are core–shell or (full) concentration gradient structures, surface coatings or doping of the NCM host structure. Those optimization strategies will be discussed in the following chapters.

1.3.3. NCM with core–shell and concentration gradient structure

To overcome the problems of the high-capacity Ni-rich cathodes and achieve optimum performance of layered NMC, core–shell (CS) cathode materials have been introduced. The design of core–shell cathode materials generally follows the principle that a high-capacity active material acts as core, and a structurally and thermally stable material acts as shell. The prerequisite is that the crystal structures of the core and shell should match and that the synthesis (especially the lithiation reaction) is possible at temperatures below 850 °C to prevent cross-diffusion of transition metals between core and shell [40]. The first NCM cathode with core–shell structure was reported by Y-K. Sun *et al.*[73] in 2005 (Figure 11).

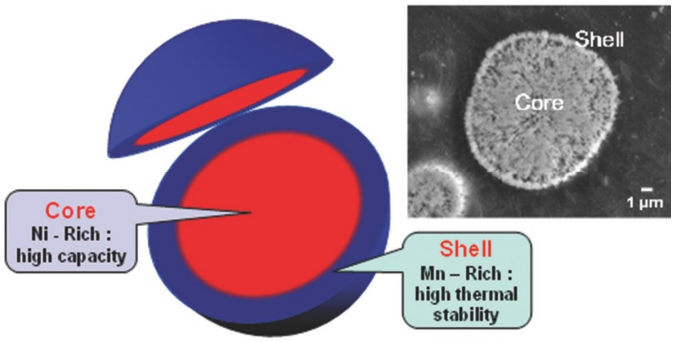

Figure 11: Schematic drawing and SEM image of a core–shell (CS) structured NCM particle. Reproduced (adapted) with permission from ref. [74], Copyright 2015 WILEY-VCH Verlag GmbH & Co. KGaA, Weinheim.

The high capacity NCM811 and the structurally and thermally stable $Li[Ni_{0.5}Mn_{0.5}]O_2$ were selected as the core and shell, respectively. The specific discharge capacity of 188 mAh g^{-1} obtained for the core–shell material $Li[(Ni_{0.8}Co_{0.1}Mn_{0.1})_{0.8}(Ni_{0.5}Mn_{0.5})_{0.2}]O_2$ is overall lower than that of the pure core material NCM811, which is known to deliver up to 200 mAh g^{-1}. However, the capacity retention after 500 cycles was significantly improved from 81 % for the core material to 98 % for the core–shell material. The onset temperature of the exothermic peak measured by DSC was shifted significantly to higher temperatures for the core–shell material, reaching 180 °C and 220 °C for NCM811 and $Li[(Ni_{0.8}Co_{0.1}Mn_{0.1})_{0.8}(Ni_{0.5}Mn_{0.5})_{0.2}]O_2$, respectively [40, 73].

After the first introduction of the core–shell materials, various materials with different core and shell compositions were established [75-77]. All these core–shell materials perform significantly better than their bare core and/or bulk components. Double-shell [78, 79] structured materials with a high-capacity Ni-rich core (NCM811), an inner shell composed of NCM111 that provides excellent rate capability, and an outer shell of $Li[Ni_{0.4}Co_{0.2}Mn_{0.4}]O_2$ (NCM424) that provides structural stability and high safety have also been synthesized to achieve the desired cycle life and rate capability. The synergistic effect of the core–shell structure was confirmed by testing cathode materials with the average composition of core and shell, which showed significantly lower performance compared to the core–shell material [40].

In addition to core–shell structured NCM particles, a concentration-gradient (CG) cathode material was reported by Y.-K. Sun *et al.*[41] in 2009. In this material, each particle has a core of Ni-rich NCM811 and a Mn-rich outer layer. A schematic representation of a NCM particle with concentration gradient is shown in Figure 12a.

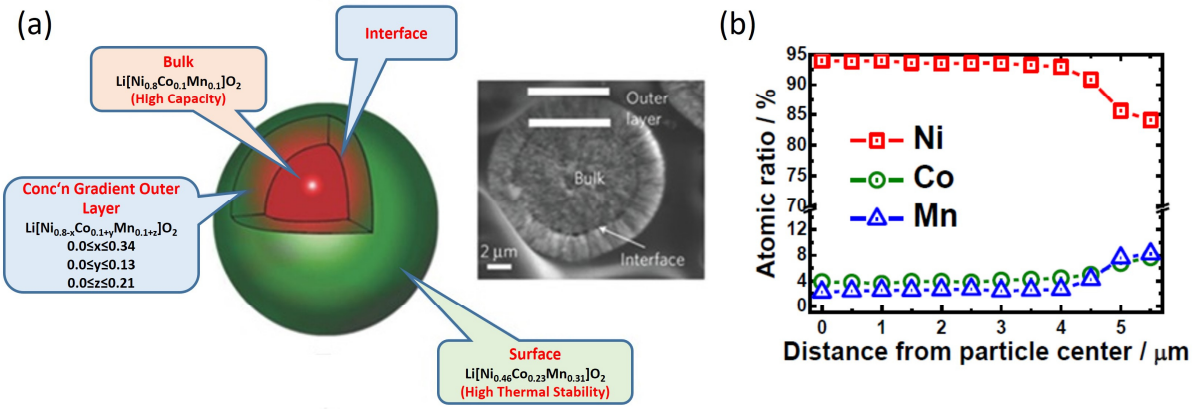

Figure 12: (a) Illustration and SEM image of a NCM particle with concentration-gradient (CG). Reproduced (adapted) with permission from ref. [74], Copyright 2015 WILEY-VCH Verlag GmbH & Co. KGaA, Weinheim. (b) Electron probe microanalysis (EPMA) compositional scan across the CG particle. Reproduced (adapted) with permission from ref. [80], Copyright 2019 WILEY-VCH Verlag GmbH & Co. KGaA, Weinheim.

In CG CAMs, there is a transition metal concentration gradient between the core and the surface, where the Ni-concentration decreases while Co- and Mn-concentrations increase towards the surface (Figure 12b). The concentration gradient layer is about 2 µm thick. Electrochemical tests under aggressive conditions (55 °C between 3.0 and 4.4 V) resulted in a discharge capacity of 209 mAh g^{-1} and a capacity retention of 96 % after 50 cycles, demonstrating that the concentration-gradient structure improves cycling stability due to lower reactivity and volume expansion in the Mn-rich surface region compared to the pure Ni-rich core component. Thus, the CG cathode exhibits high energy and thermal stability and is suitable to meet the performance and safety requirements for electric vehicles [41]. In the last decade, various concentration-gradient layered oxides cathodes with different core, gradient, and surface compositions have been developed, all of each show the synergistic effect of the high-capacity core and the structurally stable concentration-gradient shell layer [40, 43, 50, 80, 81]. In 2012, Y.-K. Sun *et al.*[51] reported the further optimized nanosized layered oxide cathode $Li[Ni_{0.75}Co_{0.1}Mn_{0.15}]O_2$ with full-concentration-gradient (FCG), in which the Ni-concentration decreases and the Mn-concentration increases linearly from the center to the surface layer of each particle (Figure 13). NCM particles with full-concentration-gradient are synthesized by a hydroxide co-precipitation route (see Chapter 1.3.1), where the concentration ratio of Ni/Co/Mn in the transition metal solution continuously changes with the reaction time. The advantage of these materials is the more effective use of the high energy density of the nickel-rich core and the high thermal stability and long lifetime of the manganese-rich outer layers.

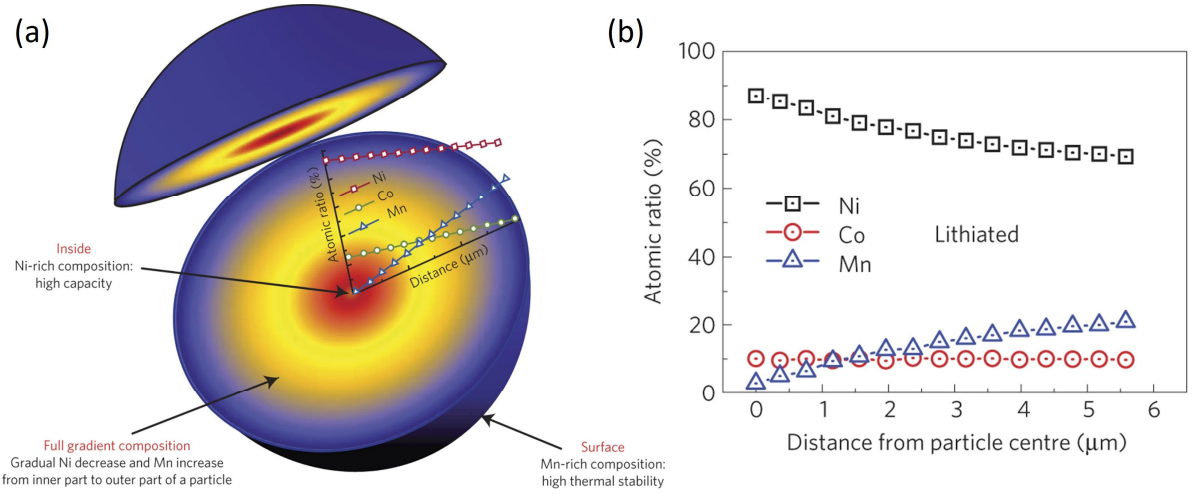

Figure 13: (a) Schematic drawing of a full-concentration-gradient (FCG) NCM particle with Ni concentration decreasing from the center towards the outer layer while the Mn concentration is increasing accordingly. (b) EPMA line scan of the integrated atomic ratio of transition metals as a function of the distance from the particle center to the surface. Reproduced (adapted) with permission from ref. [51], Copyright 2012 Nature Publishing Group.

The FCG structure avoids structural mismatch between core and shell or concentration gradient layer and avoids different volume changes during cycling, which can lead to large void formation and capacity drop. The full concentration-gradient cathode delivers a very high capacity of 215 mAh g^{-1} with 90 % capacity retention after 1000 cycles, indicating a superior structural stability during cycling. This nano-functional FCG cathode material is promising for applications requiring high energy density, long calendric life, and a high safety level [51]. The FCG concept has also been applied to different NCM compositions such as $Li[Ni_{0.600}Co_{0.121}Mn_{0.272}Al_{0.007}]O_2$, which could be cycled for 3000 cycles (3.0 – 4.2 V, 1 C, 30 °C) in a full-cell with graphite anode while maintaining 84 % of its initial capacity. Thus, it fulfills the requirements for a daily charge/discharge cycle during the expected service life (≈ 10 years) of an EV [82].

Finally, the FCG concept was extended by introducing cathode materials with two sloped full concentration gradients (TSFCG), such as $Li[Ni_{0.65}Co_{0.13}Mn_{0.22}]O_2$ (TSFCG65) or $Li[Ni_{0.84}Co_{0.06}Mn_{0.09}Al_{0.01}]O_2$ (TSFCG-Al). In these particles, the concentration gradients of Ni, Co, and Mn are uniform throughout the particle core, but then change abruptly near the particle surface (Figure 14). The TSFCG structure allows the Ni content in the particle core to be maximized, resulting in even higher energy densities while maintaining the improved safety characteristics described previously. After 1500 cycles, the TSFCG electrode material retains both its structural and mechanical integrity, while an $Li[Ni_{0.8}Co_{0.15}Al_{0.05}]O_2$ (NCA) electrode almost pulverizes due to the strain during cycling [83-85].

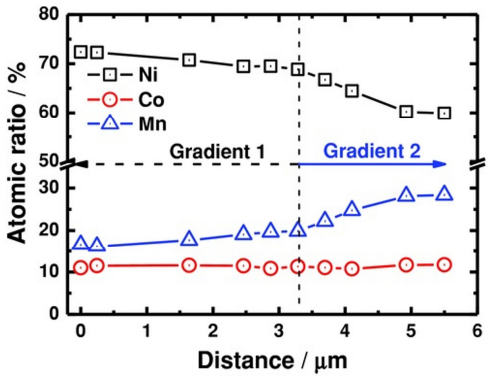

Figure 14: EPMA line scan showing the atomic ratio of transition metals as a function of the distance from the particle center to the surface for a two-sloped full concentration gradient (TSFCG) cathode material. Reproduced (adapted) with permission from ref. [84], Copyright 2015 WILEY-VCH Verlag GmbH & Co. KGaA, Weinheim.

The CS, CG, FCG, and TSFCG cathode materials show strongly improved electrochemical performance compared to their bare core and shell components. These modifications make it is possible to take advantage of the high capacity of Ni-rich NCM by the presence of a less reactive and mechanically very stable Mn-rich shell. As a result, the mechanical degradation is minimized and the thermal stability and safety are maximized by suppressing structural transformations, oxygen loss, and volume expansions. This great development is the first to enable the commercialization of high-capacity Ni-rich NCM for automotive and other applications. Thus, CS, CG, FCG, and TSFCG cathode materials are the state-of-the-art CAMs. However, they suffer from difficulties in synthesis and problems with cross diffusion during calcination. This difficult process regulation and control leads to unsatisfactory repeatability and consistency of these cathode materials [40].

In contrast to the NCM modifications discussed above, coatings on the NCM particles are easier to implement. The effects of surface coatings on the electrochemical performance of NCM will be discussed in the following chapter.

1.3.4. Coating of NCM particles

In addition to the core-shell and the concentration gradient structured NCM, surface modification by coating of the cathode active material particles is a widely used method. Surface coatings can prevent the direct contact between cathode material and liquid electrolyte by acting as protective shield that can suppress undesired side reactions between Ni-rich NCM and liquid electrolyte. Chemical composition, size, thickness, uniformity, density, and conductivity of a coating determine the effects on the NCMs electrochemical performance [86]. Intensive research on cathode material coatings has shown that coatings such as Li_3VO_4[87],

Li_2ZrO_3[88], LiF[89], $LiAlO_2$[90], Li_3PO_4[91] $LiNbO_3$[92], Li_2WO_4[93, 94], and RuO_2[95] lead to an improved electrochemical performance of Ni-rich NCM. In particular, highly Li-ion conducting coatings such as $LiAlO_2$, Li_3PO_4, $LiNbO_3$, and Li_2WO_4 are promising candidates as they provide pathways that enable rapid diffusion of Li ions. In the synthesis of Li_3PO_4, $LiNbO_3$ and Li_2WO_4 coated NCM particles, the precursors used react with the detrimental lithium residues (LiOH and Li_2CO_3) on the surface of Ni-rich NCM to form the coating. Thus, the removal of the isolating surface impurities can be considered as a double benefit of the surface modification. The coatings protect the NCM particles from erosion by the electrolyte, thus preventing the collapse of the spherical particle shape and improving the mechanical stability. In addition, a coating can effectively suppress the oxygen release from the cathode material and therefore has a positive effect on the structural and thermal stability in the presence of electrolyte. Due to the reduced contact between the highly reactive Ni^{4+} and the liquid, organic electrolyte, the degradation of the active material can be strongly inhibited, which is reflected in significantly improved long-term cycling performance. In addition, a coating can reduce the lithium-ion transfer resistance, which also contributes to a better long-term performance and rate capability [91-94]. As an example, 80 % state-of-health after more than 800 cycles (Figure 15) was demonstrated by D. Becker *et al.*[94] for a full-cell with a graphite anode and a tungsten oxide (Li_2WO_4)-coated NCM811 cathode.

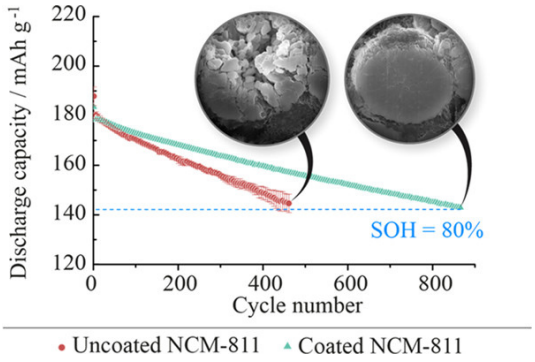

Figure 15: Comparison of long-term charge/discharge performance of LIBs using tungsten oxide (Li_2WO_4) coated and uncoated NCM811 as cathode material. Reprinted with permission from ref. [94], Copyright 2019 American Chemical Society.

In the case of RuO_2 coated Ni-rich NCM, the same positive effects of the coating were observed. The RuO_2 coating also provides an extremely high electronic conductivity, so that the overall electronic conductivity of the cathode material can be improved, resulting in a low polarization degree, low charge-transfer resistance, and improved rate performance. Overall, surface coatings enable a safer and high-performance application of Ni-rich NCM in advanced LIBs [91-95]. Problematics are inhomogeneous, incomplete, too thin, or inefficient coatings as well

as reduced electronic conductivity and low specific capacity due to thick, electrochemically inactive buffer layers [52].

1.3.5. Doped NCM

Doping of the NCM host structure is another effective and promising approach to stabilize Ni-rich NCM cathodes during extended lithium extraction. As described in Chapter 1.3.2, the structural changes of NCM are associated with oxygen release and volume changes [24, 69, 96]. These undesired phenomena are hindered by higher bond dissociation energies between metals and oxygen in the MO_6 octahedron. Higher *M*–O bond dissociation energies provide a better structural and thermal stability and can be achieved by doping. Doping affects the lattice parameters and the cell volume depending on the ionic radius of the dopant element. In the case of NCM, in particular the lattice parameter *a* is directly influenced by the ionic radius of the dopant, while the *c* values are influenced by the different bond dissociation energies of the dopant. A higher bond dissociation energy of the metal oxygen bond (e.g., Co–O = 368 kJ mol^{-1} vs. Sn–O = 548 kJ mol^{-1}) leads to a lower repulsion of the transition metal layer during delithiation (Figure 16), the *M*–O bond lengths become shorter, and the electron density is shifted more toward the metal ions. This leads to a lower electron density in the O-orbitals and thus to a lower repulsion of the O-atoms. Therefore, the contraction/expansion of the *c* parameter during cycling can be minimized by choosing a suitable dopant. Smaller changes in the lattice parameters during the cycling the cell have a positive effect on the structural stability of the cathode material. Thus, doping can strongly improve the Li interaction stability during long-term cycling, which dramatically improves the capacity retention. Furthermore, doping inhibits phase transitions, the resulting oxygen release, and exothermic reactions due to higher bond dissociation energies. Therefore, doping can significantly improve the safety of a battery by reducing the probability of a thermal runaway. However, doping of the NCM lattice leads to changes in the electronic structure of the oxygen ions near the migrating Li ions. In this way, the doping affects the Li interlayer distance, which is determined by the lattice parameter *c* and electrostatic interactions between the O-layers. This means that lithium-ion mobility, which depends on the Li-interlayer distance and is the key aspect for rate capability, is also affected by the doping. The activation barrier for Li-ion migration increases with decreasing lithium interlayer distance and increasing valance state of the dopant. A higher activation barrier for Li-ion mobility is generally observed for the doped cathode materials, which decreases the Li diffusion rate and leads to a lower capacity of the doped CAMs, especially at high currents (C-rates). The specific capacity further decreases

when an electrochemically inactive dopant is incorporated. Usually, dopant concentrations between 1 % and 5 % are chosen, but since doping reduces the electrochemical performance in terms of lower discharge capacities, the dopant concentration is a tradeoff between electrochemical performance and structural stability (reduced volume expansion and increased cycle life) [69, 97].

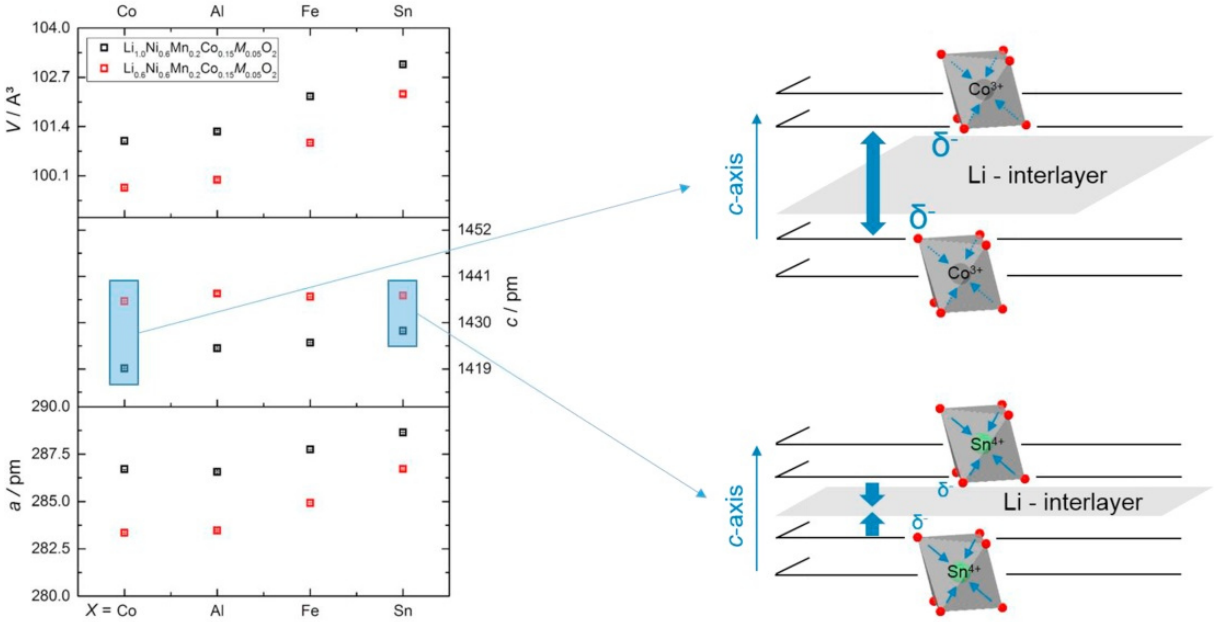

Figure 16: Lattice parameters trends of doped NCM622 in the fully lithiated (black squares) and the 60 % delithiated (red squares) state (left). Illustration of the Li-interlayer movement along the *c*-axis due to doping effects (right). Reproduced with permission from ref. [69], Copyright 2018 Elsevier B.V.

Various dopants for NMC have already been described in the literature, such as Mg[36, 98], Al[35, 36, 69, 99-101], Ti[102], Nb[103] Cr[35], Ce[104] Y[35], Ga[105], Fe[36, 69], Sn[69], Zr[106], B[107-110], Mo[111], and W[112, 113]. However, comparing the electrochemical performance of the obtained materials as a function of doping elements is difficult because each study used different NCM compositions and cell test parameters such as C-rate, voltage ranges, and temperatures, making a reasonable comparison impossible. Nevertheless, the effect of selected doping elements is discussed below.

In the first studies dealing with doped NCM cathodes, Al was found to dramatically improve the thermal stability of NCM111 [98]. In addition to that, the Al doping also increases the stability of NCM upon cycling. The doped material exhibits capacity retention of 96 % in comparison to 68 % for the pristine material. However, Al doping reduces the capacity, especially at high Al contents, since it is electrochemically inactive [99, 101]. It has also been reported that substitution of Al for Mn can suppress the average voltage decay during cycling. Aluminum has a surface and bulk stabilizing effect. Therefore, the impedance of electrodes

containing Al-doped NCM does not change significantly during extended cycling as compared to the undoped cathode materials. In addition, Al doping stabilizes the layered phase by suppressing the layered to spinel phase transition upon cycling, as reported for Li- and Mn-rich NCM [99]. These findings were confirmed by U.-H. Kim *et al.*[100] who investigated Al-doped Ni-rich NCM with a full concentration-gradient (FCG). It was shown that the Al doping together with the FCG structure suppresses the microcracking and the mechanical integrity of the cathode material particles is maintained even after 1000 cycles [100]. With respect to the Al-doped NCM, the related quaternary $Li[Ni_{0.89}Co_{0.05}Mn_{0.05}Al_{0.01}]O_2$ (NCMA) should also be mentioned. The incorporation of Al into the structure of this Ni-rich cathode reduces the volume change accompanying the phase during charge and discharge. This reduction in volume change and the enhanced intrinsic mechanical strengths are sufficient to suppress the formation and propagation of microcracks, which is the key to ensure long-term cycling stability. In addition, the increased structural stability also improves the thermal stability and safety of the cathode [114].

The impact of the highly charged dopant Zr^{4+} on the electrochemical performance of NCM622 was investigated by F. Schipper *et al.*[106]. They found out that Zr-doped NCM exhibits faster electrochemical kinetics, a lower charge-transfer resistance, and higher discharge capacities at high rates. The Zr-doped NCM622 retained its layered structure upon electrochemical cycling, and structural transformation to a spinel structure was hindered. Underlined by computational studies, it was demonstrated that the highly charged dopant has two crucial functions in preventing the structural transformation. First, Zr doping hinders the Ni migration across tetrahedral sites, and second, it reduces the concentration of Jahn-Teller active Ni^{3+} ions, which could lead to instability of the layered structure [106].

Among the above-mentioned dopant elements, tungsten is one of the most promising dopants for Ni-rich layered cathode materials, as it offers the highest degree of stabilization. As an example, 1 mol% W-doped $Li[Ni_{0.8}Co_{0.15}Mn_{0.05}]O_2$ provides a specific capacity of 165 mAh g^{-1} even after 1000 cycles at full depth of discharge. W doping leads to a partial phase transition from the layered to rock salt phase ($Fm\bar{3}m$) near to the surface, which protects the main hexagonal phase. The rock salt phase contains Ni^{2+} ions that reduce the concentration of oxidizing Ni^{4+} ions at the surface. Therefore, undesirable side reactions with the electrolyte are prevented, and the thermal and cycling stability are significantly improved [112].

Among a large variety of dopants, boron (B^{3+}) is a remarkably interesting doping element. Even with its small ionic radius of 0.27 Å, boron is able to block transition metal (TM) migration paths and to hinder the phase transition from layered to spinel structure during cycling of Ni-

rich NCM. Furthermore, boron reinforces the transition metal-oxygen (TM–O) bond and stabilizes the Li–TM–O host structure during lithiation and delithiation. Due to the high boron–oxygen (B–O) binding force, the surface structure of layered NCM could be modified by B-doping [107, 110]. S.-H. Han *et al.* were the first to report on the addition of B_2O_3 to $Li[Ni_{0.7}Co_{0.2}Mn_{0.1}]O_2$ (NCM721) [108]. Especially at a high cutoff voltage of 4.5 V, the boron-containing sample showed significantly improved electrochemical performance due to a higher compressive stress and reduced crack formation during cycling. K.-J. Park *et al*. reported an improved capacity retention for 1 mol% B-doped, Ni-rich $Li[Ni_{0.9}Co_{0.05}Mn_{0.05}]O_2$ (NCM90), which was attributed to a reduced mechanical degradation during cycling [107]. Recently, C.-H. Jung *et al.* demonstrated that B-doped layered cathodes display better cycling stability. This effect was attributed not only to a suppressed microcrack formation, but also to the changed shape of the primary particles with an increased proportion of lateral facets ((003) plane), which are stable against oxygen release [115]. Although the positive effect of boron doping on the electrochemical performance of NCM is undeniable, it is still not clear how this effect is achieved and where the boron is located. Based on the results of X-ray diffraction, S.-H. Han *et al.* suggested that the small boron ions partially occupy the Li positions, while L. Pan *et al.* assumed a dual occupation of tetrahedral and octahedral interstitials (transition metal vacancies) by boron in the NCM structure [108, 110]. On the other hand, it is not clear whether boron is incorporated in the bulk NCM structure or preferentially resides on its surface. Thus, K.-J. Park *et al*. observed that boron doping changes the microstructure of the NCM90 particles. This effect was attributed to a decreased energy of the (003) surface in the presence of boron, leading to the formation of microstructures with radially oriented primary particles that can relieve the strain induced by lithiation or delithiation during cycling. For the B-doped $LiNiO_2$ (LNO), DFT calculations have predicted the increase in bulk lattice energy after the incorporation of boron atoms. As the most likely scenario for the structure stabilization, it was proposed that boron (together with neighbor O atoms) migrates into the topmost layer of Li ions with the formation of an ordered lithium boron oxide structure (α-Li_3BO_3) on the particle surface [107]. However, clear experimental evidence for one of these hypotheses is still pending, and the exact position of boron in B-doped NCM morphologies is still unknown. In Chapter 4, the effect of B doping on the crystal structure, microstructure, and electrochemical properties of NCM811 with different boron concentrations is systematically investigated by using a combined experimental and theoretical approach [116].

In summary, doping affects cell volume, lattice parameters, volume change during cycling, and Li-ion mobility. The volume change and the resulting microcrack formation can be minimized,

and surface structural degradation due to oxygen release can be prevented by dopants with extremely high M–O bond dissociation energies. Electrochemical tests have shown that the resulting discharge capacities are lower, but the cells cycle life as well as the thermal stability and safety are significantly increased.

In this chapter, it was shown that the energy density of LIBs can be greatly improved by selecting a suitable cathode material such as NCM and adjusting its composition toward high-capacity Ni-rich NCM. With the help of suitable optimization approaches, the cathode materials can be optimized to produce LIBs with high energy density, high-capacity retention, long lifetime, and high safety that meet the demands of today's applications. In addition to the further optimization of already established LIBs, the development and commercialization of alternative battery technologies such as all-solid-state batteries (ASBs), which are expected to solve several challenges of conventional LIBs, should also be consider. The concept of ASBs is introduced in the following chapter.

1.4. All-solid-state lithium batteries as future energy storage system

Today, Li-ion batteries offer specific energy densities of up to 260 $Wh\,kg^{-1}$, which was unimaginable 30 years ago. The gravimetric energy density could be increased by a factor of 2 – 3. This was made possible by a continuous improvement in battery and cell designs to improve the packing density. However, to meet the demands of today's portable electronic devices, electric vehicles, and grid-energy storage systems, a further improvement of batteries towards higher energy and power densities, longer cycle life, and higher safety levels is needed. Unfortunately, the physicochemical limit of these conventional Li-ion battery systems will soon be reached – there are no more possibilities for further improvement – but on the other hand, the demand for batteries with even higher energy and power densities is increasing.

All-solid-state batteries (ASBs) are among the next-generation battery technologies expected to solve many problems associated with conventional LIBs. Unlike conventional LIBs, ASBs use solid-state electrolytes (SSEs) instead of liquid, organic electrolytes. This makes them non-flammable and reduces the risk of thermal runaway. ASBs have attracted considerable attention since the safety issues of conventional LIBs became more apparent as their energy density increases. The growing interest in the fields of SSE and ASBs is reflected in the number of published papers, which has increased from around 50, in 1997, to 450 in 2017. The expected benefits of ASBs include a longer calendric and cycle life in addition to higher safety. Minimized side and decomposition reactions at the electrode-electrolyte interface are expected due to an overall higher stability of the SSE.

The working principle of ASBs is identical to that of conventional LIBs (Chapter 1.2), but the design is simple because the SSE serves as both the Li-ion conductor and the separator, allowing a more compact cell design. If the liquid, organic electrolyte is completely replaced by an SSE and a Li metal anode is used, the volumetric and gravimetric energy density can be strongly increased by 70 % and 40 %, respectively. The enhanced energy densities of polymer and ceramic based ASBs compared to current technologies are shown in Figure 17.

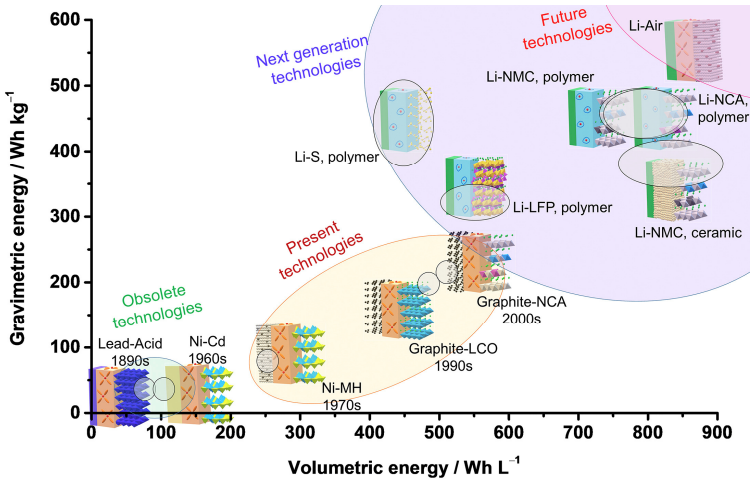

Figure 17: Overview of battery technology evolution and the role of all-solid-state batteries. Reproduced with permission from ref. [33], Copyright 2018 Elsevier Inc.

ASBs have the potential to meet the requirements of future batteries by offering both higher safety as well as higher capacity and energy density. Higher power is available due to the absence of concentration polarization, and a higher energy density can be achieved due to the broader electrochemical window of the SSE, which allows the use of high voltage CAMs. In addition, the more compact cell design further improves the energy density and the use of solid-state electrolytes with high thermal stability enables a wide applicable temperature range, that further increases the performance [24, 31, 117-119].

1.4.1. Anodes, separators, and composite positive electrodes for ASBs

All-solid-state batteries are broadly classified into thin film and bulk-type batteries. Thin film batteries consist of pure anode, cathode, and solid electrolyte layers which can be obtained e.g. by physical vapor deposition (PVD) [120]. The thin-film approach is not practical for high-energy densities due to the low active material loadings and low applicable current densities. In contrast to thin-film batteries, bulk-type ASBs deliver significant higher specific areal capacities due to the higher active material loadings and are therefore more suitable for large scale applications. Bulk-type ASBs are usually composed of a metal anode, a solid-state electrolyte and separator, and a composite positive electrode (Figure 18) [117, 121].

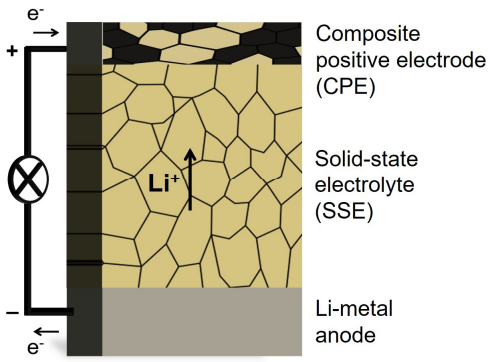

Figure 18: Schematic presentation of a bulk-type electrolyte supported ASB. The discharge process is visualized.

The use of Li metal as s anode material is favored because of its ten times higher theoretical capacity (3860 mAh g^{-1}) compared to a common graphite anode. Other attractive features of a Li metal anode include the lowest electrochemical potential as well as a low material density of only 0.53 g cm^{-3}. However, the application of a Li metal anode is limited by the incompatibility between certain solid electrolytes and metallic lithium. The poor chemical stability of the SSE in contact with lithium can be overcome by a surface modification of the SSE or a passivation of the Li metal electrode. Another problem is the growth of lithium dendrites in the voids along the grain boundaries of the SSE during galvanostatic cycling, which causes short circuits. This challenge can be overcome by introducing a Li alloy as a buffer layer between the Li metal anode and the SSE. Lithium alloys such as Li–In, Li–Si, and Li–Al can be used instead of Li metal to achieve more safety at high capacity. The advantages of the Li–In alloy anodes are relatively high working voltage, fast electron transfer kinetics, and reversible electrochemical reaction, which is why they are the most commonly used anodes in ASBs [31, 33, 121, 122].

The most important key to develop an ASB is a suitable solid-state ionic conductor as electrolyte. A preferred SSE should have high ionic conductivity (~10^{-3} S cm^{-1}) at room temperature and low electronic conductivity (<10^{-8} S cm^{-1}; electronic insulating) to prevent self-discharge and short circuits. A wide electrochemical window, good chemical stability over the operating temperature and towards the electrode materials, environmental friendliness, as well as low toxicity and cost are preferred properties of an SSE. Different Li-ion conducting solid electrolyte materials have been investigated in the past (Figure 19). They are divided into organic polymer solid electrolytes and inorganic solid electrolytes. The advantages of polymer electrolytes are facile processing, low fabrication costs, and softness. Problems include the poor Li-ion conductivity (less than 10^{-5} S cm^{-1}), low thermal and mechanical stability, and limited stability of the electrolyte/electrode interface, especially at very positive potentials. In contrast,

inorganic SSE are non-flammable, mechanically very stable and, most importantly, they have higher Li-ion conductivities [31, 121, 123, 124]. In the following, this work focuses on the class of inorganic solid-state electrolytes.

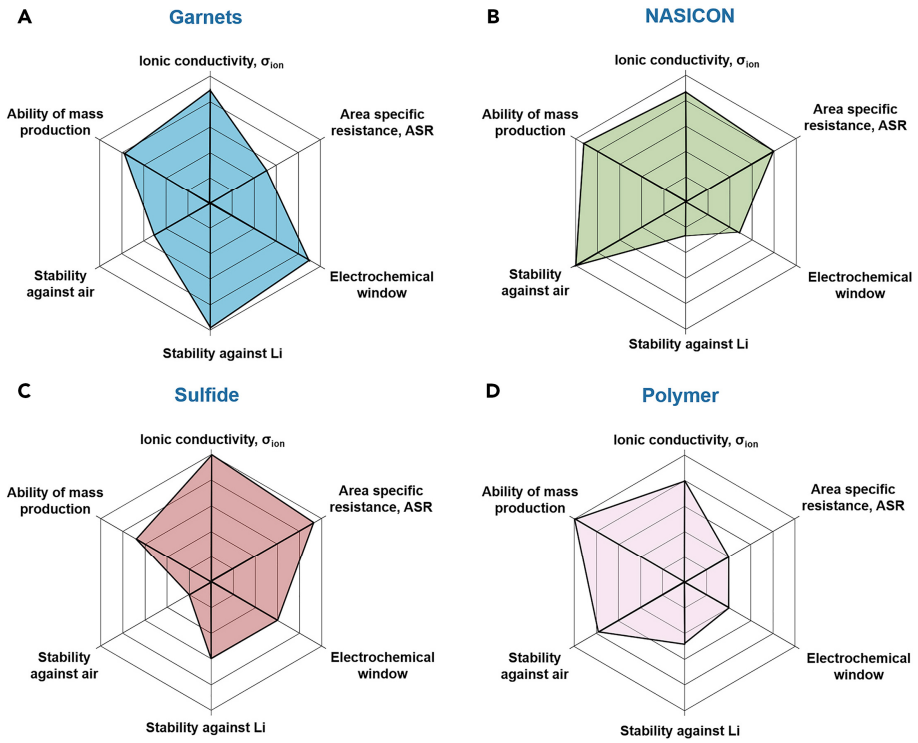

Figure 19: Properties of four common solid-state electrolyte materials. Reproduced with permission from ref. [125], Copyright 2019 Elsevier Inc.

Inorganic glass-ceramic sulfide-based solid electrolytes have been known since 1986, when $Li_2S–SiS_2$ was synthesized. In addition, a new material family, namely the lithium super ionic conductors (*thio*-LISICON), has been discovered within the $Li_2S–GeS_2–P_2S_5$ system. These sulfide-based solid electrolytes exhibit ionic conductivities in the range of 10^{-6} – 10^{-3} S cm^{-1}. An enhanced ionic conductivity of $1.2 \cdot 10^{-2}$ S cm^{-1} is exhibited by $Li_{10}GeP_2S_{12}$ which is close to that of liquid electrolytes. Solid sulfide-based electrolytes are known to be soft and ductile, which is a great advantage in terms of their elastic properties (low Young's modulus) during cell fabrication and operation. Flexible solid electrolytes in a composite cathode might reduce the impact of the volume change of the active material during lithium inter- and deintercalation. However, the sulfides react with moisture by the generation of toxic H_2S gas, have insufficient compatibility with high voltage cathode materials, and are sensitive to oxygen, which makes the manufacturing more complex [31, 117, 126].

In addition to the sulfides, a special attention has been paid to oxide-based ceramic solid-state electrolytes because of their high Li-ion conductivity, the possibility of synthesis in air, nonflammability, and high oxidation stability. Lithium phosphorus oxynitride (LiPON) is a

known Li-ion conductor with a high electrochemical stability, but its applications are limited to thin-film batteries due to high costs and relatively low ionic conductivities of around 10^{-6} S cm^{-1} [127]. Additionally, perovskite-structured $Li_{3x}La_{2/3-x}TiO_3$ is of interest since it shows a significantly higher ionic conductivity of 10^{-3} S cm^{-1} at room temperature. Unfortunately, this electrolyte is not stable in contact with Li metal due to the reduction of Ti^{4+} to Ti^{3+} [128]. The phosphate-based system, $Li_{1.4}Al_{0.4}Ti_{1.6}(PO_4)_3$ (LATP) with the NASICON (sodium super ionic conductor) structure is a potential SSE because of a suitable room temperature ion conductivity of up to $6.9 \cdot 10^{-4}$ S cm^{-1} at a relative density of 95 %, good chemical stability under ambient conditions, a wide electrochemical window, and a high mechanical strength. However, LATP is also unstable in direct contact with lithium metal [31, 126, 129]. In contrast to LATP, the oxide-based ceramic materials with garnet structure attract a lot of attention since they are stable against a Li metal anode. Cubic $Li_7La_3Zr_2O_{12}$ (LLZO), which was synthesized by Weppner *et al.* [130] in 2007 for the first time, shows ionic conductivity of $3.0 \cdot 10^{-4}$ S cm^{-1} at room temperature and an activation energy of 0.3 eV. In contrast, a significant lower conductivity of only $1.63 \cdot 10^{-6}$ S cm^{-1} was found for the tetragonal LLZO phase. In recent years a series of dopants and substituents such as Al[126, 131], Ta[132, 133], Ga[61, 134, 135], W[136], and Nb[137, 138] has been investigated to stabilize the cubic LLZO structure at room temperature to improve its ionic conductivity. Due to these efforts, the room temperature ionic conductivity of the state of the art, cubic LLZO reaches 10^{-3} S cm^{-1} [31, 126, 132-134, 139]. In particular, Ta-substituted LLZO (LLZO:Ta) shows an outstanding performance in terms of a relatively high ionic conductivity of up to 1.2 S cm^{-1} at room temperature, as well as a good stability towards Li metal and CAMs [122, 140-142]. LLZO exhibits a high shear modulus of 55 GPa as compared to lithium with only 3.4 GPa. In previous publications it was proposed that the high shear modulus would prevent the lithium dendrite formation, which unfortunately could not be confirmed experimentally [33, 122]. Nevertheless, garnet-type LLZO is one of the most promising SSEs for ASBs with its high ionic and low electronic conductivity, high safety (nonflammable), wide electrochemical window (0 – 5 V), compatibility with Li metal, and inertness to oxygen [126, 132, 143]. The successful integration of LLZO:Ta into a fully inorganic, bulk-type ASBs was recently demonstrated by M. Finsterbusch *et al.*[118] and C.-L. Tsai *et al.*[121].

The cathode active material is a very important component of an ASB. So far, no special CAMs have been developed for ASBs. When choosing the cathode material, attention should be paid to a high specific energy density since ASBs have to compete with conventional LIBs. The CAMs listed in Table 1, which are also used in conventional LIBs, can be integrated into ASBs.

All-solid-state batteries based on LCO[118, 121, 144], NCA[145], NCM[146-148], LFP[148-150], and LMO[151] are known. The requirements of a CAM for ASBs strongly depend on the nature of used solid-state electrolyte, the composition of the composite cathode, and the processing conditions of the battery. For this reason, the requirements for a promising cathode material for ASBs are different from those developed and optimized for traditional LIBs.

Especially in bulk-type ASBs, the CAM is integrated into a composite positive electrode. Composite cathodes consist of a mixture of active material, additives and/or solid electrolyte particles. Solid electrolyte particles are blended with the positive electrode layer to form Li-ion conducting paths to improve the contact areas between the composite cathode and solid separator. As electronically conducting additives such as carbon black generally cannot be added, the electronic conduction should be provided by a CAM. The design of the composite cathode is one of the most important factors to optimize the electrochemical performance of ASBs. In addition to good ionic conductivity of the SSE and a high capacity of the active material, the combination of both should result in a low resistance of the CAM/SSE interface as well as in homogenous Li-ion and electron conduction paths. This is necessary to achieve a low cell internal resistance in the ASB because most active materials have poor ionic conductivity and there is no liquid electrolyte to penetrate the cathode material and to form a solid electrolyte interface (SEI) to provide a sufficient contact area. To achieve a high energy density, the content of active material within the composite cathode should be maximized. On the other hand, the Li-ion conduction must be ensured by a sufficient SSE content. Obviously, there is a tradeoff between a high active material loading and a high Li-ion conduction. The ratio between active material and SSE is one of the parameters to optimize to obtain a high-performance composite cathode. In addition, the use of active materials with small volume changes during galvanostatic cycling is beneficial to avoid mechanical degradation of the composite cathode. Microstructure design of a dense composite cathode without macropores is critical to achieve high conductivity, low cell resistance, and high gravimetric and volumetric energy densities. Dense composite positive electrodes with low resistance ionic diffusion paths are usually fabricated by co-sintering of both components at elevated temperatures above 1000 °C. In the case of ceramic solid-state electrolytes, the thermal expansion coefficients and sintering temperatures must also be matched to the cathode material used. Furthermore, the chemical stability of these CAM/SSE mixtures up to their sintering temperature is desired [117, 121, 152]. This issue of material compatibility during co-sintering at elevated temperatures will be addressed in the following chapter.

1.4.2. Compatibility between solid-state electrolytes and cathode active materials

The major challenge in fabricating dense composite cathodes, consisting only of SSE and CAM, is the material compatibility during co-sintering at elevated temperatures. Numerous theoretical and experimental investigations have demonstrated that the thermodynamic stability of the SSE strongly decreases in the presence of a CAM. The decomposition temperature of such a mixture is significantly lower as compared to the single components (Figure 20). This compatibility issue was reported by L. Miara *et al.*[153] for the high-voltage spinel materials, $Li_2NiMn_3O_8$, $Li_2FeMn_3O_8$, and Li_2CoMnO_4, in combination with LATP and LLZO:Ta. The reason for the reduced thermal stability is an oxygen and lithium exchange when two ceramics are in contact at elevated temperatures. At temperatures above 600 °C, various high impedance interfacial decomposition products such as $La_2Zr_2O_7$, La_2O_3, La_3TaO_7, TiO_2, and $LaMnO_3$ were detected for the spinel CAMs mixed with LLZO:Ta. The same mixtures with LATP lead at the same temperature to the formation of MnO_2/Mn_2O_3, Li_3PO_4, $AlPO_4$, and $LiMPO_4$ (M = Mn, Ni) [153].

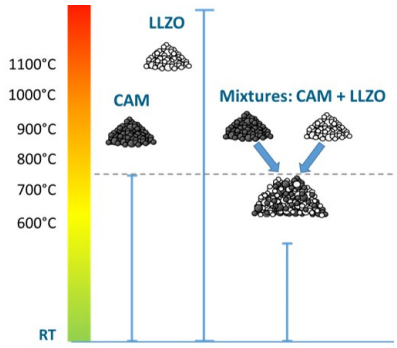

Figure 20: Schematic representation of the decomposition behavior of pure cathode material, pure LLZO, and a mixture of both materials. The graphic was created based on references [140, 154].

The thermal compatibility of different cathode active materials (LCO, NCM, LMO, and LFP) with LLZO has been previously studied by Y. Ren *et al.*[140] and J. Wakasugi *et al.*[154]. LMO and LFP react with LLZO:Ta at temperatures below 600 °C. The main decomposition products during co-sintering of LMO and LLZO:Ta are $La_xZr_{1-x}O_{2-x/2}$, $La_2Zr_2O_7$, and $La_{1-x}MnO_{3\pm\delta}$. For the mixture of LFP + LLZO:Ta, Li_3PO4 and Fe have been found as secondary phases. The NCM111 is stable up to 800 °C, while above $LaCo_{1-x}Mn_xO_3$ ($x < 0.4$) as Co- and Mn- containing secondary phase was detected. S. Ohta *et al.*[146] have additionally found $LaNiO_3$ or $La_2(Ni_{0.5}Li_{0.5})O_4$ as a secondary phase during annealing of NCM111 and LLZO. Based on X-ray diffraction (XRD), a mixture of LCO and LLZO:Ta is stable up to 900 °C. $LaCoO_3$ as secondary phase is only detectable by Raman spectroscopy after an extended dwell

time of 10 h at 900 °C. S. Uhlenbruck *et al*.[141] have used differential scanning calorimetry (DCS) to analyze the thermal compatibility between LLZO:Ta and LCO and found out that the mixture is stable up to 1085 °C [121, 140, 141].

In addition to the type of the CAM and SSE, the morphology also affects the thermal compatibility. In general, higher reactivities are reported for nano-sized LMO/LFP and LLZO:Ta due to a larger surface area. Larger particles of LCO and NCM in the µm range are less reactive and are preferred for the fabrication of composite cathodes. In the case of LMO and LFP, a bulk reaction with LLZO:Ta is suggested, since both original phases disappear during co-sintering. In contrast, for LCO and NCM, the reaction with LLZO:Ta is confined to surface impurities, since a complete decomposition of both phases is not observed [140]. These findings are also in agreement with the theoretical study by L. Miara *et al*.[155], which emphasizes that LCO is the best choice for combination with garnet LLZO, while LMO and LFP react rather strongly. In summary, µm-sized LCO and NCM are the preferred cathode materials for the fabrication of a composite cathode with LLZO. However, only LCO was shown to be thermodynamically stable in combination with LLZO at temperatures of up to 1085 °C. In addition, the thermal expansion coefficient of LCO also matches with that of the LLZO, which allows a fast sintering of LCO/LLZO composite electrode without crack formation [121]. Additionally, LCO is favored for its outstanding electronic conductivity in both the lithiated and delithiated states, which enables rapid lithiation/delithiation of the cathode without any electronically conductive additives [144]. Due to this fact, LCO with a relatively low theoretical specific capacity of 140 mAh g^{-1} has been the CAM of choice for the fabrication of the few reported fully inorganic bulk-type LLZO-based cells manufactured via conventional sintering [118, 121].

To further increase the areal capacity and thus the energy density of these garnet-type ASBs, the incorporation of high-capacity CAMs like NCM111 with a practical specific capacity of 160 mAh g^{-1} or Ni-rich NCM811 with 200 mAh g^{-1} into the composite cathode is necessary. However, the thermal stability of NCMs combined with LLZO is generally insufficient to manufacture ceramic composite cathodes via co-sintering. As a practical solution to mitigate the secondary phase formation during co-sintering of LLZO and NCM powders, the addition of Li_3BO_3 (LBO) as a sintering additive has been suggested to lower the fabrication temperature. LBO has a low melting point of around 700 °C and shows a Li-ion conductivity of $2 \cdot 10^{-6}$ S cm^{-1} [147, 156]. However, such electrochemically inactive additives strongly reduce the areal active material loadings as well as the energy density of the ASB.

Therefore, protecting surface coatings on NCM particles are proposed to reduce the reactivity between NCM and SSE during co-sintering, as surface coatings have already proven to be an effective method for optimizing NCM for the use in conventional liquid electrolyte-based LIBs (Chapter 1.3.4). An ideal cathode coating material for ASBs should not only act as protective layer, but also have a wide electrochemical window that spans the cathodes operating voltage and overlaps with the electrochemical window of the electrolyte. In addition, high Li-ion mobility and low electronic conductivity are required in the case of electrolytes that are unstable at high voltages [157]. Accordingly, the computational study by Y. Xiao *et al*.[157] presented $LiNbO_3$, $LiTaO_3$, and $LiBa(B_3O_5)_3$ as promising coating materials to improve the compatibility between NCM and LLZO. However, there is no practical evidence that these coatings effectively prevent side reactions between CAM and SSE. Only the $Li[Ti_{0.1}Mn_{0.9}]_2O_4$ spinel, formed *in-situ* on the surface of $Li[Ni_{0.5}Co_{0.2}Mn_{0.3}]O_2$ (NCM523), was shown to improve the discharge capacity and the cycling performance by reducing the interfacial polarization and increasing the Li-ion transfer between cathode and electrolyte, but there is no evidence of improvement in thermal stability between NCM and LLZO[127]. Extensively investigated and proven for conventional LIBs is also the doping of the NCM host structure (Chapter 1.3.5), which leads to improved cycling and thermal stability of NCM in contact with the liquid electrolyte. Possible positive effects of doping as well as of different NCM compositions on the thermal compatibility between NCM and LLZO:Ta are discussed in this thesis (Chapter 7).

1.4.3. State of the art garnet-type ASBs

This chapter provides an overview of the electrochemical performance of current garnet-based all-solid-state batteries (ASBs). In addition to the fully inorganic bulk-type ASBs based on LCO as CAM, which is used as a benchmark in this work, the composition and performance of various garnet-type ASBs based on NCM as CAM are described. Finally, the challenges of the state of the art ASBs and ways to improve them are discussed.

In recent years, various ASBs based on garnet-type LLZO as solid-state electrolyte (SSE) were reported in literature. These ASBs utilize mainly LCO but also LFP, LFMO ($Li_2FeMn_3O_8$), NCM111, NCM523 and LTO ($Li_4Ti_5O_{12}$) as CAM. A detailed literature overview of the structure, active material loadings, working conditions, and performances is provided elsewhere [121, 148]. Most of the reported garnet-type ASBs suffer from low active material loadings of only 1 – 4 mg cm^{-2}, approaching those of thin-film batteries. “True” bulk-type all-solid state batteries with significantly higher active material loadings and high specific areal capacities, which were prepared by conventional sintering, have been demonstrated by

M. Finsterbusch *et al.*[118] and C.-L. Tsai *et al.*[121]. A schematic diagram of such an electrolyte-supported bulk ASB is shown in Figure 18. A typical battery consists of a Li metal anode, LLZO:Ta as SSE and solid separator, and a fully inorganic composite cathode consisting of LCO and LLZO:Ta. The half cells were fabricated by co-sintering the LCO/LLZO:Ta composite onto a dense LLZO:Ta pellet. The Li metal anode was then attached to the other side of the SSE pellet. Typical layer thicknesses are 200 µm for the Li metal anode, 500 µm for the garnet separator, and 25 µm for the composite cathode [118].

The satisfactory performance of the first fully inorganic garnet-based cells demonstrated in 2018 by M. Finsterbusch *et al*.[118]was achieved only by appropriate material selection and processing without complicated interface modifications. Thus, an indium metal anode was used instead of Li to avoid the formation of Li dendrites, cubic LLZO:Ta with a high ionic conductivity was used as an SSE, and a mixture of crystalized LCO and cubic LLZO:Ta was used for the composite positive electrode. Sintering of the composite cathode at 1050 °C was possible without chemical reaction, as confirmed by micro-Raman spectroscopy and EDS mapping. The resulting ASBs are characterized by high active material loadings of up to 12.6 mg cm^{-2} and a low area resistance of 1150 Ωcm, which is around ten times lower than reported for other ASBs. Galvanostatic cycling with a discharge current density of 50 µA cm^{-2} leads to initial specific areal discharge capacity of 1.63 mAh cm^{-2} and to specific gravimetric discharge capacity of 110 mAh g^{-1}. An irreversible capacity loss in the first cycle is often observed for different types of ASBs. In the case of an oxide-based SSE, the loss of Li-ion conducting paths and an irreversible formation of new interfaces are possible reasons for the observed irreversible capacity. The capacity retention was 33 % (36 mAh g^{-1}) after 100 cycles, but the Coulomb efficiency stays around 98 % [121]. Long-term galvanostatic cycling is accompanied by rapid capacity degradation due to an increasing cell polarization and areal resistance. Capacity fade despite the high Coulomb efficiency is generally observed for various ASBs with a composite cathode, but not for the thin layer cells. This behavior seems to be a typical problem for ASBs with thick composite cathodes. The formation of micro-cracks in the composite cathode due to CAM expansion and contraction during discharge and charge (lithium inter- and deintercalation) is considered to be the main reason for the rapid capacity degradation, based on the experimental observation of trans-granular fractures in the LCO grains as well as a loss of contact between LCO and LLZO:Ta. More importantly, most cracks occur adjacent to the macropores in the composite cathode. Non-uniform electrochemical reactions take place adjacent to the free space, causing non-uniform volume change and the

build-up of stresses that are released into the free space by the formation of cracks in the composite cathode material [118, 121].

The fully inorganic bulk ASBs based on LCO as CAM offer high specific areal capacities. In principle, these capacities should be significant higher if a high-capacity active material such as NCM is integrated into the composite cathode. However, due to the compatibility issue discussed in Chapter 1.4.2, the fabrication of thick, dense composite cathodes consisting only of NCM and LLZO by conventional sintering is limited. Nevertheless, several ASBs based on NCM and garnet-type LLZO were demonstrated, showing different strategies to overcome the compatibility problem. Table 2 provides an overview of the state of the art ASBs based on NCM as a CAM. A garnet-type ASB with a composite cathode based on NCM523, Li_3BO_3 (LBO) as sintering aid, and In_2O_5Sn (ITO) as electronically conducting additive was demonstrated by Liu *et al.*[127] in 2018 (Figure 21).

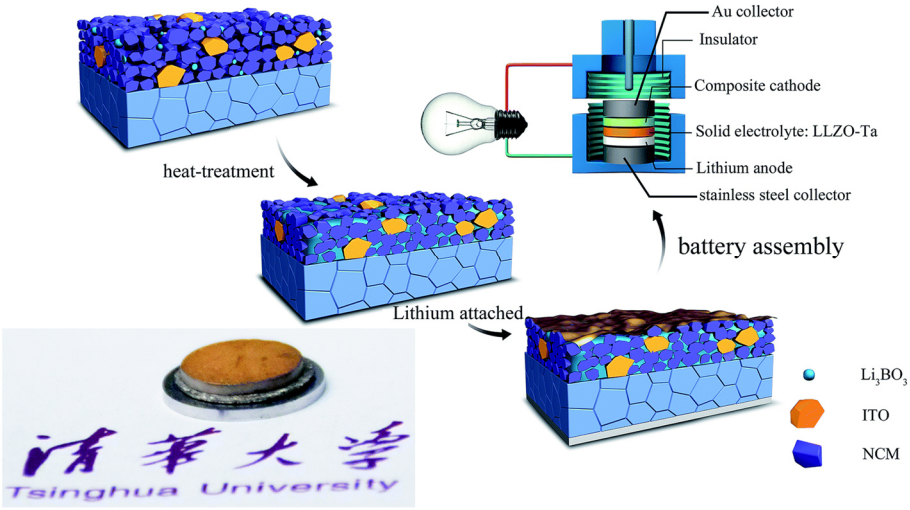

Figure 21: Schematic of the processes of an ASB assembly. The bottom-left inset shows a photo of the assembled battery by Liu *et al.* Reproduced with permission from ref. [127], Copyright 2018 The Royal Society of Chemistry.

The interfacial contact between CAM and SSE was improved by *in-situ* $Li[Ti_{0.1}Mn_{0.9}]_2O_4$ (LTMO) coating of NCM particles, which reduces the interfacial resistance between electrolyte and electrode. The surface modification of NCM decreases the charge-transfer resistance and thus the cell polarization. The initial gravimetric and areal discharge capacities were 123 mAh g^{-1} and 0.19 mAh cm^{-2}, respectively, and the capacity retention after five cycles was 62 %. However, the areal specific capacity is very low due to the low active material loading (1.0 mg cm^{-2}) of the composite cathode [127]. Also, Y. Shao *et al.*[158] demonstrated an oxide ceramic ASB based on NCM523 as CAM. They modified the interface between lithium metal and W-substituted LLZO (LLZO:W) by simply drawing a soft graphite-based interphase with a pencil. A lithiated connecting interface (LiC_6) with good Li-ion and electronic conductivity

was formed. The toothpaste-like composite cathode consisting of LiTFSI, ionic liquid PY14TFSI (IL), and Super-P, was deposited on the LLZO:W separator without heat treatment. The resulting ASB provided an initial specific discharge capacity of 175 mAh g^{-1}, and a capacity retention of 80 % was reached after 500 cycles. This battery exhibits one of the best cycle lives reported for garnet-type ASBs batteries. However, the areal specific discharge capacity of only 0.16 mAh cm^{-2} is still insufficient to compete with conventional LIBs. Similarly, Alexander *et al.*[159] improved the lithium wettability of Al-substituted LLZO (LLZO:Al) with a graphite (G) interlayer between the Li metal anode and LLZO:Al separator. A lithium ion conducting gel polymer electrolyte (GPE) buffer layer was integrated to reduce the high interfacial resistance at the cathode side. The composite cathode of this battery consists of NCM111, acetylene black (AB) and polyvinylidene fluoride (PVDF). An initial discharge capacity of 162 mAh g^{-1} was obtained for a cell with a slightly higher active material loading of 2 mg cm^{-2} as compared to the cell of Y. Shao *et al.* [159]. An oxide ceramic ASB based on Ga and Nb substituted LLZO separator and only NCM111 as CAM was demonstrated by W. Lan *et al.*[160], who sintered the NCM111 cathode without further additives onto the LLZO separator at 700 °C and obtained 120 mAh g^{-1} with an active material loading of 2 mg cm^{-2}. By choosing Sr-substituted LLZO (LLZO:Sr) as the SSE support, S. Ohta *et al*.[146] were able to avoid the secondary phase formation when fabricating an ASB with a composite cathode consisting of NCM111 and LBO by annealing at 750 °C in air. Their battery delivered 186 mAh g^{-1} at an extended voltage window of 2.5 – 4.6 V. Recently, S. Chen *et al*.[148] showed that the critical interfacial impedance between the SSE and cathode can be reduced by placing a succinonitrile (SN)-based plastic crystal electrolyte (PCE) on a LLZO:Ta separator. NCM111 mixed with polyethylene oxide (PEO), LiTFSI and SN as ionic conductors, and carbon as electronic conductor were used as composite cathode. The cell exhibited an NCM loading of 2 mg cm^{-2} and delivered an initial discharge capacity of 0.33 mAh cm^{-2}.

Table 2: Overview about garnet-type ASBs based on NCM as cathode active material. The capacities of the first discharge cycle are shown.

Battery structure	T [°C]	Loading	Current density/ C-rate	Voltage [V vs. Li/Li^+]	Discharge capacity [mAh g^{-1}]	Discharge capacity [mAh cm^{-2}]	Cycles
Li/LLZO:Ta/NCM811, LLZO:Ta, LBO C. Roitzheim *et al.*[161], 2022, see Chapter 4.5	60	5.7 mg cm^{-2}	40 µA cm^{-2}	3.0 – 4.2	120	0.7	30
Li/LLZO:Ta/PCE/NCM111, PEO, LiTFSI, SN, C S. Chen *et al.*[148], 2021	25	2 mg cm^{-2}	0.1 C	2.8 – 4.5	167	0.33	26
Li/LLZO:Sr/NCM111, LBO S. Ohta *et al.*[146], 2021	25	2.8 mg cm^{-2}	11.3 µA cm^{-2}	2.5 – 4.6	186	–	3
Li/LLZO:Ga,Nb/NCM111 W. Lan *et al.*[160], 2020	30	2 mg cm^{-2}	0.1 C	2.5 – 4.3	120	–	50
Li/LLZO:Nb/NCM111, LLZO:Nb S. Ohta *et al.*[162], 2020	25	13.4 mg cm^{-2}	40 µA cm^{-2} 0.02 C	3.0 – 4.3	127	1.7	3
Li/G/LLZO:Al/GPE/NCM111, AB, PVDF Alexander *et al.*[159], 2020	25	2 mg cm^{-2}	50µA cm^{-2} 100 µA cm^{-2}	2.0 – 4.8	162 149	–	100
Li/GPE/LLZO:Ta/NCM622, LBO, LLZO:Ta D. Wang *et al.*[147], 2019	RT	1.5 – 2 mg	0.05	3.0 – 4.2	106	–	30
Li/C/LLZO:W/IL/NCM523 Y. Shao *et al.*[158], 2018	RT	0.9 mg cm^{-2}	0.1 C	3.0 – 4.3	175	0.16	500
Li/LLZO:Ta/$NCM523^{LTMO}$, ITO, LBO T. Liu *et al.*[127], 2018	80	1.0 mg cm^{-2}	5 µA cm^{-2}	3.0 – 4.6	123	0.19	5

The above-mentioned ASBs based on NCM as CAM do not use LLZO inside the composite cathode to improve its ionic conductivity. So far, only D. Wang *et al.*[147] have presented a garnet-type ASB with a composite cathode consisting of high capacity NCM622 as active material, LLZO:Ta as SSE, and LBO as sintering aid and buffer layer. The materials were co-sintered at 700 °C. LBO melts and fills the gaps between the particles and binds the NCM and LLZO particles together. The XRD patterns after co-sintering confirmed the thermal stability of NCM622, LLZO:Ta, and LBO. A GPE interfacial layer was used to enhance the wetting between the Li metal anode and LLZO:Ta separator. When NCM622 with small primary particles (~ 500 nm) was used, an initial discharge capacity of 106 mAh g^{-1} could be achieved, which was attributed to better interfacial properties and 20 times shorter Li^+ diffusion paths compared to larger NCM particles. The capacity retention after 30 cycles was around 65 %. However, relatively low Coulomb efficiencies of 70 –80 % were obtained. In addition, the battery suffers from mechanical degradation due to microcracks within LBO and at the interfaces between NMC and LLZO. These microcracks were possibly caused by a volume change of around 2 % during the cycling of the battery and lead to capacity deterioration [147]. In this thesis, a similar cell as reported by D. Wang *et al*. but with higher loadings of Ni-rich NCM811 and without GPE was assembled to realize a fully inorganic garnet ASB based on NCM as CAM (Chapter 8).

All of the above mentioned ASBs have only low active material loadings of 1 – 3 mg cm^{-2}, which are not higher than the values for thin film batteries. In addition, many of the approaches shown still use organic components within the batteries, so these batteries are not fully inorganic. Although the composition, performance, and degradation of D. Wang's battery are similar to the LCO based ASBs reported by M. Finsterbusch *et al.* and C.-L. Tsai *et al.*, there are still few reports on bulk-type, fully inorganic, oxide ceramic ASBs based on NCMs. Thus, S. Ohta *et al*.[162] achieved an active material loading of 13.4 mg cm^{-2} for their garnet ASB based on a composite cathode of NCM111 and LLZO:Nb. The cell was fabricated by low temperature sintering, triggered by a H^+/Li^+ ion-exchange (LTI) process at 400 °C and 98 MPa for 6 h. In the first discharge cycle the resulting cell delivered 127 mAh g^{-1} and an exceptionally high specific areal capacity of 1.7 mAh cm^{-2}, which is even higher than LCO-based garnet-type ASBs (1.63 mAh cm^{-2}) fabricated by conventional sintering at above 1000 °C.

The overview of garnet-type ASBs based on NCM as CAM (Table 2) shows that the integration of higher capacity CAMs has so far not led to the required performance increase to compete with today's LIBs. Despite the use of various additives, in the case of NCM as CAM, only special sintering techniques lead to higher active material loadings and specific areal capacities

compared to the LCO-based cells. The general drawback of ASBs is the relatively high interfacial resistance between CAM and SSE. This high resistance can be attributed to a poor contact between both components in the composite cathode as well as at the interface between the cathode and the solid-state separator layers. In general, it is necessary to increase the relative density of the composite cathode, which increases the energy density and decreases the cell resistance due to lower tortuosity of the ionic and electronic conducting paths. Simulations have shown that filling the pores within the composite cathode with active material improves contact with the SSE and leads to significantly higher capacities and energy densities. In addition, reducing the thickness of the solid separator (e.g., by tape casting or screen printing) has a large impact on the Li-ion conductivity, rate performance, and overall energy density of the battery. A further increase in the capacity and energy density can be achieved by increasing the thickness of the composite cathode. However, this will make the ionic conductivity of the SSE inadequate, since a higher loading of active material will result in larger currents at the same C-rate. An improved Li-ion conductivity of LLZO ($>2.0 \cdot 10^{-3}$ S cm^{-1}) is required. In general, fast kinetics are needed to increase the power density, which can be realized if the SSE exhibits large thermal conductivities so that possible heat produced during fast charge and discharge processes can be dissipated faster to avoid hot spots. In view of a possible commercialization of fully inorganic, bulk-type ASBs based on oxide ceramic materials, an improvement of the specific capacity up to 3 mAh cm^{-2} is needed to be competitive with current LIBs [31, 118, 119, 121, 144].

1.5. Objective of this thesis

One of the future battery concepts being intensively investigated in the ceramics industry is the solid-state lithium battery (ASB) based on oxide ceramic materials. The overall research goal of the community in this field is the development of a high-performance ASB, which is competitive with conventional lithium-ion batteries. In this work, a fully inorganic bulk battery based on a Li metal anode, a solid-state electrolyte (SSE) of the garnet-type $Li_7La_3Zr_2O_{12}$ (LLZO), and a composite cathode consisting only of the active cathode material (CAM) and SSE is targeted. Thick composite cathodes with high active material loading and percolating paths for Li-ion and electron conduction provided by cubic LLZO and CAM, respectively, are required to enhance of the energy density up to 250 Wh kg^{-1}, so that they can compete with advanced polymer-based solid-state batteries already on the market. This can be achieved by using either higher capacity or high voltage cathode active materials. However, due to the need for high temperature processing of ceramic components, the fabrication of garnet-type ASBs is

challenging as co-sintering of high-voltage and high-capacity CAMs with LLZO leads to material compatibility issues. Therefore, this thesis focuses on strategies to optimize and integrate high-capacity active materials, such as $Li[Ni_{1-x-y}Co_xMn_y]O_2$ (NCM), into composite cathodes for oxide ceramic ASBs. In addition to its higher capacity, NCM is also favored for its lower toxicity and price due to its lower cobalt content. Although NCM cathodes are already optimized for the use in conventional liquid electrolyte cells, the adaptation to the requirements of garnet-type ASBs is necessary. In this work, the effects of different NCM compositions (different Ni/Co/Mn ratios) and doping of the NCM host structure with boron (B) and ruthenium (Ru) on the thermal compatibility towards cubic, Ta-substituted LLZO (LLZO:Ta) are investigated. It is known that the type and concentration of dopants in the NCM structure strongly affect the electronic and ionic conductivity, thermal stability, volume change during galvanostatic cycling, cation interdiffusion at the electrolyte/electrode interface, defect formation, and morphology. Based on previous theoretical studies, the dopant boron with its small ionic radius was found to segregate on the particles surface to form a lithium borate-like layer. Therefore, boron doping was investigated as it could form a protective surface coating that reduces the reactivity between CAM and LLZO:Ta during co-sintering at elevated temperatures. Considering that Li_3BO_3 is used as a sintering aid for the NCM/garnet composite cathodes and may eventually diffuse in the NCM, the effects of B doping on material compatibility should be also investigated. The significantly larger and highly charged ruthenium ions (up to Ru^{5+}) were chosen because the Ru–O bond is known to have a covalent character and thus could have an impact on the compatibility between NCM and SSE.

The previous chapter (Chapter 1) has provided a motivation for battery research and a literature review of NCM and ASBs. In the following, Chapter 2 introduces characterization methods relevant for this thesis and describes the applied experimental parameters. The synthesis of pristine and doped NCM, the synthesis of SSEs, the compatibility tests between NCM and LLZO:Ta, and the cell fabrication were described in Chapter 3. Before analyzing the material compatibility between NCM and LLZO:Ta, this work focused on the detection and localization of the dopants in NCM and the study of the effects of different Ni/Co/Mn ratios and dopants on the morphology and the electrochemical performance in liquid electrolyte-based cells (Chapter 4 and 5). The effects of optimizing and upscaling of the NCM synthesis by using a Couette-Taylor-Flow-Reactor is demonstrated in Chapter 6. Then, the co-sintering behavior of SSE and CAM is analyzed in Chapter 7 to evaluate the thermal compatibility between LLZO:Ta and five different NCMs. Finally, the most promising NCM is integrated into a composite cathode to demonstrate a garnet-type NCM-based ASB with enhanced energy density (Chapter 8).

2. Material characterization – theory and application

In this chapter, the theoretical background of the analytical techniques used for the characterization of the synthesized powders, the prepared active material/solid electrolyte composites and the resulting batteries is explained. At the end of each chapter, the setup details and the performed sample preparation for the characterization is explained.

2.1. X-ray diffraction

X-ray diffraction (XRD) is a technique for the non-destructive analysis of samples in the solid state. It is widely used to determine the lattice structure, lattice parameters, and phase composition of crystalline samples. X-rays, discovered by W.C. Röntgen in 1895, are electromagnetic waves with a wavelength in the order of 1 Å, which is much shorter than the visible light, but in the order of magnitude of the atomic distances within the crystal lattice of the material to be analyzed. X-rays are produced in a vacuum tube, where accelerated electrons bombard a metal anode, consisting typically of Cu or Mo, leading to the emission of characteristic X-rays. The resulting X-ray emission spectrum is composed of a continuous spectrum (white radiation) and characteristic radiation. The characteristic lines that are the most useful for X-ray diffraction are superimposed on the characteristic spectrum. There is more than one characteristic line due to the electron transition between different energy levels (Kß, $K\alpha_1$, $K\alpha_2$). Usually a crystal monochromator (graphite) is used, which only diffracts Kα radiation to obtain a monochromatic beam for X-ray studies. The wavelength of the characteristic X-rays is anode material-specific ($\lambda_{Cu\text{-}K\alpha1}$ = 1.54 Å and $\lambda_{Mo\text{-}K\alpha1}$ = 0.71 Å). A simple way to obtain structural information is via the Bragg equation. It describes the principle of X-ray diffraction in terms of a reflection of X-rays by sets of crystallographic lattice planes. Parallel planes have the same Miller indices (*hkl*) and an equal distance d_{hkl}. All X-rays are reflected in the same direction, superposition of the scattered rays occurs, while the second wave (Figure 22) shows a longer path length. Constructive interference occurs only if the path difference of second wave is a multiple of the wavelength, while in all other cases destructive interference results. Sharp intensity maxima emerge from the sample only at special angles. In this case the Bragg's law (equation (6)) is fulfilled.

$$n\lambda = 2d \sin\theta \tag{6}$$

The Braggs' law describes the relationship between the incident X-ray beam with its wavelength λ, the interplanar lattice spacing of parallel lattice planes d, the diffraction angle θ

between incoming and outcoming X-ray beams, and *n* which gives the order of diffraction [163-165].

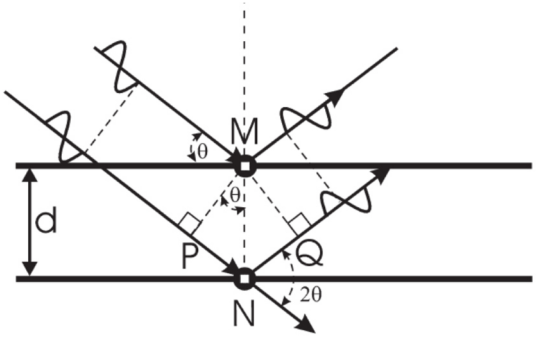

Figure 22: Diffraction of X-rays by a crystal. Reproduced from ref. [163], Copyright 2008 Royal Society of Chemistry.

In order to determine the lattice parameters, the diffraction angle 2θ is available from an experiment and by equation (7), the correlation between the lattice spacing d_{hkl}, the Miller indices *hkl*, and the lattice parameters *a*, *b*, and *c* are given.

$$d_{hkl} = \frac{1}{\sqrt{\left(\frac{h}{a}\right)^2 + \left(\frac{k}{b}\right)^2 + \left(\frac{l}{c}\right)^2}} \tag{7}$$

Equation (7) shows the correlation for the orthorhombic crystal system. For tetragonal and cubic crystal systems, this correlation is simplified due to symmetry [163-165].

In this thesis, X-ray powder diffraction was carried out using a D4 ENDEAVOR (Bruker AXS, Bruker Corporation, USA) with Cu-K_α radiation. For the qualitative phase analysis, powder XRD data were collected in a 2θ range of 10 – 80 °, with a step of 0.02 ° and a collecting time of 0.75 s/step. In the case of measurements for Rietveld refinement, a 2θ range of 10 – 140 ° was chosen. Powder samples were prepared on a silicon low background sample holder (Bruker AXS, Bruker Corporation, USA), whereby for pellets a specimen holder for clay samples (Bruker AXS, Bruker Corporation, Billerica, MA, USA) was used to fix pellet during the measurement. *In-situ* high temperature XRD (HT-XRD) analysis was performed at an Empyrean diffractometer (Malvern Panalytical Ltd., UK) with Cu-K_α radiation. Here, 13 mm pellets (height of ~1.7 mm) placed on an Al_2O_3 sample holder were analyzed. The *in-situ* measurements were performed in air for isotherms at selected temperatures of 25, 100, 200, 300, 350, 400, 450, 500, 550, 600, 650, 700, 750, 800, 900, 1000, 1100, and 1200 °C. The applied heating rate for reaching the next temperature was 5 K min^{-1}. An interval of 10 – 80 °2θ, a step width of 0.026 °, and an accumulation time of 200 s by using a 255 channel PIXcel detector were chosen, so that the resulting holding time at the selected temperatures during the *in-situ* measurement was roughly 37 min. The qualitative phase analysis of the

diffraction patterns was carried out based on the powder diffraction file (PDF) database and the inorganic crystal structure database (ICSD) using the software HighScore (Malvern Panalytical, UK) [166]. Crystal structural refinement and determination of lattice parameters by means of Rietveld refinements were carried out with the software Topas V 4.2 (Bruker AXS, Bruker Corporation, USA) [167]. Rietveld refinements for the samples NCM811_o, 2B-NCM811_o, and 2Ru-NCM811 were performed using the program FullProf [168].

2.2. Inductively coupled plasma – optical emission spectrometry

Inductively coupled plasma-optical emission spectrometry (ICP-OES) is one of the most important techniques of the instrumental analytic for qualitative and quantitative analysis. ICP-OES enables the detection of about 70 elements in a multitude of matrices. The application of the ICP-OES is attractive because of its short measurement times and the overall low labor costs. During one operating procedure it is possible to determine simultaneously several elements and their concentrations. A schematic representation of the working principle of ICP OES is shown in Figure 23.

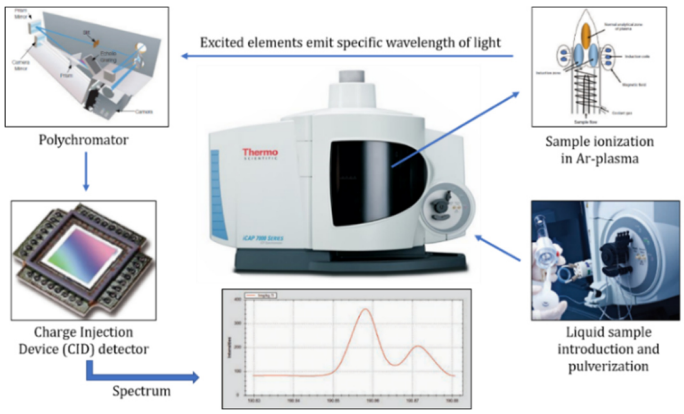

Figure 23: Schematic representation of the working principle of ICP OES (images reproduced from ref. [122], Copyright 2017 Thermo Fischer Scientific).

As a rule, liquid samples are analyzed. The sample is dissolved in an acid solution (usually nitric acid) and diluted. Through an injection system, the liquid sample is introduced into the analysis system. The nebulized sample is fed to the inductively coupled argon plasma. When the sample is exposed to the high temperatures of about 10000 K, all chemical bonds break and the sample is ionized. In the inductively coupled plasma, atoms and ions are excited and element-specific electromagnetic radiation is emitted. The emitted light is split into element-specific wavelengths by an optical system, focused and transmitted through the polychromator to the detector, which detects and measures the intensity. Finally, a two-dimensional spectrum (intensity vs. wavelength) is obtained showing the element peaks and their intensity. Modern

charge injection device (CID) detectors enable the access to the full spectrum between 166 nm and 847 nm. The contained elements are identified by the element specific wavelength, and the peak intensity is a measure for the element concentration. Elements can be detected in the range of μg L^{-1} to g L^{-1}, but the detection limit depends on the element and the instrument [122, 169, 170].

In this work, the chemical composition was analyzed by using a Thermo Scientific iCAP7600 (Thermo Fischer Scientific, USA). In the case of active materials, 50 mg of NCM was dissolved in 3 ml of HCl, 3 ml of HNO_3, and 4 ml of H_2O_2 at room temperature. In the case of solid electrolyte, 50 mg of LLZO:Ta was dissolved in 4 ml of H_2SO_4 by adding 2 g of $(NH_4)_2SO_4$ under strong heating. All solutions were finally diluted to a total volume of 50 ml. The ICP-OES analysis was performed at the Central Institute for Engineering, Electronics and Analysis (ZEA-3) at Forschungszentrum Jülich GmbH.

2.3. Electron microscopy

Electron microscopy is a powerful technique to investigate the morphology (particle size and shape) and phase composition with special resolution up to the atomic scale. The materials in this thesis were analyzed mainly by two methods, namely, scanning electron microscopy (SEM) and transmission electron microscopy (TEM), in combination with energy dispersive X-ray spectroscopy (EDS) and electron energy loss spectroscopy (EELS).

2.3.1. Scanning electron microscopy

Scanning electron microscopy (SEM) is a multi-purpose technique that can produce detailed, high-quality images with a spatial resolution of 1 nm and up to 300,000-fold magnifications. For imaging, a primary electron beam scans the surface of a sample in a raster pattern. The primary electrons generated and emitted by an electron gun are accelerated by a voltage in the range of 1 – 40 keV. The emitted electrons are focused into a monochromatic beam that scans the sample surface and interacts with the sample surface to a certain depth. The high energy electrons hitting the sample lose their energy, resulting in the emission of photons and electrons (Figure 24). The interaction volume depends strongly on the accelerating voltage, the angle of incidence, and the atomic number and concentration of atoms present in the analyzed specimen. The emitted signals shown in Figure 24 were gathered by detectors to form the required image. Mainly secondary electrons (SEs), backscattered electrons (BSEs) and X-rays were used for characterization and imaging.

SEs have a low energy (< 50 eV) and result from inelastic scattering of the primary electrons. SEs escape from a depth of approximately 5 – 50 nm of the sample and therefore provide information about the topography (surface features such as texture, smoothness or roughness) and morphology (particle size and shape) [171].

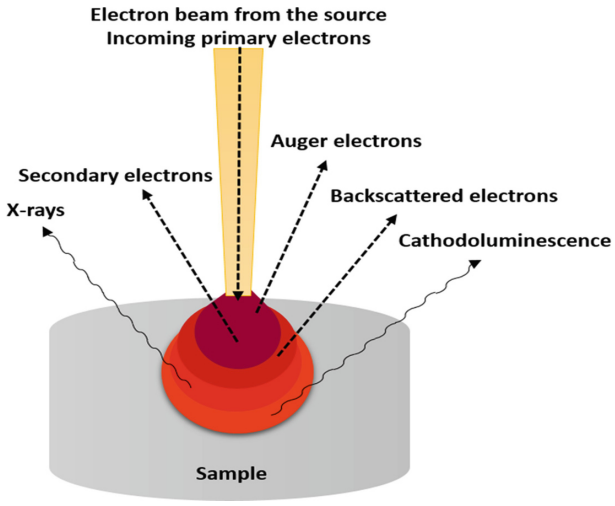

Figure 24: Interaction of an electron beam with a specimen and the emitted signals from the sample. Reproduced with permission from ref. [171], Copyright 2018, Springer International Publishing AG.

The emission of a secondary electron creates a hole that is filled by an electron from a higher energy level, and at the same time an X-ray characteristic of this energy transition is generated. The wavelength/energy of the emitted X-ray is characteristic for each element and can be directly used to determine the elemental composition of the sample. This spectroscopy technique is called energy dispersive X-ray spectroscopy (EDS) and is used in SEM as well as in TEM for chemical analysis [171, 172].

BSEs originate from elastically scattered primary electrons. They have the same energy as the primary electrons and escape from a depth many times greater than that of the SEs. Therefore, their interaction volume and lateral dimensions are larger, but the resolution can be lower. BSEs are used to visualize the material contrast (elemental distribution) in multiphase samples [171]. The combination of both SEs and BSEs analyses with EDS investigations provides complementary information about the morphology, topography, and chemical composition of a sample.

SEM images were taken by the scanning electron microscope Zeiss Gemini 450 (Carl Zeiss Microscopy, Germany) having a field emission gun operated at 1.3 – 15 kV. For EDS analysis, the device is combined with an Ultim® Max 170 (Oxford Instruments, UK) EDS detector and an AZTec acquisition software (Oxford Instruments, UK). The specimens were prepared in three different ways. For powder analysis, the sample was prepared on a sticky carbon tape and

coated with a thin platinum layer. For cross sectional SEM images of a fracture surface, the specimen was contacted with a copper tape and sputtered with a thin platinum layer. Selected samples were embedded into EpoFix epoxy (Struers, Germany), mirror polished, contacted with a copper tape, and coated with a thin platinum layer. Secondary particle cross sections were prepared by a focused ion beam (FIB) with a 15 nA (initial) and 700 pA (final) Ga beam and analyzed by using the scanning electron microscope Zeiss Crossbeam 540 (Carl Zeiss Microscopy, Germany) having a field emission gun operated at 3 kV.

2.3.2. Transmission electron microscopy

Transmission electron microscopy (TEM) is an advanced and versatile characterization technique, which provides both structural and chemical information with a very high resolution of up to 0.05 nm. In comparison to SEM, TEM detects transmitted electrons that require a very high accelerating voltage (> 100 kV) and very thin samples (< 100 nm). The signals generated by electron sample interactions and scattered electrons are focused by an objective lens and projected onto a CCD detector. In TEM, contrast arises from the three contrast mechanisms, namely, mass thickness contrast, diffraction/amplitude contrast and phase contrast. The resulting contrast in the image depends on the size and position of the objective aperture, which determines the imaging mode, i.e. whether it is bright-field or dark-field (Figure 25).

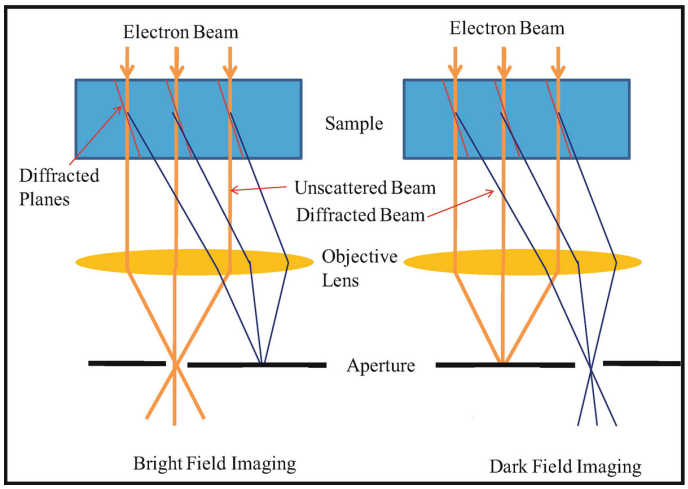

Figure 25: Schematic ray diagrams of the bright-field and dark-field imaging mode. Reproduced with permission from ref. [172], Copyright 2018, Springer International Publishing AG.

In the bright field mode, the aperture is at the center and allows the unscattered electron beam to pass. In this mode, the mass thickness contrast dominates and thicker or high density parts of the sample appear darker. The aperture can also be placed to block the unscattered primary electron beam while allowing the scattered electrons to pass through (dark-field mode).

Therefore, in dark-field mode, areas that scatter electrons strongly (high crystallinity or heavier elements) appear brighter.

High-resolution TEM (HRTEM) or phase-contrast imaging is a powerful imaging technique that provides micrographs of a crystal surface with atomic resolution of approximately 0.05 nm. Here, the elastically scattered electrons are important to obtain high-resolution micrographs. Therefore, high-resolution imaging is always performed in the bright-field imaging mode. HRTEM images provide the atomic structure of a specimen as well as information about stacking faults, dislocations, and point defects.

In addition to elastic signals, inelastic signals can also be used for imaging. In scanning transmission electron microscopy (STEM), the electron beam is focused on an optical probe. A beam diameter of 0.8 Å can be obtained for instruments with aberration correction, which scans the sample at every point allowing to raster the sample. STEM is usually operated in the high-angle annular dark-field mode (HAADF). HAADF-TEM is useful for microanalysis since it is sensitive to variations in the atomic number of elements in the specimen. The HAADF mode is also called the Z-contrast mode because the contrast depends on the Rutherford scattering, which is proportional to the atomic number $\sim Z^2$. Here, the inner shell electrons scatter forward at high angles $\theta > 60$ mrad enabling a chemically sensitive imaging mode with high contrast.

Selected area electron diffraction (SAED) is another important TEM method. It is based on the fact that the distances between atoms in a sample act as diffraction gratings to which electrons can diffract. Similar to a X-ray diffractometer, diffraction patterns of the sample were obtained, which are very useful for structural analysis and the study of crystal defects [172].

Two spectroscopic techniques are available in TEM for analyzing the chemical composition of a sample, namely, energy-dispersive X-ray spectroscopy (EDS), which is also used in SEM (described in Chapter 2.3.1), and electron energy loss spectroscopy (EELS).

EELS is based on the energy loss of fast primary electrons during inelastic scattering in a thin sample. It provides chemical, physical, and optical characteristics of the specimen. An EELS spectrum consists of three parts. The zero-loss region mainly shows an intense peak at 0 eV representing the elastically scattered and non-scattered electrons. The low-loss region between 0 and 50 eV provides information about the optical properties, band structure and dielectric properties of a material. In the core loss region at higher energy losses (> 50 eV), the spectrum shows the so-called ionization edges. These edges are formed when an inner-shell electron absorbs energy from a beam electron and is excited to a state above the Fermi level. The ionization edges are used for the analysis of almost all chemical elements, but especially for the lighter elements. The edge onset indicates the ionization energy and allows a qualitative

analysis. If the sample is very thin, the intensity of the edge is proportional to the element concentration, enabling element quantification [172, 173].

In this thesis, scanning transmission electron microscopy (STEM) was applied for atomic resolution. An aberration corrected FEI Titan G2 80-200 ChemieSTEM field emission electron microscope at 200 kV was used for high-angle annular dark field (HAADF) imaging and acquisition of energy-dispersive X-ray (EDS) elemental mapping. The FEI Titan G2 80-200 ChemiSTEM is equipped with a Schottky type high-brightness electron gun (FEI X-FEG), a Cs probe corrector (CEOS DCOR), an in-column Super-X energy dispersive X-ray spectroscopy unit (ChemiSTEM technology), a post-column energy filter system (Gatan Enfinium ER 977) with dual electron energy-loss spectroscopy (EELS) option allowing a simultaneous read-out of EDX and EELS signals at a speed of 1000 spectra per second [174, 175]. The powder samples were prepared by deposition on a Cu C-film grid. Secondary particle cross sections were prepared by using a focused ion beam (FIB) to extract a lamella out of the center of the particle. A FEI Helios NanoLab 400S FIB-SEM with a DualBeam^{TM} focused ion beam, an Elstar^{TM} electron column operated at 5 kV for imaging, a Sidewinder^{M} ion column for cross sectioning operated at 30 kV and a FlipStage^{TM} for (S)TEM lamella sample preparation was used [174, 176]. TEM analysis was performed at the Central Facility for Electron Microscopy (GFE) at RWTH Aachen University and at the Ernst Ruska-Centre (ER-C 2) at Forschungszentrum Jülich GmbH.

2.4. X-ray photoelectron spectroscopy

X-ray photoelectron spectroscopy (XPS) is a unique surface-sensitive technique for chemical analysis of solid samples with a penetration depth of a few nanometers. XPS belongs to the photoelectron-based spectroscopic techniques, which are based on the photoelectronic effect. XPS measures the core-level binding energies of an ejected photoelectron from atoms at or near the surface of a specimen. For surface analysis by XPS, a solid sample is irradiated with X-rays under vacuum. The X-rays interact with the sample atoms, a photon is absorbed, and a photoelectron is emitted. The kinetic energy (KE) of the emitted electrons, which is the residual energy not used to overcome the binding energy (BE), is analyzed. Based on the detected KE of the electron being ejected from a sample, the original BE of the emitted electron can be calculated by equation (8):

$$\mathrm{BE} = \mathrm{h}\nu - \mathrm{KE} - \Phi_{\mathrm{s}} \tag{8}$$

where hν is the energy of the incident photon, and Φ_s is the spectrometer work function. For any material, XPS data provide three main components, namely, the peak intensity at the binding energy of the ejected electron, the position of the peaks on the energy axis, and the width/splitting of the peaks. Careful analysis of the XPS data allows conclusions to be drawn about the elemental composition, their percentage, the nature of bonding, and the spin-orbital splitting. For each element a unique set of binding energies is obtained. The detected binding energy depends on the binding behavior of an atom, e.g., the binding energies shift to higher energies when an atom is bound to a more electronegative atom, since the inner electrons are more strongly bound. Therefore, the peak shifts in the XPS spectrum provide information about the valence state of the atoms in the analyzed sample [177-179].

In this thesis, XPS was used to determine the oxidation states of boron and ruthenium in B- and Ru-doped NCM811, respectively. A 200 µm spot of the powder samples, prepared on an indium foil, was analyzed by using a Phi5000 VersaProbe II (ULVAC-Phi Inc., USA) spectrometer with monochromatic Al K_α radiation (1.486 keV). For the survey, 187.5 eV pass energy, 0.8 eV step, and 100 ms/step were used while for the detailed analysis, 23.5 eV pass energy, 0.1 eV step and 100 ms/step were applied. The charge correction was performed by setting the C-C component of the C 1s signal to 285 eV. The XPS analysis was performed at the Central Institute for Engineering, Electronics and Analysis (ZEA-3) at Forschungszentrum Jülich GmbH.

2.5. Ion beam analysis

Ion beam analysis (IBA) includes a group of methods to analyze materials compositions. The combination of the IBA methods such as Rutherford backscattering spectrometry (RBS), nuclear reaction analysis (NRA), particle induced X-ray emission (PIXE), and particle induced gamma-ray analysis (PIGE) provides the most complete analysis of all elements of the periodic table within a single measurement. In most cases, IBA is non-destructive and reference-free. Depth profiles of elements and isotopes as well as concentrations of elements can be obtained. A combination with scanning methods enables compositional tomography with resolution in the µm range. The combination of several IBA methods can provide ppm-level detection limits and sub-% accuracy for light (NRA), intermediate (PIXE), and heavy (PIGE and RBS) elements in a self-consistent way, which are particular advantages over electron beam-based analysis. Furthermore, it has a high throughput since up to 40 samples can be analyzed per day. Thus, IBA is becoming a standard characterization method with a wide range of applications, also in lithium battery development [180, 181].

An ion source generates projectiles that are accelerated and focused by beam optics into a beam with minimal spot size. The high intensity ion beam is focused onto a sample in vacuum ($2 \cdot 10^{-9}$ mbar), the projectiles hit and interact with the atoms of the sample, and the products of this ion-matter interaction are detected (Figure 26). IBA uses various kinds of projectiles (protons, deuterons, ^{3}He, or ^{4}He) with kinetic energies in the order of 1 to 10 MeV per ion and ion currents in the range of pA to µA. Since each projectile species has his individual advantage, different ion sources for distinct projectile species are selected with respect to the specific results to be obtained. Different projectile ion species show qualitative differences in the interaction aspects with the targets such as nuclear reactions and depth resolution. The projectile energy influences the possible reactions via their cross section and thresholds, and it influences the stopping power and range (e.g., high beam energy leads to high range but low depth resolution). However, the probing depth is not only defined by the range but depends also on the reaction and the target and is usually significantly smaller than the projectile range [180, 182].

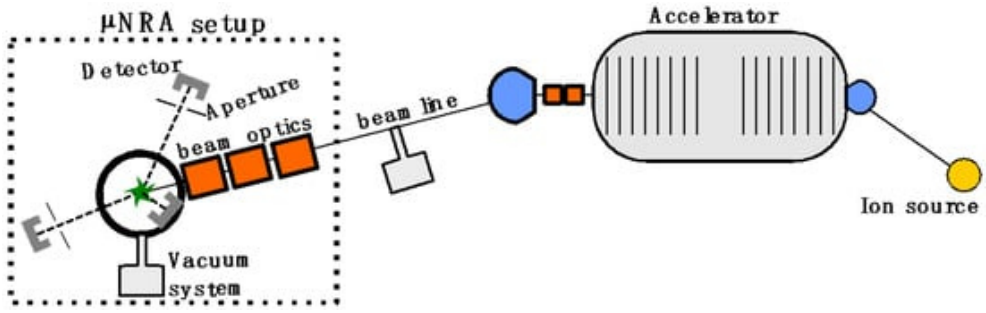

Figure 26: Scheme of an ion beam analysis setup with the required modules and the sample (green star) attached to a tandem accelerator. Reproduced from ref. [180], Copyright 2021 by the authors. Licensee MDPI, Basel, Switzerland (http://creativecommons.org/licenses/by/4.0/).

The interaction products that can be detected are X-rays, gamma-rays, secondary electrons, recoils, scattered projectiles, and nuclear reaction products (Figure 27). Several analytical methods can be used to detect the products of the ion beam-material interaction. The first class covers imaging techniques such as ion-beam-microscopy (IBM) that counts the emitted secondary electrons, and scanning-transmission-ion-microscopy (STIM) that exploits the projectile energy loss in the sample for imaging in transmission geometry. The second class of methods, including RBS and NRA, uses the information delivered by the released/backscattered ions. RBS detects the elastically scattered particles of heavy elements with depth resolution. However, RBS is not able to quantify the light elements like lithium and hydrogen. If the energy of the projectile is chosen to be high enough (some MeV), nuclear reaction cross sections become relevant that produce protons and ^{4}He with energies higher than the projectile energy.

These products enable an improved detection of the light elements by NRA. NRA of inelastic nuclear fusion reactions leads to better contrast for the light elements that results in isolated peaks in a background free region [180, 182].

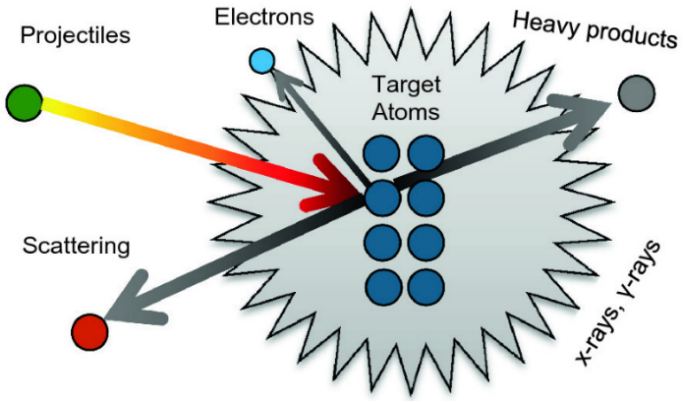

Figure 27: Illustration of the accelerated projectiles hitting atoms of a sample generating photons, electrons, and heavy particles depending on the projectile energy and nature. Reproduced with permission from ref. [183], Copyright 2020, Springer Nature Switzerland AG.

The combination of RBS and NRA enables detection of both heavy and light elements with quantity and depth resolution, where peak heights usually give element concentrations, peak width provides information about layer thickness, and peak height variations deliver information about the mixing of layers and elements. The third class of methods utilizes the photons emitted by the projectile sample interaction. PIXE is the ion equivalent to EDX that detects emitted X-rays, whereby significantly better detection limits can be achieved due to the higher ion masses and less emitted bremsstrahlung. Similar to NRA, the projectile can also induce nuclear excitations (e.g., ^{7}Li(p, nγ)^{7}Be) that can be analyzed within PIGE. The high energy gamma-rays can penetrate several mm of the material, allowing a detection even through the sample and vacuum chamber.

In the early stages of IBA, specific setups were used for each individual method, but due to the weaknesses of each single methods, the combination of methods (total-IBA) has proven superior. NRA detects light elements, RBS with its high cross section reveals intermediate to heavy elements, PIXE provides the lowest detection limits for impurities and enables separation of intermediate elements and STIM/IBM combines results with other imaging methods. Furthermore, knowledge of element identity and quantity from PIXE and PIGE is combined with depth information from RBS and NRA.

Cathode materials for lithium-ion batteries such as NCM ($Li[Ni_{1-x-y}Co_xMn_y]O_2$) contain a mixture of light and heavy elements. The heavy elements can be easily analyzed by RBS, but due to the similar atomic mass of Ni, Co, and Mn it is difficult to distinguish them. PIXE data enable clear determination of their concentration in depth, while RBS gives surface-near

information. On the other hand, lithium is practically not visible in the RBS spectrum and its PIXE X-ray energy is hardly detectable. Therefore, a nuclear reaction such as $^{7}Li(p, \alpha)^{4}He$ can be used to detect and quantify lithium. Since RBS and PIXE are independent on the projectile type, the Li, Ni, Co and Mn measurement can be conducted in one run with an energy determined by the $^{7}Li(p, \alpha)^{4}He$ threshold [182].

In this thesis, B- and Ru-doped NCM cathode materials were characterized by IBA. The focus was on the detection and localization of boron and ruthenium dopants. NRA was applied to detect the light element boron in 2 mol% B-doped NCM111 and 2 mol% B-doped NCM811 powders that were attached to adhesive carbon tapes. The area analyzed by the ion beam was 200 µm in diameter. Therefore, only large agglomerates could be analyzed without the tape background. If these were not present, the carbon tape was accounted for by normalization to the metals present in NCM. The measurement setup (µNRA) recently introduced by S. Möller *et al.*[180] was used for IBA within this work (Figure 26). The nuclear reaction $^{10}B(^{4}He, p_0)^{13}C$ was used for ^{10}B detection. For the calibration of the detection efficiency a pure boron plate was analyzed, and the data were evaluated considering the material specific stopping power. The cross sections from the work of H. Chen *et al.*[184] were used since no better matching cross sections were found in the literature. The comparison with the pure boron showed a reasonable agreement with the yields for thick target boron in spite of the different reaction angles. To improve the sensitivity of boron detection by PIGE, 2960 keV protons with a radiation dose of 4µC and a 200 µm beam spot were used. 2125 keV gamma rays were produced via the reaction $^{11}B(p, p\gamma_{1\text{-}0})^{11}B$ and measured using a Mirion HPGe detector. Furthermore, RBS was used for the detection of the heavy elements (Ni, Co and Mn) of the NCM scaffold. The Ru-doped NCM811 powder was analyzed in a sample holder specially developed for the analysis of powders by IBA (Figure 28).

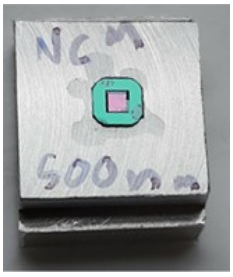

Figure 28: Photo of the powder sample holder used for the analysis of Ru-doped NCM811. In the center, the SiN window is visible.

This powder sample holder is made of aluminum and equipped with a 500 nm thick SiN window that is optically transparent for the beams. Ruthenium was detected by RBS and PIXE

using 2960 keV protons and Si-detectors for simultaneous detection of the RBS and PIXE spectra. The evaluation of the IBA data was performed with the SimNRA 7.02 software [185].

2.6. Time-of-flight secondary ion mass spectrometry

Time-of-flight secondary ion mass spectrometry (TOF-SIMS) is a mass spectrometry technique used for high resolution material characterization. It is able to detect all elements of the periodic table with high sensitivity in the ppm range, and high surface specificity with a resolution in the nm range. The analysis is performed under ultra-high vacuum of around 10^{-10} mbar, which is the key ingredient needed for the high sensitivity analysis. Usually, a dual beam instrument as shown in Figure 29 is used.

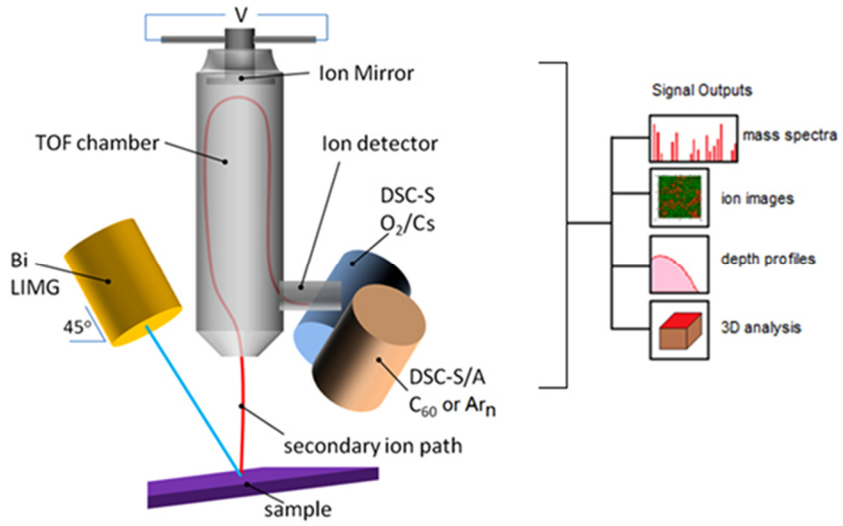

Figure 29: Schematic representation of a dual-beam time-of-flight secondary ion mass spectrometer. Reproduced from ref. [186], Copyright 2015 Morgan & Claypool Publishers.

In a dual beam system, a primary ion beam (0.1 – 20 keV) is scanned over the sample surface and generates secondary ions by bombarding the sample. The main primary ion beam is a liquid metal gun (LMIG/S), which nowadays is typically based on bismuth due to higher secondary ion yields compared to other ion sources. The secondary ions were extracted by an extraction potential (2 – 8 keV) into the time-of-flight (TOF) chamber where the separation by the mass-to charge ratio (m/z) takes place. The secondary ions were analyzed under static ion beam conditions. During their flight to the detector, light ions arrive first, while the heavier ions arrive later at the detector. Hence, the arrival times of the ions depend on the ion mass and are transformed to respective m/z rations generating a mass spectrum. The second ion beam (sputter gun) in a dual beam TOF-SIMS system can be used for a controlled erosion (sputtering) of the sample to obtain sputter depth profiles. Here, typically an Ar^+ or an O_2^+ ion beam is used. Such a sputtering process enables the analysis of a sample composition from the surface to the bulk.

A dual beam TOF-SIMS instrument can operate in different operation modes depending on how the primary and sputter ion beams are combined with each other. Depending on the operation mode, different output signals such as high-resolution mass spectra, ion images (chemical maps), and depth profiles (3D analysis) can be obtained. High resolution mass spectra from the sample surface are obtained by using only the primary ion beam under static conditions (static SIMS). Low ion beam doses are applied to ensure that the surface is not sputtered so that the analysis in this mode is non-destructive. Ion images (2D) are obtained since the spatial coordinates of the beam were recorded so that ions from the mass spectra can be coupled with their location over a defined analyzed area. For depth profiling, an additional ion source (sputter ion beam) is used that peels away atoms/molecules from the sample layer by layer and thereby the mass spectra can be measured as function of depth. Compared to the primary ion beam source, the dose of the sputter ion beam is strongly increased to remove the sample material. This analysis mode is called dynamic SIMS. The first step of depth profiling is to raster the sputter beam over a defined sputter area (e.g., 400 µm by 400 µm). Afterwards, the primary ion beam is applied to a smaller area within the larger sputter area to avoid any interaction with material on the edge of the sputter crater. The primary ion beam leads to the emission of secondary ions to be collected and analyzed as described above. Sputtering and primary ion beam analysis is repeated sequentially until the sample was analyzed until the desired depth. For the single ions detected in the resulting mass spectra, a depth profile for every species can be generated. In this mode, the detected secondary ions are registered in three dimensions, hence 3D chemical plots can be constructed [186].

In this work, TOF-SIMS was applied for boron and ruthenium depth profiling using a TOFSIMS_5.NCS system (ION-TOF GmbH, Germany). Pristine NCM811, B-doped NCM811 and Ru-doped NCM811 powders were prepared by spreading them on an indium foil and fixing them through self-adhesion. A 30 keV Bi^+ primary beam for analysis and a 1 keV O_2^+ beam for sputtering (to alter the analysis depth of the measurement) was scanned over an area of 400 µm by 400 µm, operating under a non-interlaced mode and using a 1 s:1 s sputter:analyze cycle. The analyzed area by the Bi beam was 130 µm by 130 µm, with either positive or negative secondary ions detected. Data analysis was carried out with the SurfaceLab 7.0 (ION-TOF GmbH, Germany) software. TOF-SIMS analysis was performed at the Central Institute for Engineering, Electronics and Analysis (ZEA-3) at Forschungszentrum Jülich GmbH.

2.7. Thermal analysis

Thermal analysis (TA) is defined as a group of techniques monitoring changes of physical or chemical properties of a sample with time as it is subjected to a temperature program (heating, cooling, or isothermal holds). This section gives an overview about the thermogravimetry (TG) and differential thermal analysis (DTA) methods. TG is a quantitative analytical technique that monitors the mass of a sample during a temperature program and measures changes in the mass of a specimen. As a result of the TG measurement, a thermogravimetric curve is obtained that can be plotted in its integral form (TG curve: mass against time or temperature) or in its differential form (DTG curve), which is the derivative of the TG curve with respect to time plotted against temperature. Typically, a mass loss occurs due to degradation/decomposition, vaporization of bulk or adsorbed liquids, and desorption of gases. The measuring device consists of a thermobalance, which is a combination of a sensitive analytical balance connected to a sample carrier and an electronically programmed furnace. The balance weights the sample in a furnace, while a thermocouple near the sample carrier detects its temperature. The analyzing unit is enclosed airtight inside a compartment. A dynamic purge gas, which can be oxidizing, reducing, or inert, typically enters from below the sample carrier and passes over the sample (Figure 30).

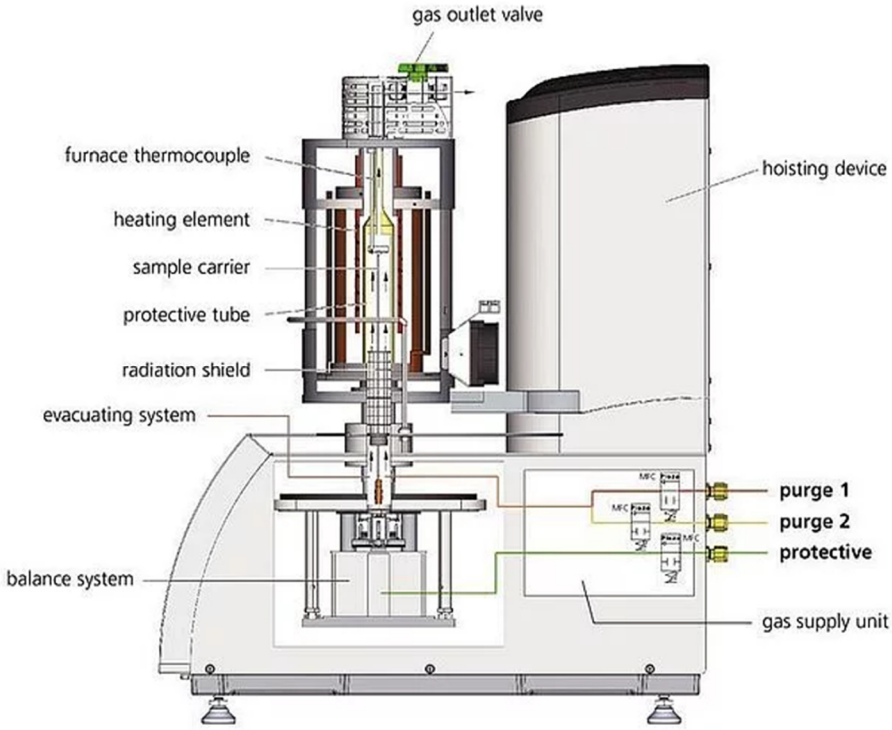

Figure 30: Schematic drawing of the device STA 449 F1 Jupiter® (NETZSCH-Gerätebau GmbH, Germany) used for DTA-TG measurements. Reproduced from ref. [187], Copyright 2021, Netzsch-Gerätebau GmbH.

In order to obtain qualitative information about the mass changes observed by TG, the outcoming gas flow during a dynamic operation can be analyzed. For this purpose, TG is often combined with mass spectrometry (MS) or gas chromatography (GC). Furthermore, for the analysis of simultaneous changes in heat flow and mass, TG can be coupled with differential thermal analysis (DTA). In addition, such a combination enables the detection of changes without mass loss or gain by melting, crystallization, glass transition, and solid-solid transitions [188-190]. In the case of DTA, the temperature difference between a sample (T_s) and reference material (T_r) is measured while both are subjected to the same heating program ($\Delta T = T_s - T_r$). If an endothermic (ΔH positive, e.g., melting) or exothermic (ΔH negative, e.g., oxidation) event occurs in the sample, the temperature of the sample will lag behind or overshoot the temperature of the reference material. In the plotted DTA curve, a negative peak is called an endotherm, which is characterized by its onset temperature. The area under endotherm (or exotherm) peaks is related to the enthalpy change ΔH for the thermal event [191].
In this thesis, the thermal behavior of NCM, LLZO:Ta and LBO powders as well as of NCM/LLZO:Ta powder mixtures was analyzed by differential thermal analysis and thermogravimetry (DTA/TG) using an STA 449 F1 Jupiter® (NETZSCH-Gerätebau GmbH, Germany) coupled with a mass spectrometer (MS) QMS 403 C Aëolos® Quadro (NETZSCH-Gerätebau GmbH, Germany).

2.8. Specific surface area by nitrogen adsorption

The specific surface area of a powder strongly depends on its porosity and morphology (particle size and shape). Powder analysis by electron microscopy gives detailed information about the morphology and porosity on the powder surface. However, information about the internal structure of pores, their dimensions, and volume as well as their contribution to the surface area are hidden. Gas molecules adsorb on the surface of each particle of a powder sample as well as in the pore interiors, and therefore the gas adsorption is a powerful method to obtain a precise value of the surface area of a powder sample. Adsorption always occurs when a clean solid surface is exposed to vapor. Depending on the strength of interaction, the adsorption process can be divided into irreversible chemisorption (adsorption due to chemical bonding) and reversible physisorption (adsorption due to dispersion forces). The physisorption is most suitable for surface area determination as the heat of adsorption is low compared to chemisorption and no structural changes occur to the surface during adsorption measurement. Physisorption is fully reversible, so that also the desorption process can be studied. Furthermore, physically adsorbed molecules are not limited to specific sites. They cover the

entire surface, and therefore it is possible to use physisorption to calculate the surface area rather than number of binding sites [192, 193]. Mathematical models are used to determine the volume of gas adsorbed in the case of a monolayer coverage of the powder surface. However, always a multilayer adsorption takes place. The BET-model proposed by Brunauer, Emmett and Teller is the most widely used procedure for evaluating the surface area by measuring the total gas volume adsorbed/desorbed. The correlation between the measured totally adsorbed gas volume V and the gas volume adsorbed in a complete monolayer V_m is described by the equation (9) (BET-equation):

$$\frac{1}{V\left(\frac{p}{p_0}-1\right)} = \frac{C-1}{V_m C}\left(\frac{p}{p_0}\right) + \frac{1}{V_m C} \tag{9}$$

with C as the constant of adsorption (BET constant), p adsorbate pressure in equilibrium and p_0 saturation pressure of adsorbing gas.

By plotting $1/(V(p/p_0 - 1))$ versus p/p_0 a straight line in the range of $0.05 \leq p/p_0 \leq 0.35$ is obtained. From the slope $s = (C - 1)/(V_m C)$ and intercept $i = 1/V_m C$, the volume adsorbed in a monolayer can be calculated by equation (10).

$$V_m = \frac{1}{s+i} \tag{10}$$

The experimental efforts can be reduced to only one data point by using the single point BET-method. The single point BET-equation (11) is obtained by assuming that the value for C is high ($>> 1$) so that ($C - 1 \approx C$) and the intercept $i = 1/V_m C$ is assumed to vanish. Equation (10) reduces to:

$$V_m = V\left(1 - \frac{p}{p_0}\right) \tag{11}$$

Knowing the volume of gas adsorbed in a monolayer and the molar volume of an ideal gas ($V_{mol} = 22.71\ 10^{-3}\ m^3\ mol^{-1}$), the specific BET surface area can be calculated by equation (12):

$$A_S(\mathrm{BET}) = \frac{V_m \cdot N_A \cdot A_x}{V_{mol} \cdot m} \tag{12}$$

where N_A is the Avogadro number, A_x is the molecular cross sectional adsorbate area and m is the mass of analyzed powder.

Nitrogen is the most commonly used adsorbate to obtain the BET surface area with a molecular cross sectional adsorbate area A_x (N_2) = 0.162 nm^2 [193-196].

In this work, the specific surface area of the NCM powders was determined by nitrogen adsorption using an AREA-mat (Jung Instruments GmbH, Germany). The surface area was calculated by using the BET-single point method at $p/p_0 = 0.05 – 0.2$.

2.9. Powder density determination

The true or real density of a powder is defined as the ratio of the mass to the volume occupied by that mass. Hence, the contribution of pores/internal voids to the occupied volume needs to be subtracted to obtain the true density. By assuming that the analyzed powder has no porosity, the true density can be measured by displacement of a fluid in which the solid remains inert. However, the solid particles of a powder usually contain pores and cracks that need to be easily penetrated by a displaced fluid. A suitable displacing fluid is a gas. Most frequently, helium is used due to its inertness and small size, which enables the penetration of fine pores up to 0.2 nm. Thereby, true volumes with high accuracy are available. Compared to liquid displacement techniques, the dry gas method does not lead to problems associated with wetting and solubility of the solid. The apparatus used to measure solid volumes is called gas expansion pycnometer. A schematic diagram of such a pycnometer is shown in Figure 31.

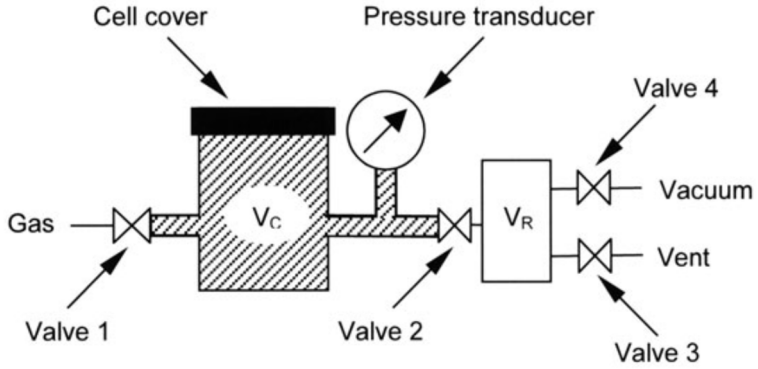

Figure 31: Schematic drawing of a gas expansion pycnometer for true density determination of powders. Reproduced with permission from ref. [197], Copyright 2004, Springer Science Business Media New York.

Simplified, the pycnometer consists of two cells, namely, the sample cell with volume V_C where a defined mass of powder is placed, and a reference cell with volume V_R. After purging and evacuation, all volumes are brought to ambient pressure. Afterwards, the sample cell is pressurized to P_1. By opening valve 2, sample and reference cell are connected so that the pressure drops in the sample cell and increases in the reference cell to a value P_2. The powder volume V_P is than calculated by equation (13).

$$V_P = V_C + \frac{V_R}{1 - (P_1/P_2)} \tag{13}$$

Based on the determined true powder volume, the density can directly be calculated as ratio of mass to volume [197, 198].

In this thesis, the true density of the NCM powders was determined by using a gas pycnometer (Ultrapycnometer 1000, Quantachrome Instruments, Germany) with helium as displacing fluid.

2.10. Particle size distribution

The particle size distribution (PSD) of a powder can be analyzed by laser diffraction (LD), which is one of the most popular methods in particle size analysis due to short measuring times and excellent reproducibility. The LD method is based on light scattering by particles. The resulting intensity pattern depends on the particle size and shape. A volumetric particle size distribution is calculated by using an optical model and a mathematical deconvolution procedure, so that the calculated scattering pattern fits to the measured pattern [199]. The interaction between small particles and light is described by the Lorenz-Mie theory. The latter is derived from the Maxwell equation for an electromagnetic field and describes the field when an interaction takes place. If the analyzed particles are large compared to the wavelength of the light source, the interaction can be interpreted in terms of diffraction. In this case, the interaction between particles and light is described by the Fraunhofer diffraction theory. If particles are suspended in a liquid, the application of the Fraunhofer diffraction theory is limited, especially if the particles are small compared to the wavelength of light and if the refractive indices are similar. In those cases, the application of the Lorenz-Mie theory leads to a more precise description of the particle size distribution [200].

In this work, the particle size distribution was measured by a laser diffraction particle size distribution analyzer (LA-950, Horiba, Japan) equipped with two laser diodes (650 nm and 405 nm). Beforehand, the powders were dispersed in ethanol. The PSD was recorded before and after 3 min sonication. If not otherwise mentioned, the presented values for D10, D50 and D90 were determined after sonication. The evaluation was based on the Mie-theory by using a refractive index of 1.24[201] and 1.833 for NCM and LLZO:Ta, respectively. In the case of Li_3BO_3, the Fraunhofer theory was applied.

2.11. Electrochemical characterization

Electrochemical characterization of the synthesized cathode active materials and of the all-solid-state batteries (ASBs) was performed by cyclic voltammetry (CV), galvanostatic charge-discharge (GCD), and electrochemical impedance spectroscopy (EIS).

For electrochemical measurements within this thesis, batteries were assembled in coin cells (CR2032) or T-shaped Swagelok cells. Coin cells based on a liquid, organic electrolyte were used for the electrochemical characterization of conventional NCM cathodes, and Swagelok cells were used for ASBs. A schematic representation of both cell types is shown in Figure 32.

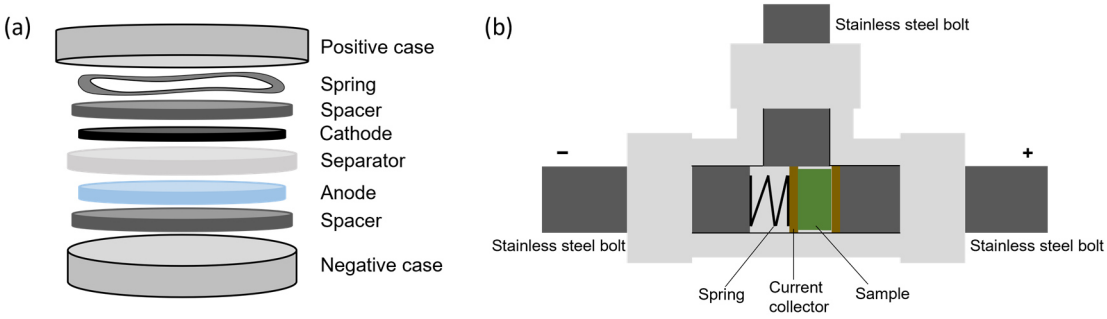

Figure 32: Scheme of a (a) coin cell and a (b) Swagelok cell used for cell tests with liquid and solid-state electrolyte, respectively.

The fabrication of conventional cathodes and ASBs as well as the cell assembly are described in the experimental section (Chapter 3.3). All electrochemical tests were carried out by using a multipotentiostat (VMP-300, BioLogic Sciences Instruments, France) combined with a climate chamber (VT 4002EMC, Vötsch Industrietechnik GmbH, Germany) at a constant temperature. Liquid electrolyte-based coin cells were tested at 25 °C, while ASBs were tested at 60 °C. The cyclic voltammograms and galvanostatic charge-discharge curves were evaluated by the software EC-lab (BioLogic Sciences Instruments, France). For evaluation and fitting of the impedance spectra, the ZView software (3.3b edn.; Scribner Associates, Inc., USA) was used.

2.11.1. Cyclic voltammetry

Cyclic voltammetry (CV) is an electrochemical analysis technique that is widely used in various fields of electrochemistry. It gives information about the processes taking place at different potentials including their quantitative values (specific potential, current density, and capacitance) and is broadly used to investigate the thermodynamics and kinetics of electrochemical systems. CV enables the analysis of the electrochemical redox reactions by recording the current, while the potential changes linearly as function of time (potential technique). The slope of the potential change over time is defined as scan rate ν (in mV s^{-1}). In comparison to linear sweep voltammetry, for CV the voltage is scanned over a potential range $E_1 - E_2$ and reverses to E_1 again (Figure 33a). The resulting current versus the voltage plot is called cyclic voltammogram (Figure 33b). Different shapes of cyclic voltammograms appear depending on the type of electrochemically active material, particle size, thickness of the electrode, electrolyte concentration, operating temperature, and chosen scan rate [202].

According to the IUPAC convention, the oxidation peak and the anodic current have positive values, while the reduction peak and the cathodic current have negative values on the *y*-axis [203] (Figure 33b). This convention is also used in this work.

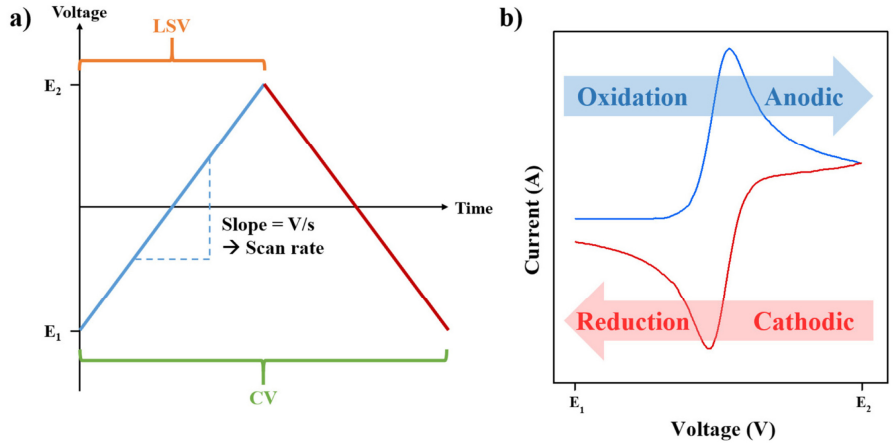

Figure 33: (a) Voltage vs. time profile for linear sweep and cyclic voltammetry. (b) Typical cyclic voltammogram of a reversible reaction showing anodic and cathodic peak. Reproduced from ref. [202], Copyright 2020 Journal of Electrochemical Science and Technology (open-access article distributed under the terms of the Creative Commons Attribution Non-Commercial License (https://creativecommons.org/licenses/by-nc/4.0/)).

The reversibility of a redox process is determined by the separation between the anodic and cathodic peak potentials, $E_{p,a}$ and $E_{p,c}$. In the case of a fast charge-transfer process, the peak separation potential ΔE_p is determined by equation (14) and depends on n, the number of transferred electrons.

$$\Delta E_p = \frac{2.3\,RT}{nF} = \frac{56.5}{n}\,\text{mV (at 25 °C)} \tag{14}$$

The lithiation/de-lithiation of NCM is a single electron process with $n = 1$ and therefore ΔE_p should be around 56.5 mV. This value can be higher, as the Li^+ intercalation reactions tend to be quasi-reversible. For a quasi-reversible process, the anodic and cathodic peak potentials depend on the scan rate and shift toward more positive and more negative potentials for oxidation and reduction scans, respectively, if the scan rate is increased [49, 202, 204].

For diffusion-controlled processes with electrochemically reversible electron transfer processes, the peak current i_p increases linearly with the square root of the scan rate ν. Higher scan rates lead to a decrease in the size of the diffusion layer and as a result of this, higher currents are obtained. This correlation is described by the Randles-Sevcik equation (15):

$$i_p = 0.446\,nFAC_{Li^+}\left(\frac{nF\nu D_{Li^+}}{RT}\right)^{1/2} \tag{15}$$

where n is the number of the transferred electrons, F is the Faraday constant ($F = 96487$ C mol^{-1}), R is the ideal gas constant ($R = 8.31447$ J mol^{-1} K^{-1}), T is the absolute temperature, A is the electrode surface area (geometrical surface area), D_{Li+} is the Li^+ diffusion coefficient and C_{Li+} is the concentration of lithium ions.

Based on the the Randles-Sevcik equation, the Li^+ diffusion coefficient can be determined by recording cyclic voltammograms at different scan rates. By plotting the resulting peak currents i_p versus the square root of the scan rate ν, the diffusion coefficient D_{Li+} can be calculated from the slope of the obtained straight line. This is only valid when no phase transitions take place during the lithiation/delithiation process. Therefore, diffusion coefficients obtained for materials undergoing phase transitions need to be checked for their reliability [202, 203].
CV enables to better understand the consecutive electrochemical reactions at the electrodes. The current follows a power law as shown in equation (16):

$$i = a\nu^b \tag{16}$$

where i is the current, ν is the scan rate and a, b are adjustable variables. The b value can be expressed by the sum of faradaic (diffusion-controlled) and non-faradaic (capacitive) currents. The value of b is 0.5 for diffusion-controlled reactions and 1.0 for the capacitive processes [202].
CV can be used for calculating the charge (specific capacity) of the lithiation/delithiation by the integration of the area below oxidation and reduction peak [202]. However, in battery research the specific capacities are usually obtained by galvanostatic charge/discharge experiments which will be introduced in the following chapter.
In this thesis, cyclic voltammetry was used to proof the electrochemical activity of the synthesised NCM cathodes by determining their redox reaction potentials. The measurements were carried out at 25 °C with a scan rate of 0.05 mV s^{-1}. In the case of NCM111, CV was performed in a potential range from 3.0 – 4.4 V vs. Li/Li^+, while for the Ni-rich NCM811 the potential was scanned between 3.0 and 4.5 V vs. Li/Li^+.

2.11.2. Galvanostatic charge/discharge technique

Galvanostatic charge-discharge (GCD) is a major electrochemical characterization technique in battery research to obtain information about the gravimetric, volumetric, and areal capacity of active electrode materials, reversibility, rate capability, and cycling stability. During GCD, the time-resolved voltage response of a battery at a constantly applied current is recorded. For charging, a positive current (i) is applied until a chosen upper cutoff potential (E_2) is reached at which the current direction is inverted to $-i$, so that the battery is discharging until the lower cutoff potential (E_1) is reached (Figure 34a,b). The applied current is usually normalized to the active material loading (A g^{-1}) or to the electrode area (A cm^{-2}). In battery research, the rate of charge and discharge is typically expressed as the C-rate (h^{-1}) which indicates how often the

full theoretical capacity can be reached within 1 h at a constant current. For example, if an electrode material (e.g., NCM111) has a practical gravimetrical capacity of 160 mAh g^{-1}, 1 C means that a current of 160 mA g^{-1} should be applied to charge or discharge this capacity within 1 h (the absolute current is then obtained by multiplication with the mass of electrode material).

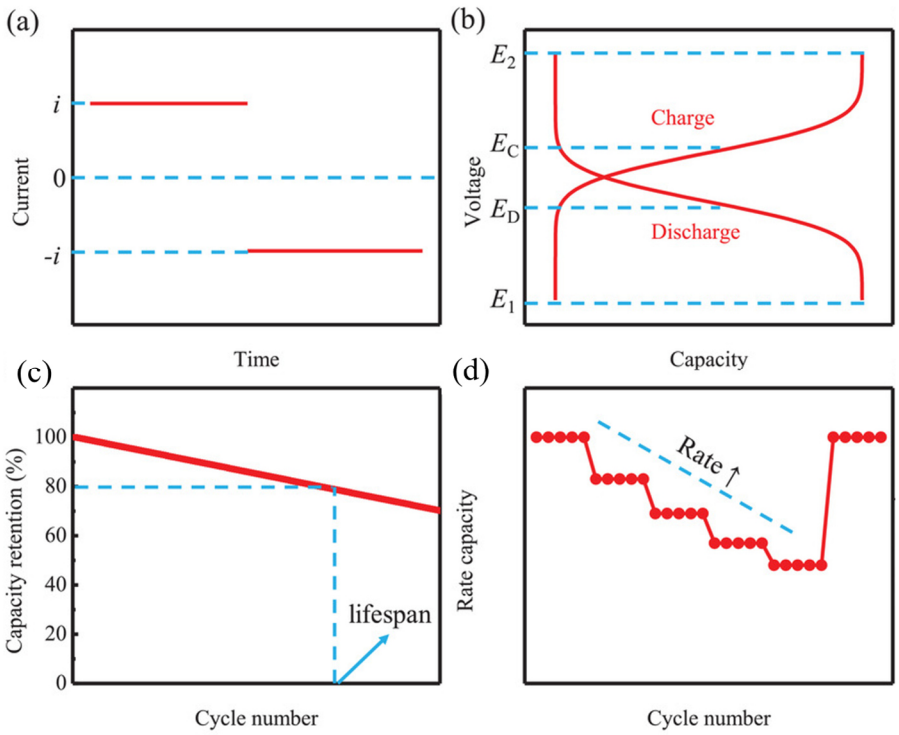

Figure 34: Schematic representation of the galvanostatic charge-discharge technique. (a) Applied current profile, (b) recorded voltage response vs. capacity, (c) capacity retention during long-term cycling, and (d) rate capability test. Reproduced (adapted) with permission from ref. [205], Copyright 2019 WILEY-VCH Verlag GmbH & Co. KGaA, Weinheim.

Galvanostatic charge-discharge experiments can be used to determine practical charge and discharge capacities as well as the voltage profiles of electrode materials. The definition of the capacity of a battery was given in Chapter 1.2. The voltage profile has the shape of a plateau (Figure 34b) at the potentials corresponding to the specific redox potential of a material (seen as a peak potential in the CVs discussed above). The ratio between the discharge and charge capacity is defined as Coulomb efficiency (CE), which is an important factor to evaluate the reversibility of a charge-discharge cycle. Typically, the charge-discharge cycles were repeated for several times at a constant C-rate to evaluate the long-term stability and capacity retention of an electrode material during repetitive charging/discharging, which are the most important parameters of a rechargeable battery (Figure 34c). To evaluate the performance of an electrode material at different C-rates, a rate capability test is performed by increasing the charge/discharge current stepwise after a certain number of cycles. Due to polarization, the capacity decreases when increasing the current. However, if the C-rate is decreased again, the

capacity should increase to its initial value in the case of a reversible capacity (Figure 34d) [205].

In this thesis, GCD was used to determine the practical capacity, rate performance, and capacity retention during long-term cycling of pristine and doped NCM in conventional LIBs based on a liquid electrolyte as well as in ASBs. In the case of liquid electrolyte-based cells, GCD was performed at different C-rates (0.04 C, 0.1 C, 0.5 C, 1 C, and 2 C; 1C = 160 mA g^{-1}) in a voltage window of 3.0 – 4.3 V vs. Li/Li^+. Long-term cycling was performed by constant current (cc) charge-discharge at 0.5 C followed by constant voltage (cv) charge-discharge until a current of C/10 was reached. For all-solid-state batteries, galvanostatic cycling was performed between 3.0 V and 4.2 V vs. Li/Li^+ at a constant current density of 40 µA cm^{-2} (0.06 C, 1 C = 115 mA g^{-1}). In the charged state, the battery was additionally held at a constant voltage of 4.2 V until the current dropped to 20 µA cm^{-2}.

2.11.3. Electrochemical impedance spectroscopy

Electrochemical impedance spectroscopy (EIS) is a powerful technique to obtain information about the resistances in an electrochemical cell at specific current or potential values. EIS enables the separation and quantification of different contributions to the cell impedance, namely, the resistance of the bulk material, impedances of an interface layer, charge-transfer reactions, and diffusion process in a single measurement and also under operating conditions. For EIS, a sinusoidal voltage (AC voltage) with a low amplitude (few mV) is applied over a wide frequency range (typically 10^5 – 10^{-2} Hz), while the current response is measured. When an AC voltage is applied to an electrochemical cell, the impedance can be expressed by the Ohm's law for an AC circuit (equation (17)):

$$Z(\omega) = \frac{V(\omega)}{I(\omega)} \tag{17}$$

where ω is the angular frequency ($\omega = 2\pi f$), $V(\omega)$ is the excitation signal, and $I(\omega)$ is the current response signal. The excitation and the current response signal can be expressed by the following equations:

$$V(\omega) = V_\mathrm{m} \sin(\omega t) \tag{18}$$

$$I(\omega) = I_\mathrm{m} \sin(\omega t + \phi) \tag{19}$$

V_m and I_m represent the amplitude (maximum values) of V and I, respectively. When V is applied with the angular frequency ω, there is a phase shift (ϕ) between voltage and current.

Inserting the equations (18) and (19) into (17), using the complex function *j*, applying Euler's equation and finally splitting into real and imaginary parts, leads to the following equation:

$$Z(\omega) = Z_0 \cos(\phi) + Z_0 \sin(\phi) j \tag{20}$$

Based on equation (20) the real and imaginary parts of $Z(\omega)$ are:

$$Z'_{\text{real}} = Z_0 \cos(\phi) \tag{21}$$

$$Z''_{\text{img}} = Z_0 \sin(\phi) \tag{22}$$

For batteries, the impedance spectrum is typically represented as Nyquist plot that provides insights into the mechanisms and governing phenomena contributing to the total cell resistance. A Nyquist plot is obtained by plotting $-Z''_{\text{img}}$ versus Z'_{real} for different values of ω. The total impedance of a cell can be represented by a suitable equivalent circuit model, which correlates each electrochemical process/component to electrical components such as resistors (R), capacitors (C), and inductors (L). Additional elements such as the constant phase element (CPE) and the Warburg impedance (W) can be used to model a non-ideal capacitor and lithium diffusion, respectively, which is often the case in LIBs. The equations for fundamental electrochemical elements used in equivalent circuit models are summarized in Table 3.

Table 3: Circuit elements used in equivalent circuit models [206].

Equivalent element	**Formula**
R (Resistance)	R
C (Capacitance)	$1/j\omega C$
L (Inductance)	$j\omega L$
W (Warburg impedance)	$A_{\text{W}}\omega^{-1/2} - jA_{\text{W}}\omega^{-1/2}$ A_{W}: Warburg coefficient
Q_{CPE} (Constant Phase Element)	$1/Q(j\omega)^{\alpha}$ ($\alpha = 1$ for ideal capacitor)

In Figure 35, the Nyquist plot and the corresponding simplified equivalent circuit model of a typical LIB half-cell system are shown. In this model, R_b represents the internal resistance of all bulk materials (electrolyte, separator, current collector, and electrodes) in a battery. As these contributions have only a resistance without capacitance, they are observed in Z_{real}. The first semicircle in the high-frequency range, represented by the R_{SEI}-CPE_{SEI} element (Figure 35), originates for the materials investigated in this work from the impedance of a SEI (solid

electrolyte interphase) layer formed on the interface between the electrode and the electrolyte, which is generated by the decomposition of electrolyte. The second semicircle in the medium-frequency range, represented by the R_{ct}-$CPE_{electrode}$ element (Figure 35), corresponds to charge-transfer resistance (R_{ct}). R_{ct} gives an insight into the kinetics of an electrochemical reaction and is strongly influenced by surface coatings, phase transitions, band gap structure, and particle size. Furthermore, the charge-transfer resistance depends on the state of charge, temperature, and thickness of the electrode. The straight line, observed in the low-frequency range immediately after the semicircles, represents the Warburg impedance (W), which is correlated to the lithium-ion diffusion process in the host material of the electrode. In practice, the equivalent circuit model discussed above needs to be modified to ensure an agreement with the experimental data. By using a suitable software, the numerical fitting of an appropriate equivalent circuit model to the experimentally obtained data enables access to the values for the resistances (R_b, R_{SEI}, and R_{ct}) and capacitances (CPE_{SEI} and $CPE_{electrode}$) [205, 206].

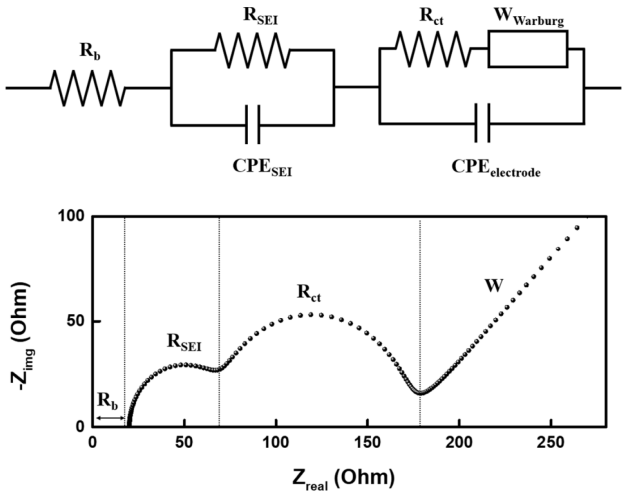

Figure 35: Equivalent circuit model and Nyquist plot of a lithium-ion battery half-cell system. Reproduced from ref. [206], Copyright 2020 Journal of Electrochemical Science and Technology (open-access article distributed under the terms of the Creative Commons Attribution Non-Commercial License (http://creativecommons.org/licenses/by-nc/4.0)).

In this work, the characterization of NCM cathodes in liquid electrolyte-based cells by EIS was performed at 4.3 V vs. Li/Li^+ in a frequency range of 1 MHz – 10 mHz with a sinusoidal amplitude of 10 mV. For ASBs, electrochemical impedance spectroscopy was performed at 4.2 V vs. Li/Li^+ in a frequency range of 3 MHz – 0.1 Hz with a sinusoidal amplitude of 10 mV. In addition to characterizing electrochemical cells, electrochemical impedance spectroscopy is also used to determine the conductivity of polycrystalline materials such as the solid-state electrolyte LLZO. A typical impedance spectrum obtained for ceramic samples is shown in Figure 36. Two semicircles are observed, one in the high-frequency and one in the medium-

frequency range, which are attributed to the bulk (grain interior) resistance (R_b) and grain boundary resistance (R_{gb}), respectively. The electrode contribution is visible in the low-frequency range and is represented by CPE_{el}. From the knowledge of the sample geometry, one can calculate the bulk conductivity based on the measured resistance, while the so-called brick layer model is applied to calculate the grain boundary conductivity [207, 208].

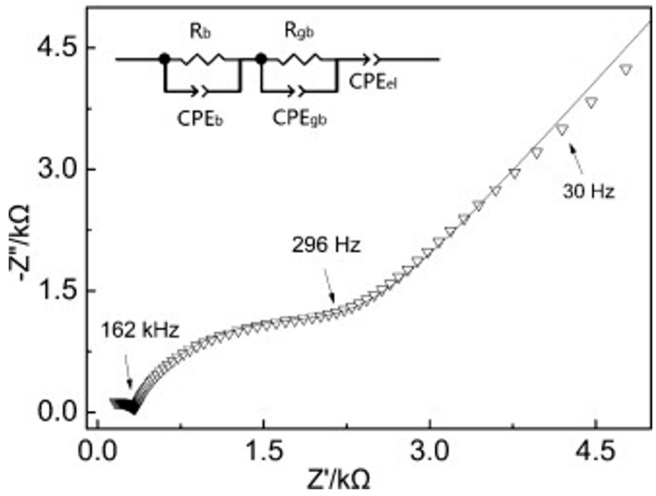

Figure 36: Room temperature impedance spectrum of a sintered ceramic sample. Reproduced (adapted) with permission from ref. [207], Copyright 2012 Elsevier Ltd.

In this thesis, electrochemical impedance spectroscopy was applied to determine the ionic conductivity of densely sintered LLZO:Ta pellets. The sintered pellets were polished with SiC-sandpaper up to 4000 grit and sputtered for 150 s with a thin gold layer as current collector on both sides using a sputter coater (Cressington 108auto Coater, TESCAN GmbH, Germany). EIS was performed at 25 °C in a Swagelok cell by using a multipotentiostat (VMP-300 BioLogic Sciences Instruments, France) combined with a climate chamber (VT 4002EMC, Vötsch Industrietechnik GmbH, Germany) in a frequency range from 7 MHz – 1 Hz with a sinusoidal amplitude of 10 mV mm^{-1}.

The total ionic conductivity (σ) of LLZO:Ta was calculated by equation (23) based on the total resistance ($R_b + R_{gb}$) obtained after fitting the impedance spectrum:

$$\sigma = \frac{L}{(R_b + R_{gb})A} = \frac{L}{(R_b + R_{gb})\frac{\pi d^2}{4}} \tag{23}$$

whereby σ is the total ionic conductivity in S cm^{-1}, L the length (height), and d the diameter of the pellet. The typical dimensions of a measured pellet were ~11 mm in diameter and 7 – 13 mm in height.

2.12. DFT calculation

The theoretical work was performed by Dr. Liang-Yin Kuo and Dr. Payam Kaghazchi (IEK-1, Forschungszentrum Jülich GmbH) in order to increase the understanding of the effects of doping on the material properties, the subsequent effects on the full-cell behavior, and the compatibility between cathode material and solid-state electrolyte.

2.12.1. Simulation of atomistic structure

Spin-polarized density functional theory (DFT) calculations were performed using the Projector Augmented-Wave (PAW)[209] pseudopotential method implemented in the Vienna Ab Initio Simulation Package (VASP) code [210]. The Perdew-Burke-Ernzerhof (PBE) functional[211] was employed to approximate the exchange-correlation (XC) energy for DFT calculations to find the most favorable structures. All the reported results in the simulation section are from DFT calculation using the strongly constrained and appropriately normed (SCAN) functional [212]. Total Coulomb-energy (E_C) calculations on various possible combinations were carried out using the *supercell* code [213]. The $Li[Ni_{0.8}Co_{0.1}Mn_{0.1}]O_2$ (NCM811) bulk was modelled using a 4×4×1 ($Li_{48}Ni_{40}Co_4Mn_4O_{96}$) supercell [214]. To determine the atomic positions for the Ni ↔ Li interchange cases, the following combinations were considered. For the case of 4 % Ni ↔ Li interchange, i.e. $(Li_{0.96}Ni_{0.04})(Li_{0.04}Ni_{0.76}Co_{0.1}Mn_{0.1})O_2$ modelled by $(Li_{46}Ni_2)(Li_2Ni_{38})Co_4Mn_4O_{96}$, all possible combinations of two Ni cations in 48 Li sites and two Li ions in 40 Ni sites, namely $\frac{48!}{2!46!} \times \frac{40!}{2!38!} = 1128 \times 780 = 8.8 \times 10^5$, were considered. For 2 mol% B doping with a 4 % Ni/Li interchange, i.e. $(Li_{0.96}Ni_{0.04})(Li_{0.02}Ni_{0.76}Co_{0.1}Mn_{0.1}B_{0.02})O_2$, all possible combinations of two Ni cations in 48 Li sites, one Li ion in 40 Ni sites, and one B cation in 40 Ni sites, namely, $\frac{48!}{2!46!} \times \frac{40!}{1!39!} \times \frac{39!}{1!38!} = 1128 \times 40 \times 39 = 1.8 \times 10^6$ configurations were modelled. DFT-PBE calculation was then performed on five structures with low E_C values for both cases, namely, 4 % Ni ↔ Li interchange and 4 % Ni ↔ Li interchange + 2 mol% B → Li doping. By comparing total energy (E_{tot}) values of five structures with minimum E_c values for the B-doped case (with 4 % Ni ↔ Li interchange), we found a structure with one B cation (2 %) in the Ni/Mn-layer and 1 Li ion (2 %) in the Ni/Ni-layer is the most favorable one. Therefore, a similar structure for the interchange case in which boron was replaced by Li was considered. The calculated E_{tot} value for this structure was found to be lower than those for structures with minimum E_c values. Thus, the lowest E_{tot} structure of 4 % Ni ↔ Li interchange was determined to be that with one Li ion (2 %) in the layer with only Ni cations (hereafter called the Ni/Ni-layer) and one Li ion (2 %)

in Ni and Mn ions (hereafter called the Ni/Mn-layer). Afterwards, another structure was checked for the case of the B doping, with 4 % Ni ↔ Li interchange in which one Li ion (2 %) was located in the Ni/Mn-layer and one B cation (2 %) in the Ni/Ni-layer. It was found that this structure has a lower E_{tot} than that with one B cation (2 %) in the Ni/Mn-layer and one Li ion (2 %) in the Ni/Ni-layer. The atomic structure of the 8 % Ni ↔ Li interchange case was modelled from the 4 % Ni ↔ Li interchange one by considering two times more numbers of interchanges. To find the positions of 2 B cations in the supercell (4 mol% B doping), i.e. $(Li_{0.92}Ni_{0.08})(Li_{0.04}Ni_{0.72}Co_{0.1}Mn_{0.1}B_{0.04})O_2$, the following replacements were considered for the structure with 8 % Ni ↔ Li interchange: 2B → 2Li (in the Ni/Ni-layer), 2B → 2Li (in the Ni/Mn-layer), and 1B → 1Li (in the Ni/Ni-layer) together with 1B → 1Li (in the Ni/Mn-layer). Finally, it was found that the first structure has the lowest total energy among the considered structures. For all the E_c calculations, an average charge state of Ni, Co, and Mn is +2.96, and +2.92 for 2 mol% and 4 mol% B doping, respectively as well as a charge state of +3.00, +1.00, and −2.00 for B, Li, and O ions, respectively, were applied. DFT-PBE and SCAN calculations were carried out using a Gamma-centered 2×2×1 *k*-point mesh and an energy cut-off of 500 eV as well as an energy and force convergence criterion of 10^{-4} eV and 10^{-3} eV $Å^{-1}$, respectively. In order to model the structure and lattice parameters of 2 mol% Ru-doped NCM811, Spin-polarized DFT calculations were performed with the PAW[209] pseudopotential method implemented in the VASP code [210]. The PBE functional with the Hubbard *U* correction (PBE+U) proposed by Dudarev *et al.*[215] was considered to approximate the XC energy for DFT calculations. The *U*−*J* (hereafter called *U*) value for Ni, Co, Mn, and Ru is U(Ni) = 6.0, U(Co) = 5.9, U(Mn) = 5.2 and U(Ru) = 8.0, respectively. Three atomic structures where a Ni cation is replaced by one Ru cation in Ni/Ni-layer, Ni/Co-layer, and Ni/Mn-layer were modelled to find the most favorable structure for 2 mol% Ru doping of $Li[Ni_{0.8}Co_{0.1}Mn_{0.1}Ru_{0.02}]O_2$ (2Ru-NCM811).

2.12.2. Simulation of interdiffusion processes

Spin-polarized DFT calculations were performed with Projector Augmented-Wave (PAW) pseudopotential method[209] implemented in the Vienna Ab Initio Simulation Package (VASP) code [210]. The Perdew-Burke-Ernzerhof (PBE)[211] functional was employed to approximate the exchange-correlation (XC) energy. The atomic structure of bulk $LiNi_{0.8}Co_{0.1}Mn_{0.1}O_2$ (NCM811) was presented in our previous work [214]. Nine possible configurations for the Zr → Ni and La → Ni substitution as well as one configuration for the

Zr → Co, La → Co, and Zr → Mn substitution in NCM811 were checked. To investigate the transition metal (TM) → Zr (La) substitution in LLZO:Al, one configuration for each case, in which one of the Zr (La) cations in the unit cell was replaced by one Ni, Co, or Mn cation, was modelled. As it was found that interchanges between cations with different charges were less likely, the $La^{3+} \leftrightarrow Mn^{4+}$ case was not considered. Because of its high charge state, the interchange of Ta^{5+} with transition metals in NCM811 was also unlikely. For this reason, this work focused on a bulk LLZO:Al structure from a previous study [216]. All DFT-PBE calculations were carried out using a gamma-centered 2×2×1 and 1×1×1 *k*-point mesh for all NCM811 and LLZO:Al structures. An energy cut-off of 500 eV and an energy and force convergence criterion of 10^{-4} eV and 10^{-3} eVÅ^{-1}, respectively, were used for all calculations.

3. Material synthesis, compatibility tests and cell fabrication: experimental part

3.1. Synthesis of cathode active materials

The cathode materials were synthesized by a hydroxide co-precipitation route reported before [38, 107], which was modified and adapted to allow the desired cathode material compositions. Within the scope of this work, the co-precipitation was mainly performed batchwise on a laboratory scale (Figure 37a). The whole synthesis was performed under a replenished argon atmosphere and degassed, deionized water (boiled for 15 min and cooling under argon bubbling) was used to prepare the starting solutions. In order to synthesize the NCM hydroxide precursor $(Ni_{1-x-y}Co_xMn_y)(OH)_2$, a 2 M transition metal (TM) solution was prepared by dissolving $NiSO_4 \cdot 6H_2O$ (Alfa Aesar, 98 %), $CoSO_4 \cdot 7H_2O$ (Alfa Aesar, 98 %) and $MnSO_4 \cdot H_2O$ (Alfa Aesar, 99 %) in deionized water. Depending on the desired NCM composition, the ratio of Ni:Co:Mn was adjusted to be 1:1:1 or 8:1:1. Additionally, aqueous solutions of 2 M NaOH (Sigma-Aldrich, 98 %) and 10 M NH_3(aq) (Alfa Aesar, 28 %) were prepared. The transition metal solution was added dropwise under vigorous stirring (magnetic stirring bar, 1000 rpm) with an average flowrate of 45 ml h^{-1} into a 500 ml flask, containing an aqueous starting solution (0.05 M NH_3(aq)). Simultaneously, the NH_3(aq) solution was added so that molar ratios, of NH_3(aq)/TM = 0.38, in the case of NCM111, and NH_3(aq)/TM = 1.00 in the case of NCM811, were adjusted. The pH value was precisely controlled to be 11 by adding the NaOH solution. After 5 h of aging, the precipitated hydroxide was filtered and washed with degassed, deionized water. The remaining solid was dried at 80 °C in a vacuum oven (VO 500, Memmert GmbH + Co.KG, Germany) for at least 14 h. To pulverize the dried precursor, a dry milling step by using a planetary ball mill (Pulverisette 7, Fritsch GmbH, Germany) was performed. A weight ratio of 1:5 (sample:5 mm ZrO_2 balls) was chosen. After milling, 5 – 6 g of a fine light, brown hydroxide precursor powder was obtained per batch (Figure 38a).

For the synthesis of 2 mol% Ru-doped NCM811 precursors, $RuCl_3 \cdot xH_2O$ (Alfa Aesar, 99.9 %) was dissolved in deionized water and a desired volume of the resulting solution, with a Ru content of 39.8 g L^{-1}, was added to the TM solution to realize a molar ratio of Ru:(Ni + Co + Mn) = 0.023:1. Afterwards, the co-precipitation of the Ru-doped hydroxide precursor was performed as described before.

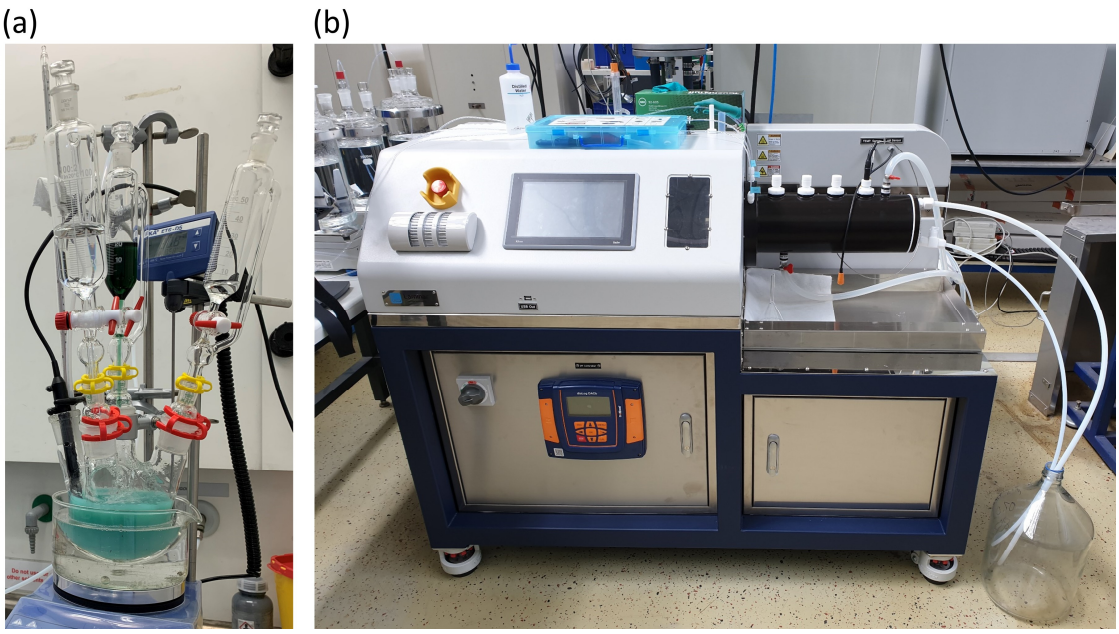

Figure 37: Experimental setups used for the synthesis of NCM via co-precipitation. (a) Batch process and (b) continuous process by using a Couette-Taylor-Flow-Reactor (CTFR).

To optimize and up scale the synthesis of the $(Ni_{0.8}Co_{0.1}Mn_{0.1})(OH)_2$ precursor for the sample referred to as NCM811_CTFR, a continuous co-precipitation using a Couette-Tylor-Flow-Reactor (LCTR®-Tera 3300-HC, Laminar Co., Ltd, Korea) was used (Figure 37b). Here no replenished argon atmosphere and degassed deionized water were needed. A 2 M transition metal solution with a Ni:Co:Mn ratio of 8:1:1, a 4 M solution of NaOH and a 8 M solution of NH_3(aq) were prepared by using the same chemicals as mentioned before. The reactants were fed automatically via membrane pumps into the CTFR, which was filled before with distilled water. The addition of the TM and NH_3(aq) solutions was kept at a constant flow rate of 1.99 ml min^{-1} and 0.50 ml min^{-1}, respectively. This corresponds to a molar ratio NH_3(aq)/TM = 0.97. The NaOH solution was automatically added to control and keep the pH value at 11. During operation a constant flow of 1.78 ml min^{-1} has adjusted itself. The CTFR was operated at a constant temperature of 50 °C, an inner cylinder rotation speed of 1300 rpm, and a mean residence time of 3.9 h. After a steady state was reached, the light green product suspension was continuously collected, filtered, washed, and dried as described above. Under the conditions applied in this work, it was possible to synthesize 400 g hydroxide precursor within one day.

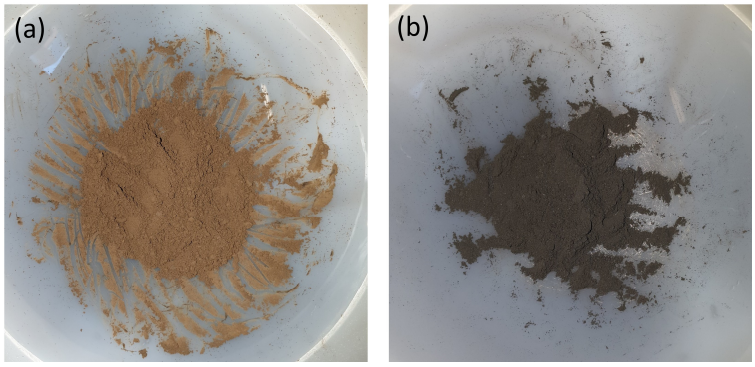

Figure 38: Optical image of (a) hydroxide precursor powder ($(Ni_{1-x-y}Co_xMn_y)(OH)_2$) and (b) lithiated NCM powder ($Li[Ni_{1-x-y}Co_xMn_y]O_2$).

In order to form the final $Li[Ni_{1-x-y}Co_xMn_y]O_2$ (NCM), the hydroxide precursor was mixed with LiOH (Merck, 98 %) in a molar ratio of Li:(Ni + Co + Mn) = 1.03:1. To obtain B-doped NCM, the hydroxide precursor was synthesized identically as described before, but, in addition to LiOH, also B_2O_3 (Sigma-Aldrich, 99.98 %) was added in a molar ratio of B:(Ni + Co + Mn) = x:1 (x = 0.013, 0.023, 0.033, and 0.043 depending on the desired boron concentration). The mixture was thoroughly ground in an agate mortar and calcined in an Al_2O_3 crucible for 5 h at 480 °C, and subsequently for 10 h at 750 °C or 800 °C for NCM111 or NCM811, respectively. A muffle furnace (LT 5/13, Nabertherm GmbH, Germany) was used for the heat treatments, whereas heating and cooling rates of 5 K min^{-1} were applied. After calcination, a fine, grey NCM powder was obtained (Figure 38b). In general, the calcination step was performed in air, but the samples NCM811_o, 2B-NCM811_o and 2Ru-NCM811 were calcined under pure oxygen atmosphere by using the same temperature program mentioned before. Calcination of these samples under pure oxygen atmosphere was carried out by TANiOBIS GmbH (Goslar, Germany) using an Inconel tube furnace with an O_2 flow of 170 L min^{-1}. Until further use, all cathode active material samples were stored in an argon filled glovebox.

3.2. Synthesis of solid-state electrolytes

Al- and Ta-substituted LLZO (nominal composition: $Li_{6.45}Al_{0.05}La_3Zr_{1.6}Ta_{0.4}O_{12}$), hereafter abbreviated as LLZO:Ta, was synthesized via a modified, four-step solid-state reaction (SSR) as described before [121, 126]. The starting materials $LiOH \cdot H_2O$ (Applichem, 99.00 %), La_2O_3 (Merck, 99.90 %, pre-dried for 10 h at 900 °C), ZrO_2 (Treibacher, 99.50 %), Ta_2O_5 (Treibacher, 99.99 %), and Al_2O_3 (Inframat, 99.90 %) were mixed in a stoichiometric ratio with an excess of 20 % $LiOH \cdot H_2O$. The starting materials were homogenized and subsequently ground with an automatic mortar grinder (RM 200, Retsch GmbH, Germany) for 1 h.

Afterwards, the powder was mixed again in the intensive mixer for 5 min at 2000 rpm. The homogenized powder was pressed uniaxial into pellets (d = 45 mm) at 19 MPa by using a hydraulic hand press (Paul-Otto Weber GmbH, Germany). The pellets were calcined in air at 850 °C and two times at 1000 °C for 20 h each. Between the calcination steps, grinding, homogenization, and pressing were repeated. For the final sintering step at 1175 °C for 10 h in air, pellets with a diameter of 13 mm consisting of approximately 6 g calcined LLZO:Ta powder were pressed uniaxial by applying 113 MPa. The pellets were placed on a LLZO:Ta powder bed on top of a MgO plate. For the further application, the sintered pellets (Figure 39a) were crushed and ground in an automatic mortar grinder (RM 200, Retsch GmbH, Germany) for 1 h or sliced into 0.6 mm thin discs (Figure 39b) using a low-speed diamond table saw (IsoMet, Buehler, ITW Test & Measurement GmbH, Germany) and polished using up to 4000 grit SiC-sandpaper.

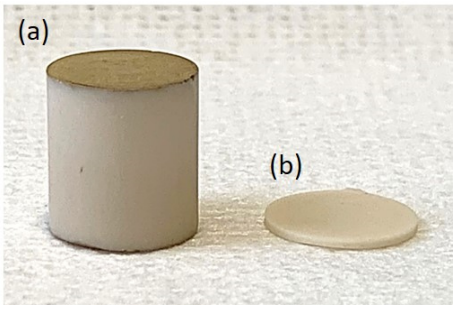

Figure 39: (a) Sintered LLZO:Ta pellet (d = 11.3 mm, h = 12.6 mm) and (b) sliced LLZO:Ta disc (d = 11.4 mm, h = 0.61 mm).

Li_3BO_3 (LBO) was synthesized by an SSR. LiOH (Merck, 98 %) and H_3BO_3 (Alfa Aesar, 99+ %) were mixed in a molar ratio. The raw material mixture was homogenized and thoroughly ground in an agate mortar and calcined in air at 500 °C for 1 h and at 600 °C for 2 h.

For all heat treatments, Al_2O_3 crucibles and a muffle furnace (LT 5/13, Nabertherm GmbH, Germany) with heating and cooling rates of 5 K min^{-1} were used. Until further use, all-solid-state electrolyte samples were stored in an argon filled glovebox.

3.3. Fabrication of conventional cathodes and assembly of coin cells

In order to investigate the electrochemical activity of pristine and doped NCM, electrodes with an active material loading of around 5 mg cm^{-2} were fabricated by casting a cathode slurry onto an Al foil current collector. The slurries were prepared by mixing NCM, carbon black (Alfa Aesar, Super P® Conductive, 99+ % metal basis) and poly(vinylidene fluoride) (PVDF) (Alfa Aesar, mp:155 – 160 °C) with a weight ratio of 90:5:5 in N-methyl-2-pyrolidone (NMP) (Alfa

Aesar, 99+ %). For homogenization of the slurry, an ultrasonic bath (Sonorex, BANDELIN electronic GmbH & Co. KG, Germany) and a planetary vacuum mixer (Thinky-mixer ARV-310, Thinky Corporation, Japan) were used. A gap-bar coater (MSK-AFA-HC100, MTI Corporation, USA) with vacuum and heating function was used to cast the slurry on an Al foil (Figure 40). The resulting tape was afterwards dried for 30 min at 120 °C on the gap-bar coater and further dried in a vacuum furnace (VO 500, Memmert GmbH + Co.KG, Germany) at 80 °C for 12 h.

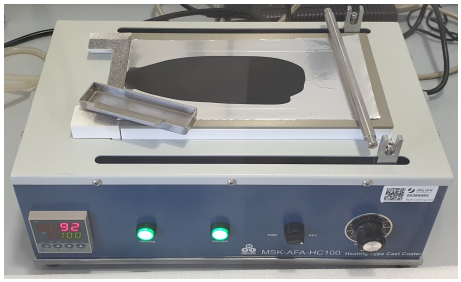

Figure 40: Photo of the gap-bar coater with cathode tape on top during drying.

For electrochemical investigations in coin cells (CR2032), cathodes with a diameter of 15 mm were punched. The cells were assembled in an argon filled glovebox by using the NCM cathodes, a glass fiber separator (Whatman), and a Li metal foil (Alfa Aesar) as anode.
The electrolyte used was a 1.0 M solution of $LiPF_6$ (Sigma Aldrich, battery grade) dissolved in an ethylene carbonate (EC, Sigma Aldrich, 99 %)/dimethyl carbonate (DMC, Sigma Aldrich, 99 %)/ethylmethyl carbonate (EMC, Sigma Aldrich, 99 %) mixture (1:1:1 by volume) with 2 wt% vinylene carbonate (VC, Sigma Aldrich, 99.5 %) additive. The electrochemical characterization of the cells is described in Chapter 2.11.

3.4. Compatibility tests between NCM and LLZO:Ta

For compatibility tests between different CAMs, NCM powders were used as synthesized and mixed 1:1 by volume with sintered and ground, cubic LLZO:Ta. Both components were homogenized by pestling in an agate mortar. These NCM + LLZO:Ta powder mixtures were used as prepared for thermal analysis by differential thermal analysis and thermogravimetry (DTA/TG) coupled with mass spectrometry (MS) (see Chapter 2.7). The secondary phase evolution during heating was further investigated by *in-situ* high temperature XRD (HT-XRD), scanning electron microscopy (SEM), and energy dispersive X-ray spectroscopy (EDS) as described in Chapters 2.1 and 2.3.1, respectively. For this purpose, the NCM/LLZO:Ta powder mixtures were pressed uniaxial into pellets (diameter: 13 mm, height: ~1.7 mm) with a force of 38 kN by using a hydraulic hand press (Paul-Otto Weber GmbH, Germany).

3.5. Fabrication of all-solid-state batteries

Prior to all-solid-state battery (ASB) fabrication, $LiNi_{0.8}Co_{0.1}Mn_{0.1}O_2$ (NCM811) (battery grade, MTI Corporation USA), cubic LLZO:Ta (synthesized as described in Chapter 3.2, sintered and ground), and (Li_3BO_3) LBO (synthesized as described in Chapter 3.2) were separately ball milled by using a planetary ball mill (Pulverisette 7, Fritsch GmbH, Germany) to reduce the particle size. For ball milling of all composite cathode components, 5 mm ZrO_2 balls, anhydrous isopropanol (Alfa Aesar, 99.8 %) as solvent, and a 1:18:4 mass ratio (powder:balls:solvent) were chosen. NCM811 was milled for 2 h at 200 rpm, LLZO:Ta for 1.25 h at 500 rpm and LBO for 1.5 h at 200 rpm. The resulting D50 values for NCM811, LLZO:Ta, and LBO were 0.9 µm, 2.9 µm, and 6.6 µm, respectively (see appendix, Figure S 29, Figure S 30d, Figure S 31c).

Solid-state half-cells were fabricated by sintering a composite cathode onto a densely sintered LLZO:Ta disc. In advance, a composite cathode ink was prepared by using a 44:44:12 mass ratio of the ball milled NCM811, LLZO:Ta, and LBO powders. The powder mixture was thoroughly homogenized by a mortar and pestle, and mixed 1:1 by weight with terpineol (Sigma Aldrich, mixture of isomers, anhydrous) containing 6 wt.% ethyl cellulose (Sigma Aldrich, 45 cp). The terpineol-ethyl cellulose mixture was prepared beforehand by dissolving ethyl cellulose in terpineol under stirring vigorously for 24 h. Afterward, a composite cathode ink was homogenized by using a three-roll mill (Exakt 50, EXAKT Advanced Technologies GmbH, Germany). The homogenized ink was applied with a paintbrush onto a LLZO:Ta discs which was before polished up to 4000 grit SiC-sandpaper. After drying at 55 °C, the coated LLZO:Ta discs were sintered in a tube furnace (RT 50/250/11, Nabertherm GmbH, Germany) with a heating rate of 2 K min^{-1} to 600 °C, followed by 10 K min^{-1} to 750 °C with a 45 min dwell time in air and natural cooling down.

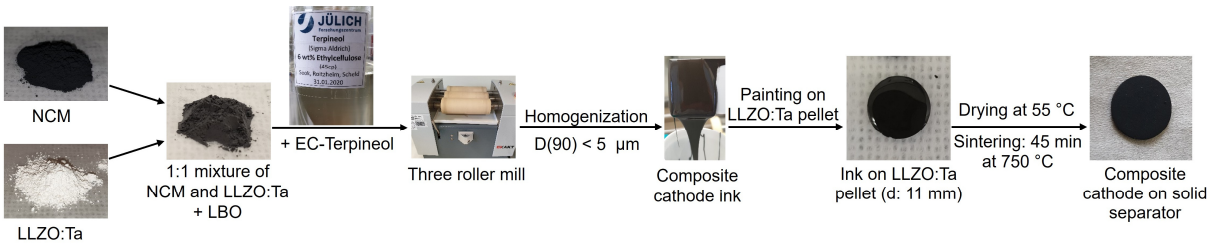

Figure 41: Schematic representation of the all-solid-state battery fabrication process.

For full-cell assembly, a sintered half-cell was polished on the LLZO:Ta side with up to 4000 grid SiC-sandpaper to remove possible impurities. A thin gold layer, serving as a current collector, was sputtered on top of the composite cathode using a sputter coater (Cressington 108auto Coater, TESCAN GmbH, Germany). Afterwards, the half-cell was transferred to a Ar-

filled glove box to assemble the full-cell by attaching a thin metallic Li-foil (Alfa Aesar, 99.9 %) as an anode to the polished LLZO:Ta side. The cell was heated up to 300 °C for 5 min on a hot plate to melt the lithium in order to increase the adhesion between LLZO:Ta and lithium. After cooling down, the full-cell was sandwiched in between two Ni plates as current collector and installed in a Swagelok cell. The electrochemical testing of the ASBs is described in Chapter 2.11.

4. Detection and localization of boron in B-doped $Li[Ni_{0.8}Co_{0.1}Mn_{0.1}]O_2$

This chapter is based on the following publication:

Christoph Roitzheim, Liang-Yin Kuo, Yoo Jung Sohn, Martin Finsterbusch, Sören Möller, Doris Sebold, Helen Valencia, Maria Meledina, Joachim Mayer, Uwe Breuer, Payam Kaghazchi, Olivier Guillon, and Dina Fattakhova-Rohlfing, *ACS Appl. Energy Mater.* **2022**, 5, 1, 524-538.

Christoph Roitzheim synthesized the samples, performed the electrochemical characterization, analyzed all data, and wrote the manuscript with contributions from all authors. Liang-Yin Kuo and Payam Kaghazchi performed the theoretical studies. Yoo Jung Sohn conducted the Rietveld refinements. Sören Möller performed the ion beam analysis. Doris Sebold took the SEM images. Helen Valencia, Maria Meledina, and Joachim Mayer did the TEM investigations. Uwe Breuer conducted the TOF-SIMS. Martin Finsterbusch, Payam Kaghazchi, Olivier Guillon, and Dina Fattakhova-Rohlfing initiated the idea, provided the resources, and supervised the work.

Link to the published article: https://doi.org/10.1021/acsaem.1c03000

Doping of Ni-rich cathode active materials (CAMs) with boron is a promising way to improve their cycling stability and mitigate their degradation, but it is still not understood how this effect is achieved and where the boron is located since different lattice positions were reported in literature [107-110]. To receive deeper insights into the impact of doping on the atomic and microscale properties, B-doped $Li[Ni_{0.8}Co_{0.1}Mn_{0.1}]O_2$ (NCM811) cathode material was synthesized as a model compound to verify the presence and location of boron in B-doped, Ni-rich NCM as well as its impact on the microstructure and electrochemical properties, by a combined experimental and theoretical approach.

Pristine NCM811 as well as B-doped NCM811 materials with varying B content, namely, 1, 2, 3, and 4 mol% assigned further as 1B-NCM811, 2B-NCM811, 3B-NCM811, and 4B-NCM811, respectively, were synthesized via a hydroxide co-precipitation route as described in Chapter 3.1. Chemical analysis (Table S 1) confirms that the calcined materials have a targeted NCM composition and boron concentration. Powder XRD patterns correspond to phase pure materials with a hexagonal α-$NaFeO_2$ structure corresponding to the $R\bar{3}m$ (166) space group for pristine and B-doped NCM811 (Figure 42) [217]. The clear peak splitting of (006)/(102) at 38 – 38.5 °(2θ) and (108)/(110) at 64 – 65 °(2θ) (Figure 42b,c) indicates the presence of an ordered hexagonal layered structure with high crystallinity [218]. No impurity phases were observed even for higher boron concentrations, and no additional reflections appeared. In

Figure 42c, there is an additional reflection beside (108) and (110) for NCM811 and 1B-NCM811 that is visible at 65° (2θ), which is device-specific and caused by $k_{\alpha 2}$ radiation. The sample 1B-NCM811 shows a slight peak shift toward a higher angle due to the sample displacement, while only the highly doped 4B-NCM811 shows a peak shift toward a lower angle, which indicates a lattice expansion only for this sample (Figure 42b,c). This is in agreement with the obtained lattice parameters that will be discussed below (Table 4). Based on the results of the XRD analysis of 4B-NCM811, it can be therefore concluded that boron trioxide was successfully incorporated into the lattice of NCM.

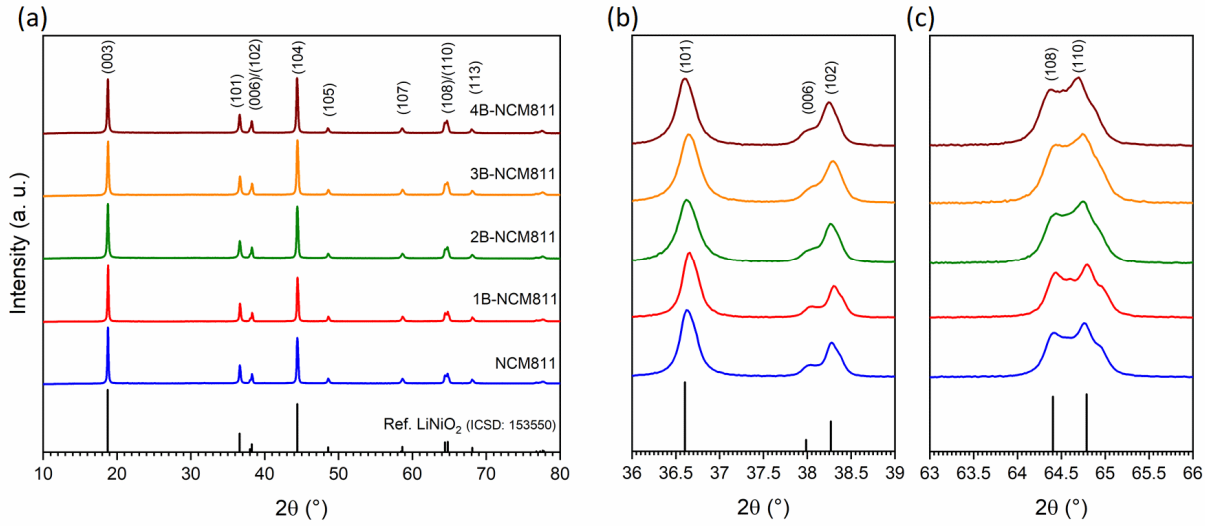

Figure 42: (a) Powder XRD patterns of pristine and B-doped NCM811 calcined at 800 °C. (b, c) Magnification of selected 2θ regions from (a). Reprinted with permission from ref. [116], Copyright 2021, American Chemical Society.

The possible effect of B doping on the particle size and morphology was investigated. The particle size distribution (PSD) of NCM811 is unaffected by B doping for our synthesis approach. The powders consist of hard agglomerates (secondary particles) with D50 values of 15.0 and 14.2 µm for pristine NCM811 and 2B-NCM811, respectively. The PSDs are shown in the supporting information (Figure S 1). A further increase of the boron concentration does not influence the particle size distribution, as displayed in Table S 2.

SEM analysis indicates that all synthesized powders are composed of spherical agglomerates (Figure 43a, Figure S 10c,d). Higher magnifications (Figure 43b–f) of these secondary particles indicate that each individual agglomerate is composed of nano sized cuboidal primary particles. From Figure 43, it is obvious that the shape of those primary particles changes slightly from cuboidal to plate-like for higher boron concentrations. The 2B-NCM811 and 4B-NCM811 primary particles are thinner and more densely packed, which results in a denser and smoother surface of the agglomerates (Figure 43d,f).

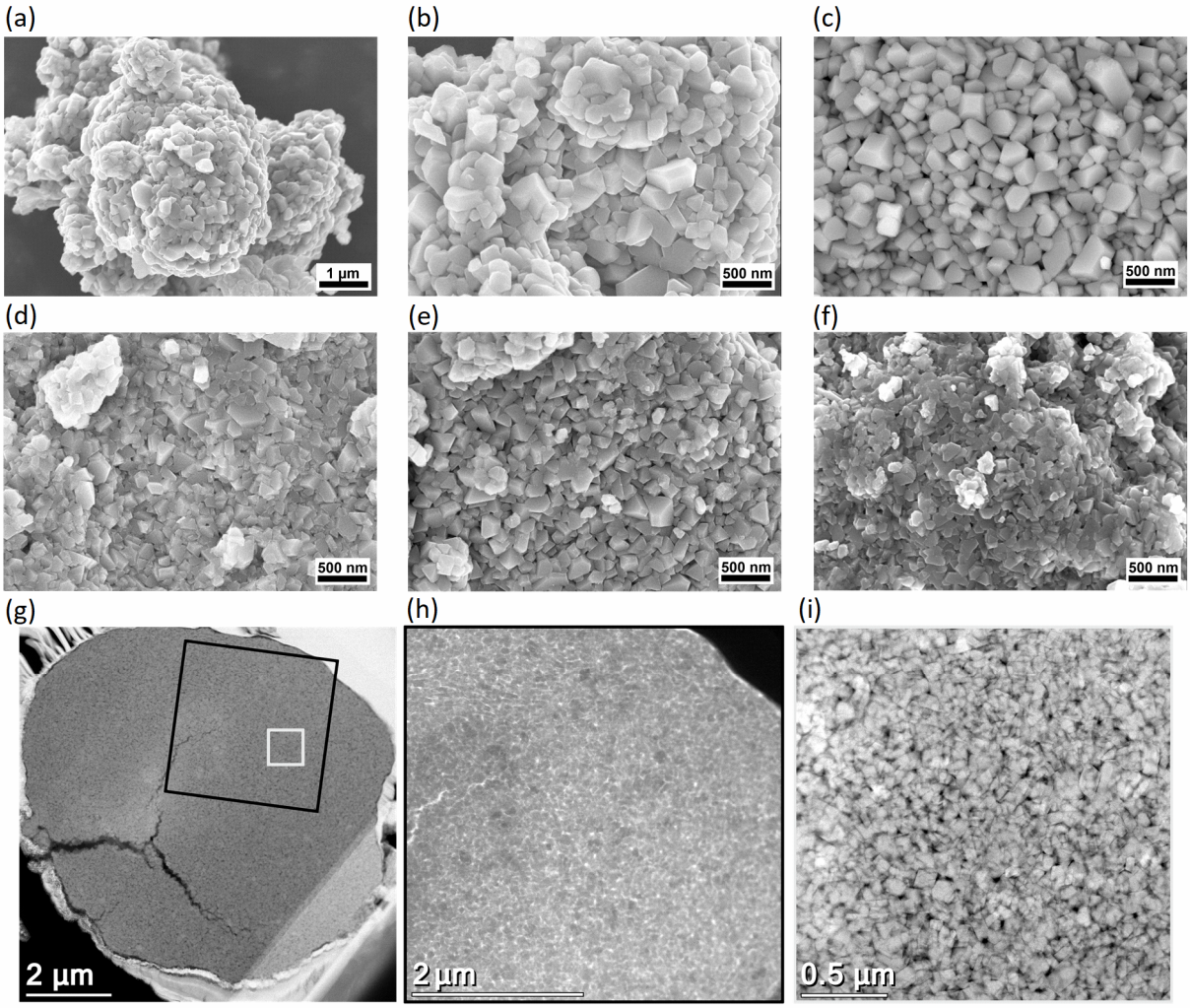

Figure 43: SEM secondary electron (SE) images (8 kV) visualizing (a) a typical secondary particle of pristine NCM811 as well as higher magnifications of primary particles of (b) pristine NCM811, (c) 1B-NCM811, (d) 2B-NCM811, (e) 3B-NCM811 and (f) 4B-NCM811. (g–i) Cross sectional HAADF-STEM images of an agglomerate of 2B-NCM811 with different magnifications. Magnifications of the cross sectional surface marked with black and white squares in (g), respectively. Reprinted with permission from ref. [116], Copyright 2021, American Chemical Society.

In contrast to calcined NCM811, the NCM811 hydroxide precursor (Figure S 11b) consists of thin plate-like primary particles, which indicates that during calcination, a densification and particle growth toward a cuboidal shape is taking place especially for pristine NCM811. The doping has a strong effect on the average primary particle size, which progressively decreases with an increase in boron content. The primary particle size is around 200 nm for the pristine NCM811 and 1B-NCM811 whereas it decreases to only 147 nm for the 4B-NCM811. In the presence of boron (especially for 4 mol%) the particle growth during calcination appears to be inhibited resulting in smaller and thinner primary particles as reported by C.-H. Jung *et al.*[115]. A similar reduction of primary particle size due to B doping was also reported by K.-J. Park *et al.*[107] for B-doped highly Ni-rich NCM90. While the primary particle size decreases, the

specific BET surface area reduces dramatically from 1.56 to 0.69 $m^2 g^{-1}$ and further to 0.32 $m^2 g^{-1}$ for pristine NCM811, 2B-NCM811, and 4B-NCM811, respectively, indicating an overall densification of the agglomerate surface. This result agrees with the work of L. Pan *et al*.[110], who also reported a strongly reduced specific surface area by B doping of cathode materials. The density of our NCM811 powders was slightly increased by 2 mol% B doping.

High-angle annular dark filed scanning transmission electron microscopy (HAADF-STEM) images and energy-dispersive X-ray (EDS) element analysis of 2B-NCM811 reveal a homogeneous distribution of Ni, Co, Mn, and O within the primary particle (Figure S 18). No significant signal of boron was seen which could be related to a low concentration of boron of only 2 mol%, its homogeneous distribution within the grains, and the detection limit of EDS analysis.

A cross sectional HAADF-STEM image of a 2B-NCM811 secondary particle prepared by focused ion beam (FIB) (Figure 43g–i) clearly demonstrates that the secondary particles are composed of randomly oriented primary particles. This morphology is different from the one reported by K.-J. Park *et al*.[107] for highly Ni-enriched $Li[Ni_{0.9}Co_{0.05}Mn_{0.05}]O_2$ (NCM90) doped with 1 mol% B. In particular, K.-J. Park *et al.* have demonstrated that the non-doped NCM90 agglomerates consist of randomly oriented short and thick primary particles, while B-doping results in a very different secondary particles morphology composed of the radially grown elongated primary particles. The change in the microstructure was attributed by the authors to a surface energy modification by B doping [107]. In contrast to this publication, we did not observe similar microstructure for our 2B-NCM811 under the applied synthesis conditions, which leads to the conclusion that the microstructure optimization is not the only effect of the B doping. In fact, an ammonia concentration gradient during the precursor co-precipitation can also lead to radially arranged primary particles [219]. Additionally, the oxygen partial pressure during the calcination step further influences the growing direction of the primary particles [220]. Thus, we assume that the B doping leads to a preferred growing direction only in combination with a precise adjustment of the synthesis conditions or only for highly Ni-enriched cathode materials.

The absence of a secondary phase in the XRD patterns and the modified microstructure of B-doped NCM811 indicate a successful B doping of the NCM lattice. The lattice parameters for pristine NCM calculated from the XRD patterns using the Rietveld refinement (Table 4 and Figure S 5) fall within the span reported in literature. It should be noted that the literature values scatter a lot due to the variation in Li and transition metal (TM) concentration as well as cation disorder (a = 2.8661 – 2.8805 Å; c = 14.2021 – 14.249 Å; c/a = 4.937 – 4.972) [221-224]. For

the B-doped NCM811, the obtained lattice parameters do not dramatically change when considering the measurement uncertainties, indicating a high structural similarity to the pristine sample. A slightly increased *a* parameter was found only for 4B-NCM811. Our findings differ from the observations of other groups for Li-rich and highly Ni-rich NCM, for which expansion of the lattice parameters and unit cell due to B doping was reported [107, 109, 110].

Table 4: Summary of lattice parameters and Rietveld refinement results of pristine and B-doped NCM [116]. Ni_{Li} gives the fraction of Ni ions occupying Li sites.

Active material	***a* [Å]**	***c* [Å]**	**V [Å^3]**	***c*/*a***	***I*(003)/*I*(104)**	**Ni_{Li} [%]**
NCM811	2.878(1)	14.206(6)	101.90	4.94	1.09	7.5
1B-NCM811	2.877(1)	14.206(6)	101.83	4.94	1.07	7.5
2B-NCM811	2.878(1)	14.202(9)	101.87	4.93	1.01	6.3
3B-NCM811	2.879(1)	14.207(9)	101.98	4.93	1.00	8.8
4B-NCM811	2.881(1)	14.215(9)	102.18	4.93	1.00	10.0

The *c*/*a* ratio can be used as an indicator for the degree of cation disorder/cation mixing (interchange between Li and Ni sites), which is a critical factor for Ni-rich NCM. For an ideal hexagonal closed packed lattice with $R\bar{3}m$ (166) and layered structure, *c*/*a* = 4.99. Partial cation mixing is indicated by *c*/*a* < 4.96. If *c*/*a* = 4.90, a phase transition took place, an ideal cubic close packed lattice ($Fm\bar{3}m$ (255), rock-salt structure) is present, and the peak splitting of the (006)/(102) and (108)/(110) Bragg reflections completely disappears [225, 226]. For our pristine NCM811, the *c*/*a* ratio is smaller than 4.96 indicating a severe cation disorder in our reference material. The degree of disorder can be estimated from the work of S. Gao *et al*.[224], who reports 11.37 % Ni on Li sites for the *c*/*a* = 4.937. For our B-doped NCM811, the *c*/*a* ratio slightly decreases, indicating that the introduction of boron results in a further increase in the cation disorder. An increasing Ni amount on Li sites is additionally verified by the Bragg refection intensity ratio *I*(003)/*I*(104) (Figure 42a and Table 4), which continuously decreases by increasing the boron doping level in NCM811. The expansion of lattice parameter *a* and the changes in cation disorder for the B-doped NCM811 are further indications for the incorporation of boron into the NCM lattice.

L. Pan *et al*.[110] proposed a possible lattice site occupation of the incorporated boron. In trace amounts, B^{3+} mainly occupies the tetrahedral interstitial of the packed oxygen in the transition metal and lithium layer, which notably enlarges lattice parameters *a* and *c*. When the concentration of boron increases, it mainly occupies the transition metal vacancies in addition to the tetrahedral interstices, like for low boron amounts. Thus, the cell parameters of the high-

doped samples show no obvious increase as compared to the low-doped one since the volume of the octahedral interstice in the TM layer is significantly larger than that of B^{3+}. To confirm this hypothesis for our materials, Rietveld refinement was exemplary performed for 4B-NCM811, placing boron in the tetrahedral interstitials (Figure S 5 and Table S 3). No reasonable results could be obtained when boron was placed on the 6*c*-Wyckoff position. Much better fitting, however, was obtained for the boron on the TM positions (3*b*-Wyckoff position), which is in good agreement with the results of L. Pan *et al*., who chose the same position for high and low B occupancy [110].

Based on the Rietveld refinement, different degrees of cation disorder were found in the dependence of the doping level for our material (Table 4) – the interchange fraction increases with B doping, especially for 4B-NCM811 with 10.0 % Ni on Li sites. 2B-NCM811 shows the smallest Li–Ni interchange; however, for pristine NCM811 and lower doping concentrations, the level of cation disorder is very similar. The determined percentages of Ni on Li sites based on Rietveld refinement show the same trend of an enhanced cation disorder by B doping, as found by studying the *c*/*a* and *I*(003)/*I*(104) ratios. Slight deviations from the observed trend of cation disorder have been observed, especially for the 1B-NCM811 and 2B-NCM811 samples, which can, however, result from the accuracy of refinement and the made assumptions.

In general, the similar ionic radii of Li^+ (0.72 Å) and Ni^{2+} (0.69 Å) allow the migration of Ni^{2+} to the Li-layer [113]. It is well known that the valence state of the TM ions in NCM is not fixed. It is usually a combination of Ni^{2+}/Ni^{3+}, Co^{3+}/Co^{4+}, and Mn^{3+}/Mn^{4+} [224], which explains the possibility of cation disorder in pristine NCM. If B^{3+} is introduced, a reduction of the valence state of the TM ions is assumed to obtain charge neutrality. If Ni^{3+} (0.56 Å) is reduced to maintain the charge balance, the abundant Ni^{2+} increases the probability for cation disorder [113]. The oxidation states of Ni and B in pristine NCM811 and 2B-NCM811 were determined by XPS (Figure S 27a–c). Based on refence data, the oxidation state of B was determined to be 3+ [227]. For both samples, the Ni 2p3 region can be fitted with a set of peaks derived for NiOOH [228]. A quantification of Ni^{3+} and Ni^{2+} species is not possible, but for 2B-NCM811 an overall slight shift to lower binding energies is observed which probably indicates a somewhat higher electron density for Ni in the B-doped sample.

Atomic resolution *Z*-contrast HAADF-STEM imaging was performed for pristine and 2B-NCM811 to address and visualize cation disorder as well as possible structural changes induced by B doping on the atomic scale. HAADF-STEM images for pristine NCM811 (Figure 44a) show a surface region (green squares) with a clear structural defect and an inner region (blue square) with a well-ordered layered structure. An overlap with the schematic structure of

NCM811 (Figure 44a, purple square) shows that in the surface region (2 – 3 nm in thickness), atomic contrast in the Li columns was obtained, while Li is too light to be imaged in HAADF-STEM mode. The contrast on the Li positions might result from transition metal ions (most probably Ni^{2+}) occupying the Li sites. These results come in a good agreement with the cation disorder for pristine NCM811 proposed on the base of XRD analysis. STEM analysis reveals that the cation disorder is mainly found in the surface region. Fourier transforms (FFTs) of the surface region (green squares) and the interior region (blue square) display that the desired layered structure ($R\bar{3}m$) is present in the inner region, while the surface region shows a rock-salt structure ($Fm\bar{3}m$). Based on XRD investigations, an enhanced degree of cation disorder was found for 2B-NCM811, and therefore, changes in atomic structure could be assumed. The HAADF-STEM image of a 2B-NCM811 primary particle is depicted in Figure 44b.

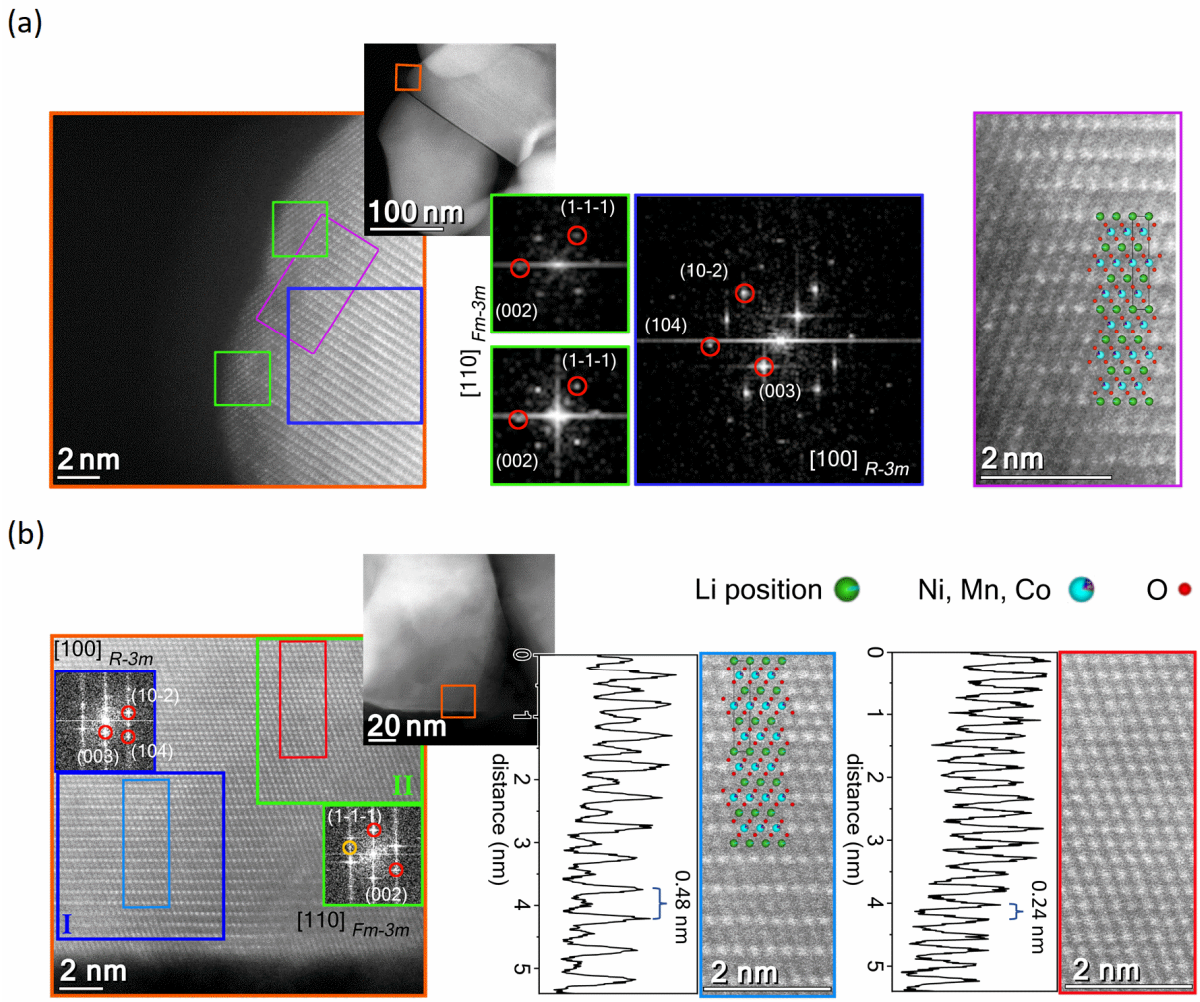

Figure 44: STEM analysis of pristine and 2B-NCM811 primary particles on the surface of agglomerates. (a) Overview and high-resolution (HR) HAADF-STEM images of pristine NCM811 together with FFTs from the labelled areas. (b) Overview and HR HAADF-STEM images of 2B-NCM811 together with FFTs and the contrast line scans from the labelled areas. Reprinted with permission from ref. [116], Copyright 2021, American Chemical Society.

Similar to the pristine NCM811, two regions with a different structure (region-I, blue square and region-II, green square) were identified also for the B-doped NCM (Figure 44b). The FFT of region-I (surface) reveals the desired layered structure ($R\bar{3}m$). In region-II, a rock-salt structure ($Fm\bar{3}m$) has formed, where some remnant spots similar to the FFT of region-I are marked with a yellow circle. In Figure 44b, a line scan showing the intensity distribution along the [100] ($R\bar{3}m$) direction on the surface of region-I (light blue rectangle) shows an alternating atomic contrast with a periodicity of 0.48 nm caused by transition metal (TM) atoms. Atomic contrast with significantly lower intensity is visible in the rows where the Li sites are expected. This could be due to TM ions (most probably Ni^{2+}) partially occupying the Li site (cation disorder). For 2B-NCM811, the cation disorder found in the surface region is less severe than that reported for the pristine NCM811. For the interior region-II (red rectangle) shown on the right of Figure 44b, the contrast line scan along the [110] ($Fm\bar{3}m$) direction indicates a

periodicity of 0.24 nm, which indicates that in region-II, intense atomic contrast is present on all Li positions. The most possible reason for this observation is (i) severe cation disorder when the amount of the TM in their initial sites is similar to the amount of TM in Li sites. However, this effect could also be caused by (ii) defects in the under lying atomic layers shifting the TM atom column to the position of Li or (iii) the thickness contrast if the particle is thicker at the center than on the surface. For pristine NCM811, a well-ordered hexagonal layered structure was found in the bulk of the primary particle, while a surface layer with strong cation disorder and rock-salt structure was visible. In contrast to pristine NCM811, the B-doped NCM811 does not show a rock-salt structure on the surface region. By B doping, an ordered surface region with only a weak cation disorder and layered structure was found.

Based on our X-ray diffraction and Rietveld refinement, it is indicative that small-sized boron occupies the larger TM positions, which is confirmed by the similar lattice parameters for B-doped NCM. However, the lattice position of boron in B-doped NCM and the reason for the nearly constant lattice parameters are still unclear since other factors like cation disorder as well as changes of the electronic environment in the NCM lattice cannot be excluded. Therefore, DFT calculation was used to study the location of boron atoms and their influence on the NCM811 lattice. Since the experimental analysis of the powders by XRD showed a Ni $\leftrightarrow$ Li interchange in the absence of B doping, we first considered the influence of cation interchange on the lattice parameters for pristine NCM811. It was found that the Ni $\leftrightarrow$ Li interchange without B doping causes the lattice parameters *a* and *c* to shrink (Figure 45a). This is due to the strengthening of electrostatic attraction between Li- and O-layers with $Ni^{2+} \leftrightarrow Li^{+}$ interchanges by which the O–TM–O interlayer separation, namely, d_z(O–Li–O) (average O–Li–O distance), reduces from 2.588 to 2.555 Å. The average O–TM–O intralayer distance d_z(O–TM–O) only slightly expands from 2.112 to 2.121 Å.

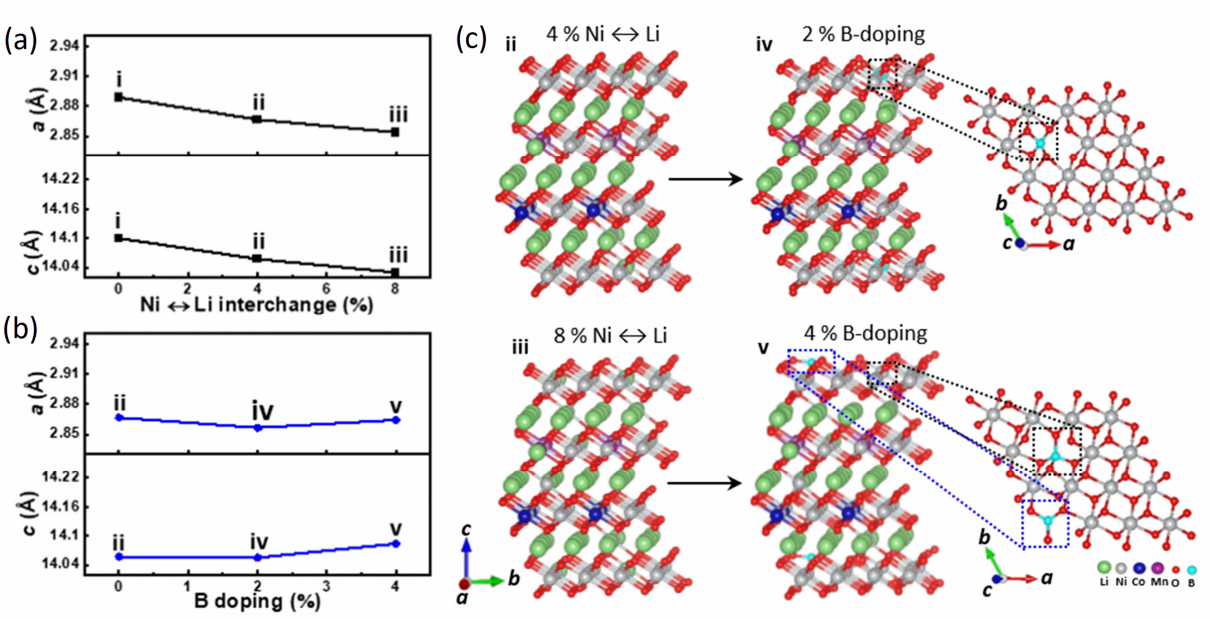

Figure 45: Calculated changes in lattice parameters *a* and *c* in NCM811 with (a) Ni↔Li interchange and (b) B doping. (c) Atomic structures of NCM811 before and after B doping as well as coordination of boron to oxygen. Reprinted with permission from ref. [116], Copyright 2021, American Chemical Society.

Doping with a large amount of boron alleviates the lattice size change induced by the $Ni^{2+} \leftrightarrow Li^{+}$ interchange (Figure 45b). Thus, in agreement with experimental data, we found that when boron is incorporated in the structure and the $Ni^{2+} \leftrightarrow Li^{+}$ interchange is enhanced, no significant impact on the *a* and *c* values is observed. This is in strong contrast to the non-doped system, for which even the slight increase in the degree of Ni ↔ Li interchange (from 0 % to 4 %) results in a linear decrease in *a* and *c* values. To better understand the effect of B doping, we focus on the 2 mol% and 4 mol% B-doped structures with magnified doping effects. Our calculations indicate that *a* remains almost unchanged, while *c* slightly expands with 4 mol% B. The increase in *c* in this case is due to the B-induced expansion of both d_z(O–Li–O) (2.56 → 2.57 Å) and d_z(O–TM–O) (2.12 → 2.13 Å). The former change is because of a stronger repulsion between B and Li compared to Ni and Li. This is due to the fact that the B–Li distances ($d_{B–Li}$: 2.31 Å – 2.60 Å) are shorter than the Ni–Li ones ($d_{Ni–Li}$:2.70 Å – 3.04 Å). The slight expansion of d_z(O–TM–O) is because of an upward displacement of O anions that bind to B to accommodate this cation. The simulation shows that 2 B cations in the supercell (4 mol% B doping) occupy a trigonal planar and an almost tetrahedral site in the O–Ni–O layer (Figure 45c, structure v). The B cation in the case of 2 mol% B doping occupies a tetrahedral site (Figure 45c, structure iv). Reported values of $d_{B–O}$ for the trigonal planar sites in the most stable phase of boron oxide, namely, B_2O_3 (P31), are ≈ 1.34 – 1.40 Å [229]. However, the experimental study by R. Shannon *et al.*[230] on a high-pressure form of B_2O_3 (Ccm21) has

found $d_{B–O}$ of 1.51 Å for three B–O bonds and 1.37 Å for one B–O bond. The calculated values of $d_{B–O}$ in the structure v are 1.37 – 1.59 Å. Note that due to the shorter bond length of B–O compared to that of Ni–O, occupation of octahedral sites is not possible for boron. Calculated values of $d_{Ni–O}$ in the Ni-layer of the structure v lie between 1.85 and 2.27 Å. Figure 45 shows that the *c* value does not change much with 2 mol% B doping. The reason behind this behavior is that B occupies a tetrahedral site so that it stays almost in the Ni-layer plane. As such, the values of $d_{B–Li}$ for nearest neighbors are 2.65 and 2.88 Å, which are longer than those for the 4 mol% B doping case ($d_{B–Li}$: 2.31 – 2.60 Å) and more comparable to $d_{Ni–Li}$ values of 2.70 – 3.04 Å. Figure 45b shows a clear increase in the *a* value of structure iii when it is doped by 4 mol% boron (structure v). This is most likely due to the migration of one of B cations from the Ni-layer plane to the O-layer plane (to form the B–O trigonal), leaving a TM vacancy and the weakening of planar TM–TM repulsion. A similar reason can be applied to explain the small increase in *c* when a larger amount of boron is incorporated (structure iv → structure v).

The theoretical approach provides an insight into the lattice position of boron atoms in B-doped NCM811. As shown by the atomic structures iv and v (Figure 45c) for 2B-NCM811 and 4B-NCM811, respectively, the coordination of boron to oxygen depends on the doping level. Boron occupies tetrahedral sites for 2 mol%, while trigonal planar as well as tetrahedral sites were occupied for 4 mol% doping. The different coordinations have an impact on the change in lattice parameter *c*. Furthermore, the simulated lattice parameters considering both effects, namely, B doping and the B-induced increase in the Ni ↔ Li interchange (Figure 45b), show only minor changes in lattice parameters *a* and *c*, which underlines that our experimentally determined lattice parameters for pristine and B-doped NCM811 are almost identical and do not strongly depend on B doping.

As shown above, the STEM analysis of the synthesized cathode materials indicated that B-doping of NCM811 affects the surface region of the cathode material. However, the B-doped cathode materials synthesized within this work do not show the expected arrangement of the primary particles within the agglomerates as known for the highly Ni-enriched NCM90 [107]. Instead, we saw an influence of B doping on the lattice parameter, cation disorder, and powder morphology. Since the detection of boron in a single primary particle by electron energy loss spectroscopy (EELS) was not successful, we applied advanced ion beam analysis to experimentally verify the exact location of boron in 2B-NCM811. In order to analyze the NCM811 host structure, Rutherford backscattering (RBS) was used since it is sensitive to heavy elements and has good depth resolution. The RBS part of the spectrum interesting for NCM811 is displayed in Figure 46a. It gives information about the composition of the heavy elements

Ni, Co, and Mn in the NCM811 powder. A comparison between the experimental and simulated data shows that there is a depletion of Ni, Co, and Mn on the surface of the secondary particles, leading to a lower experimental signal compared to the simulation which, assumes homogenous NCM811 particles. The thickness of the depletion layer is around 400 nm and can be attributed to surface impurities (e.g., carbonates, hydroxides, etc.) or due to the presence of boron on the particle surface. In the core of the particles, a homogenous composition of NCM811 is observed, which is indicated by a perfect fitting between experimental and simulated values. In contrast to RBS, nuclear reaction analysis (NRA) enables the selective detection of light elements like lithium and boron with a penetration depth of up to 5 µm. The NRA part of the spectrum (Figure 46b) shows the boron signal. For this measurement, the shown length scale for the boron detection is around 2 µm with a similar depth resolution. The detected B-NRA signal emphasizes a surface enrichment of boron. Additionally, 2B-NCM811 as analyzed by particle induced gamma emission (PIGE) which offers a lower detection limit and higher penetration depth (up to 9.9 µm) than NRA. Boron was also detectable by PIGE (Figure S 19a), but a quantification was not possible due to reduced accuracy caused by the sample preparation on a carbon tape. However, the quantification of boron based on NRA shows an average concentration of (3 ± 1) mol% boron in the first 2 µm of the analyzed particles. When considering the measurement uncertainties, the found boron amount by NRA is in good agreement with the expected 2 mol% boron verified by ICP-OES (Table S 1). Even though this is not a direct proof that boron is homogenously distributed in the crystal structure, the results indicate that boron is distributed on the secondary particle surface. Whether boron is also present in the interior of the primary NCM particles needs to be further analyzed.

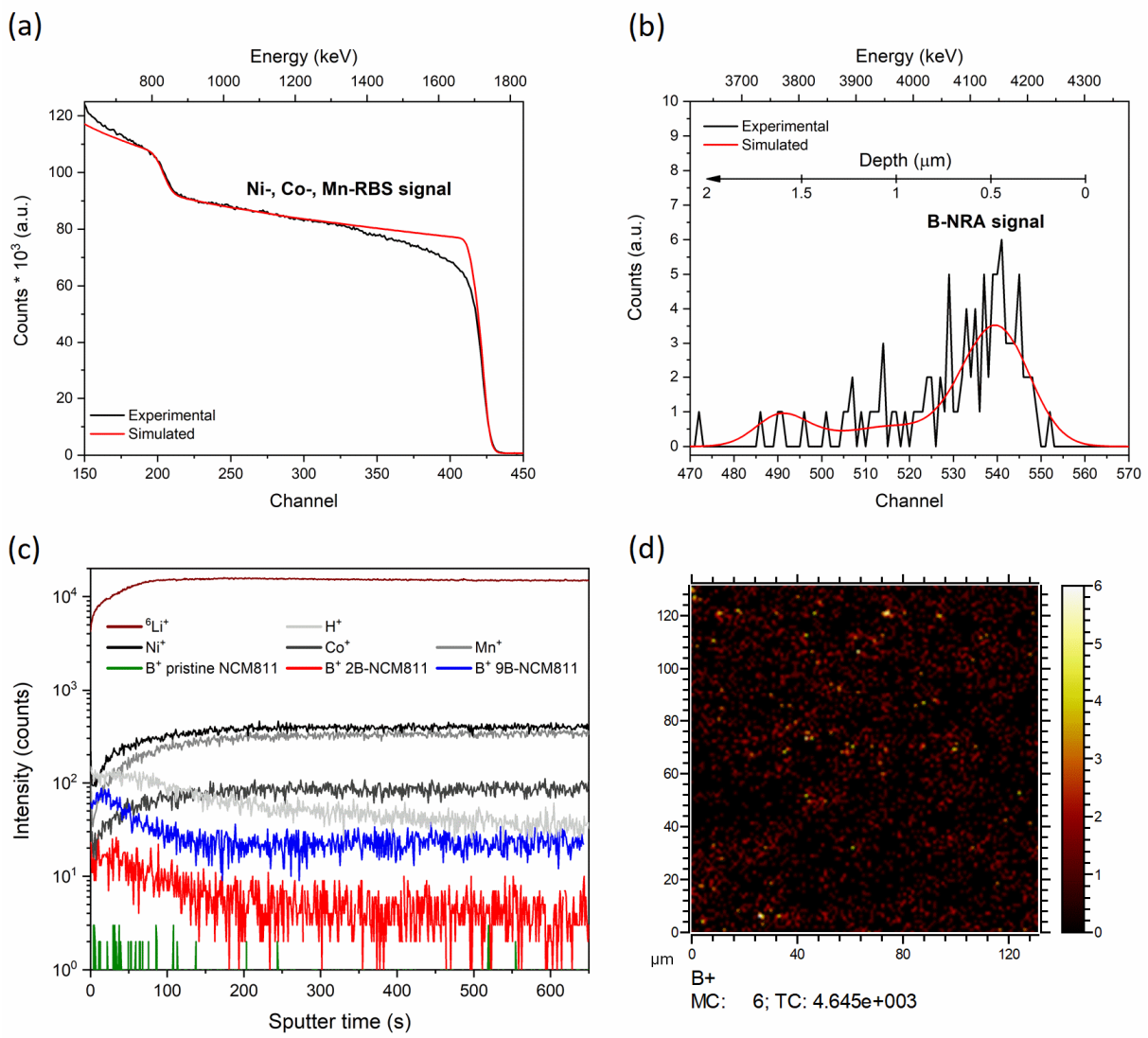

Figure 46: Detection and localization of boron in 2B-NCM811. (a) RBS spectrum showing measured and simulated data. (b) NRA spectrum showing the B-signal. (c) TOF-SIMS depth profiles and (d) boron mapping for 2B-NCM811. The depth profiles of B^+ for pristine NCM811 and 9B-NCM811 were also shown. For these samples Li^+, H^+ and the transition metal ions are identical and are not shown for simplification. Reprinted with permission from ref. [116], Copyright 2021, American Chemical Society.

To address this question, the surface of 2B-NCM811 was characterized by time-of-flight secondary ion mass spectrometry (TOF-SIMS) with positive polarity. TOF-SIMS is a technique with ultrahigh chemical selectivity that provides a high sensitivity in the detection of different elements like TM cations, as well as the light cations lithium and boron, with depth resolution [231]. The TOF-SIMS depth profiling as well as the mapping of boron for 2B-NCM811 is shown in Figure 46c,d. The depth profiles show that the Li^+, Co^+, Ni^+, and Mn^+ signals increase and stay constant after 100 s sputter time, which is in agreement with the RBS observations. Possibly, sputter ions remove surface contaminations (e.g., carbonates, hydroxides, etc.) formed during the transfer of the samples to the instrument, and after a while, a fresh layer is reached,

meaning a constant signal. This suggestion is underlined by the H^+-signal that stays constant during the first 80 s sputtering and continuously decreases afterwards. Furthermore, an enrichment of another element, probably boron, is the reason for the increasing intensity of the Li^+, Co^+, Ni^+, and Mn^+ signals. More importantly, the B^+-signal in all B-doped NCM samples decays with the sputter time and stays constant after 150 s sputtering. The B^+-signal of 2B-NCM811 is close to the detection limit. The samples containing 9 mol% boron (9B-NCM811) and pristine NCM811 were additionally analyzed to confirm that the observed signal really results from boron in NCM811. In the case of higher B-concentration (9B-NCM811), the signal intensity observed for 2B-NCM811 was increased by exactly a factor of 4.5. For pristine NCM811, no intensity for B^+ was found, which strongly indicates that the recorded signal corresponds to boron in B-doped NCM811 and linearly increases with the corresponding boron concentration. The boron mapping (Figure 46d) demonstrates that boron is homogenously distributed throughout the analyzed particles. Depth profiling via TOF-SIMS confirms a slight concentration gradient of boron from the surface to the bulk where the B-concentration stays constant. The results of the TOF-SIMS analysis support the conclusions of XRD, TEM, and NRA analyses presented above that the boron is incorporated in the bulk structure of the primary particles' core, and additionally, boron enriches the agglomerate surface.

To finally investigate the effects of boron incorporation into the NCM lattice and its enrichment on the secondary particle surface on the electrochemical properties of NCM811, electrochemical tests were performed. Here, NCM811 with 2 mol% B doping was chosen as an optimum composition to study the effects of B doping on electrochemical performance, since the lower doping levels were already investigated before[107] and the higher doping levels are expected to demonstrate an inferior electrochemical performance due a strongly enhanced degree of cation disorder. The electrochemical characterization of pristine NCM811 and 2B-NCM811 (Figure S 21) demonstrates that the materials are electrochemically active, but the low discharge capacities of around 160 mAh g^{-1} are not satisfactory for Ni-rich NCM811. These reduced capacities can be attributed to the enhanced cation disorder reported above (Table 4). In order to optimize the electrochemical performance, two additional samples (NCM811_o and 2B-NCM811_o) were synthesized under an increased oxygen partial pressure during calcination. Calcination under higher oxygen partial pressure reduces cation disorder and enhances capacities but does not change the basic structure and morphology (Figure S 2, Figure S 7, Figure S 12, Table S 1, and Table S 4) so that our fundamental findings about cation disorder, lattice position, and localization of boron remain valid.

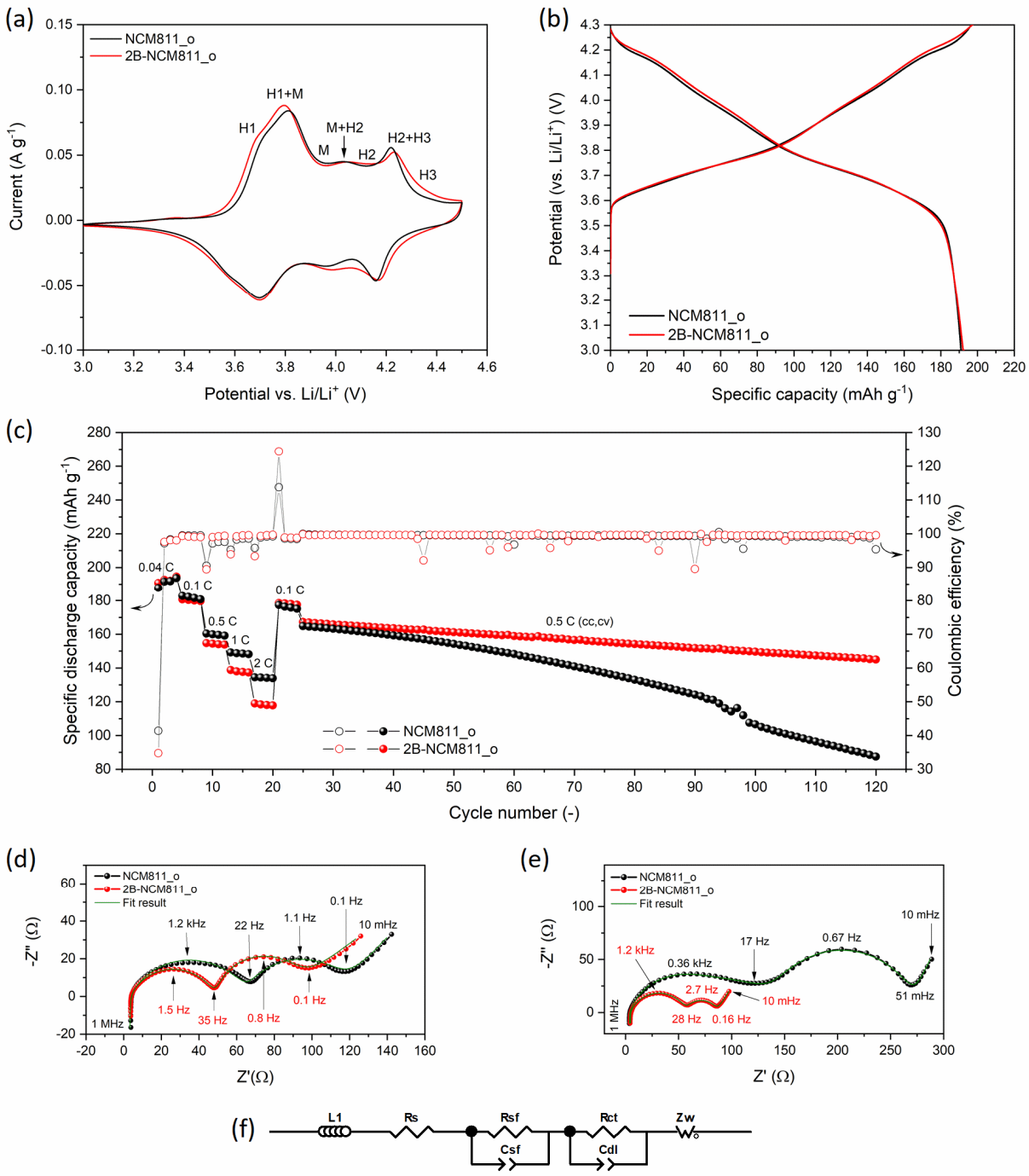

Figure 47: Electrochemical performance of NCM811_o and 2B-NCM811_o. (a) Cyclic voltammogram curves at a scan rate of 0.05 mV s^{-1} for the second cycle. (b) Galvanostatic charge-discharge profiles at 0.04 C for the second cycle. (c) Rate capability tests at various C-rates with prolonged cycling at 0.5 C (cc and cv). (d–f) Electrochemical impedance spectroscopy: (d) Nyquist plot after four cycles at 0.04 C, (e) Nyquist plot after 120 cycles, and (f) equivalent circuit model. Reprinted with permission from ref. [116], Copyright 2021, American Chemical Society.

Cyclic voltammetry (CV) curves of pristine NCM811_o and 2B-NCM811_o (Figure 47a) confirm their electrochemical activity. The shape of the CV curves does not change dramatically by B doping. Both cathode materials show multiple redox peaks corresponding to

phase transitions. During delithiation the original hexagonal structure (H1) transforms into monoclinic (M) and further to other hexagonal structures (H2 and H3). The transition from H2 to H3 is known to cause a detrimental lattice shrinkage in the *c*-direction leading to mechanical degradation [70]. The redox peaks for Ni^{2+}/Ni^{4+} are found at 3.81/3.70 V and 3.79/3.70 V for pristine NCM811_o and 2B-NCM811_o, respectively. Additionally, redox peaks were found at 4.22/4.16 V for pristine NCM811_o and at 4.23/4.17 V for 2B-NCM811_o, corresponding to Co^{3+}/Co^{4+}. For 2B-NCM811_o, the potential difference between the oxidation and reduction peak for the redox couple at around 3.80 V (0.09 V) is smaller than for pristine NCM811 (0.11 V), indicating a favorable effect of B doping on electrochemical activity. The reduced polarization by B doping is more obvious in the first CV scan (Figure S 22). All these findings are consistent with previous studies about B-doped NCM [107, 109].

Galvanostatic charge/discharge analysis confirms that the incorporation of the electrochemical inactive element boron does not lead to a significantly reduced capacity. After an initial conditioning cycle, discharge capacities of 188 and 191 mAh g^{-1} were obtained for pristine NCM811_o and 2B-NCM811_o, respectively (Figure 47b). The Coulombic efficiencies are 97 % for NCM811_o and 98 % for 2B-NCM811_o. A distinct impact of B doping on the electrochemical performance of NCM811 was found during rate capability tests and long-term cycling. While at low C-rates (0.04 C and 0.1 C), similar capacities were obtained for NCM811_o and 2B-NCM811_o; at higher C-rates (0.5 – 2 C) the B-doped NCM always shows lower capacities compared to the undoped active material (Figure 47c). The effect of boron on the discharge capacities at high C-rates appears to be more pronounced than previously reported for lower B-concentration in highly Ni-enriched NCM [107]. The lower capacities for 2B-NCM811 under high discharge rates can be explained by a reduced electronic conductivity due to B doping as previously reported by K.-J. Park *et al.*[107] and the enhanced cation disorder caused by B doping (Table 4 and Table S 4). However, the positive effect of B doping is clearly observed during the prolonged cycling at 0.5 C (Figure 47c), where 2B-NCM811_o shows significantly reduced capacity fading as compared to pristine NCM811_o. The capacity retention after 120 cycles is 87 % for 2B-NCM811_o and only 53 % for pristine NCM811_o. For both cathodes, similar Coulombic efficiencies between 90 and 99 % were obtained during long-term cycling.

Electrochemical impedance spectroscopy (EIS) was applied to study the effect of B doping on the surface-film and charge-transfer resistance after four (Figure 47d) and 120 charge/discharge cycles (Figure 47e). The fitting of the data was performed by using the equivalent circuit depicted in Figure 47f. In the case of pristine NCM811_o the surface-film resistance in the

high-frequency range increases during cycling from 63 to 105 Ω and the charge-transfer resistance in the low-frequency range also increased from 49 Ω after four cycles to 187 Ω after 120 cycles, which is in agreement with the strong capacity fading observed for NCM811_o (Figure 47c). In the case of 2B-NCM811_o, the surface-film and charge-transfer resistances are initially smaller than for pristine NCM811_o and do not strongly change after long-term cycling. The surface-film resistance slightly increases during cycling from 45 to 53 Ω, while the charge-transfer resistance decreases from 37 to 28 Ω. The stable surface-film and charge-transfer resistances as well as the improved cycling stability found for 2B-NCM811_o are possible effects of B doping, which positively affects the electrochemical performance of NCM811.

Since an easier stress release due to radial aligned primary particles is not the reason for the here observed improved capacity retention of B-doped NCM811_o during long-term cycling, we assume that the reported B-enrichment on the secondary particle surface acts as a protective surface coating that protects the NCM particles from direct contact with the electrolyte and thus suppresses side reactions at the electrode-electrolyte interface. Such performance improvement by boron-containing coatings was previously reported by S. N. Lim *et al.*[232] and K. Lee *et al.*[233]. In our case, the coatings are much thinner and not even visible by TEM. Additionally, the observed thinner, plate-like B-doped NCM811 primary particles possibly profit from more oxygen-stable lateral facets as reported by C.-H. Jung *et al.*[115]. This is a possible further explanation for the improved cycling stability without radially aligned primary particles.

In summary, it was demonstrated that boron successfully incorporated into the NCM lattice as shown by an enhanced cation disorder, modified morphology and DFT calculation. In contrast to the previous reports, the in this work synthesized B-doped NCM811 did not demonstrate the expected alignment of the primary particles along the radial direction, suggesting that not only B doping but rather a fine tuning of the synthesis conditions are required to achieve such a microstructure alteration. The dopant boron was experimentally detected, quantified, and localized by ion beam analysis (NRA) and TOF-SIMS. It was demonstrated that boron is not only located on the surface of the agglomerates but also incorporates into the bulk of the primary particles. A slight boron enrichment on the agglomerate surface but also a significant high and constant boron concentration in the bulk of the primary particles could be detected. Thus, in the bulk, the incorporation of boron does not lead to a significant lattice expansion but shows a detrimental effect on the electrochemical performance at high C-rates and increases the cation disorder. In contrast to this, the boron located on the agglomerate surface leads to a decrease in cation disorder, avoids phase transition to rock-salt structure and thus might serve as protective

surface coating, resulting in significantly improved capacity retention during long-term cycling of B-doped NCM811.

5. Impact of $Li[Ni_{1-x-y}Co_xMn_y]O_2$ composition and doping on microstructural and electrochemical properties

In the previous chapter, pristine NCM811 and B-doped NCM811 were characterized and discussed as possible CAMs for garnet-type ASBs. In addition, NCM with different transition metal composition and ruthenium as a new dopant of NCM were investigated. The effects of doping NCM111 with B and NCM811 with Ru on the morphology and electrochemical performance of NCM were analyzed in Chapter 5.1 and 5.2, respectively.

5.1. B-doped $Li[Ni_{1/3}Co_{1/3}Mn_{1/3}]O_2$

Standard, pristine $Li[Ni_{1/3}Co_{1/3}Mn_{1/3}]O_2$ (NCM111) and 2 mol% B-doped NCM111 (2B-NCM111) were synthesized via a hydroxide co-precipitation route as described in Chapter 3.1. Chemical analysis by ICP-OES (Table S 1) verifies the targeted NCM composition and boron concentration of 2 mol%. As demonstrated in Chapter 4 for 2B-NCM811, for 2B-NCM111 also (3 ± 1) mol% boron was detected by NRA surface enriched, in the first 2 µm of the analyzed particles (Figure S 19b).

Powder XRD patterns of pristine NCM111 and B-doped NCM111 indicate the presence of phase pure cathode materials with a hexagonal α-$NaFeO_2$ structure and the $R\bar{3}m$ (166) space group (Figure 48). Also for 2 mol% B doping, the reflections match well with the reference pattern for NCM111[234], indicating that boron trioxide successfully incorporated into the NCM lattice since no impurity phase is observed. The clear peak splitting of the (006)/(102) Bragg reflections at 38 – 38.5 °(2θ) and (108)/(110) at 64 – 65.5 °(2θ) (Figure 48b,c) indicates the presence of an ordered hexagonal layered structure with high crystallinity [218]. In the case of pristine NCM111, broad peaks with a less intense peak splitting are visible, whereby the peak splitting is more intense for B-doped NCM111 (Figure 48b,c). This can be attributed to different morphologies of pristine NCM111 and B-doped NCM111 which will be discussed below (Figure 50).

In order to prove that boron is incorporated into the NCM lattice, the lattice parameters were determined by Rietveld refinement (Table 5 and Figure S 6). The here obtained lattice parameters for NCM111 are in good agreement with the values reported by W. Hua *et al.* (a = 2.864 Å; c = 14.257 Å; c/a = 4.977) [225]. Lattice parameters a and c as well as the cell volume increase by 2 mol% B doping which is also visible by a peak shift toward smaller angles in Figure 48. It is known from the literature that even a doping with elements exhibiting a small ionic radius can increase the lattice parameters dramatically [110]. Lattice parameters and unit

cell expansion by B doping was previously observed for Li-rich NCM and highly Ni-rich NCM [107, 109, 110]. This is also in agreement with the results for the B-doped NCM111 considered here and thus proves the successful incorporation of boron into the NCM lattice.

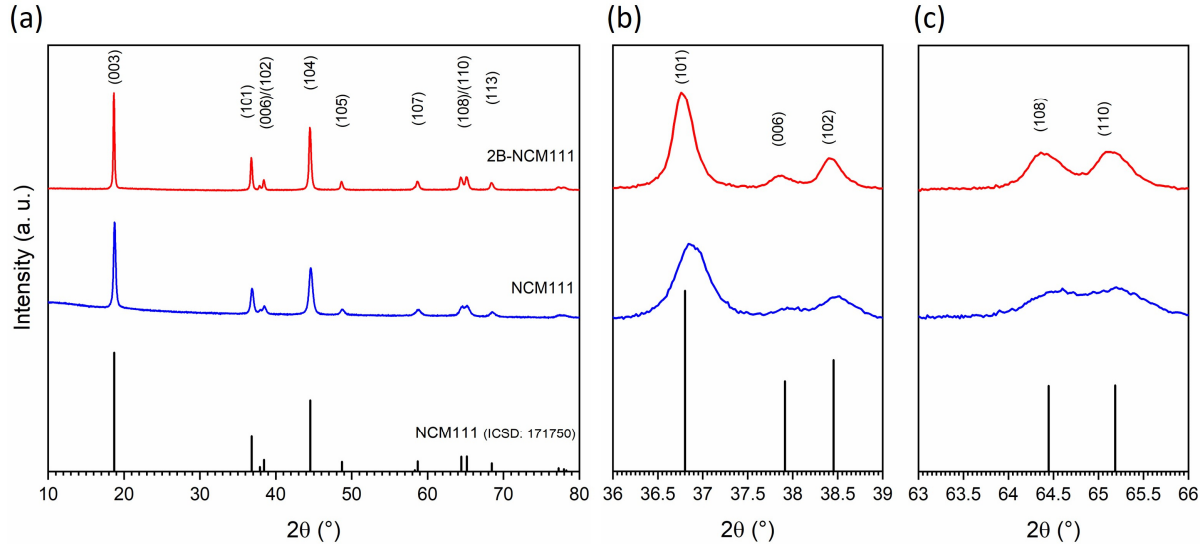

Figure 48: (a) Powder XRD patterns of pristine NCM111 and 2 mol% B-doped NCM111. (b, c) Magnifications of selected 2θ-regions of (a).

By B doping of Ni-rich NCM811, the lattice parameters and the cell volume do not strongly expand as discussed in Chapter 4 (Table 4). It was demonstrated that in the case of NCM811, the expansion of lattice parameters by B doping can be compensated by an enhanced cation disorder caused by B doping. Since cation disorder is only an issue for Ni-rich NCM811, the NCM111 shows the expected increase in lattice parameters by B doping. The significant lower degree of cation disorder in NCM111 compared to NCM811 is indicated by significant larger *c*/*a* and *I*(003)/*I*(104) ratios (Table 4 and Table 5).

Table 5: Summary of lattice parameters for pristine and B-doped NCM111.

Active material	***a* [Å]**	***c* [Å]**	**V [Å^3]**	**c/a**	***I*(003)/*I*(104)**
NCM111	2.861(1)	14.23(2)	100.87	4.97	1.27
2B-NCM111	2.863(1)	14.25(1)	101.16	4.98	1.12

To further prove that boron incorporates into the NCM lattice and possibly affects the powder morphology, the particle size and shape of pristine NCM111 and 2B-NCM111 were investigated. The particle size distribution (PSD) of NCM811 was not affected by B doping as previously discussed in Chapter 4 (Figure S 1a,b), however, much stronger effects of B doping were observed for NCM111. In the case of pristine NCM111 (Figure 49a), a narrow PSD was obtained. The formed secondary particles are weak and were partially crushed by sonication,

resulting in a bimodal PSD. The 2 mol% B doping of NCM111 (Figure 49b) led to a border PSD with a higher fraction of larger and harder agglomerates that could not be crushed by sonication. As a result of B doping, the D50 value strongly increased to 14 µm for 2B-NCM111, while for pristine NCM111 only 5 µm were obtained (Table 6).

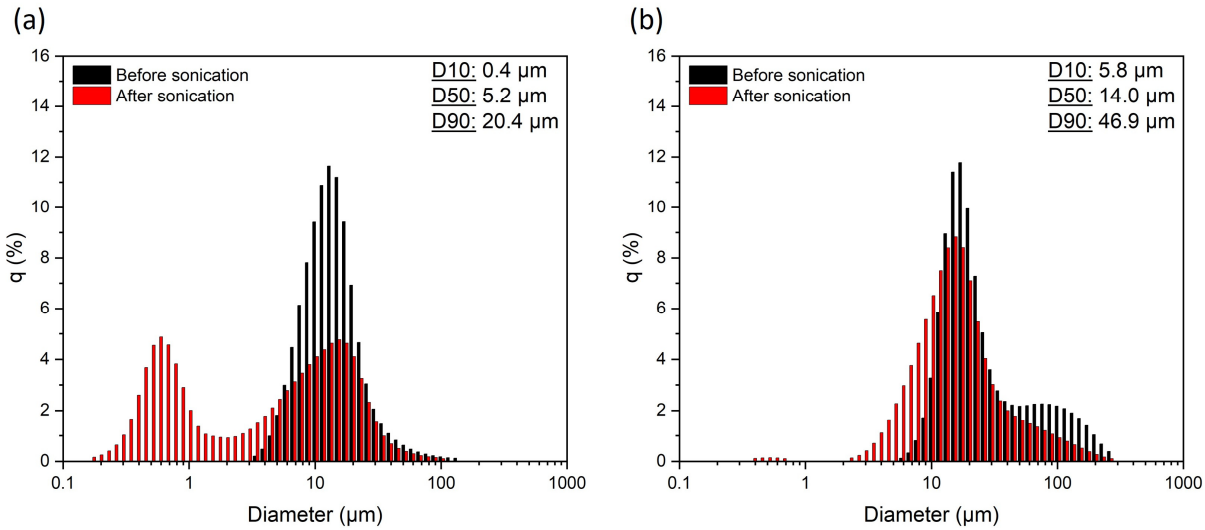

Figure 49: Particle size distribution (PSD) measured before and after sonication for (a) pristine NCM111 and (b) 2 mol% B-doped NCM111.

SEM images of the different cathode active materials indicate that all powders consist of sphere like agglomerates (secondary particles) (Figure S 10) which are composed of nano-sized primary particles (Figure 50). In the case of pristine NCM111, the agglomerates are composed of thin, flake shaped primary particles with an average diameter of 151 nm (Figure 50a, Table 6). The obtained particle shape is similar than observed for the NCM111 hydroxide precursor ($(Ni_{1/3}Co_{1/3}Mn_{1/3})(OH)_2$) before calcination and lithiation (Figure S 11a). The presence of these nano-sized flake shaped primary particles is the most probably reason for the bored reflections in the powder XRD pattern of pristine NCM111 observed in Figure 48. These loosely arranged thin, flake shaped primary particles result in an exceedingly high specific BET surface area of 10.59 $m^2 g^{-1}$. The B doping of NCM111 does not lead to a significant change in particle size and shape. In the case of 2B-NCM111, still flake shaped primary particles with an average diameter of 154 nm are observed (Figure 50b). The formation of larger and harder agglomerates by B doping goes a hand with a significantly reduces specific surface area of 3.67 $m^2 g^{-1}$ for 2B-NCM111. Additionally, B doping slightly increases the density of NCM111 (Table 6).

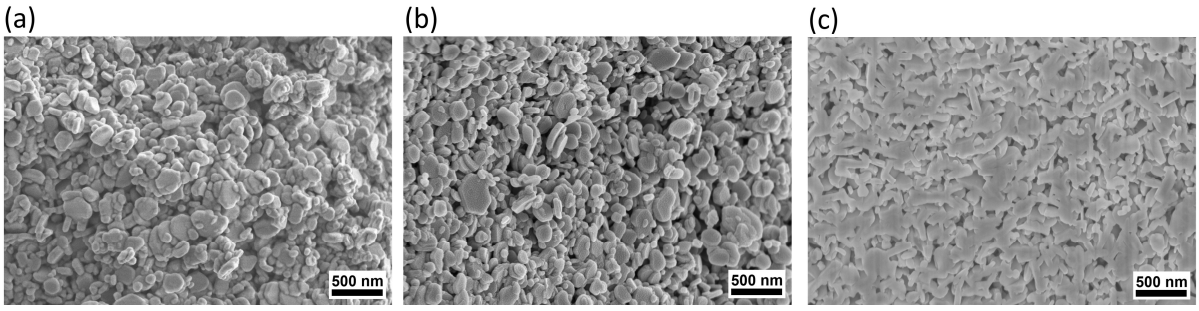

Figure 50: Secondary electron (SE) SEM images (3 kV) visualizing primary particles of (a) pristine NCM111 and (b) 2B-NCM111. (c) A cross section of a 2B-NCM111 secondary particle prepared by focused ion beam (FIB).

Compared to the morphology of the previously reported Ni-rich NCM811 (Chapter 4), it is obvious that the size and shape of the primary particles strongly depends on the NCM composition. While for pristine NCM111 and 2B-NCM111 calcined at 750 °C, thin flake shaped primary particle were observed, the agglomerates of pristine NCM811 and 2B-NCM811 calcined at 800 °C, consists of thicker, cuboidal primary particles (Figure 43) which explains the significant reduced specific surface area of the Ni-rich NCM811 compared to NCM111 (Table S 2). This change in morphology cannot be attributed to the slightly increased calcination temperature in the case of NCM811 since also after calcination at 750 °C as used for NCM111, cuboidal primary particles were obtained (Figure S 13). Since the hydroxide precursor $(Ni_{0.8}Co_{0.1}Mn_{0.1})(OH)_2$ of NCM811 is also composed of thin flake shaped primary particles (Figure S 11b) as reported for the hydroxide precursor of NCM111, the transition metal composition does not influence the morphology of the hydroxide precursor during co-precipitation. However, after calcination and lithiation, a significant change in the particle size and shape is observed, which seems to be an effect of an increased Ni and reduced Co and Mn content. It is assumed that the thin, flake shaped particles of the Ni-rich hydroxide precursor undergo a significant higher densification during calcination, leading to thicker and larger cuboidal primary particles, whereas for NCM111 the shape of the precursors primary particles retains after calcination.

Table 6: Particle size, BET surface area, and density of pristine NCM111 and 2 mol% B-doped NCM111. The average primary particle size was obtained from several SEM images. The mean value and the standard deviation are shown.

Active material	**D50 [µm]**	**Prim. particle size [nm]**	**BET surface area [$m^2\ g^{-1}$]**	**Density [$g\ cm^{-3}$]**
NCM111	5	151 ± 54	10.59	4.23
2B-NCM111	14	155 ± 59	3.67	4.30

Cross sectional SEM images of B-doped NCM111, prepared by a focused ion beam (FIB) (Figure 50c), clearly indicate that the secondary particles are composed of randomly oriented primary particles. The primary particle shape found on the surface of the secondary particles was also found in the interior of the agglomerates. Thus, the morphology of 2B-NCM111 is different from this reported by K.-J. Park *et al*.[107] who observed elongated primary particles aligned along the radial direction of the agglomerate for the highly Ni enriched $Li[Ni_{0.9}Co_{0.05}Mn_{0.05}]O_2$ (NCM90) doped with 1 mol% B. 2B-NCM811 synthesized within this thesis does also not show any alignment of the primary particles (see Chapter 4). Thus, the similar findings for 2B-NCM111 underline the hypothesis that B doping leads only to a preferred growing direction in combination with a precise adjustment of the synthesis conditions or only for highly Ni-enriched cathode active materials.

In order to finally investigate the effects of boron incorporation into the NCM lattice on the electrochemical properties of NCM111, electrochemical tests were performed in cells based on a liquid electrolyte. Cyclic voltammetry (CV) curves of pristine NCM111 and 2B-NCM111 (Figure 51a) confirm their electrochemical activity, in agreement with observation of other groups [38, 49]. The shape of the CV curves does not change dramatically by B doping, only the specific peak currents are increased. The redox peaks are found at 3.80/3.70 V and 3.84/3.72 V for pristine NCM111 and 2B-NCM111, respectively. As compared to pristine NCM111, the cyclic voltammogram of 2B-NCM111 shows an increased peak potential difference of 0.12 V (0.10 V for NCM111), which results in an enhanced polarization. The cathodic to anodic peak current ratio ($i_{p,c}/i_{p,a}$) is 0.65 for 2B-NCM111 and compared to NCM111, with 0.70, it is only slightly affected by B doping. In contrast to the Ni-rich NCM811 (Chapter 4, Figure 47a), for the NCM111 only one redox couple and no multiple phase transitions are observed during delithiation and lithiation, which indicates a higher structural stability of NCM111 during cycling.

Galvanostatic charge/discharge analysis confirms that the incorporation of the electrochemical inactive element boron, does not lead to a significantly reduced capacity. After an initial conditioning cycle, discharge capacities of 163 mAh g^{-1} and 161 mAh g^{-1} were obtained for pristine NCM111 and 2B-NCM111, respectively (Figure 51b). The Coulombic efficiencies are 93 % for NCM111 and 98 % for 2B-NCM111.

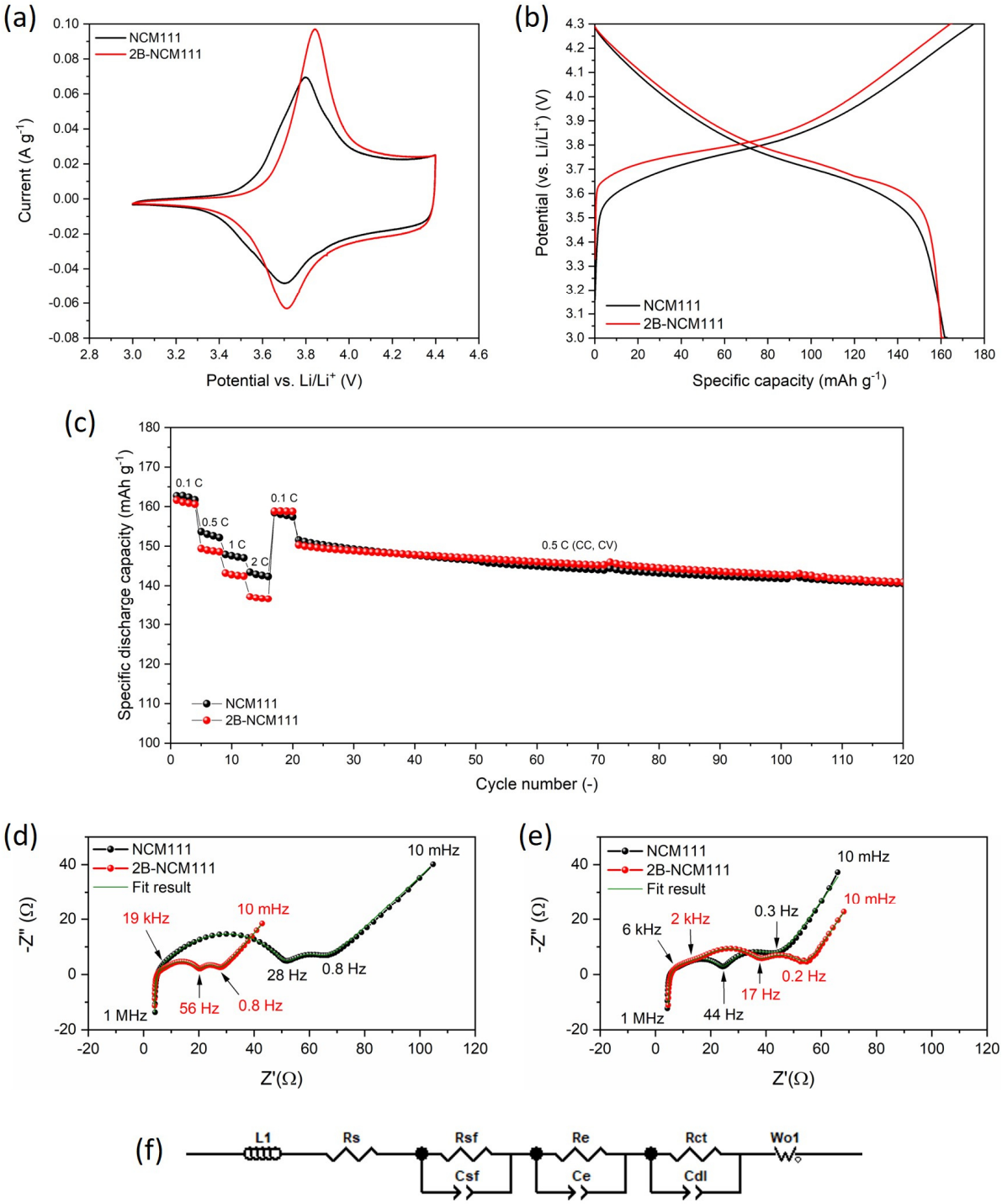

Figure 51: Electrochemical performance of NCM111 and 2B-NCM111. (a) Cyclic voltammogram curves at a scan rate of 0.05 mV s^{-1} for the second cycle. (b) Galvanostatic charge-discharge profiles at 0.1 C for the second cycle. (c) Rate capability tests at various C-rates with prolonged cycling at 0.5 C (cc, cv). (d–f) Electrochemical impedance spectroscopy: (d) Nyquist plot after four cycles at 0.1 C, (e) Nyquist plot after 120 cycles, and (f) equivalent circuit model.

A more pronounced impact of the B doping on the electrochemical performance of NCM111 was found during the rate capability test. While at a low C-rate of 0.1 C similar capacities were obtained for pristine NCM111 and 2B-NCM111, at higher C-rates (0.5 – 2 C) the B-doped

NCM shows lower capacities compared to the pristine cathode active material (Figure 51c). These findings are in agreement with the results for B-doped Ni-rich NCM811 (Chapter 4, Figure 47c). The lower capacities for B-doped NCM at high discharge rates can be explained by a reduced electronic conductivity due to B doping as previously reported by K.-J. Park *et al.*[107]. Furthermore, as explained in Chapter 1.3.5, a reduced Li-ion mobility due to the extremely high bond dissociation energy of B–O (809 kJ mol^{-1}), in comparison to Co–O (397 kJ mol^{-1}), Ni–O (366 kJ mol^{-1}), and Mn–O (362 kJ mol^{-1}) [235], can be an additional reason for the lower capacities of the B-doped NCM at high C-rates.

However, the discharge capacities for both, NCM111 and 2B-NCM111, are similar during the prolonged cycling at 0.5 C for 100 cycles (Figure 51c) and no negative effects of B doping were observed. The capacity retention after 100 cycles is 93 % for pristine NCM111 and 94 % for 2B-NCM111. For both cathodes, similar Coulombic efficiencies between 96 – 99 % were obtained during long-term cycling (Figure S 23). In comparison to NCM811 discussed before (Chapter 4), for Ni-poor NCM111 overall lower capacities but a significant enhanced capacity retention was observed even without doping. Thus, in contrast to NCM811, here no positive effects of B doping on the electrochemical performance of NCM111 in cells based on a liquid electrolyte were observed.

Electrochemical impedance spectroscopy (EIS) was applied to study the effect of B doping on the surface-film and charge-transfer resistance after four (Figure 51d) and 120 charge/discharge cycles (Figure 51e). The fitting of the data was performed by using the equivalent circuit depicted in Figure 51f. Impedance spectra of those cells usually comprise of two semicircles modelled by two RC-elements. One at high frequencies which is usually assigned to the Li-ion migration through the surface film (surface-film resistance, R_{sf}) and an additional one at medium to low frequencies which is usually assigned to a charge-transfer processes on the surface and in the bulk (charge-transfer resistance, R_{ct}). The linear feature at low frequencies is attributed to the solid state diffusion of Li^+ ions in the active material (Z_W, Warburg-impedance) [99]. The intercept at the real axis (Z´) represents the ohmic resistance (R_s) of the cell that is driven by the liquid electrolyte, separator, electrode, and contact resistance. This ohmic resistance is usually around 4 Ω, which is in agreement with the findings of this work [236]. However, for fitting of here recorded impedance spectra, an equivalent circuit model composed of three RC-elements was necessary since an additional semicircle in the high- to medium-frequency region appeared in the Nyquist plot. In the same frequency range, only one larger semicircle was found for Ni-rich NCM811 (Chapter 4, Figure 47d,e) which was assigned to the surface-film resistance.

Related to the work of Q.-C. Zhuang *et al*.[237] who studied the charge/discharge process of $LiMn_2O_4$ by EIS, the additional semicircle possibly represents the electronic properties of the cathode material. Due to the lack of publications reporting about a contribution of electronic properties to the impedance response of cathode materials such as NCM, it cannot be verified that the here observed semicircle originates from the electronic properties of NCM. The calculated capacitances (10^{-6} F and 10^{-5} F), for the impedance response in the high- to medium-frequency region, differ by one order of magnitude, which is in agreement with the work of Q.-C. Zhuang *et al*. who attributed the lower and higher capacitance to the surface-film resistance and the electronic conductivity, respectively [237]. Thus, in this thesis, only the resistance corresponding to the lower capacitance (10^{-6} F) is referred to as surface-film resistance.

For pristine NCM111, the surface-film resistance slightly reduces from 8 to 6 Ω after 120 charge/discharge cycles, while for the B-doped analogue an increase from 4 to 14 Ω was observed. During prolonged cycling, the charge-transfer resistance increases slightly from 6 to 13 Ω for NCM111 and from 4 to 12 Ω for 2B-NCM111. As expected, regarding to the excellent cycle life of NCM111 and 2B-NCM111, the total cell resistance does not increase dramatically during 120 charge/discharge cycles. More importantly, the contribution of surface-film and charge-transfer resistance are both strongly reduced in the case of NCM111 as compared to Ni-rich NCM811. This underlines the fact that Ni-rich cathode materials suffer from a significantly enhanced cation disorder, higher affinity for highly resistive surface impurities, and a high structural instability during cycling.

In summary, 2 mol% B-doped NCM111 was successfully synthesised via the hydroxide co-precipitation route and the effects of boron incorporation on microstructure and electrochemical performance were observed. NCM111 is well known for its small volume change, high chemical and structural stability, and excellent capacity retention during long-term cycling. Thus, in the case of NCM111, a modification by B doping does not further improve the long-term performance and capacity retention of liquid electrolyte-based cells. However, possible effects of B-doped NCM111 on the material compatibility between cathode active material and solid-state electrolyte are investigated in Chapter 7.

5.2. Ru-doped $Li[Ni_{0.8}Co_{0.1}Mn_{0.1}]O_2$

This chapter is based on the following publication:

Christoph Roitzheim, Liang-Yin Kuo, Helen Valencia, Martin Finsterbusch, Olivier Guillon, Dina Fattakhova-Rohlfing, and Payam Kaghazchi, Manuscript in preparation.

In comparison to the boron discussed in the previous chapters, ruthenium is a 4d transition metal that can exhibit higher oxidation states (up to 5+) and a larger ionic radius (0.68 Å for Ru^{3+} as compared to 0.27 Å for B^{3+}). In $Na[Ni_{2/3}Ru_{1/3}]O_2$ used as cathode material for sodium-ion batteries, Ru has the oxidation state 5+ and due to its higher Pauling electronegativity of 2.2 compared to Ni (1.91), the Ru–O bond is expected to be more covalent. The more pronounced covalent character of the TM–O bond stabilizes the oxygen redox-reaction, mitigated the release of oxygen gas, and enhances the structural rigidity [238-241]. Despite the fact that the Ru doping of spinel $LiNi_{0.5}Mn_{1.5}O_4$ drastically enhanced its rate performance[242], ruthenium as dopant in NCM cathodes for LIBs was so far only barely reported. To the best of the authors knowledge, only B. Song *et al*.[243] investigated the effect of Ru doping on the structure and electrochemical properties of Li-rich $Li(Li_{0.20}Mn_{0.54}Ni_{0.13}Co_{0.13})O_2$ and reported an increase in interslab spacing, an enhanced Li diffusion, and improved capacity retention during cycling.
In this work, the advantageous effects of Ru doping were studied to optimize the thermodynamic stability of Ni-rich NCM811 in contact with solid-state electrolyte LLZO during fabrication of composite cathodes for ASBs. Prior to compatibility tests with LLZO in Chapter 7, the impact of Ru doping on the atomic and micro scale properties of NCM811 was investigated. 2 mol% Ru-doped $Li[Ni_{0.8}Co_{0.1}Mn_{0.1}]O_2$ (2Ru-NCM811) was synthesized via a hydroxide co-precipitation route, as described in Chapter 3.1, and calcined under pure oxygen atmosphere. Chemical analysis by ICP-OES (Table S 1) confirms that the calcined material has the targeted NCM composition and ruthenium concentration. Powder XRD pattern corresponds to a phase pure material with a hexagonal α-$NaFeO_2$ structure and the space group $R\bar{3}m$ (166) was found for pristine as well as for Ru-doped NCM811 (Figure 52) [217].

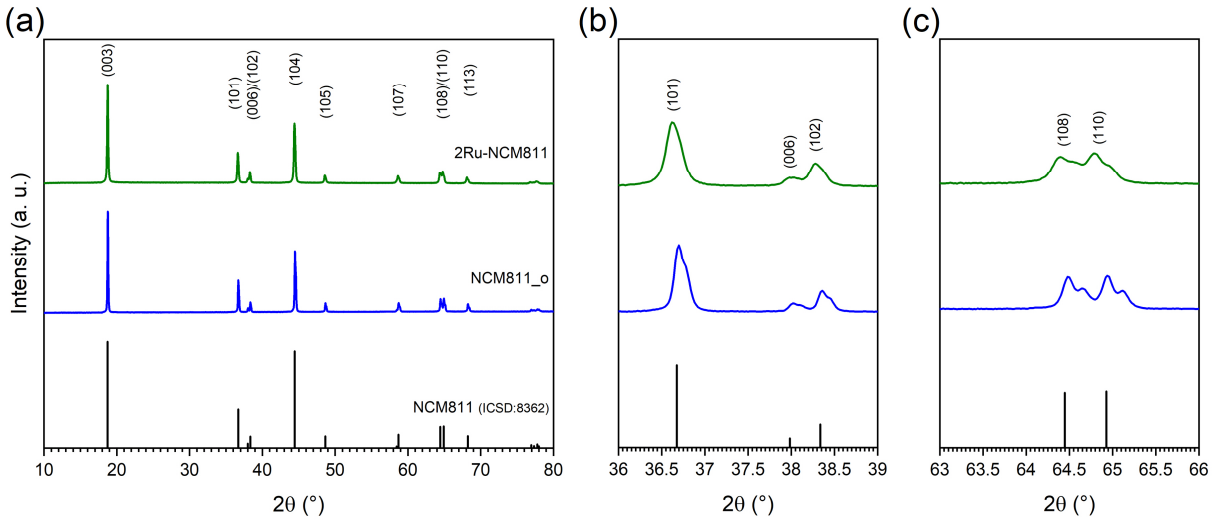

Figure 52: (a) Powder XRD patterns of pristine NCM811_o and Ru-doped NCM811 calcined at 800 °C under pure O_2 atmosphere. (b,c) Magnifications of selected 2θ-regions from (a).

The clear peak splitting of (006)/(102) at 38 – 38.5 °(2θ) and (108)/(110) at 64 – 65 °(2θ) (Figure 52b,c) indicates the presence of an ordered hexagonal layered structure with high crystallinity [218]. No impurity phases were observed, and no additional reflections appear, even for the Ru-doped sample. The slight peak shift towards smaller angles indicates a lattice expansion due to the incorporation of ruthenium (Figure 52b,c). For both materials, a splitting of the Bragg reflections (108) and (110) is observed in Figure 52c. This peak splitting is device specific and caused by $k_{\alpha 2}$ radiation.

The lattice parameters for pristine and Ru-doped NCM811 were calculated from the XRD patterns using the Rietveld refinement (Table 7 and Figure S 7a,c). In the case of NCM811_o, the lattice parameters fall within the span reported in literature. There is a scattering of the literature values due to the variation in Li and transition metal (TM) concentration as well as cation disorder (a = 2.8661 – 2.8805 Å; c = 14.2021 – 14.249 Å; c/a = 4.937 – 4.972) [221-224]. Compared to pristine NCM811, doping with 2 mol% Ru leads to a slight expansion of the lattice parameters a and c (Table 7), which was expected in view of peak shift observed in the XRD pattern and is consistent with the previous work on Ru-doped CAM [243]. Therefore, from the XRD analysis, it can be concluded that ruthenium was successfully incorporated into the NCM lattice.

Table 7: Summary of lattice parameters and Rietveld refinement results of pristine NCM811 and Ru-doped NCM811. Ni_{Li} gives the fraction of Ni ions occupying Li sites.

Active material	***a* [Å]**	***c* [Å]**	**c/a**	***I*(003)/*I*(104)**	**Ni_{Li} [%]**
NCM811_o	2.870(4)	14.196(4)	4.95	1.20	3.8
2Ru-NCM811	2.876(4)	14.208(5)	4.94	1.12	3.8

X-ray diffraction and Rietveld refinement data indicate that ruthenium occupies the TM positions. To further investigate the location of the ruthenium atoms and their influence on the NCM811 lattice, DFT calculation was performed as described in Chapter 2.12.1. As shown in Figure 53, ruthenium occupies octahedral Ni positions in the mixed Mn/Ni plane and is coordinated by six oxygen atoms. The lattice parameters obtained by DFT calculation (Table S 7) indicate that the experimentally found lattice expansion due to Ru doping must be accompanied by the formation of Li vacancies. While the lattice parameter *a* expands and *c* decreases in the case of fully lithiated 2Ru-NCM811, both *a* and *c* expand only in the case of partially delithiated 2Ru-NCM811 (98 % Li). The formation of Li-vacancies can occur to balance the charge when the positively charged Ru is incorporated into the lattice.

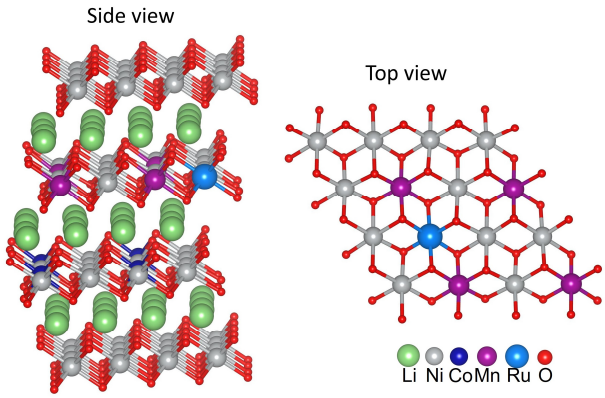

Figure 53: Simulated atomic structure of 2 mol% Ru-doped NCM811.

A closer examination of the XRD pattern (Figure 52) in terms of the Bragg reflection intensity ratio *I*(003)/*I*(104) and the splitting of the (108)/(110) Bragg reflections reveals additional effects of Ru doping. First, the *I*(003)/*I*(104) ratio decreases (Table 7) and second, the splitting of the (108)/(110) Bragg reflection is less intense in the Ru-doped sample. These observations are indicative of an enhanced cation disorder/cation mixing (interchange between Li and Ni sites). The *c*/*a* ratio is an additional indicator of the degree of cation disorder. For an ideal hexagonal closed packed lattice with $R\bar{3}m$ (166) and layered structure, *c*/*a* = 4.99. Partial cation mixing is indicated by *c*/*a* < 4.96. Thus, both the pristine and the Ru-doped NCM811 exhibit

cation disorder, which is enhanced in 2Ru-NCM811 (Table 7). The percentages of Ni on Li sites determined based on Rietveld refinement show identical amounts of Ni on Li sites (3.8 %). A possible explanation for the deviation from the trend for cation disorder derived from the lattice parameters and peak intensity ratio are uncertainties caused by the assumptions made for the Rietveld refinement. The effect of doping on the cation disorder was also observed for the B doping of NCM811 and discussed in detail in Chapter 4.

A much stronger effect of Ru doping on cation disorder is plausible, since ruthenium is expected to have a higher oxidation state than boron, so the fraction of Ni^{2+} is increased to achieve charge neutrality. To determine the oxidation state of Ru in Ru-doped NCM811, the binding energies were analyzed by X-ray photoelectron spectroscopy (XPS) as described in Chapter 2.4. The Ni $2p_3$ region of the XPS spectrum (Figure S 27d) could be fitted with a set of peaks derived from NiOOH [228], indicating that the main oxidation state of nickel is 3+. The Ru 3d spectrum (Figure 54a) shows that the Ru $3d_5$ and Ru $3d_3$ core peaks occur at 283.6 eV and 287.8 eV, respectively. The Ru $3d_5$ binding energy of 283.7 eV found here is consistent with this found by U. Manju *et al.*[244] for Ru^{5+} ions in $RuSr_2GdO_6$. Additionally, the Ru 3p XPS spectrum (Figure 54b) was analyzed since the Ru 3d spectrum partially overlaps with the C 1s spectrum. Fitting of the Ru 3p spectrum was not performed due to lack of literature data. However, the binding energies for the Ru $3p_3$ and Ru $3p_1$ core peaks can be estimated from Figure 54b to be 465.0 and 486.9 eV, respectively. The binding energies obtained here for the Ru $3p_3$ and Ru $3p_1$ core peaks are similar to those found by N. Voronina *et al.*[240] for the Ru^{5+}–O binding energy in $Na[Ni_{2/3}Ru_{1/3}]O_2$, where the peaks were found at 465 and 487 eV, respectively. Comparison with literature data suggests that the oxidation state of Ru in the Ru-doped NCM811 synthesized here is 5+. Since there are no literature data for Ru in NCM811 cathodes, this finding needs to be further substantiated by future experiments using X-ray adsorption near-edge structure spectroscopy (XANES).

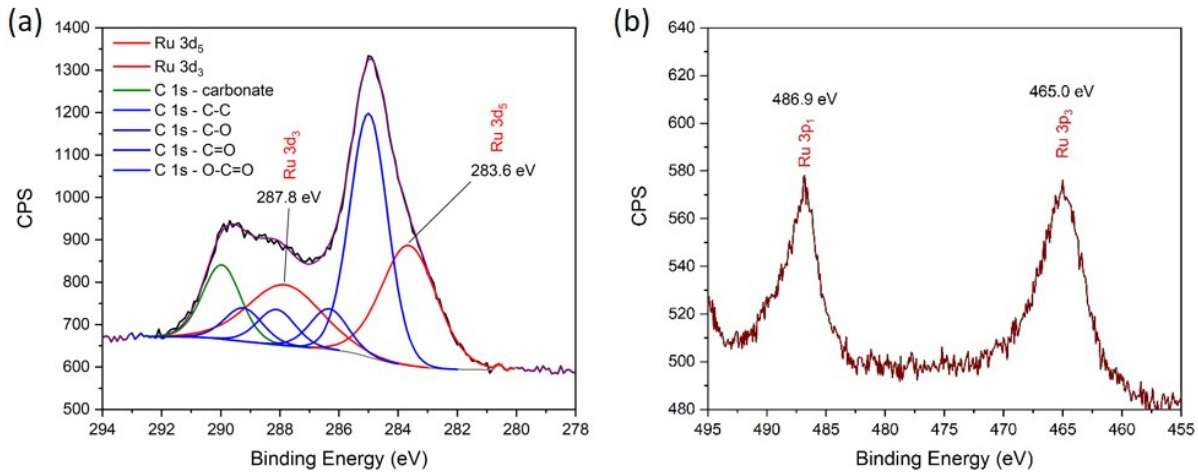

Figure 54: (a) Ru 3d and (b) Ru 3p XPS spectra collected from 2Ru-NCM811.

However, the Ru 3d spectrum does not show an intense peak at 281.8 eV corresponding to $RuCl_3$[245] used as Ru source during synthesis, indicating that the oxidation state of Ru in the Ru-doped NCM811 has increased to a higher value than 3+. This change in oxidation state is another indication of successful incorporation of Ru into the NCM811 lattice.

The possible effects of Ru doping on the particle size and morphology were investigated. The particle size distribution (PSD) of NCM811 calcined under pure O_2 atmosphere is not affected by Ru doping. The powders consist of hard secondary particles with a D50 of 13.2 and 11.0 µm for the pristine NCM811_o and 2Ru-NCM811, respectively (Figure S 2a,c). SEM analysis shows that the synthesized Ru-doped NCM811 powder consists of spherical agglomerates (Figure S 14). Each individual agglomerate is composed of nano-sized cuboidal primary particles that are randomly oriented (Figure 55). Ruthenium doping has a strong influence on the average primary particle size. While the primary particle size is around 318 nm for pristine NCM811_o (Figure 55a), it strongly decreases to only 145 nm for 2Ru-NCM811 (Figure 55b). Such reduced primary particle size is in agreement with the previous findings on Ru doping of different cathode materials [242, 243]. Moreover, the same effect of a reduced primary particle size due to doping was also reported for B-doped NCM811 in Chapter 4.

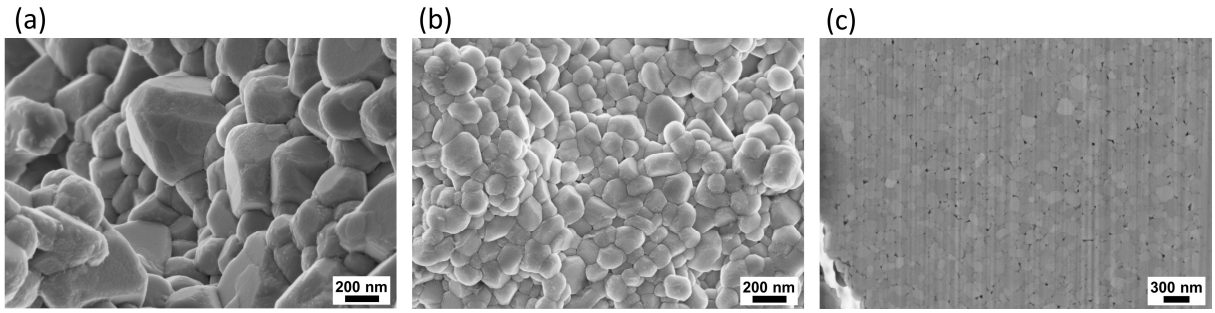

Figure 55: SE-SEM images (3 kV) showing primary particles of (a) NCM811_o and (b) 2Ru-NCM811. (c) Cross section of a 2Ru-NCM811 secondary particle prepared by focused ion beam (FIB).

Atomic resolution Z-contrast HAADF-STEM imaging was performed to analyze the 2 mol% Ru-doped NCM811 primary particles in more detail (Figure 56a). A higher magnification of the surface region (green square) shows that there is a strong atomic contrast at the Li positions, which could be due to transition metal ions (most probably Ni^{2+}) occupying the Li sites. This finding underlines the presence of a cation disorder detected by XRD analysis. Such a surface region with clear structural defects was also found for the pristine NCM811 described in Chapter 4, where a rock-salt structure was detected in this region. However, for the 2Ru-NCM811, the FFTs of both regions (yellow and green squares) could not be attributed to a layered structure ($R\bar{3}m$) or rock-salt structure ($Fm\bar{3}m$). The angels and atom-to-atom distances for the Ru-doped sample do not match the known values for a rock-salt structure. As shown by the red rectangle, the atoms are aligned at an angle of nearly 90 °, which is very uncommon and has not been observed previously for NCM samples. Although XRD analysis shows phase pure NCM with a hexagonal layered structure, local phase transitions might occur that are not detectable by XRD. Based on the data obtained in this work, such a phase transition cannot be attributed to Ru doping. A more in-depth analysis of the observed phenomenon and identification of the detected phase is needed. In addition, further primary particles of this batch as well as powders of different batches need to be analyzed by TEM to prove the effects of Ru doping on the atomic structure of NCM811.

Other primary particles of the same sample were analyzed by EDS (Figure 56b). The EDS spectrum shows the Ru-L_α and Ru-L_β peaks at 2.6 and 2.7 keV, respectively, in addition to the expected signals for Ni, Co and Mn, clearly confirming the incorporation of Ru into the primary particles. The EDS mapping of the 2Ru-NCM811 primary particles shows a homogenous distribution of all elements, including the dopant ruthenium.

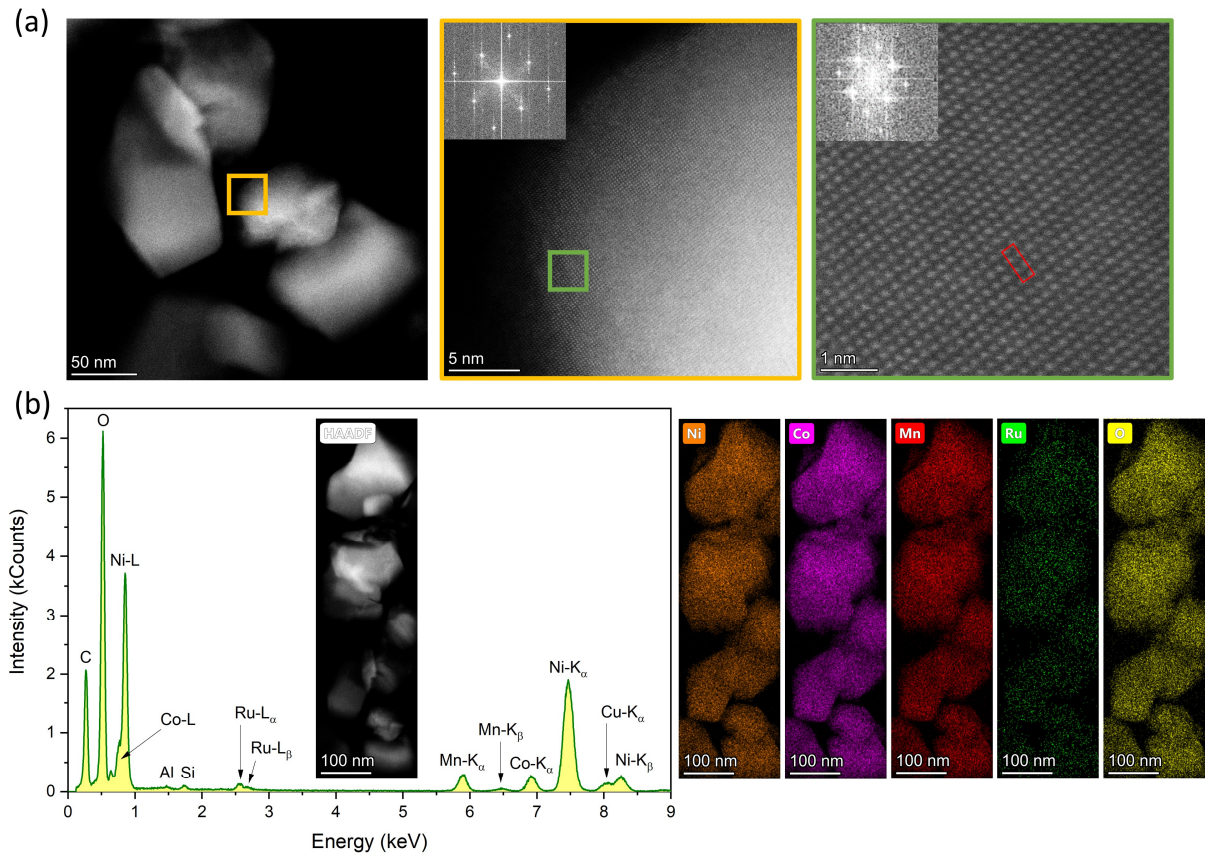

Figure 56: (a) STEM analysis of 2Ru-NCM811 primary particles showing an overview and high-resolution HAADF-STEM images together with FFTs from labeled areas. (b) HAADF-STEM image and EDS spectrum taken from primary particles as well as EDS mappings for Ni, Co, Mn, Ru, and O.

The absence of a secondary phase in the XRD patterns, the DFT calculation, the altered primary particle size of Ru-doped NCM811, and TEM/EDS indicate a successful Ru doping of the NCM lattice. Ion beam analysis and TOF-SIMS were used to experimentally verify the exact location of ruthenium in 2Ru-NCM811. Rutherford backscattering spectrometry (RBS) was used to detect and quantify ruthenium because it is sensitive to heavy elements such as ruthenium. The RBS part of the spectrum of interest for ruthenium (Figure 57a) shows a perfect match between the backscattering of Ru at around channel 780 and the simulated spectrum. A deviation between simulated and experimental data shows that there is a depletion of Ni, Co, and Mn on the surface of the secondary particles, resulting in a lower experimental signal compared to the simulation, which assumes homogenous NCM811 particles. The depletion layer can be attributed to surface impurities (e.g., carbonates, hydroxides, etc.) or to an enrichment of ruthenium on the particle surface. A homogenous composition of NCM811 is observed in the core of the particles, as indicated by a perfect agreement between experimental and simulated values. The Si peak at around channel 710 is caused by the SiN window of the powder sample holder.

Quantification of ruthenium based on RBS shows an average concentration of (2 ± 1) mol% ruthenium in the analyzed 2Ru-NCM811 powder. The amount of ruthenium found by RBS agrees well with the expected 2 mol% Ru detected by ICP-OES (Table S 1). In this measurement, the channel range of Ru is very scarce, so RBS provides only near-surface information. Therefore, particle induced X-ray emission (PIXE) was used since it enables a higher penetration depth. The PIXE spectrum (Figure 57b) shows a clear, background free K_α and K_β signal at 19 and 21.5 keV, respectively. Quantification of ruthenium based on the PIXE results was challenging and yielded an unrealistically high amount of Ru due to inaccurate efficiency calibration of the PIXE detector and the high X-ray energies of Ru. However, PIXE detects the presence of ruthenium not only on the surface but also, and more importantly, in the bulk of the Ru-doped NCM811 particles.

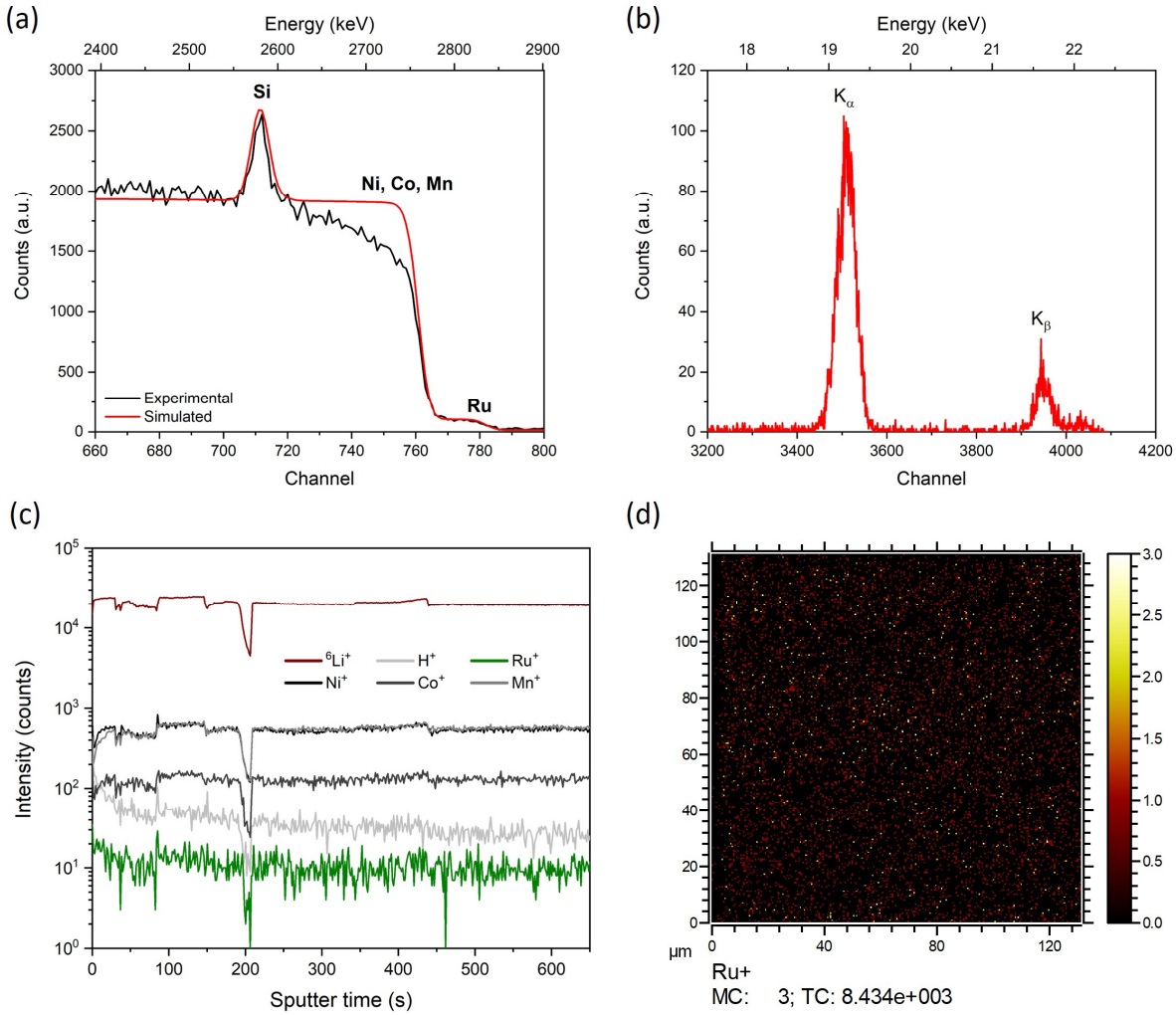

Figure 57: Detection and localization of ruthenium in 2 mol% Ru-doped NCM811. (a) RBS spectrum showing measured and simulated data. (b) PIXE spectrum showing the Ru-signals. (c) TOF-SIMS depth profiles and (d) ruthenium mapping.

The surface of Ru-doped NCM811 particles was further characterized by time-of-flight secondary ion mass spectrometry (TOF-SIMS) with positive polarity. The TOF-SIMS depth profile and the mapping of ruthenium are shown in Figure 57c,d. The depth profiles show that the Co^+, Ni^+, and Mn^+ signals slightly increase and remain constant after a certain sputtering time. It is possible that the sputter ions remove surface contaminations (e.g., carbonates, hydroxides, etc.) formed during the transfer of the samples to the instrument, and after a while a fresh layer is reached, resulting in a constant signal. This suggestion is underlined by the H^+-signal that decreases during the first seconds of sputtering and then remains almost constant. Most importantly, the Ru^+ signal is nearly constant throughout the sputtering process, indicating a constant Ru concentration on the surface of the secondary particles as well as in the bulk of the Ru-doped NCM811 primary particles. Ruthenium mapping (Figure 57d) demonstrates that Ru is uniformly distributed throughout the analyzed particles. In contrast to B doping, which leads to a surface enrichment of boron on the secondary particles (see Chapter 4), no gradient in Ru-concentration was observed for the Ru doping, but a homogenous concentration from the surface to the bulk was found. The results of TOF-SIMS analysis support the conclusions of XRD, TEM/EDS, and PIXE that the ruthenium is incorporated into the bulk structure of the core of the primary particles. As known from theoretical studies on B-doped NCM, boron atoms tend to segregate on the crystal surface [107]. Such a phenomenon is not observed in the case of Ru doping. To substantiate this claim, simulation studies similar to those shown for B doping are planned.

Finally, to investigate the effects of ruthenium incorporation into the NCM lattice on the electrochemical properties of NCM811, electrochemical tests were performed in cells based on a liquid electrolyte. The CV curve of 2Ru-NCM811 (Figure 58a) confirms its electrochemical activity. As previously discussed for Ni-rich NCM811 (Chapter 4), Ru-doped NCM811 also shows multiple redox peaks corresponding to the H1 to M, M to H2, and H2 to H3 phase transitions. However, the M to H2 and H2 to H3 transitions appear to be less pronounced for 2Ru-NCM811, as indicated by the lower peak currents compared to NCM811_o. The peak potentials for Ni^{2+}/Ni^{4+} correspond to 3.81/3.70 V and 3.83/3.69 V for pristine NCM811_o and 2Ru-NCM811, respectively. Moreover, redox peaks were found at 4.22/4.16 V for pristine NCM811_o and at 4.23/4.15 V for 2Ru-NCM811, corresponding to Co^{3+}/Co^{4+}. Although a $Ru^{4+} \leftrightarrow Ru^{5+}$ redox couple has already been reported for the spinel structure[246], the hexagonal layered structure investigated here shows no any additional peaks in the analyzed potential range. This means that Ru is not electrochemically active in the selected potential window, the amount of Ru is too small to show a significant contribution in the CV curve, or

that the redox peaks of Ru are superimposed by those of Ni and Co. The potential difference between the oxidation and reduction peaks at around 3.80 V is 0.14 V for 2Ru-NCM811 and 0.11 V for the pristine NCM811_o. Thus, the Ru-doped NCM811 exhibits a larger potential difference, suggesting a higher polarization of the Ru-doped cathode due to slower insertion/extraction of Li ions in the layered structure. The increased polarization due to Ru doping is more evident in the first CV scan (Figure S 22).

The incorporation of ruthenium is evident also from the altered galvanostatic charge/discharge profiles (Figure 58b), which exhibit shorter and less intense charge/discharge plateaus at around 4.2 V compared to the pristine NCM811_o. After an initial conditioning cycle, discharge capacities of 191 and 164 mAh g^{-1} were obtained for the pristine NCM811_o and 2Ru-NCM811, respectively (Figure 58b). The Coulombic efficiencies are 97 % for NCM811_o and only 94 % for 2Ru-NCM811. Two additional cells were tested to evaluate the rate performance (Figure 58c). While similar capacities were obtained for both samples at a low C-rate (0.1 C), at higher C-rates (0.5 – 2 C) the Ru-doped sample always shows lower capacities compared to the undoped CAM. During prolonged cycling at 0.5 C (Figure 58c), lower capacities were always obtained for 2Ru-NCM811, and both samples show a continuous capacity fading. After 120 cycles, 122 and 107 mAh g^{-1} were obtained for NCM811_o and 2Ru-NCM811, respectively. This corresponds to an identical capacity retention of 74 % for both samples. For both cathodes, similar Coulombic efficiencies were obtained during long-term cycling. The efficiencies scatter slightly, but values between 90 – 99 % were mainly obtained (Figure S 24). The rate capability test is reproducible, as shown in Figure S 25.

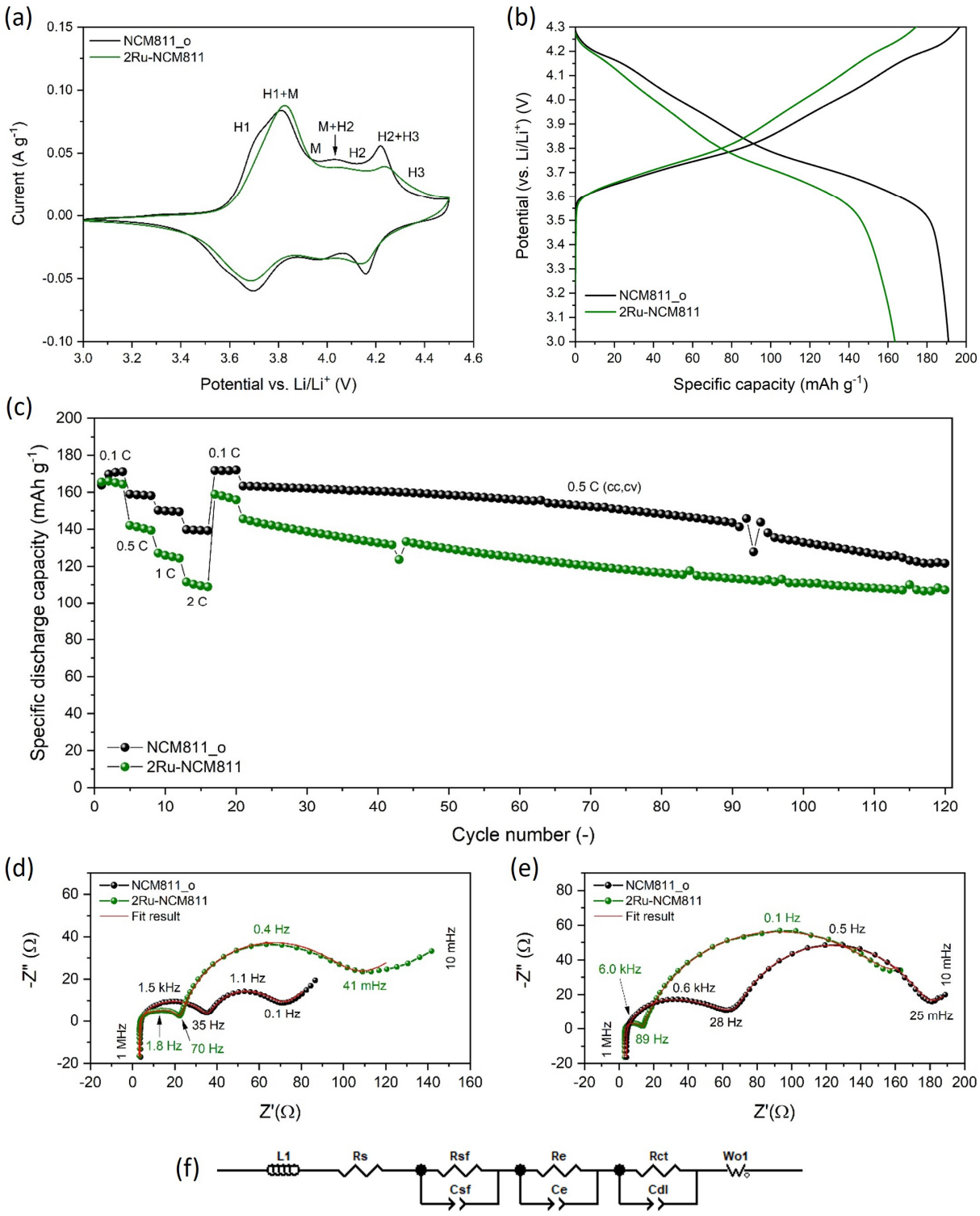

Figure 58: Electrochemical performance of pristine NCM811_o and 2Ru-NCM811. (a) Cyclic voltammogram curves at a scan rate of 0.05 mV s^{-1} for the second cycle. (b) Galvanostatic charge-discharge profiles at 0.04 C for the second cycle. (c) Rate capability tests at various C-rates with prolonged cycling at 0.5 C (cc, cv). (d–f) Electrochemical impedance spectroscopy: (d) Nyquist plot after four cycles at 0.04 C, (e) Nyquist plot after 120 cycles, and (f) equivalent circuit model.

Electrochemical impedance spectroscopy (EIS) was applied to study the effect of Ru doping on the surface layer and charge-transfer resistances (Figure 58d,e). The fitting of the impedance

spectra was performed by using the equivalent circuit depicted in Figure 58f. Two overlapping semicircles at high frequencies and an additional one at medium to low frequencies are visible. While the semicircle in the medium to low-frequency range represents the charge-transfer resistance, the semicircles in the high frequency range cannot be clearly assigned to a responsible phenomenon, as already discussed in Chapter 5.1. Also, for the cathodes investigated here, only the contribution of the resistance correlated with the lower capacitance (10^{-6} F) is assigned to the surface layer resistance. In the case of pristine NCM811_o, the surface layer resistance increased from 9 to 30 Ω after 120 charge/discharge cycles. As expected, the charge-transfer resistance also increased from 30 Ω after four cycles to 103 Ω after 120 cycles. An identical initial surface layer resistance of 9 Ω was obtained for 2Ru-NCM811_o, which surprisingly did not change during cycling. Compared to pristine NCM811_o, the charge-transfer resistance for 2Ru-NCM811 is significantly higher initially and further increased from 69 to 149 Ω after 120 cycles. The more than double charge-transfer resistance for Ru-doped NCM811 is a possible explanation for the overall lower charge/discharge capacities. Both NCMs show increasing charge-transfer resistance during cycling, which is consistent with the observed capacity fading in Figure 58c.

Compared to previous studies on Ru-doped cathode materials for LIBs [242, 243], 2 mol% Ru doping of Ni-rich NCM811 does not show the expected beneficial effects. Ru doping appears to have a detrimental effect on the electrochemical performance of NCM811. A reduced capacity is a known side effect of doping and has already been reported and explained by M. Eilers-Rethwisch *et al.* [69]. A detailed description of the effects of doping on the Li-ion mobility and capacity can be found in Chapter 1.3.5. In the case of Ru doping, there are several possible reasons for the observed cell performance. Due to the high oxidation state of ruthenium (Ru^{5+}), the charge balance results in the formation of Li vacancies, but also in the increased cation disorder, as verified by XRD (Table 7). Residual lithium migrates to the particle surface, where it is electrochemical inactive and forms resistive surface impurities such as Li_2CO_3. The cation-disordered phase has a higher activation energy barrier for lithium diffusion, which is due to the smaller distance between the slabs and the hindrance caused by the TM-ions in the lithium layer [247]. Consequently, higher polarisation and resistance occur, and only a lower percentage of lithium can de-/intercalate, limiting the resulting charge/discharge capacities for Ru-doped NCM811. In addition, Ru doping reduces the primary particle size, which could negatively affect the charge-transfer resistance that is increased for 2Ru-NCM811. Furthermore, it should be noted that there is no evidence for the electrochemical activity of Ru in NCM811. If Ru is electrochemical inactive within the applied potential window, a further

decrease in gravimetric capacity is reasonable due to the high molar mass of ruthenium. Therefore, a Ru content < 2 mol% should be considered to benefit from the positive effects of doping and to minimize the detrimental effects of the heavy and the highly charged dopant. The higher bond dissociation energy of Ru–O (528 kJ mol^{-1}) compared to Co–O (397 kJ mol^{-1}), Ni–O (366 kJ mol^{-1}), and Mn–O (362 kJ mol^{-1}) [235], as well as the high oxidation state of ruthenium, can decrease the electron density in the O orbitals, reducing the repulsion of the O atoms and the Li-slab distance, as discussed in Chapter 1.3.5. As a result, the Li-ion mobility is limited, high charge-transfer resistance occurs, and the capacity decreases especially at high C-rates, compared to pristine NCM811. However, in the case of a higher bond dissociation energy, the volume change during the cycling should be minimized, so that less mechanical degradation and improved cycling stability can be expected. Figure 58c already shows a convergence of capacities. However, to verify a positive effect of 2 mol% Ru doping on the cycling stability of NCM811, extended cell tests are required in the future.

In contrast to Ru doping, B doping improved the electrochemical performance of NCM811 during long-term cycling (Figure 47). The main difference between these dopants is their effect on the surface composition of NCM811. The Ru doping does not lead to the enrichment of the dopant on the secondary particle surface as it was reported for B doping. Due to surface enrichment of boron, the formation of a lithium boron oxide surface layer is suggested, which can serve as a protective coating and enables an improved capacity retention during long-term cycling. Therefore, the application of a Ru-containing surface coating like RuO_2, which provides additional electronic conductivity as recently demonstrated by G. Mao *et al.*[95], is beneficial to improve both rate performance and capacity retention of Ni-rich NCM.

Although 2 mol% Ru doping did not improve the electrochemical performance of NCM811 in cells based on a liquid electrolyte, the effects of Ru incorporation on the performance of NCM811 in contact with solid-state electrolyte was investigated and is discussed in Chapter 7.

6. The effects of a continuous co-precipitation in a Couette-Taylor-Flow-Reactor on the properties of NCM

Ni-rich NCM cathode powders are commercially available and are usually synthesized continuously by co-precipitation on an industrial scale using a continuous stirred tank reactor (CSTR). In addition to the large-scale production, further advantages of the synthesis in a CSTR are narrow particle size distribution, ideally spherical secondary particle shape, and outstanding high electrochemical performance in liquid electrolyte-based cells. This work focuses on the synthesis of doped NCMs that are not commercially available. Thus, the NCM precursors discussed in the previous chapters were synthesized by co-precipitation in a simple and cheap batch process on a laboratory scale. The realization of equal synthesis conditions for such a batch synthesis is challenging. Hence, similar morphology and electrochemical performance known for the commercial NCMs are not accessible by a batchwise synthesis.

In order to optimize and scale up the co-precipitation reaction on the laboratory scale, a Couette-Taylor-Flow-Reactor (CTFR) was acquired for the future CAM synthesis as a bridge between research on laboratory scale and industrial production. The working principle of a CTFR was described in detail in Chapter 1.3.1. In brief, this reactor enables a continuous co-precipitation of NCM precursors under synthesis conditions leading to NCM with the desired characteristics. In this chapter, the advantages of using a CTFR compared to a batch synthesis in a glass flask will be addressed. As a model compound, NCM811 was synthesized via the CTFR as described in Chapter 3.1 (hereafter abbreviated as NCM811_CTFR). NCM811, previously discussed in Chapter 4 and synthesized under similar conditions by the batch process, is chosen in the following for comparison.

The use of the CTFR for the synthesis of NCM precursors strongly enhances the daily throughput of CAM production. Yields of around 400 g hydroxide precursor per day can be easily realized by the continuous co-precipitation, while the batch synthesis in the glass flask only resulted in 6 g per day. More importantly, the used CTFR favorably affects the powder morphology and finally the electrochemical performance of NCM. Figure 59 shows the particle size distribution of $(Ni_{0.8}Co_{0.1}Mn_{0.1})(OH)_2$ obtained via the CTFR and the batch synthesis.

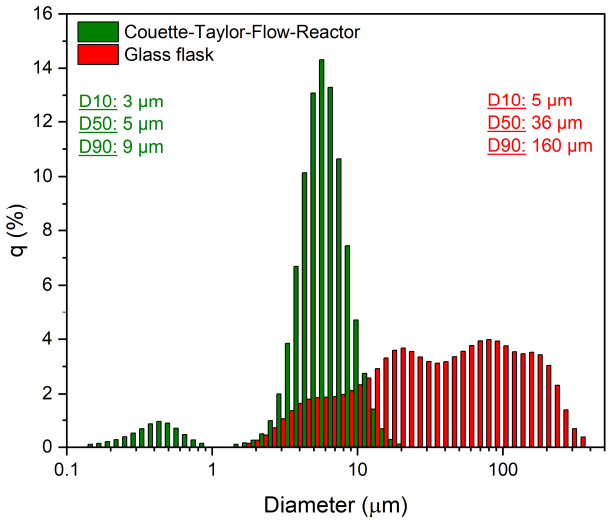

Figure 59: Particle size distribution (after sonication) of NCM811 precursors ($(Ni_{0.8}Co_{0.1}Mn_{0.1})(OH)_2$) obtained by the batch synthesis in a glass flask and by using a Couette-Taylor-Flow-Reactor (CTFR).

The batch synthesis leads to a broad PSD with a D50 of 36 µm and a huge fraction of large agglomerates (> 100 µm), while the use of the CTFR results in a bimodal and narrow PSD with a D50 of 5 µm. The formation of large agglomerates is not observed. Deeper analysis of the NCM811 hydroxide precursors morphology by SEM shows that in the case of the batch synthesis, agglomerates with undefined shapes and a broad size distribution are obtained (Figure 60a,b).

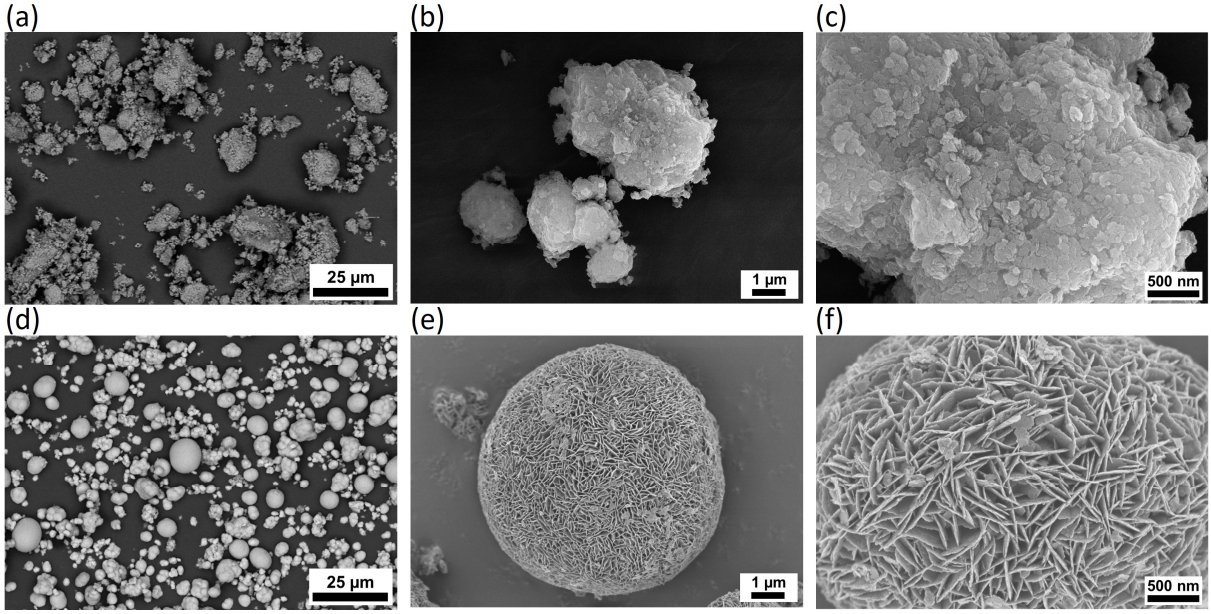

Figure 60: SE-SEM images showing secondary particles of NCM811 precursors with different magnifications obtained by the (a, b, c) batch synthesis in a glass flask (15 kV) and by the (d, e, f) CTFR (1.3 kV).

The hydroxide precursor particles synthesized by using the CTFR mainly have a defined spherical shape and a narrower size distribution (Figure 60d,e). It is well known that the particle

morphology of the NCM precursor powder strongly depends on various synthesis parameters as discussed in Chapter 1.3.1. The size and shape of the particles are governed by the crystal agglomeration mechanism, in which the primary particles aggregate due to physical adhesion followed by agglomerate growth. The agglomeration process depends, among other factors, on the type and geometry of the chemical reactor, which determines the fluid motion. Thus, the spherical shape of the secondary particles obtained by the CTFR can be explained by the optimized conditions for spherical agglomerate formation in this reactor type. In a CTFR, small crystal aggregates are effectively broken and re-dispersed by the Taylor vortexes, which are induced by the inner cylinder rotation, before being converted to agglomerates [58, 248].

For both batchwise and continuous co-precipitation, the secondary particles are composed of thin plate-like primary particles (Figure 60c,f) that are significantly larger for the NCM811 precursor synthesized via the CTFR. Interestingly, for the NCM811 precursors synthesized by the CTFR the primary particles are aligned, namely, the short side of the plate points towards the surface of the agglomerate (Figure 60f). In contrast, for the precursor synthesized in the glass flask, the long side of the plate covers the agglomerate surface (Figure 60c). J.-M. Kim *et al*.[58] analyzed their hydroxide precursor synthesized via a CTFR by selected area diffraction and found that the primary particles are stacked on the (001) plane, while the secondary particles surface is mostly covered by the (101) face. In this work, a similar crystal growth was observed, and thus a similar facet orientation is expected. However, TEM analysis is necessary to investigate the effects of the reactor type on the crystal orientation.

Basically, the facet growth of the crystals depends on the rotation speed (mass transfer) and the mean residence time (supersaturation). It is known that the (001) plane of the crystal exhibits a higher surface energy and is less stable than the (101) plane. The growth rate of the (001) plane was faster than that of the (101) plane, leading to the observed alignment and larger diameter of the primary particles obtained by the CTFR [58]. Mass transfer and supersaturation are expected to strongly differ between the batch synthesis and the continuous synthesis in the CTFR, so that the different facet orientations and primary particle sizes are reasonable.

After calcination and lithiation of the hydroxide precursor, the final NCM811 mainly retains the secondary particle shape independent on the applied synthesis approach. SEM images show NCM811 particles with irregular size and shape (Figure 61a), while for NCM811_CTFR more uniform and mainly spherical secondary particles were obtained (Figure 61c). For NCM811_CTFR, the PSD was shifted towards larger particle diameters (Figure S 2d), so that the D50 value increased from 5 to 15 µm after calcination. A similar PSD was obtained for NCM811 (D50 = 15 µm) obtained by the batch synthesis (Figure S 1a), as the large precursor

agglomerates were thoroughly crushed by grinding prior to calcination. As discussed in Chapter 4, the primary particle shape of the NCM811 precursor changes from a plate-like to a cuboidal one during calcination, which was also observed for NCM811_CTFR (Figure 61b,d). After calcination, the special alignment of the primary particles observed for the precursor is not visible anymore. The diameter of the cuboidal primary particles differs strongly depending on the reactor type. Despite identical calcination conditions, the average dimeter of the primary particles, which was determined from the SEM images, is 200 nm and 448 nm for NCM811 and NCM811_CTFR, respectively. The same trend was already observed for the hydroxide precursors as shown in Figure 60c,f, where the primary particles of the NCM811_CTFR precursor were significantly larger. It seems that the plate-like primary particles grow together during calcination. These findings underline that the precursor morphology is very important to control and tailor the morphology of the final NCM after calcination.

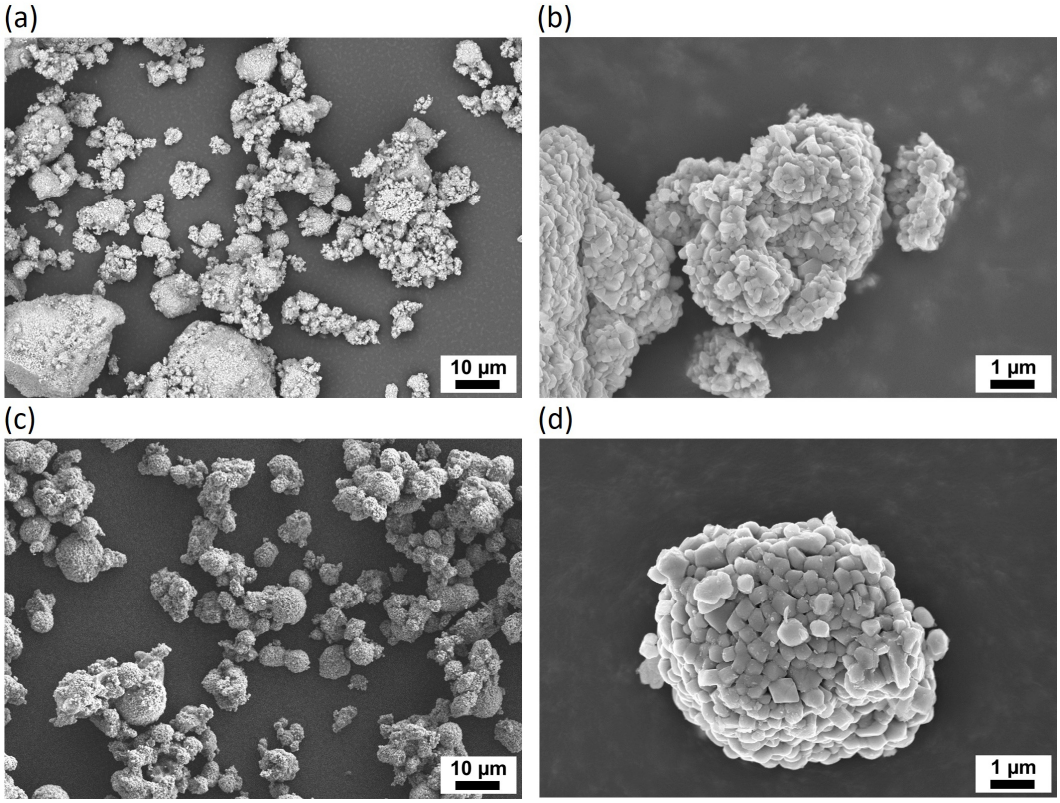

Figure 61: SE-SEM images (8 kV) visualizing NCM811 secondary particles with different magnifications obtained by (a, b) the batch synthesis in a glass flask and (c, d) the CTFR.

The chemical composition of NCM811_CTFR determined by ICP-OES (Table S 1) confirms that the calcined material has the targeted NCM composition. Furthermore, the powder XRD pattern (Figure 62) verify that also for the synthesis via the CTFR, phase pure NCM811 with a hexagonal, α-$NaFeO_2$ structure corresponding to the $R\bar{3}m$ (166) space group was obtained [218]. The clear peak splitting of (006)/(102) at 38 – 38.5 °(2θ) and (108)/(110) at 64 – 65 °(2θ)

(Figure 62b,c) indicates the presence of an ordered, hexagonal layered structure with high crystallinity [218]. The peak splitting visible for the (101), (006), (102), (108) and (110) Bragg reflections in Figure 62b,c are device-specific and caused by $k_{\alpha 2}$ radiation.

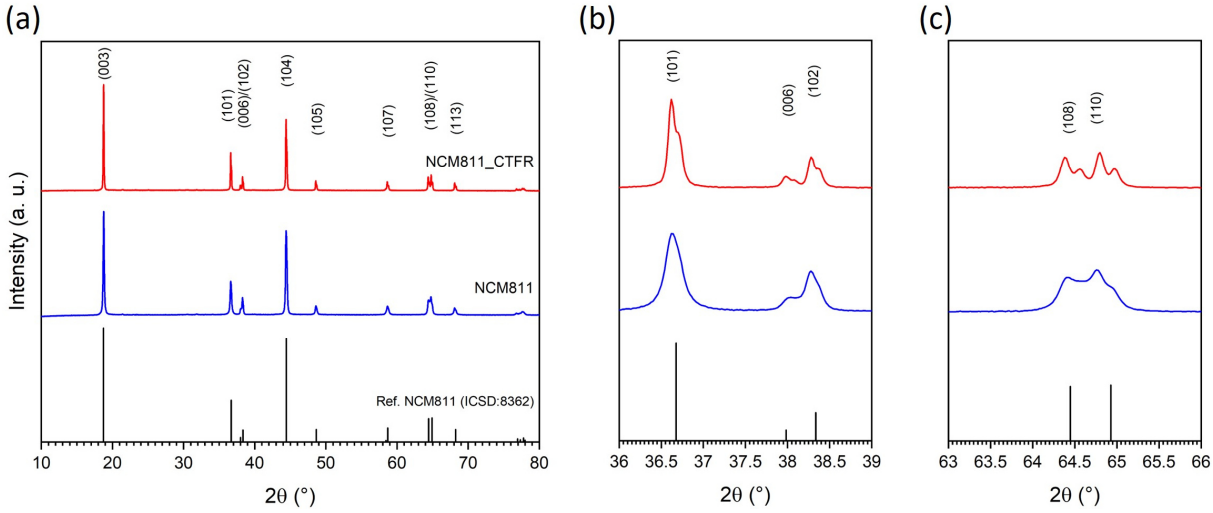

Figure 62: (a) Powder XRD patterns of NCM811 and NCM811_CTFR calcined at 800 °C. (b, c) Magnification of selected 2θ-regions from (a).

Rietveld refinement was used to calculate the lattice parameters as well as the fraction of Ni-ions occupying the Li sites (Figure S 7d). Similar lattice parameters were found for the NCM811 materials synthesized in different chemical reactors (Table 8). Thus, the lattice parameter ratio *c*/*a* is identical for both materials, indicating a similar cation disorder. However, the peak intensity ratio *I*(003)/*I*(104) and also the amount of Ni ions on the Li sites obtained from Rietveld refinement indicate a significant reduced cation disorder for NCM811_CTFR. A reason for a reduced cation disorder by using a CTFR for the precursor synthesis cannot yet be given based on the results of this thesis, but such an effect might have a positive impact of the electrochemical performance of the CAM.

Table 8: Summary of lattice parameters and Rietveld refinement results of NCM811 synthesized batchwise and continuously. Ni_{Li} gives the fraction of Ni ions occupying Li sites.

Active material	***a* [Å]**	***c* [Å]**	**V [Å^3]**	***c*/*a***	***I*(003)/*I*(104)**	**Ni_{Li} [%]**
NCM811	2.878(1)	14.206(6)	101.90	4.94	1.09	7.5
NCM811_CTFR	2.877(1)	14.214(3)	101.89	4.94	1.16	3.8

To investigate the impact of the optimized morphology of the NCM811 precursors obtained in a CTFR on the electrochemical performance of the resulting NCM811, electrochemical characterization in cells with liquid electrolyte was performed. Galvanostatic charge/discharge

analysis of NCM811 and NCM811_CTFR shows similar charge/discharge profiles (Figure S 26a). However, after an initial conditioning cycle, different discharge capacities of 186 mAh g^{-1} and only 163 mAh g^{-1} were obtained at 0.04 C for NCM811_CTFR and NCM811, respectively. The Coulomb efficiencies are 98 % for NCM811_CTFR and only 81 % for NCM811. Two additional cells were tested to evaluate the effect of different chemical reactors for the precursor synthesis on the rate capability of NCM811 (Figure 63a). For all investigated C-rates (0.04, 0.1, 0.5, 1 and 2 C), significantly higher discharge capacities were obtained for NCM811_CTFR. Additionally, the NCM811 obtained in the batch synthesis in the glass flask shows significantly lower capacities at higher C-rates compared to the material synthesized in the CTFR. During prolonged cycling at 0.5 C (Figure 63a), the NCM811_CTFR shows a continuous capacity fading, while for the NCM811 practically no capacity loss was observed. After 85 cycles, 130 mAh g^{-1} was obtained for NCM811, while only 102 mAh g^{-1} was obtained for NCM811_CTFR. This corresponds to a capacity retention of 100 % and 64 % for NCM811 and NCM811_CTFR, respectively. During long-term cycling, similar Coulomb efficiencies of around 90 – 99 % were obtained for both cathodes (Figure S 24).

The discharge capacity of the NCM811 obtained in the CTFR is higher by 55 mAh g^{-1} at 0.5 C as compared to the same material obtained by the batch synthesis in a glass flask. As a possible reason for the increased capacity, a higher degree of de-/lithiation is expected due to the improved morphology. The primary particles in the NCM811 precursor obtained by the CTFR are aligned, so that the surface of the secondary particle is mainly covered by (101) facets (Figure 60f). If this morphology remains also after calcination, the (101) facets might enhance the electrochemical performance of NCM811_CTFR due to facilitated Li de-/intercalation as was previously found by Y. Liu *et al*.[249] for NCA. To prove this assumption, the primary particle orientation needs to be studied in the future work. On the other hand, it is well known that a high Li utilization in case of NCM811_CTFR leads to volume changes during charge and discharge, which causes mechanical degradation resulting in capacity fading as observed in Figure 63a. In contrast, for the NCM811, which shows only poor capacities, the capacity fading is not observed.

EIS was applied to study the effect of different NCM811 morphologies on the resistances of surface layers and charge-transfer (Figure 63b,c). The fitting of the impedance spectra was performed by using the equivalent circuit depicted in Figure 63d. Two overlapping semicircles at high frequencies and an additional one at medium to low frequencies is visible as described in Chapters 5.1 and 5.2. On the base of the capacity value of 10^{-6} F, only this semicircle is assigned to the surface layer resistance for the cathodes investigated in this work.

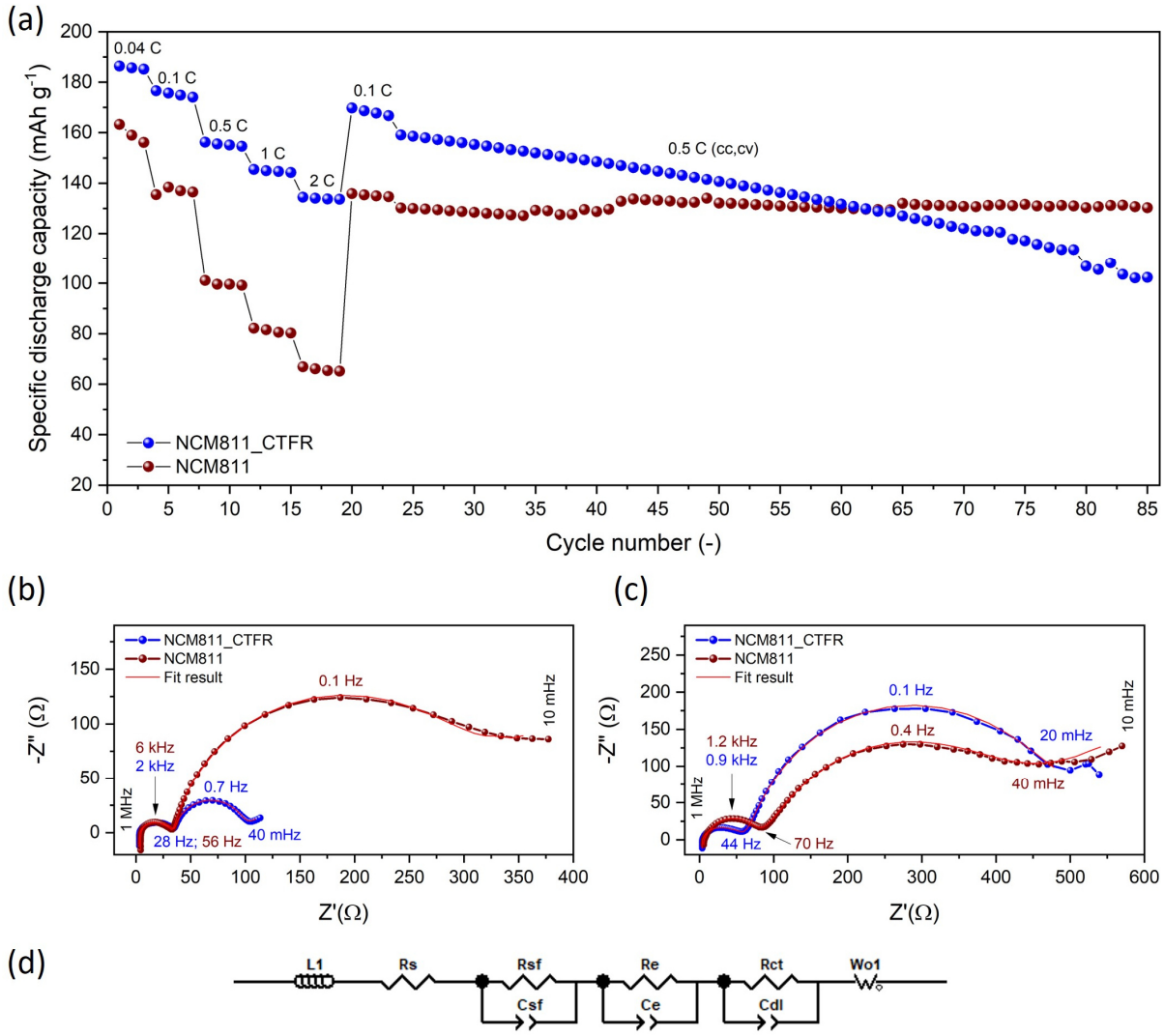

Figure 63: Electrochemical performance of NCM811 and NCM811_CTFR. (a) Rate capability tests at various C-rates with prolonged cycling at 0.5 C (cc, cv). (b–d) Electrochemical impedance spectroscopy: (b) Nyquist plot after four cycles at 0.04 C, (c) Nyquist plot after 85 cycles and (d) equivalent circuit model.

Form the initial Nyquist plot obtained after four charge/discharge cycles (Figure 63b), it can be seen that the NCM811 obtained by the batch synthesis shows a much higher charge-transfer resistance than NCM811_CTFR, while the high-frequency semicircles are similar for both CAMs. After 85 charge/discharge cycles, the surface layer resistance increases from 23 to 59 Ω for NCM811 and from 12 to 26 Ω for NCM811_CTFR. The charge-transfer resistance does not significantly increase for NCM811 (258 Ω after four cycles and 251 Ω after 85 cycles), but it strongly increases from 59 to 364 Ω after 85 cycles for NCM811_CTFR. The initial charge-transfer resistance for NCM811 is more than four times higher than that for NCM811_CTFR, which can be the reason for the overall lower charge/discharge capacities obtained for the NCM811. Furthermore, the fact that the charge-transfer resistance does not change during long-term cycling might explain the absence of the capacity fading for this material. In contrast to

NCM811, the charge-transfer resistance of NCM811_CTFR strongly increases during cycling, in agreement with the severe capacity fading observed during galvanostatic cycling.

To sum up, we have demonstrated that a CTFR can be used for a continuous synthesis of optimized NCM on a laboratory scale. In addition to increasing the daily throughput, the synthesized conditions realized within the CTFR optimize the crystal growth and the agglomeration process. As a result, spherical secondary particles with a narrow particle size distribution were obtained. Furthermore, the plate-like primary particles of the NCM811 precursor are stacked, so that the surface of the secondary particles is mostly covered by the short sides of the plates. As compared to the NCM811 obtained by the batch synthesis in a glass flask, NCM811_CTFR shows an improved morphology similar to the commercial NCM811 synthesized on an industrial scale. Even though both CAMs were calcined under the same conditions, the optimized NCM811_CTFR shows a reduced cation disorder and significantly enhanced charge/discharge capacities as compared to NCM811 obtained by the batch synthesis. The improved performance of NCM811_CTFR can be explained by the optimized particle shape and an advantageous alignment of the primary particles in the precursor.

7. Material compatibility of LLZO:Ta and NCM during co-sintering

This chapter is based on the following publication:

Christoph Roitzheim, Yoo Jung Sohn, Liang-Yin Kuo, Grit Häuschen, Markus Mann, Doris Sebold, Martin Finsterbusch, Payam Kaghazchi, Olivier Guillon, and Dina Fattakhova-Rohlfing, *ACS Appl. Energy Mater.* **2022**, 5, 6, 6913-6926.

Christoph Roitzheim synthesized the NCM and LBO powders, performed their characterization, analyzed all data, and wrote the manuscript with contributions from all authors. Yoo Jung Sohn conducted HT-XRD measurements and did the Rietveld refinements. Liang-Yin Kuo and Payam Kaghazchi performed the DFT calculations. Grit Häuschen synthesized and characterized LLZO:Ta. Markus Mann fitted and analyzed the EIS data. Doris Sebold took the SEM images and performed EDS analysis. Martin Finsterbusch, Payam Kaghazchi, Olivier Guillon, and Dina Fattakhova-Rohlfing initiated the idea, provided the resources, and supervised the work.

Link to the published article: https://doi.org/10.1021/acsaem.2c00533

It is well known that the NCM composition strongly affects the electrochemical and thermal properties of conventional cells based on a liquid electrolyte. For example, high-capacity Ni-rich NCM cathodes like NCM811 show higher heat release rates as compared to Co- and Mn-rich NCM111 with a lower capacity [24]. Doping with elements like Al, Fe, Sn, W, or B was demonstrated as an effective strategy to optimize Ni-rich NCM for application in conventional LIBs [69, 100, 113, 115]. However, detailed information about the thermal stability of NCM with different compositions and dopants in combination with LLZO is lacking. To close this knowledge gap, the thermodynamic stability between cubic, Al- and Ta-substituted LLZO ($Li_{6.45}Al_{0.05}La_3Zr_{1.6}Ta_{0.4}O_{12}$; LLZO:Ta) and two NCM compositions that are of economic importance, namely, NCM111 and Ni-rich NCM811, were investigated. In addition to analyzing the impact of the NCM composition itself on its compatibility with a garnet electrolyte, also doping of the NCM host structure with boron and ruthenium, as a possible mean of improving material compatibility, were investigated. Bearing in mind that LBO is used as a sintering additive for the NCM/garnet composite cathodes (Table 2) and can eventually diffuse in NCM, boron as a dopant of the bulk NCM structure was investigated. Furthermore, positive effects of B doping of NCM such as improved cycling stability, formation of a well ordered lithium boron oxide surface structure, blocked transition metal (TM) migration paths, and hindered phase transitions during cycling, have been reported for the conventional cells

based on a liquid electrolytes and can be expected also in combination with solid state electrolytes [107-110, 115, 116].

In order to investigate the impact of the NCM composition on the thermal stability with cubic LLZO:Ta, pristine and doped active materials have been synthesized via the same route to ensure better comparability. Two NCM compositions, namely, NCM111 and Ni-rich NCM811, both pristine and doped with 2 mol% boron (2B-NCM111 and 2B-NCM811) as well as NCM811 doped with 2 mol% ruthenium (2Ru-NCM811), were obtained via a hydroxide co-precipitation route (see Chapter 3.1). The detailed characterization of all CAMs was previously presented in the Chapters 4 and 5. The synthesis of LLZO:Ta is presented in Chapter 3.2 and its characterization is shown in the appendix (Table S 8 and Figure S 30).

The thermal decomposition behavior of different NCM + LLZO:Ta mixtures was analyzed by differential thermal analysis/thermogravimetry coupled with a mass spectrometer (DTA/TG/MS), as shown in Figure 64 and Figure S 20.

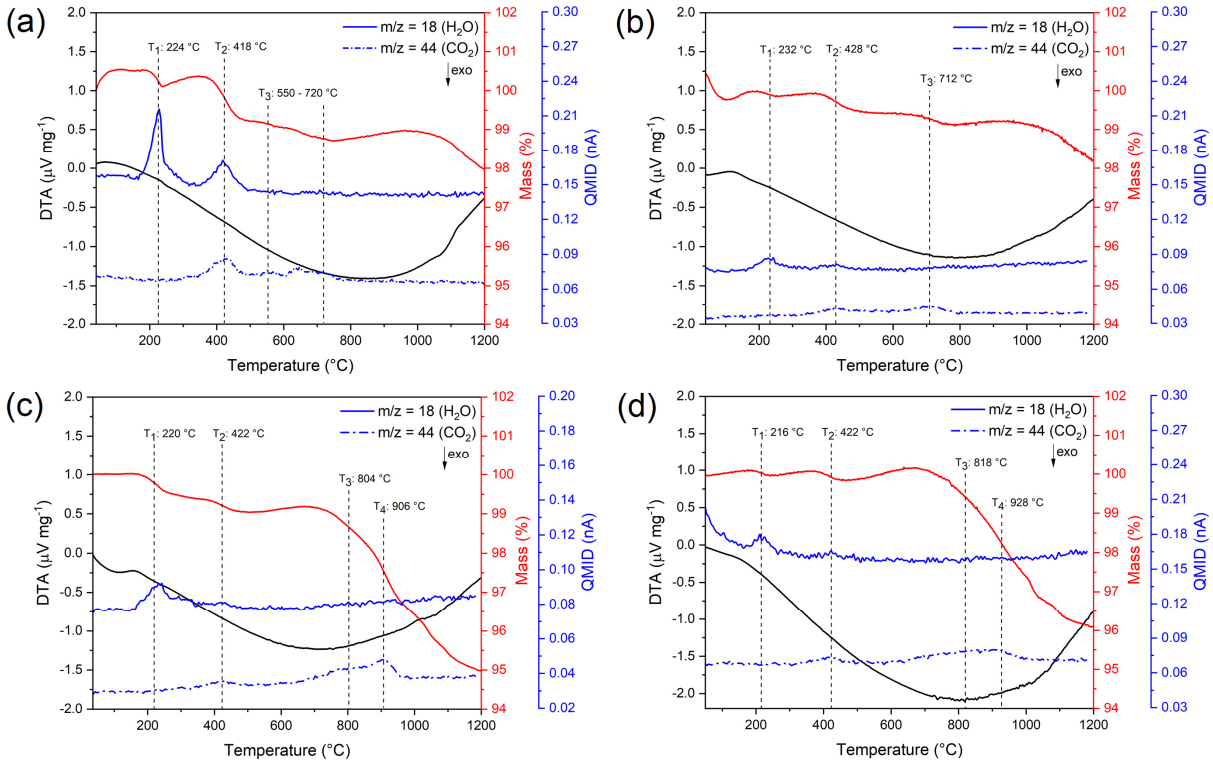

Figure 64: DTA/TG/MS analysis of 1:1 mixtures of LLZO:Ta with (a) NCM111, (b) 2B-NCM111, (c) NCM811, and (d) 2B-NCM811. Reprinted with permission from ref. [161], Copyright 2022, American Chemical Society.

All investigated NCM + LLZO:Ta mixtures demonstrate a slight, stepwise mass loss (2 wt% for the mixtures containing NCM111 and 2B-NCM111 and 4 – 5 wt% for the mixtures with NCM811 and 2B-NCM811) upon heating to 1200 °C. Comparison with the individual NCM and LLZO:Ta materials reveals that the first three mass loss steps (T_1, T_2, and T_3) are caused

mainly by processes related to the LLZO:Ta phase, namely, the desorption of surface-adsorbed water and/or water entered the garnet structure at T_1 (accompanied by the detection of H_2O (m/z = 18)), the decomposition of impurities (Li_2CO_3) formed due to Li^+/H^+ exchange on the LLZO:Ta surface, and the decomposition of lanthanum hydroxycarbonates ($La_2(OH)_2(CO_3)_2$). The latter processes take place stepwise as shown by the detection of H_2O and CO_2 (m/z = 44) at T_2 and an additional CO_2 release at T_3 [153, 250, 251]. The observed three-step weight loss is not observed for pure NCM111 and NCM811 (Figure S 20b,c). The samples containing Ni-rich NCM811 (Figure 64c,d) show an additional CO_2 loss at T_4, which has been observed also for the individual NCM811 (Figure S 20c) and is attributed to the decomposition of Li_2CO_3 impurities from NCM811, which has a higher sensitivity to atmosphere contamination (H_2O and CO_2) as compared to NCM111 [252]. Furthermore, all investigated NCM + LLZO:Ta mixtures (Figure 64) as well as pure NCM111 and NCM811 (Figure S 20b,c), but not pure LLZO:Ta (Figure S 20d), show a continuous mass loss at temperatures above 1000 °C. This can be attributed to the O_2 release from the NCM lattice [252]. It can be concluded that the thermal behavior of different NCM + LLZO:Ta mixtures is determined mainly by the contribution of the single components (NCM and LLZO:Ta). No additional endo- or exothermic processes due to possible reactions of NCM and LLZO:Ta were observed by DTA within the measured temperature range, indicating that no severe decomposition reactions took place during co-sintering of these materials. B doping did not affect the thermal behavior of NCM + LLZO:Ta mixtures.

Complementary to DTA/TG/MS, *in-situ* high temperature XRD (HT-XRD) analysis of the NCM + LLZO:Ta mixtures was performed in the same temperature range to assess possible formation of secondary phases during co-sintering. Figure 65 shows XRD patterns for some selected temperatures. For all NCM compositions, the formation of a pyrochlore phase (labeled with "X") was observed. The $La_2Zr_2O_7$ phase starts to form at 400 °C and disappears again between 650 °C and 800 °C. The pyrochlore phase forms independently of the CAM used and can be attributed to LLZO:Ta as described thoroughly [251, 253].

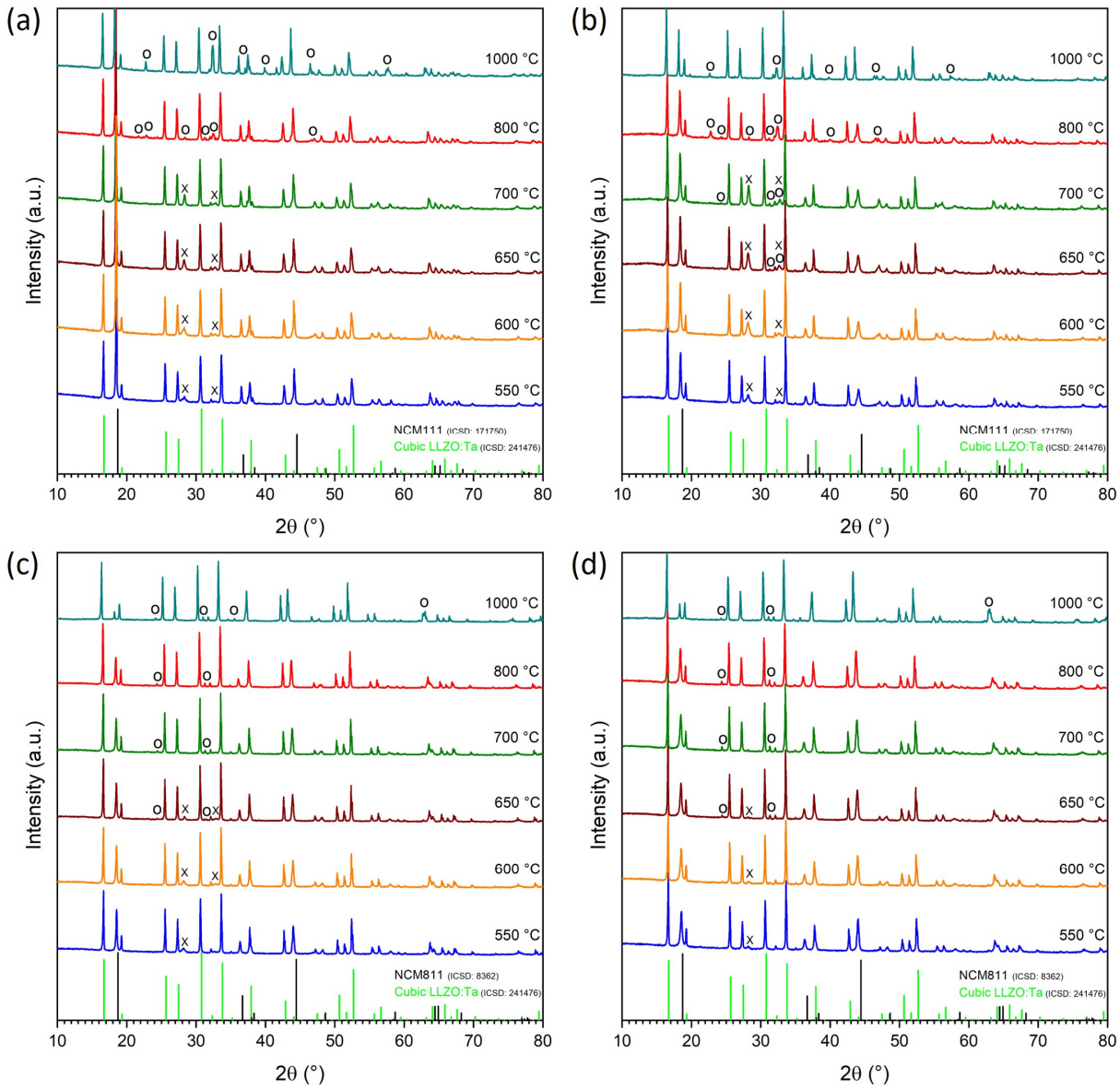

Figure 65: *In-situ* HT-XRD patterns for 1:1 mixtures of cubic LLZO:Ta with (a) pristine NCM111, (b) 2B-NCM111, (c) pristine NCM811, and (d) 2B-NCM811. Only selected temperatures are shown. Reflections attributed to the pyrochlore phase are labeled with "X" and those belonging to further secondary phases were labeled with "O". Due to thermal expansion at elevated temperatures, the reflections are slightly shifted in comparison to the reference pattern for NCM111, NCM811 and cubic LLZO:Ta. Reprinted with permission from ref. [161], Copyright 2022, American Chemical Society.

For all NCM + LLZO:Ta mixtures, the NCM and cubic LLZO:Ta phases were present as main phases up to 1000 °C, but above this temperature, a decomposition of both materials was observed (Figure S 4). NCM111 (Figure 65a) did not show secondary phases due to the reaction with LLZO:Ta up to 800 °C, while beyond this temperature, secondary phases were detected (collectively labeled with "O"). The detailed phase analysis will be presented below. Both B-doped samples as well as Ni-rich NCM811 developed secondary phases in contact with LLZO:Ta at 650°C (Figure 65b-d). Yet, while the concentration of secondary phases increased

with higher temperatures for NCM111 and 2B-NCM111 mixed with LLZO:Ta, the concentration stayed nearly constant for both NCM811 and 2B-NCM811 combined with LLZO:Ta over the whole temperature range (Figure 67). For 2Ru-NCM811 + LLZO:Ta secondary phases are detected starting from 700 °C and also for this CAM, the secondary phase concentration stays constant for higher temperatures as visible in Figure 67.

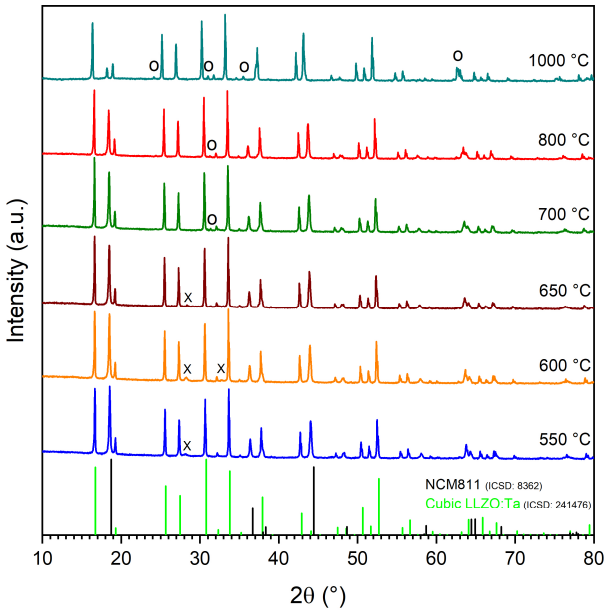

Figure 66: *In-situ* HT-XRD patterns for a 1:1 mixture of cubic LLZO:Ta with 2Ru-NCM811. Only selected temperatures are shown. Reflections attributed to the pyrochlore phase are labeled with "X", and those belonging to further secondary phases were labeled with "O". Due to thermal expansion at elevated temperatures, the reflections are slightly shifted in comparison to the reference patterns for NCM811 and cubic LLZO:Ta.

Rietveld refinement of the patterns recorded at 800 °C (Figure S 8 and Figure S 9) reveals that in fact, two La-containing secondary phases (in addition to the pyrochlore) are formed. The first phase is identified as Mn- and Co-containing $La(MnCo)O_3$ with a perovskite structure. The second phase is nickel-enriched and corresponds either to La_2NiO_4 or $La_2(Ni_{0.5}Li_{0.5})O_4$, whereby different compositions in the $La_2Li_{1-x}Ni_xO_4$ phase, as well as an Al contamination, are also possible. Our findings support the previous reports of the other groups. Y. Ren *et al.*[140] reported the formation of the solid solution $LaCo_{1-x}Mn_xO_3$ ($x < 0.4$) as a Co- and Mn-containing secondary phase during co-sintering of NCM111 and LLZO:Ta [140]. S. Ohta *et al.*[146] found $LaNiO_3$ or $La_2(Ni_{0.5}Li_{0.5})O_4$ as a secondary phase during annealing of NCM111 and LLZO. In comparison to the previous reports, we were able to identify a further Ni-containing secondary phase during co-sintering of NCM111 + LLZO:Ta, and more importantly, we investigated for the first time the secondary phase formation during co-sintering of NCM811 + LLZO:Ta.

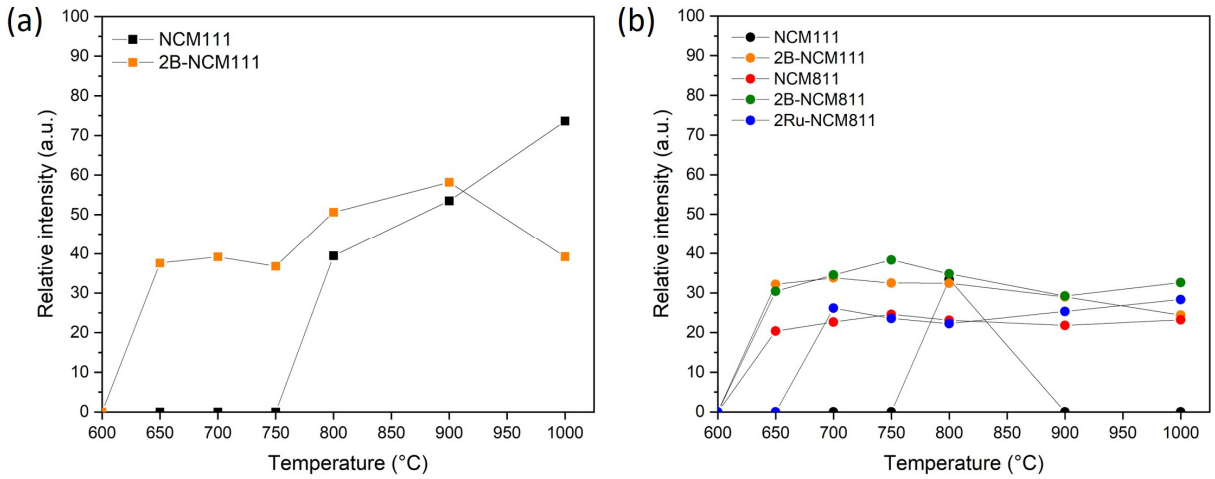

Figure 67: Relative intensities of the (a) $LaCo_{1-x}Mn_xO_3$ reflection (121) at ~32.5 °2θ and (b) $La_2(Ni_{0.5}Li_{0.5})O_4$ reflection (131) at ~31.3 °2θ for different temperatures (normalized to the LLZO:Ta reflection (024) at ~30.5 °2θ). Reprinted (adapted) with permission from ref. [161], Copyright 2022, American Chemical Society.

The NCM composition also defines the nature and the relative amount of secondary phases formed at different temperatures as summarized in Figure 67. For NCM111 + LLZO:Ta, $LaCo_{1-x}Mn_xO_3$ was formed as the main secondary phase at 800 °C, and its intensity continuously increased for higher temperatures. Furthermore, $La_2(Ni_{0.5}Li_{0.5})O_4$ was found at 800 °C as another secondary phase, but no traces of this phase can be detected at higher temperatures within the detection limits of XRD. Boron doping was found to decrease the thermodynamic stability of NCM111 + LLZO:Ta, as $LaCo_{1-x}Mn_xO_3$ was formed already at 650 °C. The total amount of this phase, however, increased only between 800 and 900 °C and decreased again at 1000 °C. Boron doping of NCM111 also resulted in the formation of $La_2(Ni_{0.5}Li_{0.5})O_4$ already at 650 °C. However, its intensity remained constant at increasing the sintering temperatures. In quantitative terms, for the HT-XRD pattern recorded at 800°C of the NCM111 + LLZO:Ta mixture, 4 wt.% $LaCo_{1-x}Mn_xO_3$ was detected, whereas only 1 wt.% $La_2(Ni_{0.5}Li_{0.5})O_4$ was found. For 2B-NCM111 + LLZO:Ta, a similar amount of $La_2(Ni_{0.5}Li_{0.5})O_4$ was found, but the content of $LaCo_{1-x}Mn_xO_3$ strongly increased to 9 wt.% in the similar conditions, indicating a strong effect of B doping on the material compatibility. For Ni-rich NCM811 + LLZO:Ta and 2B-NCM811 + LLZO:Ta, $La_2(Ni_{0.5}Li_{0.5})O_4$ was detected as the only secondary phase at 650 °C and its intensity was nearly unaffected by the further increase in temperature. In the case of NCM811 + LLZO:Ta, only 2 wt.% $La_2(Ni_{0.5}Li_{0.5})O_4$ was detected at 800 °C, whereas no effect of B doping on the amount of formed secondary phases was visible. Also, for Ru-doped NCM811 + LLZO:Ta, only $La_2(Ni_{0.5}Li_{0.5})O_4$ was detected as secondary phase with a slightly lower amount of 1 wt.% at 800 °C compared to pristine and B-doped NCM811.

From the analysis of secondary phase intensity evolution with temperature (Figure 67), it becomes obvious that the amount of $LaCo_{1-x}Mn_xO_3$ strongly increases at higher co-sintering temperatures, while the $La_2(Ni_{0.5}Li_{0.5})O_4$ phase forms once in a small amount and does not grow further after increasing the temperature. The side phase formation in the case of pristine, B-doped and Ru-doped NCM811 + LLZO:Ta has therefore a self-constraining character, which renders it more suited for integration in garnet-containing composite cathodes compared to NCM111. Furthermore, changes in the lattice parameters of NCM and LLZO:Ta were monitored during co-sintering (Table S 5). In order to consider the thermal expansion, the lattice parameters of NCM and LLZO:Ta in the mixtures during co-sintering were compared to those of the individual components recorded at the same temperature. The lattice parameters of LLZO:Ta and NCM appeared to be very stable and showed only minor expansions or contractions during co-sintering, which are mainly within the error range. Only at 800 °C, a more significant expansion of the LLZO:Ta lattice parameter *a* and a contraction of the lattice parameter *c* of NCM111, in contact with LLZO:Ta, were observed.

In addition to the materials structure and composition, particle size and shape generally strongly affect the reactivity of solid powders and should be considered as reported by Y. Ren *et al.*[140]. Based on our data (Table 6 and Table S 2), it is, however, not possible to correlate the observed trends in reactivity with the particle size or the specific surface area. It is therefore assumed that the modification of the hexagonal layered structure caused by increasing the Ni content and B doping (such as the change in lattice occupancy and cation disorder) plays a larger role in the reactivity between NCM and LLZO:Ta than the particle size and the surface area.

To further locate the formation of secondary phases after co-sintering, 1:1 mixtures of NCM and LLZO:Ta powders, identical to the ones used for the HT-XRD analysis, were prepared and sintered for 1 h at 800 °C. Scanning electron microscopy (SEM) and energy dispersive X-ray spectroscopy (EDS) analysis of polished cross sections did not show any presence of $LaCo_{1-x}Mn_xO_3$ or $La_2(Ni_{0.5}Li_{0.5})O_4$ phases for the pellets containing NCM111 or 2B-NCM111 despite their relatively high total amount (up to 10 wt.%) determined via Rietveld refinement. The possible explanation for this effect is that the secondary phases grow as a thin layer on the interface between NCM111 and LLZO:Ta grains, which is below the resolution limit of the SEM. In contrast to NCM111, the pellets containing NCM811 and 2B-NCM811 clearly show the presence of side phases as small (1.5 µm), isolated bright particles (marked red in Figure 68a) in addition to the larger grains corresponding to LLZO:Ta and NCM811 (Figure 68), although the total amount of side phases is lower (2 wt.%) as compared to NCM111.

EDS analysis clearly indicates that the bright particles contain La, Ni and O (Figure 68b). In combination with the results of XRD analysis, the bright particles can be therefore assigned to the $La_2(Ni_{0.5}Li_{0.5})O_4$ secondary phase formed after co-sintering. The same secondary phase was detected also for the mixture of 2B-NCM811 + LLZO:Ta (Figure S 15), in agreement with the HT-XRD results.

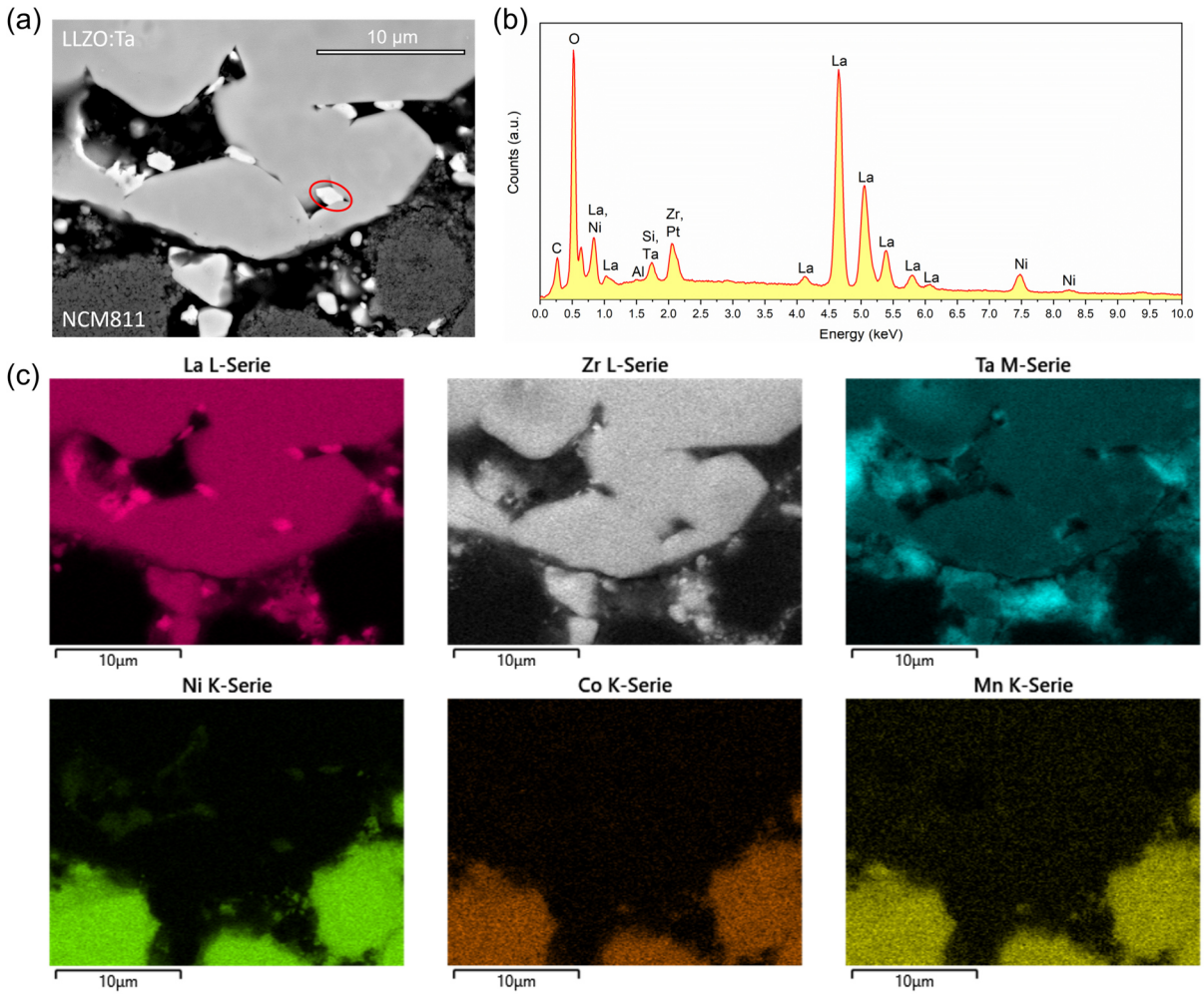

Figure 68: (a) Cross sectional, back scattered electron (BSE) SEM image (15 kV) of NCM811 + LLZO:Ta co-sintered at 800 °C. The marked particle corresponds to a secondary phase. (b) EDS point analysis of the red marked region in (a) and (c) EDS mapping. The peaks of Si and Pt detected in the EDS point scan resulted from polishing suspension and sputtering, respectively. Reprinted with permission from ref. [161], Copyright 2022, American Chemical Society.

Some amounts of Ta and Zr, detected via the EDS analysis of the bright areas in Figure 68b, probably originate from the neighboring LLZO:Ta particles in the composite cathode due to a large interaction volume of the primary electron beam in SEM, as no Ta- and Zr-containing secondary phases were found by XRD.

The formation of $LaCo_{1-x}Mn_xO_3$ and $La_2(Ni_{0.5}Li_{0.5})O_4$ during co-sintering of NCM + LLZO:Ta can be explained by an interchange between TM ions from NCM and Zr from LLZO:Ta. To

get deeper insights into the thermodynamics of this process, the interchange energies were computed using DFT calculation according to equation (24):

$$E_{\mathrm{I}}(\mathrm{Zr}{\leftrightarrow}\mathrm{TM}) = E_{\mathrm{tot}}(\mathrm{NCM811{:}\,Zr \rightarrow TM}) + E_{\mathrm{tot}}(\mathrm{LLZO{:}\,TM \rightarrow Zr}) - E_{\mathrm{tot}}(\mathrm{NCM811}) - E_{\mathrm{tot}}(\mathrm{LLZO}) \quad (24)$$

where $E_{\mathrm{tot}}(\mathrm{NCM811{:}\,Zr \rightarrow TM})$ and $E_{\mathrm{tot}}(\mathrm{LLZO{:}\,TM \rightarrow Zr})$ are the total energies of bulk NCM811 with the substitution of TMs with Zr and bulk LLZO with the substitution of Zr with TMs, respectively, and $E_{\mathrm{tot}}(\mathrm{NCM811})$ and $E_{\mathrm{tot}}(\mathrm{LLZO})$ are the total energies of bare bulk NCM811 and LLZO.

It is found out that the Zr ↔ Mn interchange is more favorable than Zr ↔ Ni and Zr ↔ Co as well as La ↔ Ni and La ↔ Co. The calculated interchange energy of the first case is 0.88 eV and lower than those for the second case (1.23 eV) and the third case (1.27 eV). The interchange of La with Ni or Co is very unfavorable. The high values of $E_{\mathrm{I}}(\mathrm{La} \leftrightarrow \mathrm{Ni})$ = 4.76 eV and $E_{\mathrm{I}}(\mathrm{La} \leftrightarrow \mathrm{Co})$ = 4.97 eV are due to the large size of La^{3+} (1.1172 Å) compared with Ni^{3+} (0.700 Å) and Co^{3+} (0.685 Å) [241].

To study the reason behind this finding as well as to understand the mechanism of interchange, we computed spin density differences and magnetic moments in bare and substituted NCM811 and LLZO (Figure 69). Calculated magnetic moments (μ) of 0.82, 0.10, and 2.75 for (most of) Ni, Co, and Mn cations indicate that these cations in bare NCM811 are in the oxidation states of 3^+, 3^+, and 4^+, respectively. Substitution of Ni^{3+} or Co^{3+} with Zr^{4+} (μ = 0.01 – 0.02) causes several Ni cations to undergo partial oxidation or reduction (Figure S 28). The recent simulation on bare bulk NCM811 indicates that the presence of Ni^{4+} in the delithiated cases can change the oxidation state of other Ni cations in their vicinity so that the overall electrostatic energy is reduced [214]. To better understand this phenomenon in the preset work, the interchange-induced change in μ of Ni cations were computed (Figure S 28). It was found out that for $Zr^{4+} \rightarrow Ni^{3+}$, five Ni and two Ni cations undergo large partial reductions and oxidations, respectively. The sum of changes in charges is –0.97, which can compensate for the arising one extra positive charge due to $Zr^{4+} \rightarrow Ni^{3+}$. For the case of $Zr^{4+} \rightarrow Co^{3+}$, four Ni and one Ni cations undergo a large partial reduction and an oxidation, respectively. The sum of changes in charge is –0.90, which can compensate the arising one extra positive charge due to $Zr^{4+} \rightarrow Co^{3+}$. On the other hand, to preserve the charge neutrality, both Ni and Co undergo an oxidation of $3^+ \rightarrow 4^+$ when they are substituted for Zr^{4+} in LLZO. The charge state of 4^+ on Ni can be clearly seen from the spin density difference (SDD) plot (Figure 69) where no SDD feature is observed on Ni. The appearance of an SDD feature on Co in LLZO confirms its oxidation. Due to the involvement of two simultaneous reactions, namely, reduction of Ni in NCM811 and oxidation

of Ni or Co in LLZO, the Zr ↔ Ni and Zr ↔ Co interchange energies are remarkably high. However, the $Zr^{4+} \rightarrow Mn^{4+}$ substitution does not lead to a considerable change in the oxidation state of the other ions in both NCM811 and LLZO. This results in a much lower interchange energy for $Zr^{4+} \rightarrow Mn^{4+}$. Thus, the substitution of Zr with Mn in LLZO might lead to the formation of La-based, Mn-rich secondary phases, such as $LaCo_{1-x}Mn_xO_3$, as experimentally detected for the Mn-rich NCM111 + LLZO:Ta mixtures. However, in the case of Ni-rich NCM811 + LLZO:Ta, such a secondary phase was not observed. This might be because the contents of Mn and Co are too low to form secondary phases detectable by XRD. Although from the thermodynamics point of view, the substitution of Zr with Ni in LLZO was calculated to be less likely than that with Mn, $La_2(Ni_{0.5}Li_{0.5})O_4$ was found as the secondary phase for both NCM compositions in contact with LLZO:Ta. A possible explanation for this result is the faster diffusion of Ni^{2+}, occupying the Li sites of the NCM lattice that might result in a kinetically preferred interchange between Ni^{2+} and Zr from LLZO. In particular, the amount of Ni^{2+} in the Li sites is higher in Ni-rich NCM811 (enhanced cation disorder, Table S 4) as compared to NCM111, which can explain the higher amount of $La_2(Ni_{0.5}Li_{0.5})O_4$ and the lower onset temperature for the secondary phase formation observed for NCM811 + LLZO:Ta. However, the amount of Ni^{2+} in the NCM lattice is limited, and therefore, the formation of $La_2(Ni_{0.5}Li_{0.5})O_4$ is self-constrained.

According to the ICSD database, atom–atom distances in $LaCo_{1-x}Mn_xO_3$ and $La_2(Ni_{0.5}Li_{0.5})O_4$ are not very different from those in cubic LLZO:Ta (see Table S 6). The formation of secondary phases can thus be explained by cation interchanges between the cathode and the solid-state electrolyte followed by a slight restructuring of the LLZO:Ta region where the diffused cation from the cathode is accommodated.

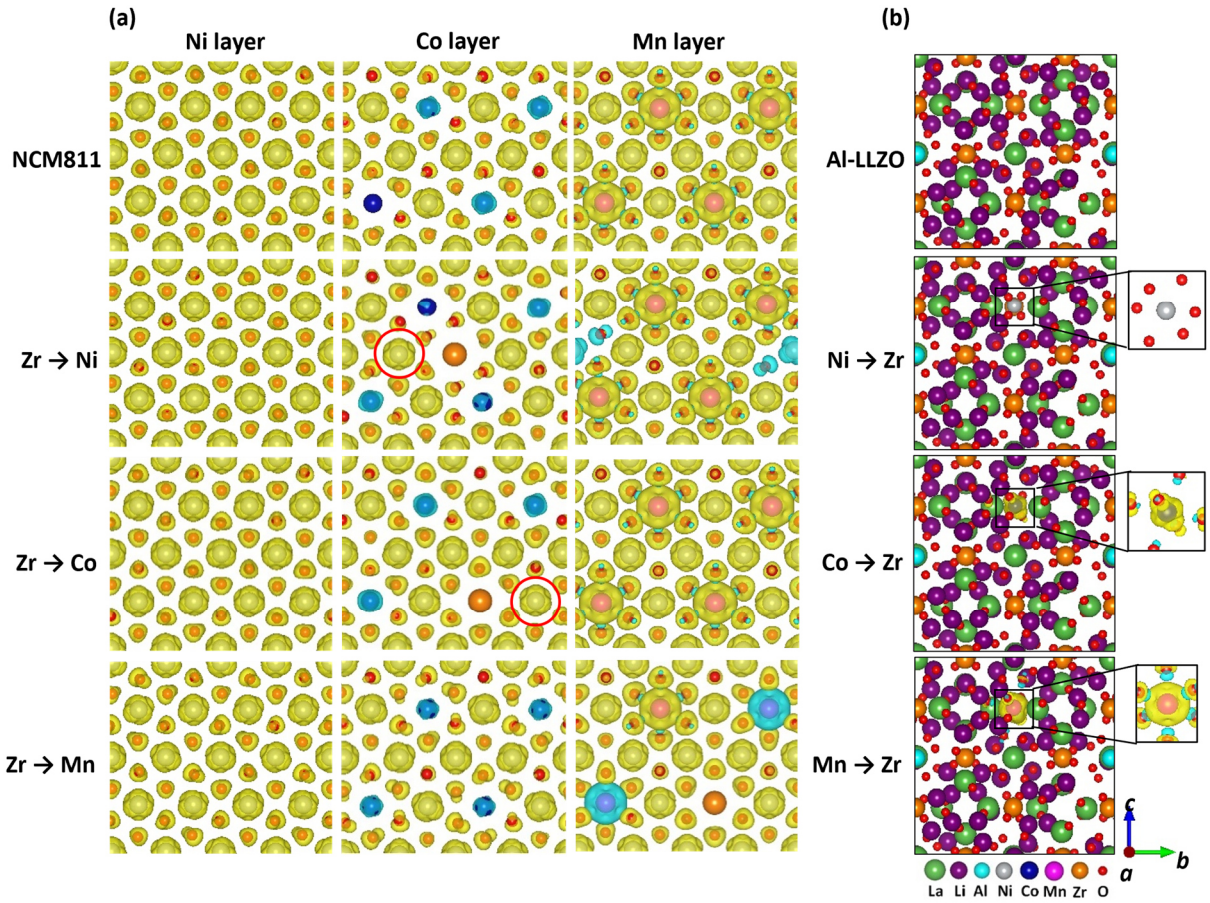

Figure 69: Spin density differences (SDDs) for (a) NCM811 without and with substitution of Ni, Co, and Mn with Zr as well as (b) LLZO:Al without and with substitution of Zr with Ni, Co, and Mn. The up- and down-spin electrons are in yellow and blue, respectively. An isosurface of 0.006 eV $Å^{-3}$ was used for all NCM811 structures as well as the zoomed-in image in LLZO. An isosurface of 0.01 eV $Å^{-3}$ was used for all LLZO structures. Reprinted with permission from ref. [161], Copyright 2022, American Chemical Society.

Experimental and computational investigations of the material compatibility render Ni-rich NCM811 more suited for the combination with LLZO:Ta in ceramic composite cathodes as compared to NCM111. NCM811, 2B-NCM811 and 2Ru-NCM811 form a lower amount of secondary phases than NCM111 during co-sintering with LLZO:Ta. The secondary phase formation for Ni-rich NCM811 seems to have a self-constrained character with the formation of isolated particles and areas of a clean NCM811/LLZO:Ta interface, although atomically resolved interface characterization using TEM would be required to confirm this hypothesis. Aligned with the experimental findings, DFT calculations clearly underline that a cathode material with a low Mn content like NCM811 is more suitable for the combination with LLZO:Ta since Mn is the most favorable TM ion for an interchange with Zr from LLZO:Ta. Furthermore, B doping of NCM811 does not reduce its thermal stability toward LLZO:Ta, which also validates the utilization of Li_3BO_3 (LBO) as a sintering aid.

8. Garnet-type all-solid-state battery with a NCM811 based composite cathode

This chapter is based on the following publication:

Christoph Roitzheim, Yoo Jung Sohn, Liang-Yin Kuo, Grit Häuschen, Markus Mann, Doris Sebold, Martin Finsterbusch, Payam Kaghazchi, Olivier Guillon, and Dina Fattakhova-Rohlfing, *ACS Appl. Energy Mater.* **2022**, 5, 6, 6913-6926.

Christoph Roitzheim synthesized the NCM and LBO powders, performed their characterization, analyzed all data, and wrote the manuscript with contributions from all authors. Yoo Jung Sohn conducted HT-XRD measurements and did the Rietveld refinements. Liang-Yin Kuo and Payam Kaghazchi performed the DFT calculations. Grit Häuschen synthesized and characterized LLZO:Ta. Markus Mann fitted and analyzed the EIS data. Doris Sebold took the SEM images and performed EDS analysis. Martin Finsterbusch, Payam Kaghazchi, Olivier Guillon, and Dina Fattakhova-Rohlfing initiated the idea, provided the resources, and supervised the work.

Link to the published article: https://doi.org/10.1021/acsaem.2c00533

Based on the results of the compatibility study described above (Chapter 7), NCM811 was selected as the most thermodynamically stable NCM composition to fabricate all-solid-state cells with LLZO:Ta as a solid-state electrolyte and LBO as a sintering additive. The cells were fabricated as described in Chapter 3.5.

After co-sintering at 750 °C, electrolyte supported half-cells consisting of a composite positive electrode on top of a dense LLZO:Ta separator were obtained. SEM images of a freshly prepared fracture surface (Figure 70a) show that the thickness of the composite cathode is 100 µm while the LLZO:Ta separator layer is 560 µm thick. BSE images of the composite cathode (Figure 70b) show the presence of three different phases, which were identified as NCM811 (grey region, I), LBO (dark region, II) and LLZO:Ta (bright region, III) using EDS point analysis (Figure 70b,c). No secondary phase formation could be detected at the interfaces between NCM811, LLZO:Ta and LBO within the composite cathode (Figure 70d) as well as at the interface between the composite cathode and the LLZO:Ta separator (Figure 70e). It can be seen that LBO fills the gaps between NCM811 and LLZ:Ta particles and acts as a sintering aid since LBO in its liquid phase infiltrates the empty space during sintering at 750 °C (T_m (LBO) = 690 °C, Figure S 31b). Furthermore, LBO enables a good adhesion between the composite positive electrode and the separator as visible in Figure 70e. Both effects are beneficial for the battery performance via decreasing interfacial resistance and enabling Li-ion

transfer between the separator and the composite cathode as well as via providing conducting pathways within the composite cathode.

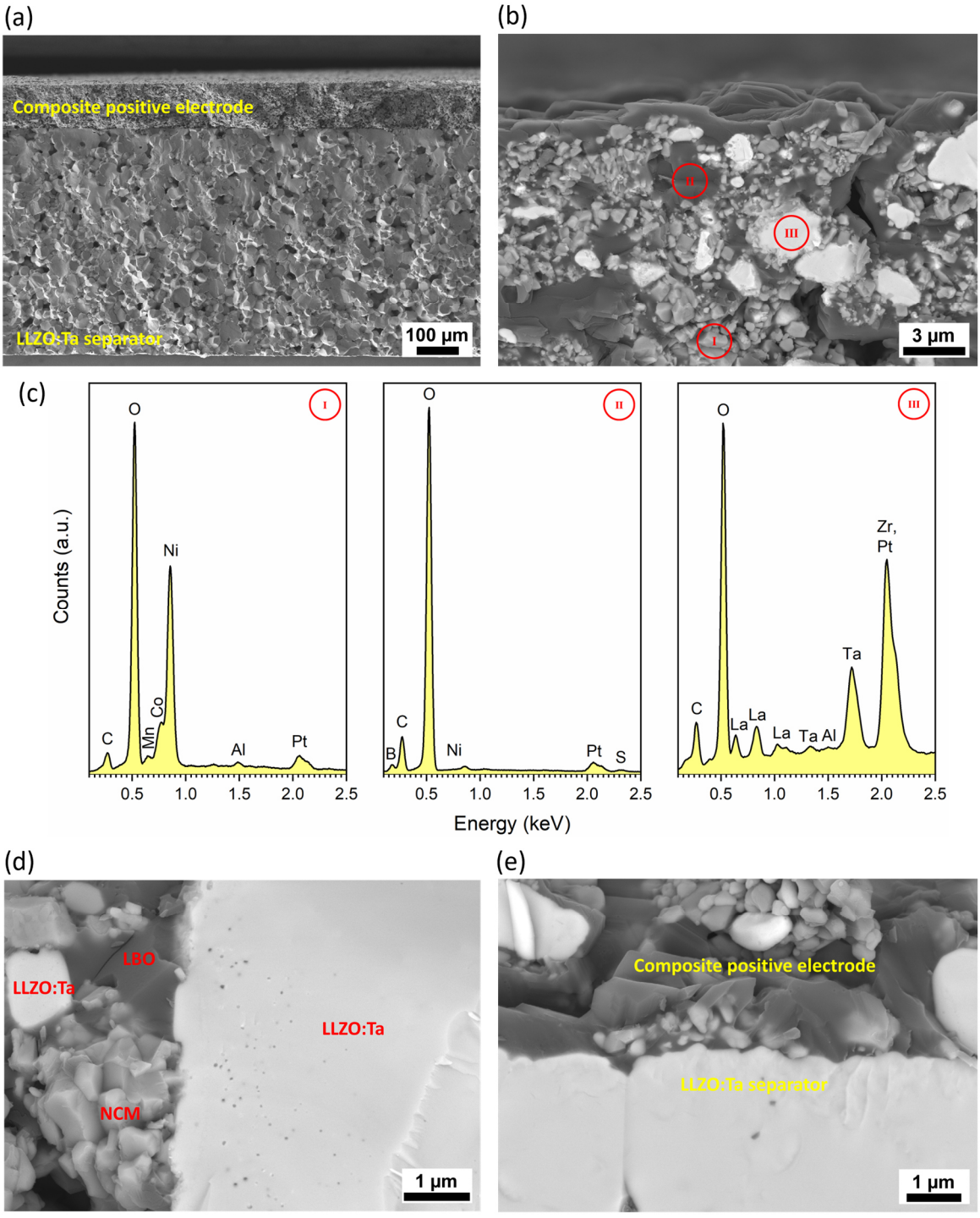

Figure 70: SEM images (8 kV) and EDS analysis of the fabricated half-cell. (a) Cross sectional secondary electron image of a fracture surface of the half-cell showing the composite cathode on top of the LLZO:Ta separator. (b) BSE image of the composite cathode showing the phase distribution. (c) EDS spectra of points marked in (b). (d) Higher magnification BSE image at the interface between NCM811, LBO, and LLZO:Ta within the composite cathode and (e) at the interface between the composite cathode and the separator. For all SEM images, the corresponding secondary electron or BSE images are shown in Figure S 16. Reprinted with permission from ref. [161], Copyright 2022, American Chemical Society.

SEM analysis (Figure 70b) demonstrates that all three components are present on the composite cathode surface (Figure S 16e,f) and can be therefore contacted to a current collector (gold layer) during cell assembly.

The XRD pattern (Figure 71) of the composite positive electrode shows the presence of LLZO:Ta and NCM811 as the main phases as well as reflections (labeled with #) of LBO used as a sintering aid. In addition to the main phases, reflections of another phase (labeled with *) were detected, which are in good agreement with the XRD pattern of the $Li_{2.3-x}C_{0.7+x}B_{0.3-x}O_3$ interphase reported by F. Han *et al.*[144]. It is assumed that $Li_{2+y}C_{1-y}B_yO_3$ (LCBO) is formed *in-situ* during co-sintering at 750 °C via a possible reaction between the Li_3BO_3 sintering additive and the Li_2CO_3 impurity on the LLZO:Ta and NCM surface. The formation of an LCBO interface can be beneficial to the cell performance since LCBO exhibits significantly higher Li-ion conductivity ($Li_{2.3}C_{0.7}B_{0.3}O_3$ with ~ 10^{-5} S cm^{-1} at 100 °C)[144] than Li_2CO_3. The utilization of LBO as a sintering additive does not avoid the secondary phase formation since a trace amount of the side phase (labeled with +), structurally similar to $La_2(Ni_{0.5}Li_{0.5})O_4$ described above, was detected in the XRD pattern, although this phase was not observed in the SEM images (Figure 70).

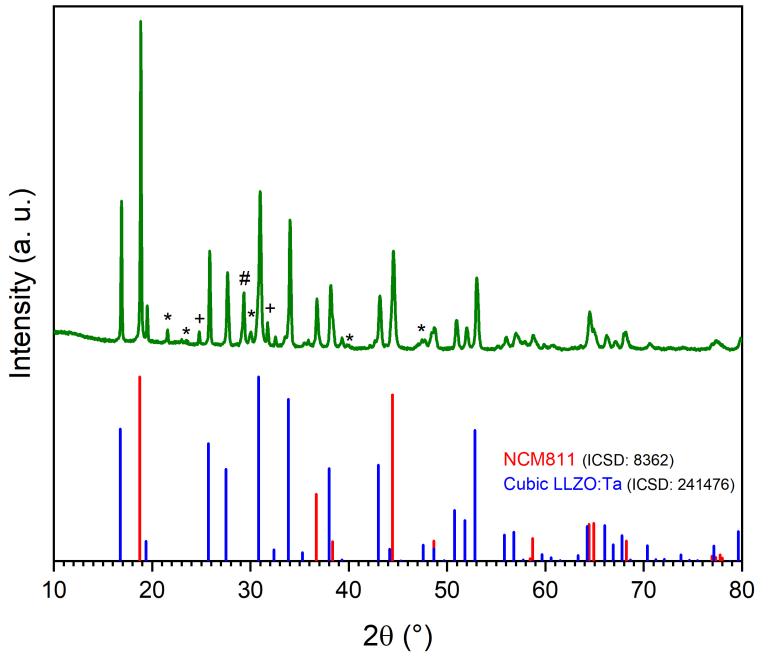

Figure 71: XRD pattern of the composite positive electrode sintered at 750 °C. The reflections of further phases, in addition to LLZO:Ta and NCM, are marked with # for Li_3BO_3 (LBO), * for $Li_{2+y}C_{1-y}B_yO_3$ (LCBO), and + for $La_2Li_{0.5}Ni_{0.5}O_4$. Reprinted with permission from ref. [161], Copyright 2022, American Chemical Society.

For the full-cell assembly, a Li metal anode was attached to the LLZO:Ta separator of a ceramic half-cell. The active material loading (NCM811) in the co-sintered composite cathode was 5.9 mg (5.7 mg cm^{-2}). The battery was cycled at 60 °C between 3.0 and 4.2 V vs. Li/Li^+ at

40 µA cm^{-2} (0.06 C). In the first cycle, the fully inorganic battery delivered a specific discharge capacity of 120 mAh g^{-1} and a specific areal capacity of 0.7 mAh cm^{-2} (Figure 72a), which is one of the best performances reported for this cell configuration so far. The Coulombic efficiency increases strongly from 84 % in the first cycle to values between 97 and 99 % for the further cycles (Figure 72b). The only comparable all-solid-state cell with an NCM active material was reported by D. Wang *et al.*[147] who obtained 106 mAh g^{-1} for a cell with a Li metal anode, a gel polymer electrolyte, an LLZO:Ta separator, and a co-sintered NCM622/LLZO:Ta/LBO cathode (3.0 – 4.2 V, 0.05 C) with an active material loading of 2 mg. A slightly higher gravimetric capacity of 186 mAh g^{-1} was achieved by S. Ohta *et al.*[146] using NCM111 as a CAM but for much lower active material loadings of only 2.8 mg cm^{-2} and cycling in a broader potential range at lower rates (2.5 – 4.6 V, 0.02 C) as compared to our cell. Additionally, the cathode consisted only of NCM and LBO and was not mixed with LLZO, which limits the loading due to the lower ionic conductivity of LBO compared to LLZO.

The high gravimetric capacity in the first cycle obtained for our cell demonstrates that the processing-induced decomposition of LLZO and NCM can be sufficiently mitigated via a choice of the suitable NCM composition and that the fabrication of co-sintered NCM-containing garnet-based cathode layers is generally possible. The remaining challenge is however the cycling stability of such cathodes, which still remains too low for the practical application. For our cell, continuous capacity fading was observed during prolonged cycling (Figure 72a,b), whereby a capacity retention of 59 % was obtained after 30 cycles. The observed capacity fading is consistent with the degradation behavior observed by other groups for comparable ceramic ASBs [121, 147].

To assess the contribution of different processes to the observed capacity degradation, electrochemical impedance spectroscopy (EIS) was performed before and after 30 cycles in the charged state (4.2 V) at 60 °C (Figure 72c). The Nyquist plots in Figure 72c show a depressed semicircle, which is composed of two overlapping semicircles in the high-frequency (MHz) and medium-frequency range (kHz). The tail in the low-frequency range (Hz) is characteristic of the Li^+ diffusion in NCM811. The EIS data were fitted with an equivalent circuit shown in Figure 72d, where R represents an ohmic resistance, L an inductance, and CPE a constant phase element. The fitted capacities cannot be directly assigned to possible contributions of the single interfaces (NCM/LLZO:Ta, NCM/LBO, and LLZO:Ta/LBO) or grain boundaries [254]. Therefore, only the total impedance (sum of *R0*, *R1*, and *R2*) of the cell before and after cycling is compared. The total cell impedance has more than doubled from 374 to 776 Ω after 30 cycles (Figure 72c,d). The strongly increasing cell impedance during cycling is the most probable

reason for the observed capacity degradation of the battery. Interfacial degradation at the Li metal/LLZO:Ta and LLZO:Ta/NCM811 interfaces and mechanical degradation in the form of microcrack formation within the composite cathode due to the volume expansion of NCM811 during charging/discharging are possible reasons for the increased resistances after cycling. Although other groups found microcrack formation during cycling as the main reason for the capacity loss [121, 147], no severe microcracks were found for our cell after 30 cycles (Figure S 17). Therefore, it can be suggested that the electrochemical stability of LLZO:Ta and/or of the LLZO:Ta/NCM interface is the reason for the observed degradation. A detailed understanding of the interfacial behavior during electrochemical operation will be the focus of the future work to improve the cycling stability of such fully ceramic ASBs.

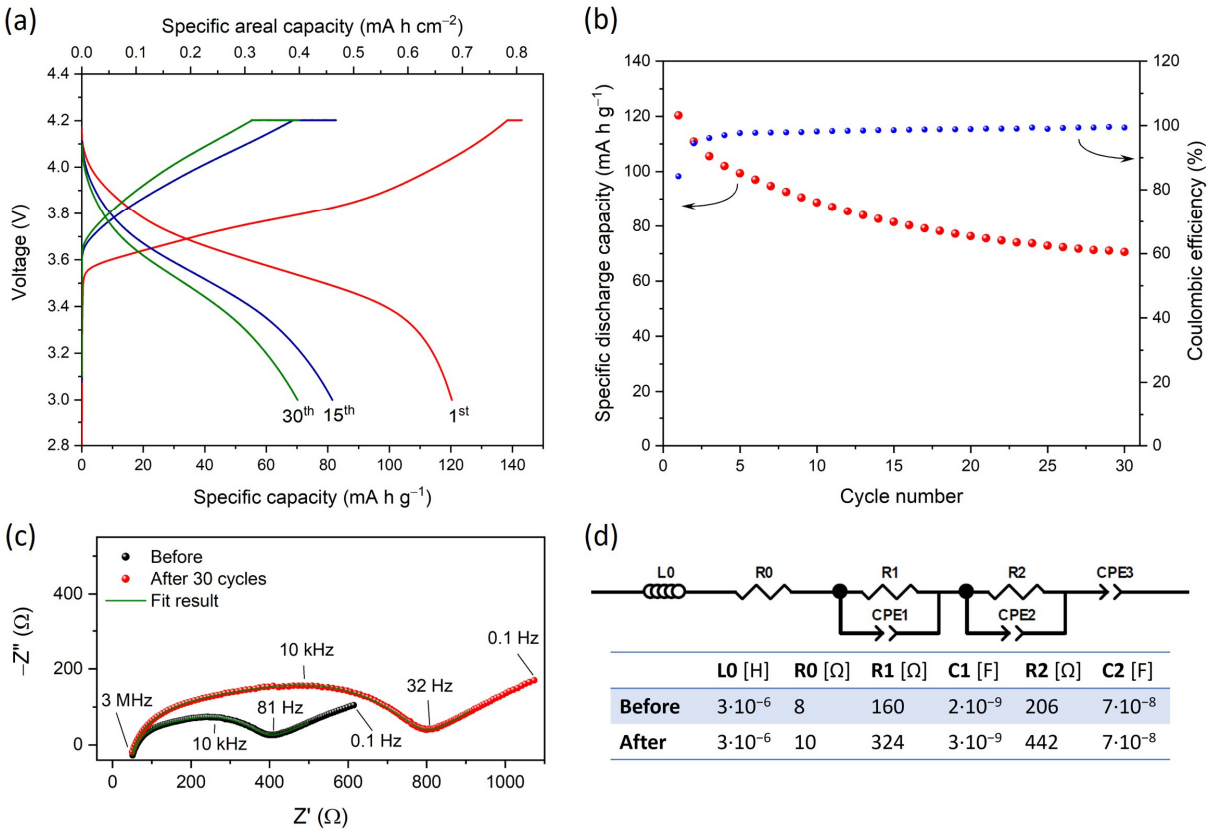

	L0 [H]	R0 [Ω]	R1 [Ω]	C1 [F]	R2 [Ω]	C2 [F]
Before	$3 \cdot 10^{-6}$	8	160	$2 \cdot 10^{-9}$	206	$7 \cdot 10^{-8}$
After	$3 \cdot 10^{-6}$	10	324	$3 \cdot 10^{-9}$	442	$7 \cdot 10^{-8}$

Figure 72: Electrochemical performance of the ASB (Li/LLZO:Ta/NCM811+LLZO:Ta+LBO) at 60 °C. (a) Charge-discharge profiles of the 1st, 15th, and 30th cycle, (b) specific discharge capacity and Coulombic efficiency for long-term cycling, (c) Nyquist plots of EIS spectra before and after 30 cycles measured at 4.2 V, and (d) equivalent circuit and fitting results of the impedance spectra. Reprinted with permission from ref. [161], Copyright 2022, American Chemical Society.

In summary, a fully inorganic ASB based on a Li metal anode, a LLZO:Ta separator, and a composite cathode consisting of Ni-rich NCM811, LBO, and LLZO:Ta was manufactured. The XRD analysis of the composite cathode showed that the surface impurity Li_2CO_3 reacts with LBO during co-sintering forming a Li-ion conducting LCBO interphase which is highly desired

as it might be helpful to overcome the drawback of the air sensitive materials LLZO:Ta and NCM811. However, in general the amount of LBO in the composite positive electrode should be reduced as much as possible, due to its low conductivity and electrochemical inactivity. Most promising for application seems a thin coating of LBO on the NCM and LLZO:Ta particles prior to cathode fabrication. Nevertheless, the here demonstrated ceramic ASB exhibits one of the highest active material loading (5.7 mg cm^{-2}) reported so far and delivers significant higher specific areal capacities (0.7 mAh cm^{-2}) than comparable ceramic ASBs.

9. Conclusions and outlook

The aim of this thesis was the synthesis of optimized cathode materials for fully inorganic, garnet-type ASBs based on a composite cathode consisting of LLZO:Ta and a cathode active material. Different NCM compositions, namely, NCM111 and NCM811 as well as doping of both systems with boron and ruthenium was investigated. For the synthesis of pristine, B- and Ru-doped NCM a hydroxide co-precipitation route on a laboratory scale was used. The batch synthesis in a glass flask was successfully applied to obtain phase pure CAMs with a hexagonal layered structure. Morphology characterization by SEM showed that the synthesized powders consist of sphere-like secondary particles, which are composed of nano-sized primary particles. In addition to the calcination temperature, the primary particle shape strongly depends on the TM composition in NCM, thus for NCM111 thin flake-shaped and for NCM811 cuboidal primary particles were obtained.

The doped CAMs were analyzed to verify the incorporation of the dopant into the NCM lattice and to localize it in the NCM particles. In the case of B-doped NCM811, the determined lattice parameters based on XRD were not strongly influenced by B doping, but an increased cation disorder was found with the increasing boron content. A theoretical study based on DFT calculation showed that a lattice expansion due to the incorporation of boron is suppressed by the increased cation disorder. This finding demonstrates that an incorporation of boron into the NCM811 lattice is possible even thought, no lattice expansion is observed. Up to now, the precise location of the light element boron in NCM as well as the experimental proof of its incorporation was not reported at all. Therefore, in this thesis, 2 mol% B-doped NCM811 was used as model compound to experimentally detect, quantify, and localize boron by ion beam analysis and TOF-SIMS. By NRA (3 ± 1) mol% boron was detected and located to be surface enriched. The successful detection, localization, and quantification of boron by NRA was also demonstrated for 2 mol% B-doped NCM111. Thus, NRA turned out as suitable method for the light element detection and quantification in CAMs with depth resolution. TOF-SIMS analysis of 2B-NCM811 verified a boron enrichment on the agglomerate surface but, more importantly, also a significant, high, and constant boron concentration in the bulk of the primary particles was found. As a result of this thesis, it was experimentally proven that boron tends to segregate on the surface, as predicted in previous publications, but it also incorporates into the primary particles core. Furthermore, it was demonstrated that the incorporation of boron into the lattice of NCM111 and NCM811 leads to an alteration of the morphology, but in contrast to the previous reports, the B-doped secondary particles did not show the expected alignment of the

primary particles along the radial direction. It is therefore assumed that not only the B doping but a fine tuning of the synthesis conditions, including the pH value, the ammonia concentration, and the reactor type are required to achieve a significant change in the particle alignment. The electrochemical activity of pristine and B-doped NCM was proven in cells based on a liquid electrolyte. Independent on the TM composition, B doping shows a detrimental effect on the electrochemical performance at high C-rates which can be explained by enhanced cation disorder, reduced electronic conductivity, and hindered Li-ion mobility due to the B doping. During the long-term cycling at 0.5 C, similar capacities were obtained for both pristine NCM111 and 2B-NCM111 but in the case of Ni-rich NCM811, the B doping results in a significantly improved capacity retention during the long-term cycling. Since the pristine NCM111 itself is well known for its small volume change, high stability, and excellent capacity retention during the long-term cycling, the modification by B doping does not further improve the capacity retention. However, in the case of the less stable Ni-rich NCM811, the formation of a protective boron enriched surface layer strongly improves the cycling stability. The findings thus show that the boron localization both in the bulk and at the surface leads to two different effects on the atomic and microstructural scale. In the bulk, the incorporation of boron does not lead to a significant lattice expansion but shows a detrimental effect on the electrochemical performance at high C-rates and increases the cation disorder. In contrast to this, the boron located on the agglomerate surface leads to a decrease in cation disorder, avoids phase transition to rock-salt structure, and thus might have beneficial effects on the surface properties, resulting in a significantly improved capacity retention during the long-term cycling of B-doped NCM811. As a further conclusion of this thesis, the widely known microstructure alteration toward radially aligned primary particles by B doping of Ni-rich NCM is not the only reason for the optimized electrochemical performance. Based on the results of this work, the formation of a very thin boron containing surface coating, is an additional explanation since surface coatings are well known to enhance the performance of Ni-rich CAM.

In addition to the B-doped NCM811, also Ru-doped NCM811 was investigated as possible CAM for ASBs. This thesis showed that Ru successfully incorporated into the NCM811 lattice and results in a lattice expansion, an enhanced cation disorder, smaller primary particles, and Li loss. In comparison to the B^{3+} in B-doped NCM, ruthenium was found to be present as Ru^{5+} in Ru-doped NCM811. Due to the high oxidation state, the charge balancing causes an increase in cation disorder and a Li migration to the particle surface. Additional lithium on the particle surface enhances the formation of highly resistive surface impurities. Furthermore, the high Ru–O bond dissociation energy results in a reduced Li-ion mobility and the increased number

of grain boundaries due to the smaller primary particle size further negatively affects the Li-ion conductivity. Thus, the electrochemical performance of 2Ru-NCM811 in cells based on a liquid electrolyte suffers from a high charge-transfer resistance and low charge/discharge capacities also at low C-rates and during the long-term cycling. The main difference compared to B doping is that Ru doping does not automatically result in a ruthenium enrichment on the secondary particle surface. The localization of ruthenium by TOF-SIMS showed a constant Ru concentration on the secondary particles surface as well as in the bulk of the primary particles. Therefore, no protecting Ru containing surface coating is achieved by Ru doping of NCM811. In the future work, the impact of Ru doping on the gravimetric capacity needs to be considered by investigating lower dopant concentrations. Additionally, Ni-rich NCM with Ru containing coatings, like RuO_2, will be investigated as CAM for ASBs since RuO_2 additionally offers electronic conductivity, so that a high-rate performance as well as an improved capacity retention due to the protecting effect of the coating might be achieved.

The powder morphology and electrochemical performance of the NCM powders obtained by the batch synthesis within this thesis could not compete with commercial powders obtained by a continuous co-precipitation. The ideal crystallization and agglomeration conditions realized during the large scale, industrial CAM production which result in ideally spherical secondary particles with outstanding high electrochemical performance, are not accessible by the small-scale batch process. Therefore, a CTFR was purchased for the continuous laboratory scale synthesis of spherical NCM particles. The ideal synthesis conditions in this reactor, leading to NCM with a strongly improved morphology and electrochemical performance were proven in this thesis and therefore the CTFR will be used as standard for the NCM synthesis in the future. In addition, it would also be interesting to investigate the effect of B doping on the retention of the aligned plate-like primary particles during calcination of the hydroxide precursor synthesized by the CTFR.

Finally, the thermal compatibility between the garnet-type solid state electrolyte (LLZO:Ta) and the different CAMs synthesized within this thesis was investigated. No exo- or endothermic reactions, indicating a severe reaction between NCM and LLZO:Ta, were detected, and their thermal behavior is only governed by the air sensitivity of the samples themselves. This result was confirmed by *in-situ* HT-XRD, showing the stability of the main phases NCM and LLZO:Ta up to 1000 °C. However, small amounts of secondary phases were observed during co-sintering, whereby the NCM composition and doping strongly affect the nature and the amount of the formed secondary phase. Based on Rietveld refinement of the XRD pattern obtained at 800 °C, in general, two secondary phases ($LaCo_{1-x}Mn_xO_3$ and $La_2(Ni_{0.5}Li_{0.5})O_4$)

were identified. For NCM111 and 2B-NCM111 mixed with LLZO:Ta, both secondary phases were found, and more importantly, B doping strongly enhanced the formation of $LaCo_{1-x}Mn_xO_3$. In contrast to this, for Ni-rich NCM811 (pristine and 2B-NCM811), only 2 wt.% $La_2(Ni_{0.5}Li_{0.5})O_4$ was detected, and B doping did not influence the secondary phase formation. By Ru doping of NCM811, the secondary phase formation was slightly inhibited to 1 wt.%. The formation of $La_2(Ni_{0.5}Li_{0.5})O_4$ was found to occur in a self-constrained way since the corresponding reflection intensity does not further increase for longer co-sintering times and higher temperatures. SEM and EDS analyses indicate that $La_2(Ni_{0.5}Li_{0.5})O_4$ forms as a localized phase, and probably, no homogeneous, resistive interlayers were formed at the NCM811/LLZO:Ta interface. $LaCo_{1-x}Mn_xO_3$ was not detectable in all samples by SEM and EDS analyses. Aligned with the experimental findings, DFT calculation clearly underlined that a cathode material with low Mn content like NCM811 is more suitable for the combination with LLZO:Ta since Mn is the most favorable transition metal ion to undergo an interchange with Zr form LLZO:Ta. This interchange and secondary phase formation could not be hindered by B and Ru doping, nor by the boron enrichment on the surface of the secondary particles. Thus, doping is not the right way to enhance the thermodynamic stability of NCM/LLZO:Ta mixtures during co-sintering. Nevertheless, based on the experimental and theoretical results, the most important conclusion of the compatibility study is that the Ni-rich NCM811 is the most promising CAM for the combination with garnet-type LLZO:Ta in composite cathodes of ceramic ASBs. Further advantages of NCM811 are higher electronic conductivity and higher theoretical capacity compared to NCM111.

Furthermore, the sintering temperature of garnet-type ceramic ASBs can be reduced to 750 °C by using LBO as a sintering aid since the presence of boron did not negatively influence the secondary phase formation in the case of NCM811. Therefore, a fully inorganic ASB based on a Li metal anode, a LLZO:Ta separator, and a composite cathode consisting of Ni-rich NCM811, LBO, and LLZO:Ta was manufactured. The XRD analysis of this composite cathode showed that the surface impurity Li_2CO_3 reacts with LBO during co-sintering forming a Li-ion conducting LCBO interphase, which is highly desired as it might be helpful to overcome the drawback of the air sensitive materials LLZO:Ta and NCM811. The here demonstrated ceramic ASB exhibits one of the highest active material loadings (5.7 mg cm^{-2}) reported so far and delivers a significantly higher specific areal capacity (0.7 mAh cm^{-2}) than those of comparable ceramic ASBs based on LLZO:Ta as an SSE and NCM as a CAM.

The development of the garnet-type ASBs based on NCM811 as CAM will be continued within the future work. First, the impact of the secondary phase $La_2(Ni_{0.5}Li_{0.5})O_4$ on the

electrochemical performance of the ASB needs to be investigated. Second, an optimization of the composite cathode composition is intended, especially the amount of LBO in the composite cathode should be reduced as much as possible due to its low conductivity and electrochemical inactivity. The most promising for application seems a thin coating of LBO on NCM and LLZO:Ta particles prior to cathode fabrication. Such a coating has ideally two effects, namely, serving as a sintering aid and as a protection layer to avoid the direct contact between the CAM and the SSE. Third, the use of single-crystalline instead of poly-crystalline CAMs in the composite positive electrode is promising since the detrimental secondary particle fracture due to volume change during cycling can be reduced. Negligible cracking in the case of a single-crystalline CAM allows to maintain a proper contact between the cathode material and the SSE in the composite cathode and thus leads to improved capacity retention during the long-term cycling. Fourth, to further enhance the energy density of the ASBs, the thickness but at the same time also the electronic conductivity of the composite cathode needs to be enhanced which can be either realized by using a suitable conducting additive or by enhancing the electronic conductivity of the CAM itself. An enhanced electronic conductivity of NCM, can be for example realized by a RuO_2 coating that is also expected to enhance the thermal compatibility between the CAM and the SSE during co-sintering.

List of abbreviations

ASB; ASBs	All-solid-state battery; All-solid-state batteries
BE	Binding energy
BET	Brunauer-Emett-Teller
BSE; BSEs	Backscattered electron; backscattered electrons
CAM; CAMs	Cathode active material; Cathode active materials
cc	Constant current
CE	Coulombic efficiency
CG	Concentration-gradient
CPE	Constant phase element
CS	Core–shell
CSTR	Continuous stirred tank reactor
CTFR	Couette-Taylor-Flow-Reactor
CV	Cyclic voltammetry
cv	Constant voltage
DFT	Density functional theory
DMC	Dimethyl carbonate
DSC	Differential scanning calorimetry
DTA	Differential thermal analysis
EC	Ethylene carbonate
EDS	Energy dispersive X-ray spectroscopy
EELS	Electron energy loss spectroscopy
EIS	Electrochemical impedance spectroscopy
EMC	Ethylmethyl carbonate
EPMA	Electron probe microanalysis
EVs	Electric vehicles
FCG	Full-concentration-gradient
FIB	Focused ion beam
GC	Gas chromatography
GCD	Galvanostatic charge-discharge
GPE	Gel polymer electrolyte
HAADF	High-angle annular dark-field mode
HRTEM	High-resolution TEM

HT-XRD	*In-situ* high temperature XRD
IBM	Ion-beam-microscopy
IL	Ionic liquid
K_{sp}	Solubility product constant
LATP	$Li_{1.4}Al_{0.4}Ti_{1.6}(PO_4)_3$
LBO	Li_3BO_3
LCO	$LiCoO_2$
LD	Laser diffraction
LFP	$LiFePO_4$
LIB; LIBs	Lithium-ion battery; Lithium-ion batteries
LiPON	Lithium phosphorus oxynitride
LLZO	$Li_7La_3Zr_2O_{12}$
LLZO:Ta	$Li_{6.45}Al_{0.05}La_3Zr_{1.6}Ta_{0.4}O_{12}$
LMO	$LiMn_2O_4$
LNO	$LiNiO_2$
LTMO	$Li[Ti_{0.1}Mn_{0.9}]_2O_4$
MS	Mass spectrometry
NASICON	Sodium super ionic conductor
NCA	$Li[Ni_{0.8}Co_{0.15}Al_{0.05}]O_2$
NCM	$Li[Ni_{1-x-y}Co_xMn_y]O_2$
NCM111	$LiNi_{1/3}Co_{1/3}Mn_{1/3}O_2$
NCM424	$LiNi_{0.4}Co_{0.2}Mn_{0.4}O_2$
NCM523	$Li[Ni_{0.5}Co_{0.2}Mn_{0.3}]O_2$
NCM622	$Li[Ni_{0.6}Co_{0.2}Mn_{0.2}]O_2$
NCM721	$Li[Ni_{0.7}Co_{0.2}Mn_{0.1}]O_2$
NCM811	$Li[Ni_{0.8}Co_{0.1}Mn_{0.1}]O_2$
NCM85	$LiNi_{0.85}Co_{0.075}Mn_{0.075}O_2$
NCM90	$Li[Ni_{0.9}Co_{0.05}Mn_{0.05}]O_2$
NCM95	$LiNi_{0.95}Co_{0.025}Mn_{0.025}O_2$
NCMA	$Li[Ni_{0.89}Co_{0.05}Mn_{0.05}Al_{0.01}]O_2$
NMP	N-methyl-2-pyrolidone
PAW	Projector Augmented-Wave
PBE	Perdew-Burke-Ernzerhof
PCE	Plastic crystal electrolyte

PEO	Polyethylene oxide
PSD	Particle size distribution
PVDF	Poly(vinylidene fluoride)
SAED	Selected area electron diffraction
SCAN	Strongly constrained and appropriately normed
SE; SEs	Secondary electron; secondary electrons
SEI	Solid electrolyte interphase
SEM	Scanning electron microscopy
SN	Succinonitrile
SSE	Solid-state electrolyte
SSR	Solid-state reaction
STEM	Scanning transmission electron microscopy
STIM	Scanning-transmission-ion-microscopy
TA	Thermal analysis
TEM	Transmission electron microscopy
TG	Thermogravimetry
thio-LISICON	Lithium super ionic conductors
TM	Transition metal
TOF-SIMS	Time-of-flight secondary ion mass spectrometry
TSFCG	Two-sloped full concentration gradient
TSFCG65	$Li[Ni_{0.65}Co_{0.13}Mn_{0.22}]O_2$
TSFCG-Al	$Li[Ni_{0.84}Co_{0.06}Mn_{0.09}Al_{0.01}]O_2$
VASP	Vienna Ab Initio Simulation Package
VC	Vinylene carbonate
XC	Exchange-correlation
XPS	X-ray photoelectron spectroscopy
XRD	X-ray diffraction

References

[1] BMWi, For a future of green energy. http://www.bmwi.de/Redaktion/EN/Dossier/renewable-energy.html, **2019**, Accessed: 2019-02-13.

[2] FachagenturNachwachsendeRohstoffee.V.; (FNR), Brutto-Stromerzeugung. https://factsandfigures.fnr.de/bioenergy/energetic-figures, **2021**, Accessed: 2021-10-13.

[3] Rahman, M. A.; Wang, X.; Wen, C., High Energy Density Metal-Air Batteries: A Review. *Journal of The Electrochemical Society* **2013,** 160, (10), A1759-A1771.

[4] Myung, S.-T.; Amine, K.; Sun, Y.-K., Nanostructured cathode materials for rechargeable lithium batteries. *Journal of Power Sources* **2015,** 283, (0), 219-236.

[5] Wang, Y.; He, P.; Zhou, H., Olivine LiFePO4: development and future. *Energy & Environmental Science* **2011,** 4, (3), 805-817.

[6] Pitchai, R.; Thavasi, V.; Mhaisalkar, S. G.; Ramakrishna, S., Nanostructured cathode materials: a key for better performance in Li-ion batteries. *Journal of Materials Chemistry* **2011,** 21, (30), 11040-11051.

[7] Cheng, F.; Chen, J., Metal-air batteries: from oxygen reduction electrochemistry to cathode catalysts. *Chemical Society Reviews* **2012,** 41, (6), 2172-2192.

[8] Roitzheim, C. Electrochemical characterization of non-aqueous Si–air batteries under intermittent operating conditions. Master thesis, RWTH Aachen, **2018**.

[9] Steilen, M.; Jörissen, L., Chapter 10 - Hydrogen Conversion into Electricity and Thermal Energy by Fuel Cells: Use of H2-Systems and Batteries. In *Electrochemical Energy Storage for Renewable Sources and Grid Balancing*, Moseley, P. T.; Garche, J., Eds. Elsevier: Amsterdam, **2015**; pp 143-158.

[10] Zubi, G.; Dufo-López, R.; Carvalho, M.; Pasaoglu, G., The lithium-ion battery: State of the art and future perspectives. *Renewable and Sustainable Energy Reviews* **2018,** 89, 292-308.

[11] Dehghani-Sanij, A.; Tharumalingam, E.; Dusseault, M.; Fraser, R., Study of energy storage systems and environmental challenges of batteries. *Renewable and Sustainable Energy Reviews* **2019,** 104, 192-208.

[12] Aneke, M.; Wang, M., Energy storage technologies and real life applications – A state of the art review. *Applied Energy* **2016,** 179, 350-377.

[13] Volta, A., On the Electricity Excited by the Mere Contact of Conducting Substances of Different Kinds. *Abstracts of the Papers Printed in the Philosophical Transactions of the Royal Society of London* **1800,** 1, 27-29.

[14] Goodenough, J. B.; Park, K.-S., The Li-Ion Rechargeable Battery: A Perspective. *Journal of the American Chemical Society* **2013,** 135, (4), 1167-1176.

[15] Linden, D.; Reddy, T. B., Handbook of Batteries. 3rd ed.; McGraw-Hill: **2002**.

[16] Cohn, G.; Starosvetsky, D.; Hagiwara, R.; Macdonald, D. D.; Ein-Eli, Y., Silicon–air batteries. *Electrochemistry Communications* **2009,** 11, (10), 1916-1918.

[17] Durmus, Y. E.; Roitzheim, C.; Tempel, H.; Hausen, F.; Ein-Eli, Y.; Kungl, H.; Eichel, R.-A., Analysis on discharge behavior and performance of As- and B-doped silicon anodes in non-aqueous Si–air batteries under pulsed discharge operation. *Journal of Applied Electrochemistry* **2020,** 50, (1), 93-109.

[18] Zhang, C.; Wei, Y.-L.; Cao, P.-F.; Lin, M.-C., Energy storage system: Current studies on batteries and power condition system. *Renewable and Sustainable Energy Reviews* **2018,** 82, 3091-3106.

[19] Whittingham, M. S., Electrical Energy Storage and Intercalation Chemistry. *Science* **1976,** 192, (4244), 1126-1127.

[20] Deng, D., Li-ion batteries: basics, progress, and challenges. *Energy Science & Engineering* **2015,** 3, (5), 385-418.

[21] Tarascon, J. M.; Armand, M., Issues and challenges facing rechargeable lithium batteries. *Nature* **2001,** 414, (6861), 359-367.

[22] Kamat, P. V., Lithium-Ion Batteries and Beyond: Celebrating the 2019 Nobel Prize in Chemistry – A Virtual Issue. *ACS Energy Letters* **2019,** 4, (11), 2757-2759.

[23] Reddy, M. V.; Mauger, A.; Julien, C. M.; Paolella, A.; Zaghib, K., Brief History of Early Lithium-Battery Development. *Materials* **2020,** 13, (8), 1884.

[24] Noh, H.-J.; Youn, S.; Yoon, C. S.; Sun, Y.-K., Comparison of the structural and electrochemical properties of layered $Li[Ni_xCo_yMn_z]O_2$ (x = 1/3, 0.5, 0.6, 0.7, 0.8 and 0.85) cathode material for lithium-ion batteries. *Journal of Power Sources* **2013,** 233, 121-130.

[25] Campbell, I. D.; Gopalakrishnan, K.; Marinescu, M.; Torchio, M.; Offer, G. J.; Raimondo, D., Optimising lithium-ion cell design for plug-in hybrid and battery electric vehicles. *Journal of Energy Storage* **2019,** 22, 228-238.

[26] Warner, J. T., The handbook of lithium-ion battery pack design: chemistry, components, types and terminology. Elsevier: **2015**.

[27] Cheng, H.; Shapter, J. G.; Li, Y.; Gao, G., Recent progress of advanced anode materials of lithium-ion batteries. *Journal of Energy Chemistry* **2021,** 57, 451-468.

[28] Dühnen, S.; Betz, J.; Kolek, M.; Schmuch, R.; Winter, M.; Placke, T., Toward Green Battery Cells: Perspective on Materials and Technologies. *Small Methods* **2020,** 4, (7), 2000039.

[29] Whittingham, M. S., Lithium Batteries and Cathode Materials. *Chemical Reviews* **2004,** 104, (10), 4271-4302.

[30] Wang, L.; Chen, B.; Ma, J.; Cui, G.; Chen, L., Reviving lithium cobalt oxide-based lithium secondary batteries-toward a higher energy density. *Chemical Society Reviews* **2018,** 47, (17), 6505-6602.

[31] Yao, X.; Huang, B.; Yin, J.; Peng, G.; Huang, Z.; Gao, C.; Liu, D.; Xu, X., All-solid-state lithium batteries with inorganic solid electrolytes: Review of fundamental science. *Chinese Physics B* **2015,** 25, (1), 018802.

[32] Mizushima, K.; Jones, P. C.; Wiseman, P. J.; Goodenough, J. B., Li_xCoO_2 (0<x<-1): A new cathode material for batteries of high energy density. *Materials Research Bulletin* **1980,** 15, (6), 783-789.

[33] Judez, X.; Eshetu, G. G.; Li, C.; Rodriguez-Martinez, L. M.; Zhang, H.; Armand, M., Opportunities for Rechargeable Solid-State Batteries Based on Li-Intercalation Cathodes. *Joule* **2018,** 2, (11), 2208-2224.

[34] Padhi, A. K.; Nanjundaswamy, K. S.; Goodenough, J. B., Phospho-olivines as Positive-Electrode Materials for Rechargeable Lithium Batteries. *Journal of The Electrochemical Society* **1997,** 144, (4), 1188-1194.

[35] Wang, M.; Chen, Y.; Zhang, L.; Chen, L. In The doping effect on the electrochemical performance of $LiNi_{0.305}Mn_{0.33}Co_{0.33}M_{0.025}O_2$ (M=Al, Y, Cr) for lithium-ion batteries, 2013 International Conference on Materials for Renewable Energy and Environment, 19-21 Aug. 2014, 2013; **2013**; pp 532-536.

[36] Samarasingha, P. B.; Wijayasinghe, A.; Behm, M.; Dissanayake, L.; Lindbergh, G., Development of cathode materials for lithium ion rechargeable batteries based on the system $Li(Ni_{1/3}Mn_{1/3}Co_{(1/3-x)}M_x)O_2$, (M=Mg, Fe, Al and x=0.00 to 0.33). *Solid State Ionics* **2014,** 268, 226-230.

[37] Lengyel, M.; Zhang, X.; Atlas, G.; Bretscher, H. L.; Belharouak, I.; Axelbaum, R. L., Composition Optimization of Layered Lithium Nickel Manganese Cobalt Oxide Materials Synthesized via Ultrasonic Spray Pyrolysis. *Journal of The Electrochemical Society* **2014,** 161, (9), A1338-A1349.

[38] Lee, M. H.; Kang, Y. J.; Myung, S. T.; Sun, Y. K., Synthetic optimization of $Li[Ni_{1/3}Co_{1/3}Mn_{1/3}]O_2$ via co-precipitation. *Electrochimica Acta* **2004,** 50, (4), 939-948.

[39] Peralta, D.; Salomon, J.; Colin, J.-F.; Boulineau, A.; Fabre, F.; Bourbon, C.; Amestoy, B.; Gutel, E.; Bloch, D.; Patoux, S., Submicronic $LiNi_{1/3}Mn_{1/3}Co_{1/3}O_2$ synthesized by co-precipitation for lithium ion batteries - Tailoring a classic process for enhanced energy and power density. *Journal of Power Sources* **2018,** 396, 527-532.

[40] Hou, P.; Zhang, H.; Zi, Z.; Zhang, L.; Xu, X., Core–shell and concentration-gradient cathodes prepared via co-precipitation reaction for advanced lithium-ion batteries. *Journal of Materials Chemistry A* **2017,** 5, (9), 4254-4279.

[41] Sun, Y.-K.; Myung, S.-T.; Park, B.-C.; Prakash, J.; Belharouak, I.; Amine, K., High-energy cathode material for long-life and safe lithium batteries. *Nature Materials* **2009,** 8, 320.

[42] van Bommel, A.; Dahn, J. R., Analysis of the Growth Mechanism of Coprecipitated Spherical and Dense Nickel, Manganese, and Cobalt-Containing Hydroxides in the Presence of Aqueous Ammonia. *Chemistry of Materials* **2009,** 21, (8), 1500-1503.

[43] Hou, P.; Wang, X.; Wang, D.; Song, D.; Shi, X.; Zhang, L.; Guo, J.; Zhang, J., A novel core-concentration gradient-shelled $LiNi_{0.5}Co_{0.2}Mn_{0.3}O_2$ as high-performance cathode for lithium-ion batteries. *RSC Advances* **2014,** 4, (31), 15923-15929.

[44] Pimenta, V.; Sathiya, M.; Batuk, D.; Abakumov, A. M.; Giaume, D.; Cassaignon, S.; Larcher, D.; Tarascon, J.-M., Synthesis of Li-Rich NMC: A Comprehensive Study. *Chemistry of Materials* **2017,** 29, (23), 9923-9936.

[45] Hou, P.; Xu, L.; Song, J.; Song, D.; Shi, X.; Wang, X.; Zhang, L., A high energy density Li-rich positive-electrode material with superior performances via a dual chelating agent co-precipitation route. *Journal of Materials Chemistry A* **2015,** 3, (18), 9427-9431.

[46] Myung, S.-T.; Amine, K.; Sun, Y.-K., Surface modification of cathode materials from nano- to microscale for rechargeable lithium-ion batteries. *Journal of Materials Chemistry* **2010,** 20, (34), 7074-7095.

[47] Cabelguen, P.-E.; Peralta, D.; Cugnet, M.; Maillet, P., Impact of morphological changes of $LiNi_{1/3}Mn_{1/3}Co_{1/3}O_2$ on lithium-ion cathode performances. *Journal of Power Sources* **2017,** 346, 13-23.

[48] van Bommel, A.; Dahn, J. R., Synthesis of Spherical and Dense Particles of the Pure Hydroxide Phase $Ni_{1/3}Mn_{1/3}Co_{1/3}(OH)_2$. *Journal of The Electrochemical Society* **2009,** 156, (5), A362-A365.

[49] Cabelguen, P.-E.; Peralta, D.; Cugnet, M.; Badot, J.-C.; Dubrunfaut, O.; Mailley, P., Rational Analysis of Layered Oxide Power Performance Limitations in a Lithium Battery Application. *Advanced Sustainable Systems* **2017,** 1, (11), 1700078.

[50] Liao, J.-Y.; Manthiram, A., Surface-modified concentration-gradient Ni-rich layered oxide cathodes for high-energy lithium-ion batteries. *Journal of Power Sources* **2015,** 282, 429-436.

[51] Sun, Y.-K.; Chen, Z.; Noh, H.-J.; Lee, D.-J.; Jung, H.-G.; Ren, Y.; Wang, S.; Yoon, C. S.; Myung, S.-T.; Amine, K., Nanostructured high-energy cathode materials for advanced lithium batteries. *Nature Materials* **2012,** 11, 942.

[52] Li, X.; Jin, L.; Song, D.; Zhang, H.; Shi, X.; Wang, Z.; Zhang, L.; Zhu, L., $LiNbO_3$-coated $LiNi_{0.8}Co_{0.1}Mn_{0.1}O_2$ cathode with high discharge capacity and rate performance for all-solid-state lithium battery. *Journal of Energy Chemistry* **2020,** 40, 39-45.

[53] Bai, X.; Li, W.; Zhang, L.; Liu, Z. In Effects of $LiAlO_2$ coating on electrochemical performance of single-crystal $LiNi_{0.6}Co_{0.2}Mn_{0.2}O_2$, IOP Conference Series: Earth and Environmental Science, 2018; IOP Publishing: **2018**; p 032050.

[54] Zhang, X.-D.; Shi, J.-L.; Liang, J.-Y.; Wang, L.-P.; Yin, Y.-X.; Jiang, K.-C.; Guo, Y.-G., An effective $LiBO_2$ coating to ameliorate the cathode/electrolyte interfacial issues of $LiNi_{0.6}Co_{0.2}Mn_{0.2}O_2$ in solid-state Li batteries. *Journal of Power Sources* **2019,** 426, 242-249.

[55] Choi, M.; Kim, H.-S.; Kim, J.-S.; Park, S.-J.; Lee, Y. M.; Jin, B.-S., Synthesis and electrochemical performance of high-capacity $0.34Li_2MnO_3 \cdot 0.66LiMn_{0.63}Ni_{0.24}Co_{0.13}O_2$ cathode materials using a Couette–Taylor reactor. *Materials Research Bulletin* **2014,** 58, 223-228.

[56] Han, D.; Park, I.; Kim, M.; Kim, D.; Jung, H., Study on the Optimum Conditions for Synthesizing a Cathode Active Material Precursor in Li-Ion Batteries Using a Taylor Reactor. *Korean J. Met. Mater.* **2019,** 57, (6), 360-365.

[57] Kim, J.-E.; Kim, W.-S., Synthesis of Core–Shell Particles of Nickel–Manganese–Cobalt Hydroxides in a Continuous Couette-Taylor Crystallizer. *Crystal Growth & Design* **2017,** 17, (7), 3677-3686.

[58] Kim, J.-M.; Chang, S.-M.; Chang, J. H.; Kim, W.-S., Agglomeration of nickel/cobalt/manganese hydroxide crystals in Couette–Taylor crystallizer. *Colloids and Surfaces A: Physicochemical and Engineering Aspects* **2011,** 384, (1), 31-39.

[59] Thai, D. K.; Mayra, Q.-P.; Kim, W.-S., Agglomeration of Ni-rich hydroxide crystals in Taylor vortex flow. *Powder Technology* **2015,** 274, 5-13.

[60] Seenivasan, M.; Yang, C.-C.; Wu, S.-h.; Chien, W.-C.; Wu, Y.-S.; Jose, R.; Lue, S. J., Using a Couette–Taylor vortex flow reactor to prepare a uniform and highly stable $Li[Ni_{0.80}Co_{0.15}Al_{0.05}]O_2$ cathode material. *Journal of Alloys and Compounds* **2021,** 857, 157594.

[61] Yang, S. H.; Kim, M. Y.; Kim, D. H.; Jung, H. Y.; Ryu, H. M.; Han, J. H.; Lee, M. S.; Kim, H.-S., Ionic conductivity of Ga-doped LLZO prepared using Couette–Taylor reactor for all-solid lithium batteries. *Journal of Industrial and Engineering Chemistry* **2017,** 56, 422-427.

[62] Laminar, Taylor flow. https://www.laminarm.com/taylor-flow/, **2021**, Accessed: 2021-10-15.

[63] Helbig, J.; Beuse, T.; Siozios, V.; Placke, T.; Winter, M.; Schmuch, R., Finding the sweet spot: Li/Mn-rich cathode materials with fine-tuned core–shell particle design for high-energy lithium ion batteries. *Electrochimica Acta* **2021,** 366, 137413.

[64] Laminar, Battery. http://www.laminarm.com/battery/, **2020**, Accessed: 2020-10-08.

[65] Heo, K.; Lee, J.; Im, J.; Kim, M.-Y.; Kim, H.-S.; Ahn, D.; Kim, J.; Lim, J., A composite cathode material encapsulated by amorphous garnet-type solid electrolyte and self-assembled $La_2(Ni_{0.5}Li_{0.5})O_4$ nanoparticles for all-solid-state batteries. *Journal of Materials Chemistry A* **2020,** 8, (43), 22893-22906.

[66] Nitta, N.; Wu, F.; Lee, J. T.; Yushin, G., Li-ion battery materials: present and future. *Materials Today* **2015,** 18, (5), 252-264.

[67] Islam, M. S.; Fisher, C. A., Lithium and sodium battery cathode materials: computational insights into voltage, diffusion and nanostructural properties. *Chemical Society Reviews* **2014,** 43, (1), 185-204.

[68] Tsutomu, O.; Yoshinari, M., Layered Lithium Insertion Material of $LiCo_{1/3}Ni_{1/3}Mn_{1/3}O_2$ for Lithium-Ion Batteries. *Chemistry Letters* **2001,** 30, (7), 642-643.

[69] Eilers-Rethwisch, M.; Winter, M.; Schappacher, F. M., Synthesis, electrochemical investigation and structural analysis of doped $Li[Ni_{0.6}Mn_{0.2}Co_{0.2-x}M_x]O_2$ (x = 0, 0.05; M = Al, Fe, Sn) cathode materials. *Journal of Power Sources* **2018,** 387, 101-107.

[70] Ryu, H.-H.; Park, K.-J.; Yoon, C. S.; Sun, Y.-K., Capacity Fading of Ni-Rich $Li[Ni_xCo_yMn_{1-x-y}]O_2$ ($0.6 \leq x \leq 0.95$) Cathodes for High-Energy-Density Lithium-Ion Batteries: Bulk or Surface Degradation? *Chemistry of Materials* **2018,** 30, (3), 1155-1163.

[71] Kondrakov, A. O.; Schmidt, A.; Xu, J.; Geßwein, H.; Mönig, R.; Hartmann, P.; Sommer, H.; Brezesinski, T.; Janek, J., Anisotropic Lattice Strain and Mechanical Degradation of High- and Low-Nickel NCM Cathode Materials for Li-Ion Batteries. *The Journal of Physical Chemistry C* **2017,** 121, (6), 3286-3294.

[72] Koerver, R.; Zhang, W.; de Biasi, L.; Schweidler, S.; Kondrakov, A. O.; Kolling, S.; Brezesinski, T.; Hartmann, P.; Zeier, W. G.; Janek, J., Chemo-mechanical expansion of lithium electrode materials – on the route to mechanically optimized all-solid-state batteries. *Energy & Environmental Science* **2018,** 11, (8), 2142-2158.

[73] Sun, Y.-K.; Myung, S.-T.; Kim, M.-H.; Prakash, J.; Amine, K., Synthesis and Characterization of $Li[(Ni_{0.8}Co_{0.1}Mn_{0.1})_{0.8}(Ni_{0.5}Mn_{0.5})_{0.2}]O_2$ with the Microscale Core–Shell Structure as the Positive Electrode Material for Lithium Batteries. *Journal of the American Chemical Society* **2005,** 127, (38), 13411-13418.

[74] Manthiram, A.; Knight, J. C.; Myung, S.-T.; Oh, S.-M.; Sun, Y.-K., Nickel-Rich and Lithium-Rich Layered Oxide Cathodes: Progress and Perspectives. *Advanced Energy Materials* **2016,** 6, (1), 1501010.

[75] Lee, K.-S.; Myung, S.-T.; Sun, Y.-K., Synthesis and electrochemical performances of core-shell structured $Li[(Ni_{1/3}Co_{1/3}Mn_{1/3})_{0.8}(Ni_{1/2}Mn_{1/2})_{0.2}]O_2$ cathode material for lithium ion batteries. *Journal of Power Sources* **2010,** 195, (18), 6043-6048.

[76] Shi, H.; Wang, X.; Hou, P.; Zhou, E.; Guo, J.; Zhang, J.; Wang, D.; Guo, F.; Song, D.; Shi, X.; Zhang, L., Core–shell structured $Li[(Ni_{0.8}Co_{0.1}Mn_{0.1})_{0.7}(Ni_{0.45}Co_{0.1}Mn_{0.45})_{0.3}]O_2$ cathode material for high-energy lithium ion batteries. *Journal of Alloys and Compounds* **2014,** 587, 710-716.

[77] Jun, D.-W.; Yoon, C. S.; Kim, U.-H.; Sun, Y.-K., High-energy density core–shell structured $Li[Ni_{0.95}Co_{0.025}Mn_{0.025}]O_2$ cathode for lithium-ion batteries. *Chemistry of Materials* **2017,** 29, (12), 5048-5052.

[78] Hou, P.; Wang, X.; Song, D.; Shi, X.; Zhang, L.; Guo, J.; Zhang, J., Design, synthesis, and performances of double-shelled $LiNi_{0.5}Co_{0.2}Mn_{0.3}O_2$ as cathode for long-life and safe Li-ion battery. *Journal of Power Sources* **2014,** 265, 174-181.

[79] Song, D.; Hou, P.; Wang, X.; Shi, X.; Zhang, L., Understanding the Origin of Enhanced Performances in Core–Shell and Concentration-Gradient Layered Oxide Cathode Materials. *ACS Applied Materials & Interfaces* **2015,** 7, (23), 12864-12872.

[80] Kim, U.-H.; Ryu, H.-H.; Kim, J.-H.; Mücke, R.; Kaghazchi, P.; Yoon, C. S.; Sun, Y.-K., Microstructure-Controlled Ni-Rich Cathode Material by Microscale Compositional Partition for Next-Generation Electric Vehicles. *Advanced Energy Materials* **2019,** 9, (15), 1803902.

[81] Liang, L.; Du, K.; Lu, W.; Peng, Z.; Cao, Y.; Hu, G., Synthesis and characterization of concentration–gradient $LiNi_{0.6}Co_{0.2}Mn_{0.2}O_2$ cathode material for lithium ion batteries. *Journal of Alloys and Compounds* **2014,** 613, 296-305.

[82] Kim, U.-H.; Lee, E.-J.; Yoon, C. S.; Myung, S.-T.; Sun, Y.-K., Compositionally Graded Cathode Material with Long-Term Cycling Stability for Electric Vehicles Application. *Advanced Energy Materials* **2016,** 6, (22), 1601417.

[83] Lim, B.-B.; Myung, S.-T.; Yoon, C. S.; Sun, Y.-K., Comparative Study of Ni-Rich Layered Cathodes for Rechargeable Lithium Batteries: $Li[Ni_{0.85}Co_{0.11}Al_{0.04}]O_2$ and $Li[Ni_{0.84}Co_{0.06}Mn_{0.09}Al_{0.01}]O_2$ with Two-Step Full Concentration Gradients. *ACS Energy Letters* **2016,** 1, (1), 283-289.

[84] Lim, B.-B.; Yoon, S.-J.; Park, K.-J.; Yoon, C. S.; Kim, S.-J.; Lee, J. J.; Sun, Y.-K., Advanced Concentration Gradient Cathode Material with Two-Slope for High-Energy and Safe Lithium Batteries. *Advanced Functional Materials* **2015,** 25, (29), 4673-4680.

[85] Yoon, C. S.; Park, K.-J.; Kim, U.-H.; Kang, K. H.; Ryu, H.-H.; Sun, Y.-K., High-Energy Ni-Rich $Li[Ni_xCo_yMn_{1-x-y}]O_2$ Cathodes via Compositional Partitioning for Next-Generation Electric Vehicles. *Chemistry of Materials* **2017,** 29, (24), 10436-10445.

[86] Yan, W.; Yang, S.; Huang, Y.; Yang, Y.; Guohui, Y., A review on doping/coating of nickel-rich cathode materials for lithium-ion batteries. *Journal of Alloys and Compounds* **2020,** 819, 153048.

[87] Zhang, B.; Dong, P.; Tong, H.; Yao, Y.; Zheng, J.; Yu, W.; Zhang, J.; Chu, D., Enhanced electrochemical performance of $LiNi_{0.8}Co_{0.1}Mn_{0.1}O_2$ with lithium-reactive Li_3VO_4 coating. *Journal of Alloys and Compounds* **2017,** 706, 198-204.

[88] Liang, H.; Wang, Z.; Guo, H.; Wang, J.; Leng, J., Improvement in the electrochemical performance of $LiNi_{0.8}Co_{0.1}Mn_{0.1}O_2$ cathode material by Li_2ZrO_3 coating. *Applied Surface Science* **2017,** 423, 1045-1053.

[89] Xiong, X.; Wang, Z.; Yin, X.; Guo, H.; Li, X., A modified LiF coating process to enhance the electrochemical performance characteristics of $LiNi_{0.8}Co_{0.1}Mn_{0.1}O_2$ cathode materials. *Materials Letters* **2013,** 110, 4-9.

[90] Wu, J.; Tan, X.; Zhang, J.; Guo, L.; Jiang, Y.; Liu, S.; Zhao, T.; Liu, Y.; Ren, J.; Wang, H.; Kang, X.; Chu, W., Improvement of Electrochemical Performance of Nickel Rich $LiNi_{0.8}Co_{0.1}Mn_{0.1}O_2$ Cathode by Lithium Aluminates Surface Modifications. *Energy Technology* **2019,** 7, (2), 209-215.

[91] Sattar, T.; Sim, S.-J.; Jin, B.-S.; Kim, H.-S., Dual function Li-reactive coating from residual lithium on Ni-rich NCM cathode material for Lithium-ion batteries. *Scientific Reports* **2021,** 11, (1), 18590.

[92] Hu, G.; Tao, Y.; Lu, Y.; Fan, J.; Li, L.; Xia, J.; Huang, Y.; Zhang, Z.; Su, H.; Cao, Y., Enhanced Electrochemical Properties of $LiNi_{0.8}Co_{0.1}Mn_{0.1}O_2$ Cathode Materials Modified with Lithium-Ion Conductive Coating $LiNbO_3$. *ChemElectroChem* **2019,** 6, (18), 4773-4780.

[93] Sim, S.-J.; Lee, S.-H.; Jin, B.-S.; Kim, H.-S., Effects of lithium tungsten oxide coating on $LiNi_{0.90}Co_{0.05}Mn_{0.05}O_2$ cathode material for lithium-ion batteries. *Journal of Power Sources* **2021,** 481, 229037.

[94] Becker, D.; Börner, M.; Nölle, R.; Diehl, M.; Klein, S.; Rodehorst, U.; Schmuch, R.; Winter, M.; Placke, T., Surface Modification of Ni-Rich $LiNi_{0.8}Co_{0.1}Mn_{0.1}O_2$ Cathode Material by Tungsten Oxide Coating for Improved Electrochemical Performance in Lithium-Ion Batteries. *ACS Applied Materials & Interfaces* **2019,** 11, (20), 18404-18414.

[95] Mao, G.; Yu, W.; Zhou, Q.; Li, L.; Huang, Y.; Yao, Y.; Chu, D.; Tong, H.; Guo, X., Improved electrochemical performance of high-nickel cathode material with electronic conductor RuO_2 as the protecting layer for lithium-ion batteries. *Applied Surface Science* **2020,** 531, 147245.

[96] Mu, L.; Lin, R.; Xu, R.; Han, L.; Xia, S.; Sokaras, D.; Steiner, J. D.; Weng, T.-C.; Nordlund, D.; Doeff, M. M.; Liu, Y.; Zhao, K.; Xin, H. L.; Lin, F., Oxygen Release Induced Chemomechanical Breakdown of Layered Cathode Materials. *Nano Letters* **2018,** 18, (5), 3241-3249.

[97] Kang, K.; Ceder, G., Factors that affect Li mobility in layered lithium transition metal oxides. *Physical Review B* **2006,** 74, (9), 094105.

[98] Luo, W.; Zhou, F.; Zhao, X.; Lu, Z.; Li, X.; Dahn, J. R., Synthesis, Characterization, and Thermal Stability of $LiNi_{1/3}Mn_{1/3}Co_{1/3-z}Mg_zO_2$, $LiNi_{1/3-z}Mn_{1/3}Co_{1/3}Mg_zO_2$, and $LiNi_{1/3}Mn_{1/3-z}Co_{1/3}Mg_zO_2$. *Chemistry of Materials* **2010,** 22, (3), 1164-1172.

[99] Nayak, P. K.; Grinblat, J.; Levi, M.; Levi, E.; Kim, S.; Choi, J. W.; Aurbach, D., Al Doping for Mitigating the Capacity Fading and Voltage Decay of Layered Li and Mn-Rich Cathodes for Li-Ion Batteries. *Advanced Energy Materials* **2016,** 6, (8), 1502398.

[100] Kim, U.-H.; Myung, S.-T.; Yoon, C. S.; Sun, Y.-K., Extending the Battery Life Using an Al-Doped Li $[Ni_{0.76}Co_{0.09}Mn_{0.15}]$ O_2 Cathode with Concentration Gradients for Lithium Ion Batteries. *ACS Energy Letters* **2017,** 2, (8), 1848-1854.

[101] Zhou, F.; Zhao, X.; Lu, Z.; Jiang, J.; Dahn, J. R., The effect of Al substitution on the reactivity of delithiated $LiNi_{1/3}Mn_{1/3}Co_{(1/3-z)}Al_zO_2$ with non-aqueous electrolyte. *Electrochemistry Communications* **2008,** 10, (8), 1168-1171.

[102] Kam, K. C.; Mehta, A.; Heron, J. T.; Doeff, M. M., Electrochemical and Physical Properties of Ti-Substituted Layered Nickel Manganese Cobalt Oxide (NMC) Cathode Materials. *Journal of The Electrochemical Society* **2012,** 159, (8), A1383-A1392.

[103] Jia, X.; Yan, M.; Zhou, Z.; Chen, X.; Yao, C.; Li, D.; Chen, D.; Chen, Y., Nd-doped $LiNi_{0.5}Co_{0.2}Mn_{0.3}O_2$ as a cathode material for better rate capability in high voltage cycling of Li-ion batteries. *Electrochimica Acta* **2017,** 254, 50-58.

[104] Xia, L.; Qiu, K.; Gao, Y.; He, X.; Zhou, F., High potential performance of Cerium-doped $LiNi_{0.5}Co_{0.2}Mn_{0.3}O_2$ cathode material for Li-ion battery. *Journal of Materials Science* **2015,** 50, (7), 2914-2920.

[105] Yu, A.; Subba Rao, G. V.; Chowdari, B. V. R., Synthesis and properties of $LiGa_xMg_yNi_{1-x-y}O_2$ as cathode material for lithium ion batteries. *Solid State Ionics* **2000,** 135, (1), 131-135.

[106] Schipper, F.; Dixit, M.; Kovacheva, D.; Talianker, M.; Haik, O.; Grinblat, J.; Erickson, E. M.; Ghanty, C.; Major, D. T.; Markovsky, B., Stabilizing nickel-rich layered cathode materials by a high-charge cation doping strategy: zirconium-doped $LiNi_{0.6}Co_{0.2}Mn_{0.2}O_2$. *Journal of Materials Chemistry A* **2016,** 4, (41), 16073-16084.

[107] Park, K.-J.; Jung, H.-G.; Kuo, L.-Y.; Kaghazchi, P.; Yoon, C. S.; Sun, Y.-K., Improved Cycling Stability of $Li[Ni_{0.90}Co_{0.05}Mn_{0.05}]O_2$ Through Microstructure Modification by Boron Doping for Li-Ion Batteries. *Advanced Energy Materials* **2018,** 8, (25), 1801202.

[108] Han, S.-H.; Song, J. H.; Yim, T.; Kim, Y.-J.; Yu, J.-S.; Yoon, S., Communication—Improvement of Structural Stability during High-Voltage Cycling in High-Nickel Cathode Materials with B_2O_3Addition. *Journal of The Electrochemical Society* **2016,** 163, (5), A748-A750.

[109] Lee, S.-H.; Jin, B.-S.; Kim, H.-S., Superior Performances of B-doped $LiNi_{0.84}Co_{0.10}Mn_{0.06}O_2$ cathode for advanced LIBs. *Scientific Reports* **2019,** 9, (1), 17541.

[110] Pan, L.; Xia, Y.; Qiu, B.; Zhao, H.; Guo, H.; Jia, K.; Gu, Q.; Liu, Z., Structure and electrochemistry of B doped $Li(Li_{0.2}Ni_{0.13}Co_{0.13}Mn_{0.54})_{1-x}B_xO_2$ as cathode materials for lithium-ion batteries. *Journal of Power Sources* **2016,** 327, 273-280.

[111] Susai, F. A.; Kovacheva, D.; Chakraborty, A.; Kravchuk, T.; Ravikumar, R.; Talianker, M.; Grinblat, J.; Burstein, L.; Kauffmann, Y.; Major, D. T.; Markovsky, B.; Aurbach, D., Improving Performance of $LiNi_{0.8}Co_{0.1}Mn_{0.1}O_2$ Cathode Materials for Lithium-Ion Batteries by Doping with Molybdenum-Ions: Theoretical and Experimental Studies. *ACS Applied Energy Materials* **2019,** 2, (6), 4521-4534.

[112] Kim, U.-H.; Jun, D.-W.; Park, K.-J.; Zhang, Q.; Kaghazchi, P.; Aurbach, D.; Major, D.; Goobes, G.; Dixit, M.; Leifer, N., Pushing the limit of layered transition metal oxide cathodes for high-energy density rechargeable Li ion batteries. *Energy & Environmental Science* **2018,** 11, (5), 1271-1279.

[113] Park, G.-T.; Ryu, H.-H.; Park, N.-Y.; Yoon, C. S.; Sun, Y.-K., Tungsten doping for stabilization of $Li[Ni_{0.90}Co_{0.05}Mn_{0.05}]O_2$ cathode for Li-ion battery at high voltage. *Journal of Power Sources* **2019,** 442, 227242.

[114] Kim, U.-H.; Kuo, L.-Y.; Kaghazchi, P.; Yoon, C. S.; Sun, Y.-K., Quaternary Layered Ni-Rich NCMA Cathode for Lithium-Ion Batteries. *ACS Energy Letters* **2019**.

[115] Jung, C.-H.; Kim, D.-H.; Eum, D.; Kim, K.-H.; Choi, J.; Lee, J.; Kim, H.-H.; Kang, K.; Hong, S.-H., New Insight into Microstructure Engineering of Ni-Rich Layered Oxide Cathode for High Performance Lithium Ion Batteries. *Advanced Functional Materials* **2021,** 31, (18), 2010095.

[116] Roitzheim, C.; Kuo, L.-Y.; Sohn, Y. J.; Finsterbusch, M.; Möller, S.; Sebold, D.; Valencia, H.; Meledina, M.; Mayer, J.; Breuer, U.; Kaghazchi, P.; Guillon, O.; Fattakhova-Rohlfing, D., Boron in Ni-Rich NCM811 Cathode Material: Impact on Atomic and Microscale Properties. *ACS Applied Energy Materials* **2022,** 5, (1), 524-538.

[117] Sakuda, A., Favorable composite electrodes for all-solid-state batteries. *JOURNAL OF THE CERAMIC SOCIETY OF JAPAN* **2018,** 126, (9), 675-683.

[118] Finsterbusch, M.; Danner, T.; Tsai, C.-L.; Uhlenbruck, S.; Latz, A.; Guillon, O., High Capacity Garnet-Based All-Solid-State Lithium Batteries: Fabrication and 3D-Microstructure Resolved Modeling. *ACS Applied Materials & Interfaces* **2018,** 10, (26), 22329-22339.

[119] Janek, J.; Zeier, W. G., A solid future for battery development. *Nature Energy* **2016,** 1, 16141.

[120] Lobe, S.; Bauer, A.; Uhlenbruck, S.; Fattakhova-Rohlfing, D., Physical Vapor Deposition in Solid-State Battery Development: From Materials to Devices. *Advanced Science* **2021,** 8, (11), 2002044.

[121] Tsai, C.-L.; Ma, Q.; Dellen, C.; Lobe, S.; Vondahlen, F.; Windmüller, A.; Grüner, D.; Zheng, H.; Uhlenbruck, S.; Finsterbusch, M.; Tietz, F.; Fattakhova-Rohlfing, D.; Buchkremer, H. P.; Guillon, O., A garnet structure-based all-solid-state Li battery without interface modification: resolving incompatibility issues on positive electrodes. *Sustainable Energy & Fuels* **2019,** 3, (1), 280-291.

[122] Tsai, C.-L.; Roddatis, V.; Chandran, C. V.; Ma, Q.; Uhlenbruck, S.; Bram, M.; Heitjans, P.; Guillon, O., $Li_7La_3Zr_2O_{12}$ Interface Modification for Li Dendrite Prevention. *ACS Applied Materials & Interfaces* **2016,** 8, (16), 10617-10626.

[123] Kali, R.; Mukhopadhyay, A., Spark plasma sintered/synthesized dense and nanostructured materials for solid-state Li-ion batteries: Overview and perspective. *Journal of Power Sources* **2014,** 247, 920-931.

[124] Long, L.; Wang, S.; Xiao, M.; Meng, Y., Polymer electrolytes for lithium polymer batteries. *Journal of Materials Chemistry A* **2016,** 4, (26), 10038-10069.

[125] Zhao, N.; Khokhar, W.; Bi, Z.; Shi, C.; Guo, X.; Fan, L.-Z.; Nan, C.-W., Solid Garnet Batteries. *Joule* **2019,** 3, (5), 1190-1199.

[126] Tsai, C.-L.; Dashjav, E.; Hammer, E.-M.; Finsterbusch, M.; Tietz, F.; Uhlenbruck, S.; Buchkremer, H. P., High conductivity of mixed phase Al-substituted $Li_7La_3Zr_2O_{12}$. *Journal of Electroceramics* **2015,** 35, (1), 25-32.

[127] Liu, T.; Zhang, Y.; Zhang, X.; Wang, L.; Zhao, S.-X.; Lin, Y.-H.; Shen, Y.; Luo, J.; Li, L.; Nan, C.-W., Enhanced electrochemical performance of bulk type oxide ceramic lithium batteries enabled by interface modification. *Journal of Materials Chemistry A* **2018,** 6, (11), 4649-4657.

[128] Gao, Z.; Sun, H.; Fu, L.; Ye, F.; Zhang, Y.; Luo, W.; Huang, Y., Promises, Challenges, and Recent Progress of Inorganic Solid-State Electrolytes for All-Solid-State Lithium Batteries. *Advanced Materials* **2018,** 30, (17), 1705702.

[129] Ma, Q.; Xu, Q.; Tsai, C.-L.; Tietz, F.; Guillon, O., A Novel Sol–Gel Method for Large-Scale Production of Nanopowders: Preparation of $Li_{1.5}Al_{0.5}Ti_{1.5}(PO_4)_3$ as an Example. *Journal of the American Ceramic Society* **2016,** 99, (2), 410-414.

[130] Murugan, R.; Thangadurai, V.; Weppner, W., Fast Lithium Ion Conduction in Garnet-Type $Li_7La_3Zr_2O_{12}$. *Angewandte Chemie International Edition* **2007,** 46, (41), 7778-7781.

[131] Deviannapoorani, C.; Ramakumar, S.; Janani, N.; Murugan, R., Synthesis of lithium garnets from $La_2Zr_2O_7$ pyrochlore. *Solid State Ionics* **2015,** 283, 123-130.

[132] Li, Y.; Han, J.-T.; Wang, C.-A.; Xie, H.; Goodenough, J. B., Optimizing Li^+ conductivity in a garnet framework. *Journal of Materials Chemistry* **2012,** 22, (30), 15357-15361.

[133] Wang, Y.; Lai, W., High Ionic Conductivity Lithium Garnet Oxides of $Li_{7-x}La_3Zr_{2-x}Ta_xO_{12}$ Compositions. *Electrochemical and Solid-State Letters* **2012,** 15, (5), A68-A71.

[134] Luo, Y.; Li, X.; Zhang, Y.; Ge, L.; Chen, H.; Guo, L., Electrochemical properties and structural stability of Ga- and Y- co-doping in $Li_7La_3Zr_2O_{12}$ ceramic electrolytes for lithium-ion batteries. *Electrochimica Acta* **2019,** 294, 217-225.

[135] El Shinawi, H.; Janek, J., Stabilization of cubic lithium-stuffed garnets of the type "$Li_7La_3Zr_2O_{12}$" by addition of gallium. *Journal of Power Sources* **2013,** 225, 13-19.

[136] Li, Y.; Wang, Z.; Cao, Y.; Du, F.; Chen, C.; Cui, Z.; Guo, X., W-Doped $Li_7La_3Zr_2O_{12}$ Ceramic Electrolytes for Solid State Li-ion Batteries. *Electrochimica Acta* **2015,** 180, 37-42.

[137] Ohta, S.; Kobayashi, T.; Asaoka, T., High lithium ionic conductivity in the garnet-type oxide $Li_{7-X}La_3(Zr_{2-X}, Nb_X)O_{12}$ (X=0–2). *Journal of Power Sources* **2011,** 196, (6), 3342-3345.

[138] Huang, M.; Shoji, M.; Shen, Y.; Nan, C.-W.; Munakata, H.; Kanamura, K., Preparation and electrochemical properties of Zr-site substituted $Li_7La_3(Zr_{2-x}M_x)O_{12}$ (M = Ta, Nb) solid electrolytes. *Journal of Power Sources* **2014,** 261, 206-211.

[139] Ohta, S.; Kobayashi, T.; Seki, J.; Asaoka, T., Electrochemical performance of an all-solid-state lithium ion battery with garnet-type oxide electrolyte. *Journal of Power Sources* **2012,** 202, 332-335.

[140] Ren, Y.; Liu, T.; Shen, Y.; Lin, Y.; Nan, C.-W., Chemical compatibility between garnet-like solid state electrolyte $Li_{6.75}La_3Zr_{1.75}Ta_{0.25}O_{12}$ and major commercial lithium battery cathode materials. *Journal of Materiomics* **2016,** 2, (3), 256-264.

[141] Uhlenbruck, S.; Dornseiffer, J.; Lobe, S.; Dellen, C.; Tsai, C.-L.; Gotzen, B.; Sebold, D.; Finsterbusch, M.; Guillon, O., Cathode-electrolyte material interactions during manufacturing of inorganic solid-state lithium batteries. *Journal of Electroceramics* **2017,** 38, (2), 197-206.

[142] Zhu, Y.; Connell, J. G.; Tepavcevic, S.; Zapol, P.; Garcia-Mendez, R.; Taylor, N. J.; Sakamoto, J.; Ingram, B. J.; Curtiss, L. A.; Freeland, J. W.; Fong, D. D.; Markovic, N. M., Dopant-Dependent Stability of Garnet Solid Electrolyte Interfaces with Lithium Metal. *Advanced Energy Materials* **2019,** 9, (12), 1803440.

[143] Park, K.; Yu, B.-C.; Jung, J.-W.; Li, Y.; Zhou, W.; Gao, H.; Son, S.; Goodenough, J. B., Electrochemical Nature of the Cathode Interface for a Solid-State Lithium-Ion Battery: Interface between $LiCoO_2$ and Garnet-$Li_7La_3Zr_2O_{12}$. *Chemistry of Materials* **2016,** 28, (21), 8051-8059.

[144] Han, F.; Yue, J.; Chen, C.; Zhao, N.; Fan, X.; Ma, Z.; Gao, T.; Wang, F.; Guo, X.; Wang, C., Interphase Engineering Enabled All-Ceramic Lithium Battery. *Joule* **2018,** 2, (3), 497-508.

[145] Nomura, Y.; Yamamoto, K.; Hirayama, T.; Igaki, E.; Saitoh, K., Visualization of Lithium Transfer Resistance in Secondary Particle Cathodes of Bulk-Type Solid-State Batteries. *ACS Energy Letters* **2020,** 5, (6), 2098-2105.

[146] Ohta, S.; Kihira, Y.; Asaoka, T., Spontaneous formation of a core–shell structure by a lithium ion conductive garnet-type oxide electrolyte for co-sintering with the cathode. *Journal of Materials Chemistry A* **2021,** 9, (6), 3353-3359.

[147] Wang, D.; Sun, Q.; Luo, J.; Liang, J.; Sun, Y.; Li, R.; Adair, K.; Zhang, L.; Yang, R.; Lu, S.; Huang, H.; Sun, X., Mitigating the Interfacial Degradation in Cathodes for High-

Performance Oxide-Based Solid-State Lithium Batteries. *ACS Applied Materials & Interfaces* **2019,** 11, (5), 4954-4961.

[148] Chen, S.; Zhang, J.; Nie, L.; Hu, X.; Huang, Y.; Yu, Y.; Liu, W., All-Solid-State Batteries with a Limited Lithium Metal Anode at Room Temperature using a Garnet-Based Electrolyte. *Advanced Materials* **2021,** 33, (1), 2002325.

[149] Xu, H.; Li, Y.; Zhou, A.; Wu, N.; Xin, S.; Li, Z.; Goodenough, J. B., Li_3N-Modified Garnet Electrolyte for All-Solid-State Lithium Metal Batteries Operated at 40 °C. *Nano Letters* **2018,** 18, (11), 7414-7418.

[150] He, M.; Cui, Z.; Han, F.; Guo, X., Construction of conductive and flexible composite cathodes for room-temperature solid-state lithium batteries. *Journal of Alloys and Compounds* **2018,** 762, 157-162.

[151] Delluva, A. A.; Dudoff, J.; Teeter, G.; Holewinski, A., Cathode Interface Compatibility of Amorphous $LiMn_2O_4$ (LMO) and $Li_7La_3Zr_2O_{12}$ (LLZO) Characterized with Thin-Film Solid-State Electrochemical Cells. *ACS Applied Materials & Interfaces* **2020,** 12, (22), 24992-24999.

[152] Sakuda, A.; Takeuchi, T.; Kobayashi, H., Electrode morphology in all-solid-state lithium secondary batteries consisting of $LiNi_{1/3}Co_{1/3}Mn_{1/3}O_2$ and Li_2S-P_2S_5 solid electrolytes. *Solid State Ionics* **2016,** 285, 112-117.

[153] Miara, L.; Windmüller, A.; Tsai, C.-L.; Richards, W. D.; Ma, Q.; Uhlenbruck, S.; Guillon, O.; Ceder, G., About the Compatibility between High Voltage Spinel Cathode Materials and Solid Oxide Electrolytes as a Function of Temperature. *ACS Applied Materials & Interfaces* **2016,** 8, (40), 26842-26850.

[154] Wakasugi, J.; Munakata, H.; Kanamura, K., Thermal Stability of Various Cathode Materials against $Li_{6.25}Al_{0.25}La_3Zr_2O_{12}$ Electrolyte. *Electrochemistry* **2017,** 85, (2), 77-81.

[155] Miara, L. J.; Richards, W. D.; Wang, Y. E.; Ceder, G., First-Principles Studies on Cation Dopants and Electrolyte|Cathode Interphases for Lithium Garnets. *Chemistry of Materials* **2015,** 27, (11), 4040-4047.

[156] Liu, T.; Ren, Y.; Shen, Y.; Zhao, S.-X.; Lin, Y.; Nan, C.-W., Achieving high capacity in bulk-type solid-state lithium ion battery based on $Li_{6.75}La_3Zr_{1.75}Ta_{0.25}O_{12}$ electrolyte: Interfacial resistance. *Journal of Power Sources* **2016,** 324, 349-357.

[157] Xiao, Y.; Miara, L. J.; Wang, Y.; Ceder, G., Computational Screening of Cathode Coatings for Solid-State Batteries. *Joule* **2019,** 3, (5), 1252-1275.

[158] Shao, Y.; Wang, H.; Gong, Z.; Wang, D.; Zheng, B.; Zhu, J.; Lu, Y.; Hu, Y.-S.; Guo, X.; Li, H.; Huang, X.; Yang, Y.; Nan, C.-W.; Chen, L., Drawing a Soft Interface: An Effective

Interfacial Modification Strategy for Garnet-Type Solid-State Li Batteries. *ACS Energy Letters* **2018,** 3, (6), 1212-1218.

[159] Alexander, G. V.; Indu, M. S.; Kamakshy, S.; Murugan, R., Development of stable and conductive interface between garnet structured solid electrolyte and lithium metal anode for high performance solid-state battery. *Electrochimica Acta* **2020,** 332, 135511.

[160] Lan, W.; Fan, H.; Lau, V. W.-h.; Zhang, J.; Zhang, J.; Zhao, R.; Chen, H., Realizing $Li_7La_3Zr_2O_{12}$ garnets with high Li^+ conductivity and dense microstructures by Ga/Nb dual substitution for lithium solid-state battery applications. *Sustainable Energy & Fuels* **2020,** 4, (4), 1812-1821.

[161] Roitzheim, C.; Sohn, Y. J.; Kuo, L.-Y.; Häuschen, G.; Mann, M.; Sebold, D.; Finsterbusch, M.; Kaghazchi, P.; Guillon, O.; Fattakhova-Rohlfing, D., All-Solid-State Li Batteries with NCM–Garnet-Based Composite Cathodes: The Impact of NCM Composition on Material Compatibility. *ACS Applied Energy Materials* **2022,** 5, (6), 6913-6926.

[162] Ohta, S.; Kawakami, M.; Nozaki, H.; Yada, C.; Saito, T.; Iba, H., Li^+ conducting garnet-type oxide sintering triggered by an H^+/Li^+ ion-exchange reaction. *Journal of Materials Chemistry A* **2020,** 8, (18), 8989-8996.

[163] Dinnebier, R. E.; Fitch, A.; Billinge, S. J. L.; Bail, A. L.; Le Bail, A.; Madsen, I.; Cranswick, L. M. D.; Cockcroft, J. K.; Norby, P.; Zuev, A. D., Powder Diffraction : Theory and Practice. Royal Society of Chemistry: Cambridge, UNITED KINGDOM, **2008**.

[164] Norton, M. G.; Suryanarayana, C., X-Ray diffraction: a practical approach. Plenum Press: **1998**.

[165] Spieß, L.; Behnken, H.; Genzel, C.; Schwarzer, R.; Teichert, G., Moderne Röntgenbeugung. Springer: **2009**; Vol. 2.

[166] Degen, T.; Sadki, M.; Bron, E.; König, U.; Nénert, G., The HighScore suite. *Powder Diffraction* **2014,** 29, (S2), S13-S18.

[167] Bruker AXS, Topas V4: *General profile and structure analysis software for powder diffraction data*, Karlsruhe, Germany, **2008**.

[168] Rodríguez-Carvajal, J., Recent advances in magnetic structure determination by neutron powder diffraction. *Physica B: Condensed Matter* **1993,** 192, (1), 55-69.

[169] Nölte, J., ICP Emissionsspektrometrie für Praktiker. Wiley-VCH: **2002**.

[170] Wu, B.; Wang, S.; Evans Iv, W. J.; Deng, D. Z.; Yang, J.; Xiao, J., Interfacial behaviours between lithium ion conductors and electrode materials in various battery systems. *Journal of Materials Chemistry A* **2016,** 4, (40), 15266-15280.

[171] Akhtar, K.; Khan, S. A.; Khan, S. B.; Asiri, A. M., Scanning Electron Microscopy: Principle and Applications in Nanomaterials Characterization. In *Handbook of Materials Characterization*, Sharma, S. K., Ed. Springer International Publishing: Cham, **2018**; pp 113-145.

[172] Javed, Y.; Ali, K.; Akhtar, K.; Jawaria; Hussain, M. I.; Ahmad, G.; Arif, T., TEM for Atomic-Scale Study: Fundamental, Instrumentation, and Applications in Nanotechnology. In *Handbook of Materials Characterization*, Sharma, S. K., Ed. Springer International Publishing: Cham, **2018**; pp 147-216.

[173] Hofer, F.; Schmidt, F. P.; Grogger, W.; Kothleitner, G., Fundamentals of electron energy-loss spectroscopy. *IOP Conference Series: Materials Science and Engineering* **2016,** 109, 012007.

[174] Forschungszentrum_Jülich_GmbH, Facilities. https://er-c.org/index.php/facilities-2/, **2021**, Accessed: 2021-11-02.

[175] Kovács, A.; Schierholz, R.; Tillmann, K., FEI Titan G2 80-200 CREWLEY. *Journal of large-scale research facilities JLSRF* **2016,** 2, 43.

[176] Kruth, M.; Meertens, D.; Tillmann, K., Fei Helios Nanolab 460F1 FIB-SEM. *Journal of large-scale research facilities JLSRF* **2016,** 2, 59.

[177] Chastain, J.; King Jr, R. C., Handbook of X-ray photoelectron spectroscopy. *Perkin-Elmer, USA* **1992**, 261.

[178] Kumar, J., Photoelectron Spectroscopy: Fundamental Principles and Applications. In *Handbook of Materials Characterization*, Sharma, S. K., Ed. Springer International Publishing: Cham, **2018**; pp 435-495.

[179] Corcoran, C. J.; Tavassol, H.; Rigsby, M. A.; Bagus, P. S.; Wieckowski, A., Application of XPS to study electrocatalysts for fuel cells. *Journal of Power Sources* **2010,** 195, (24), 7856-7879.

[180] Möller, S.; Höschen, D.; Kurth, S.; Esser, G.; Hiller, A.; Scholtysik, C.; Dellen, C.; Linsmeier, C., A New High-Throughput Focused MeV Ion-Beam Analysis Setup. *Instruments* **2021,** 5, (1), 10.

[181] Möller, S.; Satoh, T.; Ishii, Y.; Teßmer, B.; Guerdelli, R.; Kamiya, T.; Fujita, K.; Suzuki, K.; Kato, Y.; Wiemhöfer, H.-D.; Mima, K.; Finsterbusch, M., Absolute Local Quantification of Li as Function of State-of-Charge in All-Solid-State Li Batteries via 2D MeV Ion-Beam Analysis. *Batteries* **2021,** 7, (2), 41.

[182] Möller, S., Material Analysis and Testing. In *Accelerator Technology: Applications in Science, Medicine, and Industry*, Springer International Publishing: Cham, **2020**; pp 271-342.

[183] Möller, S., Introduction. In *Accelerator Technology: Applications in Science, Medicine, and Industry*, Springer International Publishing: Cham, **2020**; pp 1-4.

[184] Chen, H.; Wang, X. M.; Shao, L.; Liu, J. R.; Yen, A. C.; Chu, W.-k., Cross-sections of $^{10}B(\alpha, p)^{13}C$ nuclear reaction for boron analysis. *Nuclear Instruments and Methods in Physics Research Section B: Beam Interactions with Materials and Atoms* **2003,** 211, (1), 1-6.

[185] Mayer, M., SIMNRA user's guide. Max-Planck-Institut für Plasmaphysik Garching: **1997**.

[186] Fearn, S., An Introduction to Time-of-Flight Secondary Ion Mass Spectrometry (ToF-SIMS) and its Application to Materials Science. In Morgan & Claypool Publishers: **2015**.

[187] NETZSCH-Gerätebau GmbH, STA 449 F1 Jupiter®. https://www.netzsch-thermal-analysis.com/de/produkte-loesungen/simultane-thermogravimetrie-dynamische-differenzkalorimetrie/sta-449-f1-jupiter/, **2021**, Accessed: 24.09.2021.

[188] Saadatkhah, N.; Carillo Garcia, A.; Ackermann, S.; Leclerc, P.; Latifi, M.; Samih, S.; Patience, G. S.; Chaouki, J., Experimental methods in chemical engineering: Thermogravimetric analysis—TGA. *The Canadian Journal of Chemical Engineering* **2020,** 98, (1), 34-43.

[189] Vyazovkin, S., Thermogravimetric Analysis. In *Characterization of Materials*, pp 1-12.

[190] Materazzi, S.; Vecchio, S., Evolved gas analysis by mass spectrometry. *Applied Spectroscopy Reviews* **2011,** 46, (4), 261-340.

[191] Brown, M. E., Differential thermal analysis (DTA) and differential scanning calorimetry (DSC). In *Introduction to Thermal Analysis: Techniques and applications*, Springer Netherlands: Dordrecht, **1988**; pp 23-49.

[192] Lowell, S.; Shields, J. E., Gas adsorption. In *Powder Surface Area and Porosity*, Springer Netherlands: Dordrecht, **1991**; pp 7-10.

[193] Lowell, S.; Shields, J. E., Powder surface area and porosity. Springer Science & Business Media: **2013**; Vol. 2.

[194] Thommes, M.; Kaneko, K.; Neimark, A. V.; Olivier, J. P.; Rodriguez-Reinoso, F.; Rouquerol, J.; Sing, K. S. W., Physisorption of gases, with special reference to the evaluation of surface area and pore size distribution (IUPAC Technical Report). *Pure and Applied Chemistry* **2015,** 87, (9-10), 1051-1069.

[195] Brunauer, S.; Emmett, P. H.; Teller, E., Adsorption of Gases in Multimolecular Layers. *Journal of the American Chemical Society* **1938,** 60, (2), 309-319.

[196] Lowell, S.; Shields, J. E., The single point BET method [13]. In *Powder Surface Area and Porosity*, Springer Netherlands: Dordrecht, **1991**; pp 30-34.

[197] Lowell, S.; Shields, J. E.; Thomas, M. A.; Thommes, M., Density Measurement. In *Characterization of Porous Solids and Powders: Surface Area, Pore Size and Density*, Springer Netherlands: Dordrecht, **2004**; pp 326-338.

[198] Quantachrome, Density Determination-Tap, Bulk, Geometric, Envelope http://www.quantachrome.com/density/density.html, **2020**, Accessed: 23.09.2021.

[199] Mori, Y.; Yoshida, H.; Masuda, H. In Particle size analysis by laser diffraction method using reference particles, Advanced Materials Research, 2012; Trans Tech Publ: **2012**; pp 33-37.

[200] de Boer, G. B. J.; de Weerd, C.; Thoenes, D.; Goossens, H. W. J., Laser Diffraction Spectrometry: Fraunhofer Diffraction Versus Mie Scattering. *Particle & Particle Systems Characterization* **1987,** 4, (1-4), 14-19.

[201] Shizuka, K.; Okahara, K., Layered lithium nickel manganese cobalt composite oxide powder for material of positive electrode of lithium secondary battery, process for producing the same, positive electrode of lithium secondary battery therefrom, and lithium secondary battery. In Google Patents: **2013**.

[202] Kim, T.; Choi, W.; Shin, H.-C.; Choi, J.-Y.; Kim, J. M.; Park, M.-S.; Yoon, W.-S., Applications of Voltammetry in Lithium Ion Battery Research. *J. Electrochem. Sci. Technol* **2020,** 11, (1), 14-25.

[203] Elgrishi, N.; Rountree, K. J.; McCarthy, B. D.; Rountree, E. S.; Eisenhart, T. T.; Dempsey, J. L., A Practical Beginner's Guide to Cyclic Voltammetry. *Journal of Chemical Education* **2018,** 95, (2), 197-206.

[204] Heinze, J., Cyclovoltammetrie—die „Spektroskopie" des Elektrochemikers. *Angewandte Chemie* **1984,** 96, (11), 823-840.

[205] Yang, X.; Rogach, A. L., Electrochemical Techniques in Battery Research: A Tutorial for Nonelectrochemists. *Advanced Energy Materials* **2019,** 9, (25), 1900747.

[206] Choi, W.; Shin, H.-C.; Kim, J. M.; Choi, J.-Y.; Yoon, W.-S., Modeling and applications of electrochemical impedance spectroscopy (EIS) for lithium-ion batteries. *Journal of Electrochemical Science and Technology* **2020,** 11, (1), 1-13.

[207] Chen, K.; Huang, M.; Shen, Y.; Lin, Y.; Nan, C. W., Enhancing ionic conductivity of $Li_{0.35}La_{0.55}TiO_3$ ceramics by introducing $Li_7La_3Zr_2O_{12}$. *Electrochimica Acta* **2012,** 80, 133-139.

[208] Haile, S. M.; Staneff, G.; Ryu, K. H., Non-stoichiometry, grain boundary transport and chemical stability of proton conducting perovskites. *Journal of Materials Science* **2001,** 36, (5), 1149-1160.

[209] Blöchl, P. E., Projector augmented-wave method. *Physical review B* **1994,** 50, (24), 17953.

[210] Kresse, G.; Furthmüller, J., Efficient iterative schemes for ab initio total-energy calculations using a plane-wave basis set. *Physical Review B* **1996,** 54, (16), 11169-11186.

[211] Perdew, J. P.; Burke, K.; Ernzerhof, M., Generalized gradient approximation made simple. *Physical review letters* **1996,** 77, (18), 3865.

[212] Sun, J.; Ruzsinszky, A.; Perdew, J. P., Strongly Constrained and Appropriately Normed Semilocal Density Functional. *Physical Review Letters* **2015,** 115, (3), 036402.

[213] Okhotnikov, K.; Charpentier, T.; Cadars, S., Supercell program: a combinatorial structure-generation approach for the local-level modeling of atomic substitutions and partial occupancies in crystals. *Journal of cheminformatics* **2016,** 8, (1), 1-15.

[214] Kuo, L.-Y.; Guillon, O.; Kaghazchi, P., Origin of Structural Phase Transitions in Ni-Rich $Li_xNi_{0.8}Co_{0.1}Mn_{0.1}O_2$ with Lithiation/Delithiation: A First-Principles Study. *ACS Sustainable Chemistry & Engineering* **2021,** 9, (22), 7437-7446.

[215] Dudarev, S. L.; Botton, G. A.; Savrasov, S. Y.; Humphreys, C. J.; Sutton, A. P., Electron-energy-loss spectra and the structural stability of nickel oxide: An LSDA+U study. *Physical Review B* **1998,** 57, (3), 1505-1509.

[216] Moradabadi, A.; Kaghazchi, P., Effect of lattice and dopant–induced strain on the conductivity of solid electrolytes: application of the elastic dipole method. *Materialia* **2020,** 9, 100607.

[217] Chang, C.-C.; Kumta, P. N., Mechanochemical synthesis of $LiNiO_2$. *Materials Science and Engineering: B* **2005,** 116, (3), 341-345.

[218] Zhu, J.; Vo, T.; Li, D.; Lu, R.; Kinsinger, N. M.; Xiong, L.; Yan, Y.; Kisailus, D., Crystal Growth of $Li[Ni_{1/3}Co_{1/3}Mn_{1/3}]O_2$ as a Cathode Material for High-Performance Lithium Ion Batteries. *Crystal Growth & Design* **2012,** 12, (3), 1118-1123.

[219] Du, B.; Mo, Y.; Jin, H.; Li, X.; Qu, Y.; Li, D.; Cao, B.; Jia, X.; Lu, Y.; Chen, Y., Radially Microstructural Design of $LiNi_{0.8}Co_{0.1}Mn_{0.1}O_2$ Cathode Material toward Long-Term Cyclability and High Rate Capability at High Voltage. *ACS Applied Energy Materials* **2020,** 3, (7), 6657-6669.

[220] Kramer, D.; Ceder, G., Tailoring the Morphology of $LiCoO_2$: A First Principles Study. *Chemistry of Materials* **2009,** 21, (16), 3799-3809.

[221] Kondrakov, A. O.; Geßwein, H.; Galdina, K.; de Biasi, L.; Meded, V.; Filatova, E. O.; Schumacher, G.; Wenzel, W.; Hartmann, P.; Brezesinski, T.; Janek, J., Charge-Transfer-

Induced Lattice Collapse in Ni-Rich NCM Cathode Materials during Delithiation. *The Journal of Physical Chemistry C* **2017,** 121, (44), 24381-24388.

[222] Friedrich, F.; Strehle, B.; Freiberg, A. T. S.; Kleiner, K.; Day, S. J.; Erk, C.; Piana, M.; Gasteiger, H. A., Editors' Choice—Capacity Fading Mechanisms of NCM-811 Cathodes in Lithium-Ion Batteries Studied by X-ray Diffraction and Other Diagnostics. *Journal of The Electrochemical Society* **2019,** 166, (15), A3760-A3774.

[223] Zheng, X.; Li, X.; Zhang, B.; Wang, Z.; Guo, H.; Huang, Z.; Yan, G.; Wang, D.; Xu, Y., Enhanced electrochemical performance of $LiNi_{0.8}Co_{0.1}Mn_{0.1}O_2$ cathode materials obtained by atomization co-precipitation method. *Ceramics International* **2016,** 42, (1, Part A), 644-649.

[224] Gao, S.; Cheng, Y.-T.; Shirpour, M., Effects of Cobalt Deficiency on Nickel-Rich Layered $LiNi_{0.8}Co_{0.1}Mn_{0.1}O_2$ Positive Electrode Materials for Lithium-Ion Batteries. *ACS Applied Materials & Interfaces* **2019,** 11, (1), 982-989.

[225] Hua, W.; Schwarz, B.; Knapp, M.; Senyshyn, A.; Missiul, A.; Mu, X.; Wang, S.; Kübel, C.; Binder, J. R.; Indris, S.; Ehrenberg, H., (De) Lithiation Mechanism of Hierarchically Layered $LiNi_{1/3}Co_{1/3}Mn_{1/3}O_2$ Cathodes during High-Voltage Cycling. *Journal of The Electrochemical Society* **2018,** 166, (3), A5025.

[226] Choi, Y.-M.; Pyun, S.-I.; Moon, S.-I., Effects of cation mixing on the electrochemical lithium intercalation reaction into porous $Li_{1-\delta}Ni_{1-y}Co_yO_2$ electrodes. *Solid State Ionics* **1996,** 89, (1), 43-52.

[227] C.D. Wagner, A. V. N., A. Kraut-Vass, J.W. Allison, C.J. Powell, J.R.Jr. Rumble, NIST Standard Reference Database 20, Version 3.4 (web version). http:/srdata.nist.gov/xps/,**2003**, Accessed:

[228] Biesinger, M. C.; Payne, B. P.; Grosvenor, A. P.; Lau, L. W. M.; Gerson, A. R.; Smart, R. S. C., Resolving surface chemical states in XPS analysis of first row transition metals, oxides and hydroxides: Cr, Mn, Fe, Co and Ni. *Applied Surface Science* **2011,** 257, (7), 2717-2730.

[229] Gurr, G.; Montgomery, P.; Knutson, C.; Gorres, B., The crystal structure of trigonal diboron trioxide. *Acta Crystallographica Section B: Structural Crystallography and Crystal Chemistry* **1970,** 26, (7), 906-915.

[230] Prewitt, C.; Shannon, R., Crystal structure of a high-pressure form of B_2O_3. *Acta Crystallographica Section B: Structural Crystallography and Crystal Chemistry* **1968,** 24, (6), 869-874.

[231] Xie, Q.; Li, W.; Dolocan, A.; Manthiram, A., Insights into Boron-based Polyanion-tuned High-nickel Cathodes for High-energy-density Lithium-ion Batteries. *Chemistry of Materials* **2019,** 31, (21), 8886-8897.

[232] Lim, S. N.; Ahn, W.; Yeon, S.-H.; Park, S. B., Enhanced elevated-temperature performance of $Li(Ni_{0.8}Co_{0.15}Al_{0.05})O_2$ electrodes coated with Li_2O-$2B_2O_3$ glass. *Electrochimica Acta* **2014,** 136, 1-9.

[233] Lee, K.; Yang, G. J.; Kim, H.; Kim, T.; Lee, S. S.; Choi, S.-Y.; Choi, S.; Kim, Y., Composite coating of Li_2O–$2B_2O_3$ and carbon as multi-conductive electron/Li-ion channel on the surface of $LiNi_{0.5}Mn_{1.5}O_4$ cathode. *Journal of Power Sources* **2017,** 365, 249-256.

[234] Yin, S. C.; Rho, Y. H.; Swainson, I.; Nazar, L. F., X-ray/Neutron Diffraction and Electrochemical Studies of Lithium De/Re-Intercalation in $Li_{1-x}Co_{1/3}Ni_{1/3}Mn_{1/3}O_2$ ($x = 0 \rightarrow 1$). *Chemistry of Materials* **2006,** 18, (7), 1901-1910.

[235] Luo, Y.-R., Comprehensive handbook of chemical bond energies. CRC press: **2007**.

[236] Wang, H.; Liu, L.; Wang, R.; Zhang, D.; Zhu, L.; Qiu, S.; Wei, Y.; Jin, X.; Zhang, Z., Design and synthesis of high performance $LiFePO_4$/C nanomaterials for lithium ion batteries assisted by a facile H^+/Li^+ ion exchange reaction. *Journal of Materials Chemistry A* **2015,** 3, (15), 8062-8069.

[237] Zhuang, Q.-C.; Wei, T.; Du, L.-L.; Cui, Y.-L.; Fang, L.; Sun, S.-G., An Electrochemical Impedance Spectroscopic Study of the Electronic and Ionic Transport Properties of Spinel $LiMn_2O_4$. *The Journal of Physical Chemistry C* **2010,** 114, (18), 8614-8621.

[238] Sathiya, M.; Rousse, G.; Ramesha, K.; Laisa, C. P.; Vezin, H.; Sougrati, M. T.; Doublet, M. L.; Foix, D.; Gonbeau, D.; Walker, W.; Prakash, A. S.; Ben Hassine, M.; Dupont, L.; Tarascon, J. M., Reversible anionic redox chemistry in high-capacity layered-oxide electrodes. *Nature Materials* **2013,** 12, (9), 827-835.

[239] Sathiya, M.; Abakumov, A. M.; Foix, D.; Rousse, G.; Ramesha, K.; Saubanère, M.; Doublet, M. L.; Vezin, H.; Laisa, C. P.; Prakash, A. S.; Gonbeau, D.; VanTendeloo, G.; Tarascon, J. M., Origin of voltage decay in high-capacity layered oxide electrodes. *Nature Materials* **2015,** 14, (2), 230-238.

[240] Voronina, N.; Yaqoob, N.; Kim, H. J.; Lee, K.-S.; Lim, H.-D.; Jung, H.-G.; Guillon, O.; Kaghazchi, P.; Myung, S.-T., A New Approach to Stable Cationic and Anionic Redox Activity in O3-Layered Cathode for Sodium-Ion Batteries. *Advanced Energy Materials* **2021,** 11, (25), 2100901.

[241] Shannon, R., Revised effective ionic radii and systematic studies of interatomic distances in halides and chalcogenides. *Acta Crystallographica Section A* **1976,** 32, (5), 751-767.

[242] Wang, H.; Tan, T. A.; Yang, P.; Lai, M. O.; Lu, L., High-Rate Performances of the Ru-Doped Spinel $LiNi_{0.5}Mn_{1.5}O_4$: Effects of Doping and Particle Size. *The Journal of Physical Chemistry C* **2011,** 115, (13), 6102-6110.

[243] Song, B.; Lai, M. O.; Lu, L., Influence of Ru substitution on Li-rich $0.55Li_2MnO_3{\cdot}0.45LiNi_{1/3}Co_{1/3}Mn_{1/3}O_2$ cathode for Li-ion batteries. *Electrochimica Acta* **2012,** 80, 187-195.

[244] Manju, U.; Awana, V. P. S.; Kishan, H.; Sarma, D. D., X-ray photoelectron spectroscopy of superconducting $RuSr_2Eu_{1.5}Ce_{0.5}Cu_2O_{10}$ and nonsuperconducting $RuSr_2EuCeCu_2O_{10}$. *Physical Review B* **2006,** 74, (24), 245106.

[245] Biesinger, M., X-ray Photoelectron Spectroscopy (XPS) Reference Pages http://www.xpsfitting.com/search/label/Ruthenium, **2020**, Accessed: 2021-11-28.

[246] Reddy, M.; Manoharan, S. S.; John, J.; Singh, B.; Rao, G. S.; Chowdari, B., Synthesis, Characterization, and Electrochemical Cycling Behavior of the Ru-Doped Spinel, $Li[Mn_{2-x}Ru_x]O_4$ (x= 0, 0.1, and 0.25). *Journal of the Electrochemical Society* **2009,** 156, (8), A652.

[247] Liu, W.; Oh, P.; Liu, X.; Lee, M.-J.; Cho, W.; Chae, S.; Kim, Y.; Cho, J., Nickel-Rich Layered Lithium Transition-Metal Oxide for High-Energy Lithium-Ion Batteries. *Angewandte Chemie International Edition* **2015,** 54, (15), 4440-4457.

[248] Richard, S.; Vassilios, S.; Martin, W.; Tobias, P., High-Energy Lithium-Ion Batteries via a Couette–Taylor-Flow-Reactor. *Material Matters* **2020,** 15, (2), 53-57.

[249] Liu, Y.; Huang, L.; Ding, Z.; Wang, J.; Wu, J.; Zhang, H.; Lavorgna, M., On the tailoring the 1D rod-like hierarchical nano/micro $LiNi_{0.8}Co_{0.15}Al_{0.05}O_2$ structure with exposed (101) plane by template method. *Journal of Alloys and Compounds* **2019,** 791, 356-363.

[250] Wang, Y.; Lai, W., Phase transition in lithium garnet oxide ionic conductors $Li_7La_3Zr_2O_{12}$: The role of Ta substitution and H_2O/CO_2 exposure. *Journal of Power Sources* **2015,** 275, 612-620.

[251] Larraz, G.; Orera, A.; Sanjuan, M., Cubic phases of garnet-type $Li_7La_3Zr_2O_{12}$: the role of hydration. *Journal of Materials Chemistry A* **2013,** 1, (37), 11419-11428.

[252] Sicklinger, J.; Metzger, M.; Beyer, H.; Pritzl, D.; Gasteiger, H. A., Ambient Storage Derived Surface Contamination of NCM811 and NCM111: Performance Implications and Mitigation Strategies. *Journal of The Electrochemical Society* **2019,** 166, (12), A2322-A2335.

[253] Matsui, M.; Sakamoto, K.; Takahashi, K.; Hirano, A.; Takeda, Y.; Yamamoto, O.; Imanishi, N., Phase transformation of the garnet structured lithium ion conductor: $Li_7La_3Zr_2O_{12}$. *Solid State Ionics* **2014,** 262, 155-159.

[254] Irvine, J. T. S.; Sinclair, D. C.; West, A. R., Electroceramics: Characterization by Impedance Spectroscopy. *Advanced Materials* **1990,** 2, (3), 132-138.

[255] Mann, M.; Küpers, M.; Häuschen, G.; Finsterbusch, M.; Fattakhova-Rohlfing, D.; Guillon, O., The influence of hafnium impurities on the electrochemical performance of tantalum substituted $Li_7La_3Zr_2O_{12}$ solid electrolytes. *Ionics* **2022,** 28, (1), 53-62.

[256] Ohta, S.; Komagata, S.; Seki, J.; Saeki, T.; Morishita, S.; Asaoka, T., All-solid-state lithium ion battery using garnet-type oxide and Li_3BO_3 solid electrolytes fabricated by screen-printing. *Journal of Power Sources* **2013,** 238, 53-56.

Appendix

Supplementary data – Characterization pristine and doped NCM

Table S 1: Chemical composition of cathode active materials determined by ICP-OES.

Active material	Elementary composition [mol]				
	Li	Ni	Co	Mn	B/Ru
NCM811	1.04	0.80	0.09	0.09	-
1B-NCM811	1.07	0.81	0.10	0.09	0.01
2B-NCM811	1.03	0.83	0.10	0.09	0.02
3B-NCM811	1.03	0.76	0.09	0.09	0.03
4B-NCM811	0.99	0.80	0.09	0.09	0.04
NCM811_o	1.06	0.82	0.10	0.10	-
2B-NCM811_o	1.02	0.80	0.09	0.09	0.02
2Ru-NCM811	1.04	0.79	0.09	0.09	0.02
NCM111	1.03	0.34	0.33	0.32	-
2B-NCM111	1.08	0.35	0.35	0.35	0.02
NCM811_CTFR	0.99	0.79	0.1	0.1	-

Table S 2: Particle size, BET surface area, and density of pristine and doped NCM811. The primary particle size was obtained from several SEM images. The mean value and the standard deviation are given.

Active material	D50 [µm]	Prim. particle size [nm]	BET surface area [m²/g]	Density [g/cm³]
NCM811	15	210 ± 86	1.56	3.91
1B-NCM811	15	219 ± 59		
2B-NCM811	14	167 ± 52	0.69	4.04
3B-NCM811	13	157 ± 48		
4B-NCM811	15	145 ± 48	0.32	
NCM811_o	13	318 ± 38		
2B-NCM811_o	14	297 ± 71		
2Ru-NCM811	11	145 ± 38		
NCM811_CTFR	15	448 ± 137		

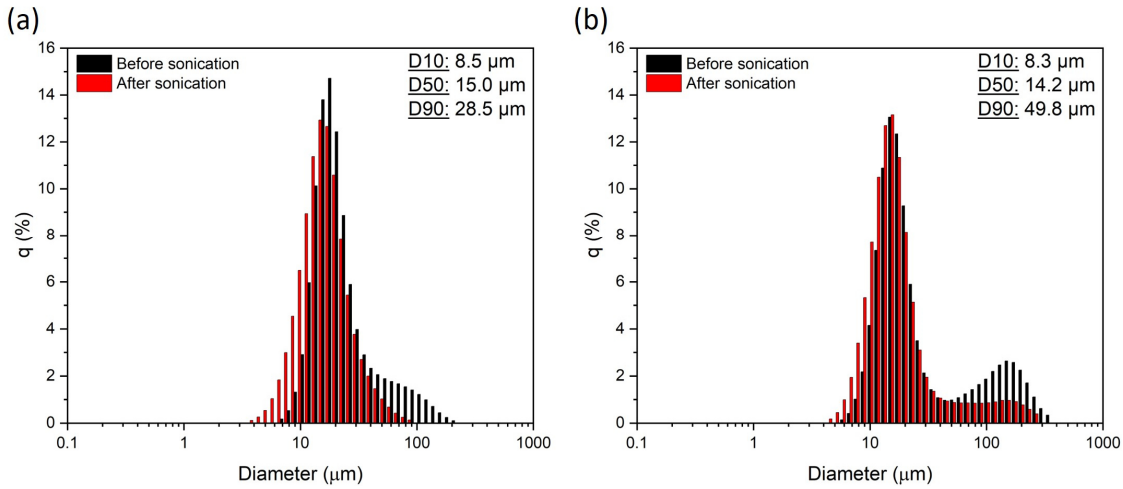

Figure S 1: Particle size distribution (PSD) of (a) pristine NCM811 and (b) 2B-NCM811.

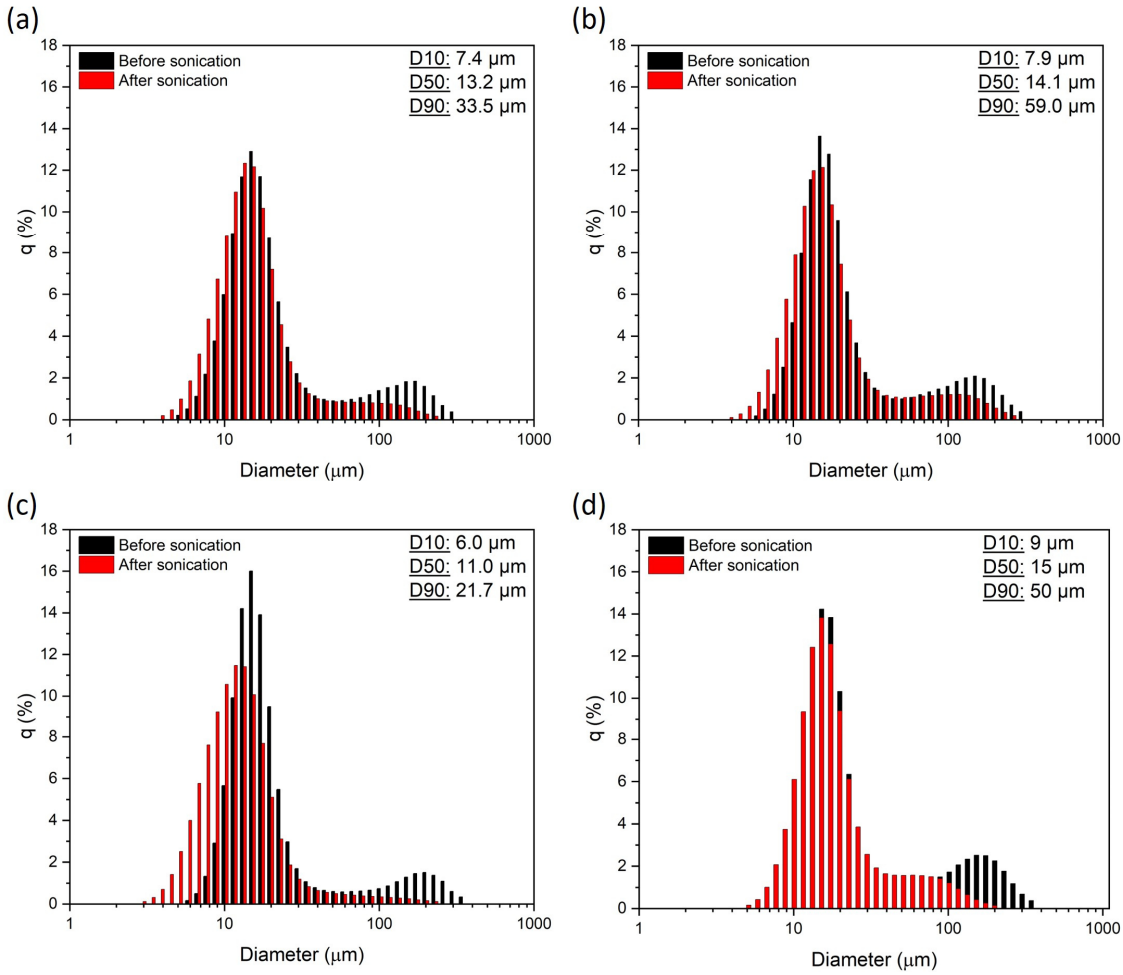

Figure S 2: Particle size distribution (PSD) of (a) pristine NCM811_o, (b) 2B-NCM811_o, (c) 2Ru-NCM811, and (d) NCM811_CTFR.

Supporting XRD patterns

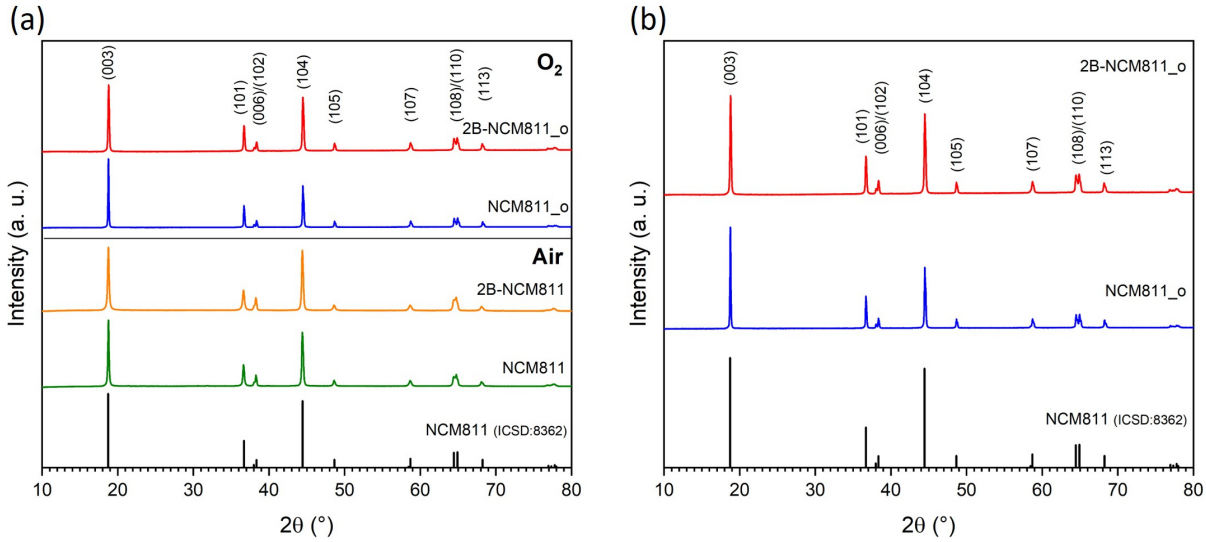

Figure S 3: (a) Comparison of the powder XRD patterns obtained after calcination in air (NCM811 and 2B-NCM811) and pure O_2 atmosphere (NCM811_o and 2B-NCM811_o). (b) Powder XRD patterns of NCM811_o and 2B-NCM811_o calcined in pure O_2 atmosphere.

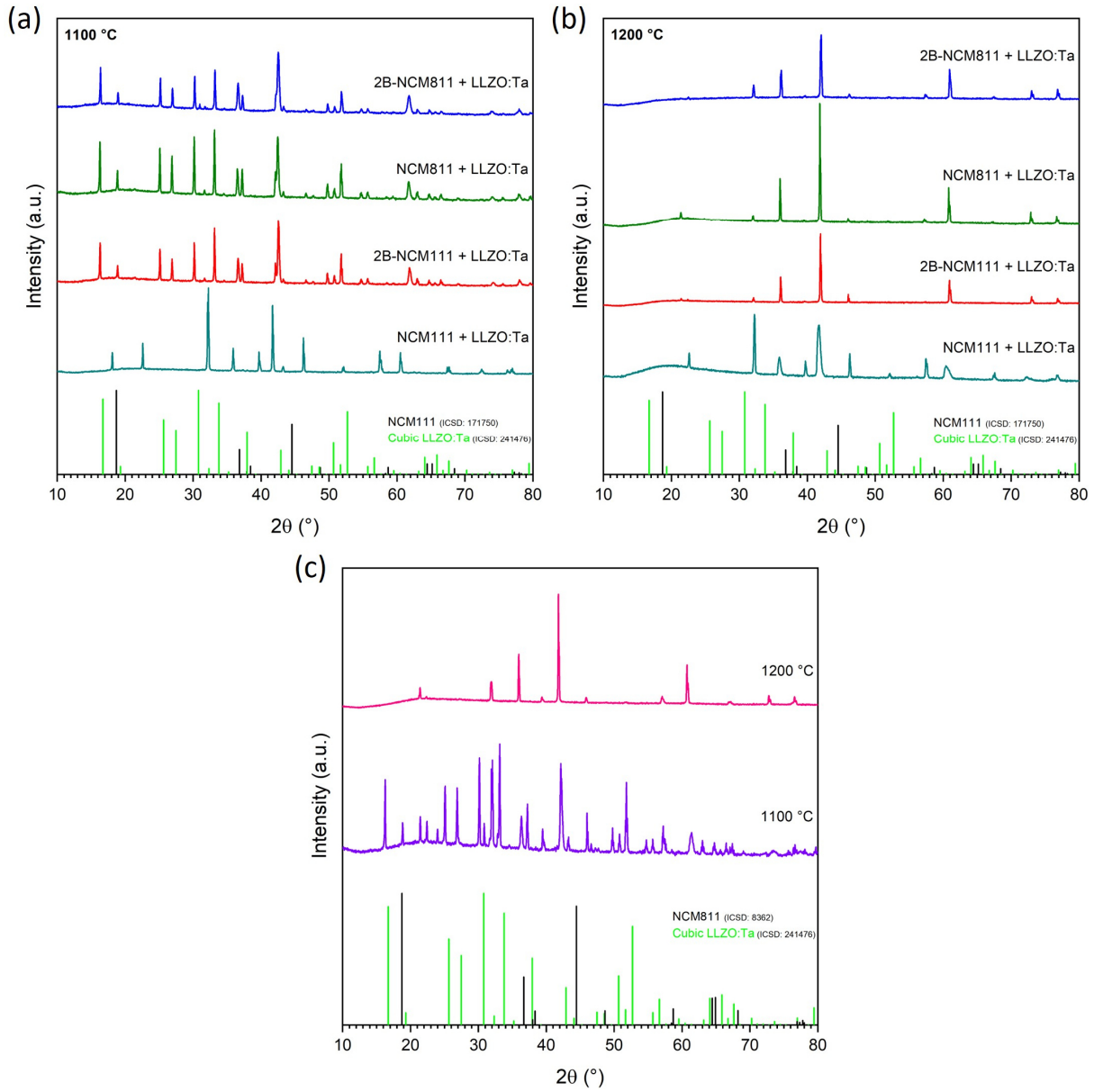

Figure S 4: *In-situ* HT-XRD patterns recorded at (a) 1100 °C and (b) 1200 °C for various NCM + LLZO:Ta mixtures. (c) HT-XRD pattern for 2Ru-NCM811 + LLZO:Ta recorded at 1100 and 1200 °C.

Supplementary data – Rietveld refinements

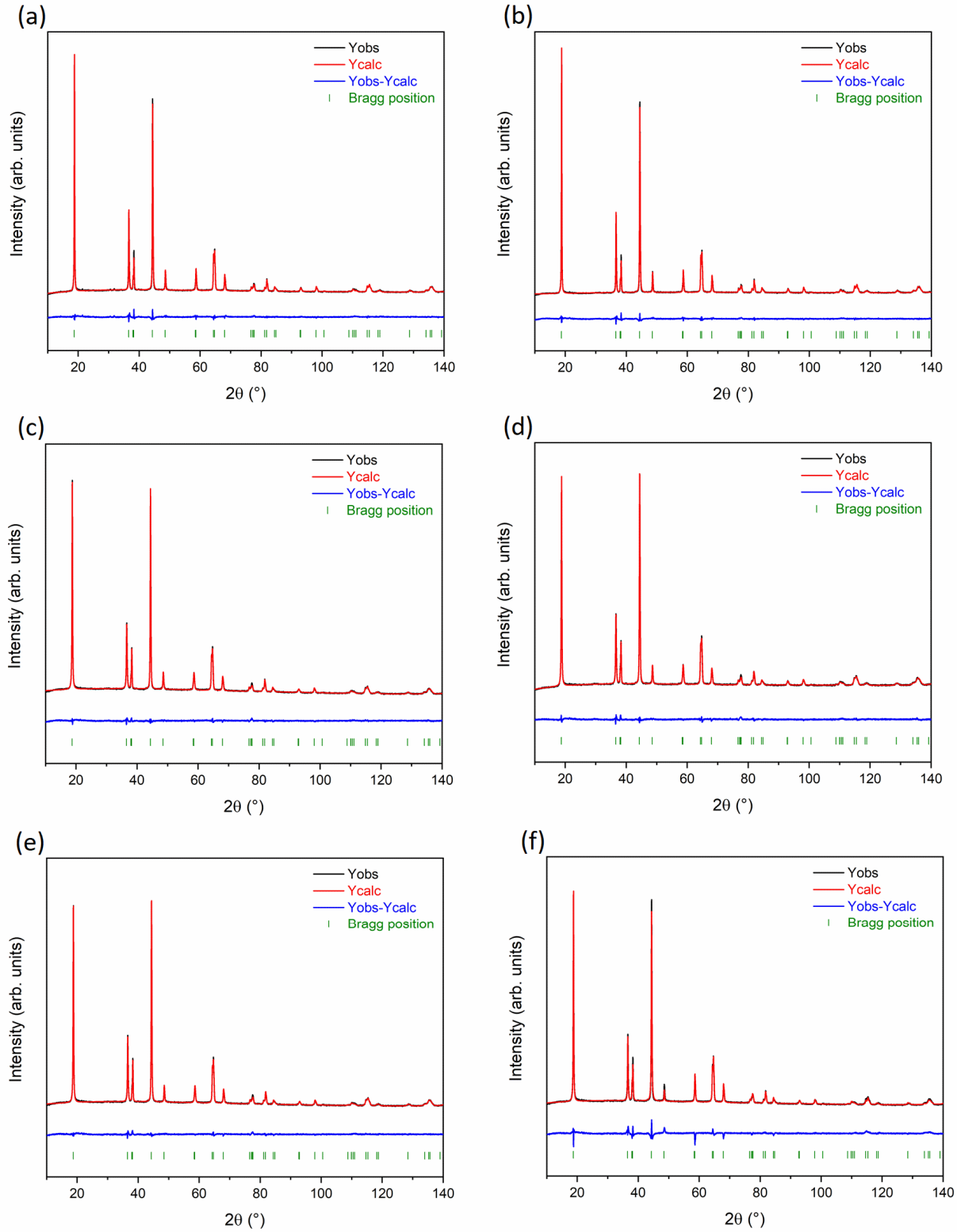

Figure S 5: Rietveld refined powder XRD pattern for (a) pristine NCM811, (b) 1B-NCM811, (c) 2B-NCM811, (d) 3B-NCM811, (e) 4B-NCM811, and (f) 4B-NCM811 with B-atoms on the tetrahedral interstitials.

Table S 3: Cation occupations and structural parameters determined by Rietveld refinement of the XRD patterns for pristine and B-doped NCM811.

	$(Li_{0.94}Ni_{0.06})(Li_{0.06}Ni_{0.74}Co_{0.1}Mn_{0.1})O_2$				Space group: $R\bar{3}m$	
a = 2.878(1) Å		c = 14.206(6) Å		D = 4.75 g/cm³	R_{wp} = 1.51 %; R_p = 1.06 %	
Atom	Wyckoff position	x	y	z	Occupancy	$B_{overall}$
Li1	3a	0	0	0	0.94	0.97
Li2	3b	0	0	0.5	0.06	0.97
Ni1	3b	0	0	0.5	0.74	0.97
Ni2	3a	0	0	0	0.06	0.97
Co1	3b	0	0	0.5	0.1	0.97
Mn1	3b	0	0	0.5	0.1	0.97
O1	6c	0	0	0.2415(1)	1	0.97
	$(Li_{0.94}Ni_{0.06})(Li_{0.05}Ni_{0.74}Co_{0.1}Mn_{0.1}B_{0.01})O_2$				Space group: $R\bar{3}m$	
a = 2.877(1) Å		c = 14.206(6) Å		D = 4.76 g/cm³	R_{wp} = 1.35 %; R_p = 0.96 %	
Atom	Wyckoff position	x	y	z	Occupancy	$B_{overall}$
Li1	3a	0	0	0	0.94	0.7
Li2	3b	0	0	0.5	0.05	0.7
Ni1	3b	0	0	0.5	0.74	0.7
Ni2	3a	0	0	0	0.06	0.7
Co1	3b	0	0	0.5	0.1	0.7
Mn1	3b	0	0	0.5	0.1	0.7
B1	3b	0	0	0.5	0.01	0.7
O1	6c	0	0	0.2413(1)	1	0.7
	$(Li_{0.95}Ni_{0.05})(Li_{0.03}Ni_{0.75}Co_{0.1}Mn_{0.1}B_{0.02})O_2$				Space group: $R\bar{3}m$	
a = 2.878(1) Å		c = 14.202(9) Å		D = 4.76 g/cm³	R_{wp} = 1.29 %; R_p = 0.97 %	
Atom	Wyckoff position	x	y	z	Occupancy	$B_{overall}$
Li1	3a	0	0	0	0.95	0.96
Li2	3b	0	0	0.5	0.03	0.96
Ni1	3b	0	0	0.5	0.75	0.96
Ni2	3a	0	0	0	0.05	0.96
Co1	3b	0	0	0.5	0.1	0.96
Mn1	3b	0	0	0.5	0.1	0.96
B1	3b	0	0	0.5	0.02	0.96
O1	6c	0	0	0.2406(1)	1	0.96

	$(Li_{0.93}Ni_{0.07})(Li_{0.04}Ni_{0.73}Co_{0.1}Mn_{0.1}B_{0.03})O_2$			Space group: $R\bar{3}m$	
a = 2.879(1) Å	c = 14.207(9) Å		D = 4.76 g/cm³	R_{wp} = 1.24 %; R_p = 0.91 %	
Atom	Wyckoff position	x	y	z	Occupancy	$B_{overall}$
Li1	3a	0	0	0	0.93	0.67
Li2	3b	0	0	0.5	0.04	0.67
Ni1	3b	0	0	0.5	0.73	0.67
Ni2	3a	0	0	0	0.07	0.67
Co1	3b	0	0	0.5	0.1	0.67
Mn1	3b	0	0	0.5	0.1	0.67
B1	3b	0	0	0.5	0.03	0.67
O1	6c	0	0	0.2408(1)	1	0.67

	$(Li_{0.92}Ni_{0.08})(Li_{0.04}Ni_{0.72}Co_{0.1}Mn_{0.1}B_{0.04})O_2$			Space group: $R\bar{3}m$	
a = 2.881(1) Å	c = 14.215(9) Å		D = 4.75 g/cm³	R_{wp} = 1.27 %; R_p = 0.94 %	
Atom	Wyckoff position	x	y	z	Occupancy	$B_{overall}$
Li1	3a	0	0	0	0.92	0.92
Li2	3b	0	0	0.5	0.04	0.92
Ni1	3b	0	0	0.5	0.72	0.92
Ni2	3a	0	0	0	0.08	0.92
Co1	3b	0	0	0.5	0.1	0.92
Mn1	3b	0	0	0.5	0.1	0.92
B1	3b	0	0	0.5	0.04	0.92
O1	6c	0	0	0.2404(1)	1	0.92

	$(Li_{0.91}Ni_{0.09})(Li_{0.09}Ni_{0.71}Co_{0.1}Mn_{0.1})B_{0.04}O_2$			Space group: $R\bar{3}m$	
a = 2.881(1) Å	c = 14.217(12) Å		D = 4.76 g/cm³	R_{wp} = 2.37 %; R_p = 1.47 %	
Atom	Wyckoff position	x	y	z	Occupancy	$B_{overall}$
Li1	3a	0	0	0	0.91	1.62
Li2	3b	0	0	0.5	0.09	1.62
Ni1	3b	0	0	0.5	0.71	1.62
Ni2	3a	0	0	0	0.09	1.62
Co1	3b	0	0	0.5	0.1	1.62
Mn1	3b	0	0	0.5	0.1	1.62
B1	6c	0	0	0.123(7)	0.02	1.62
O1	6c	0	0	0.2332(1)	1	1.62

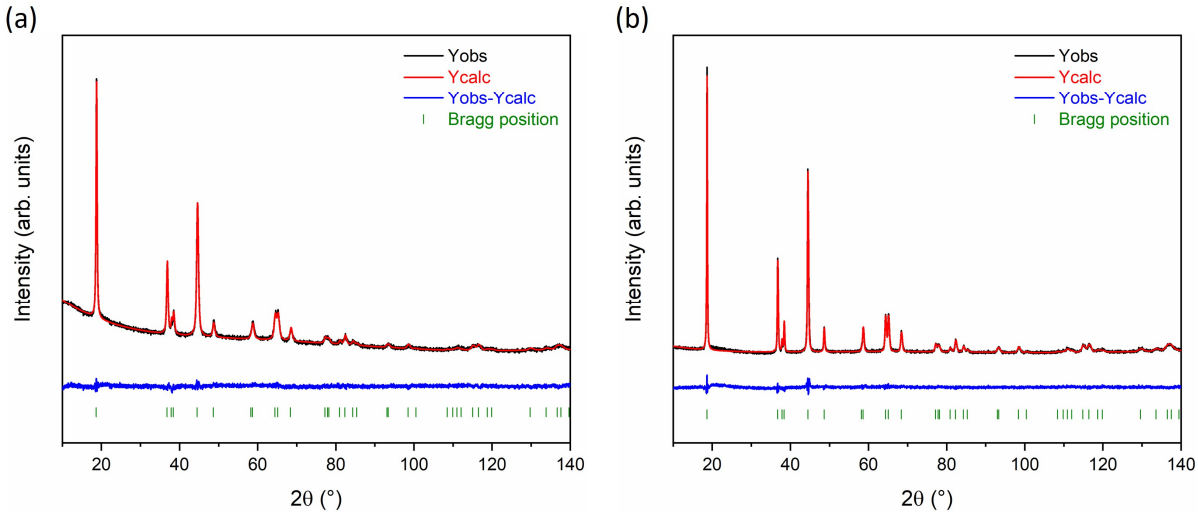

Figure S 6: Rietveld refined powder XRD pattern for (a) pristine NCM111 and (b) 2B-NCM111.

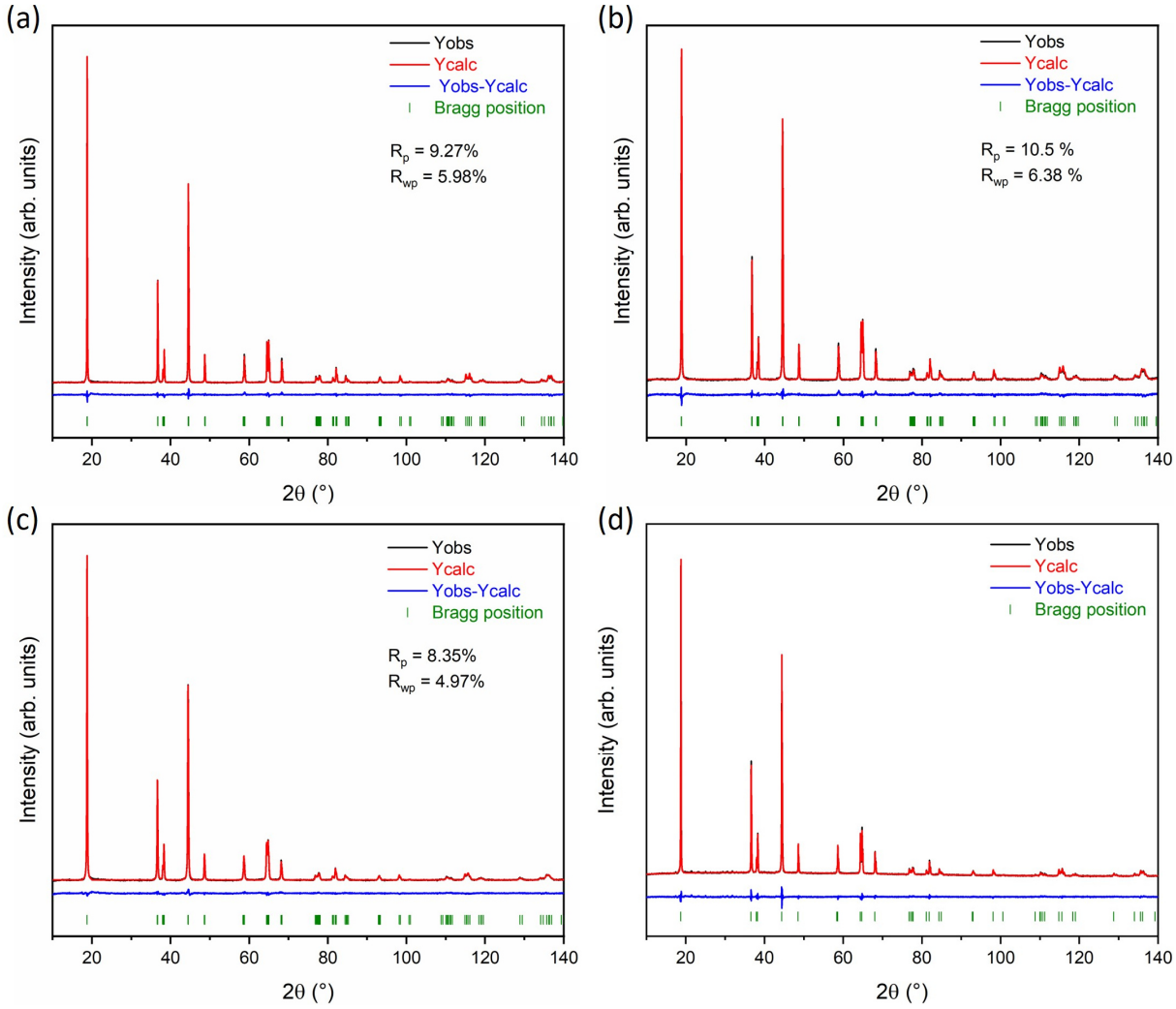

Figure S 7: Rietveld refined powder XRD pattern for (a) pristine NCM811_o, (b) 2B-NCM811_o, (c) 2Ru-NCM811, and (d) NCM811_CTFR.

Table S 4: Summary of lattice parameters and Rietveld refinement results of pristine and B-doped NCM calcined under pure oxygen atmosphere. Ni_{Li} gives the fraction of Ni ions occupying Li sites.

Active material	***a* [Å]**	***c* [Å]**	***c*/*a***	***I*(003)/*I*(104)**	**Ni_{Li} [%]**
NCM811_o	2.870(4)	14.196(4)	4.95	1.20	3.8
2B-NCM811_o	2.874(4)	14.206(4)	4.94	1.05	5.0

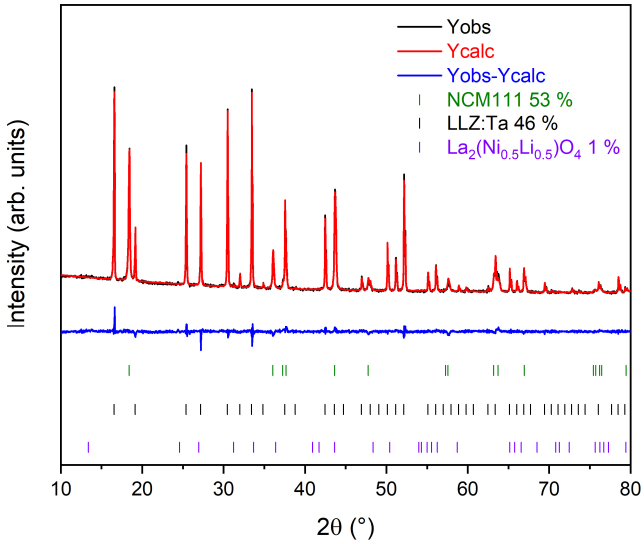

Figure S 8: Rietveld refinement plots of *in-situ* HT-XRD pattern at 800 °C for 2Ru-NCM811 + LLZO:Ta.

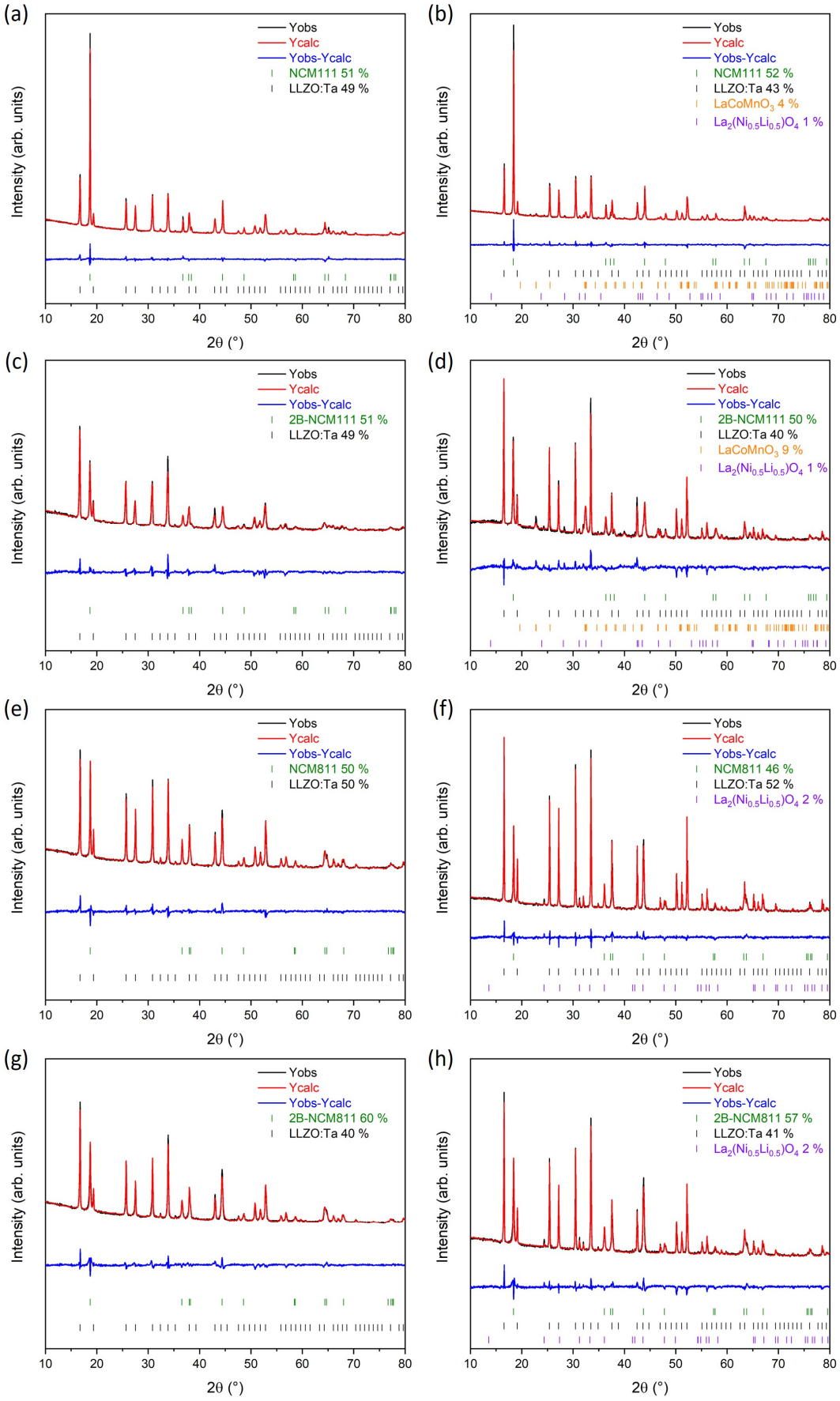

Figure S 9: Rietveld refinement plots of *in-situ* HT-XRD patterns recorded at 25 °C (left hand side) and 800 °C (right hand side) for NCM111 (a, b), 2B-NCM111 (c, d), NCM811 (e, f) and, 2B-NCM811 (g, h) mixed with LLZO:Ta.

Table S 5: Lattice parameters of LLZO:Ta, NCM111, and NCM811 determined from XRD patterns recorded at elevated temperatures, lattice parameters of NCM and LLZO:Ta obtained from the HT-XRD patterns, and differences of the lattice parameters (Δ). The values for Δ correspond to the difference between the lattice parameter of the single component and the component in the co-sintered mixture.

T [°C]	LLZO:Ta	LLZO:Ta + NCM111		LLZO:Ta + NCM811	
	a [Å]	*a* [Å]	**Δ *a* [Å]**	*a* [Å]	**Δ *a* [Å]**
600	13.063(3)	13.064(9)	**0.001**	13.065(2)	**0.002**
700	13.083(2)	13.085(9)	**0.002**	13.086(3)	**0.003**
800	13.105(2)	13.107(9)	**0.002**	13.111(3)	**0.006**

T [°C]	NCM111		NCM111 + LLZO:Ta			
	a [Å]	*c* [Å]	*a* [Å]	*c* [Å]	**Δ *a* [Å]**	**Δ *c* [Å]**
600	2.886(1)	14.411(12)	2.886(2)	14.409(15)	**0.001**	**– 0.002**
700	2.892(1)	14.445(12)	2.889(2)	14.437(18)	**0.003**	**– 0.008**
800	2.899(1)	14.483(9)	2.892(2)	14.468(12)	**0.007**	**– 0.015**

T [°C]	NCM811		NCM811 + LLZO:Ta			
	a [Å]	*c* [Å]	*a* [Å]	*c* [Å]	**Δ *a* [Å]**	**Δ *c* [Å]**
600	2.901(1)	14.380(18)	2.901(2)	14.387(12)	**– 0.001**	**0.007**
700	2.907(2)	14.411(18)	2.908(2)	14.418(15)	**0.001**	**0.006**
800	2.915(2)	14.440(20)	2.915(2)	14.449(15)	**0.001**	**0.009**

Table S 6: Atom–atom distances for cubic LLZO:Ta and the formed secondary phased obtained from the ICSD database.

	d(La-La) [Å]	**d(La-Zr) [Å]**	**d(La-Co, Mn) [Å]**	**d(La-Ni) [Å]**
Cubic LLZO:Ta (ICSD: 241476)	3.986	3.622	-	-
$LaCo_{1-x}Mn_xO_3$ (ICSD: 5993)	3.847	-	3.290	-
$La_2(Ni_{0.5}Li_{0.5})O_4$ (ICSD: 50951)	3.522	-	-	3.186

Supporting SEM images and EDS analysis

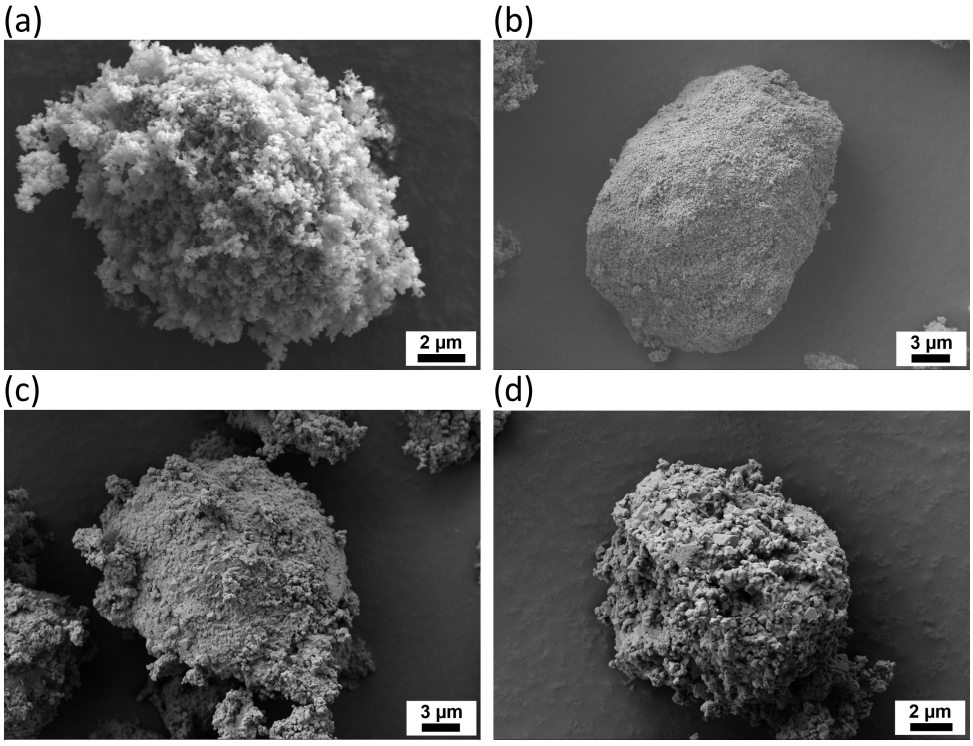

Figure S 10:SE-SEM images (3 kV) showing secondary particles of (a) NCM111, (b) 2B-NCM111, (c) NCM811, and (d) 2B-NCM811.

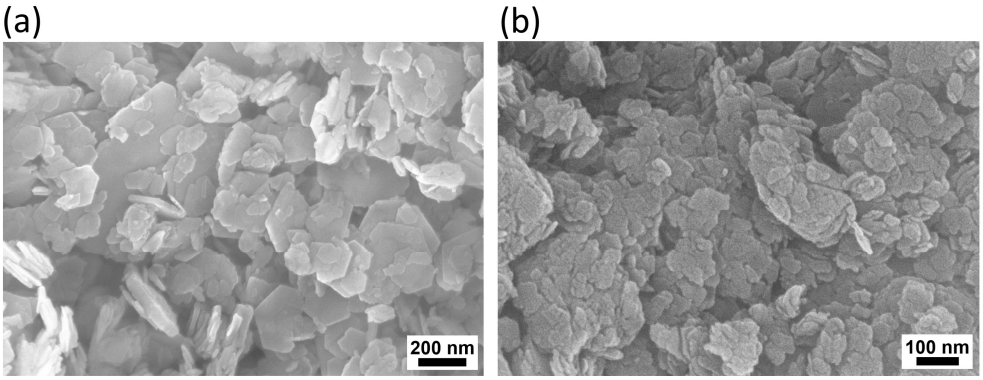

Figure S 11: SE-SEM images (15 kV) visualizing the hydroxide precursors of (a) NCM111 $(Ni_{1/3}Co_{1/3}Mn_{1/3})(OH)_2$ and of (b) NCM811 $(Ni_{0.8}Co_{0.1}Mn_{0.1})(OH)_2$.

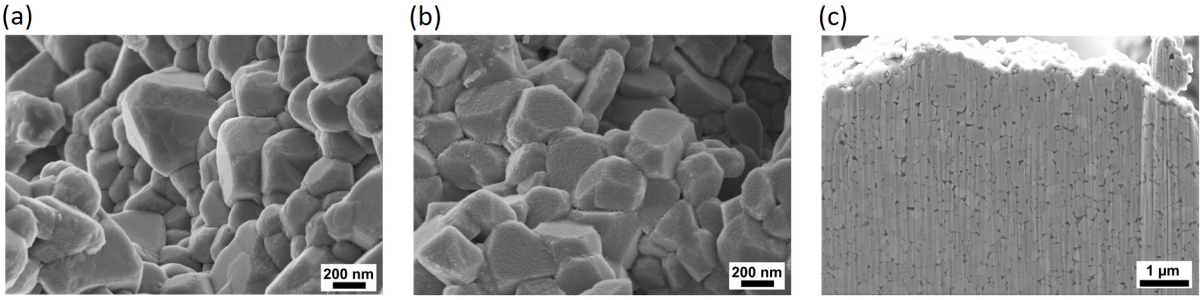

Figure S 12: SE-SEM images (3 kV) showing (a) NCM811_o, (b) 2B-NCM811_o, and (c) a cross section of a secondary particle of 2B-NCM811_o.

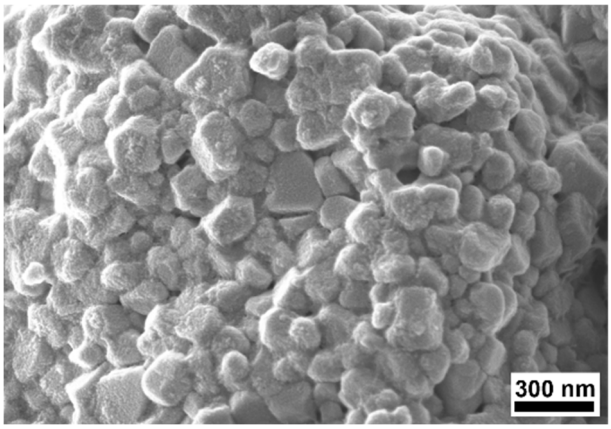

Figure S 13: SE-SEM image (2 kV) of NCM811 calcined at 750 °C.

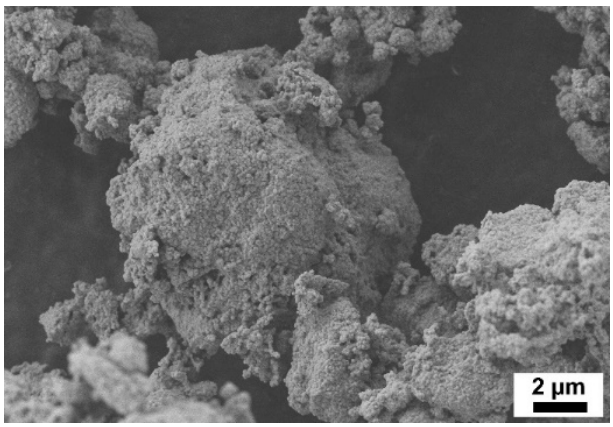

Figure S 14: SE-SEM image (3 kV) of a 2 mol% Ru-doped NCM811 secondary particle.

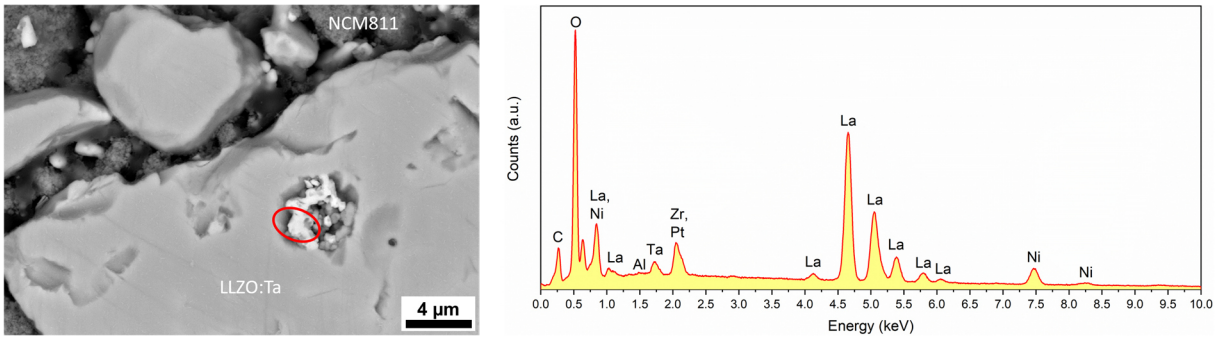

Figure S 15: Cross sectional, BSE-SEM image (15 kV) of 2B-NCM811 + LLZO:Ta after co-sintering at 800 °C for 1 h in air. The EDS point analysis was performed from the bright phase in the red marked region.

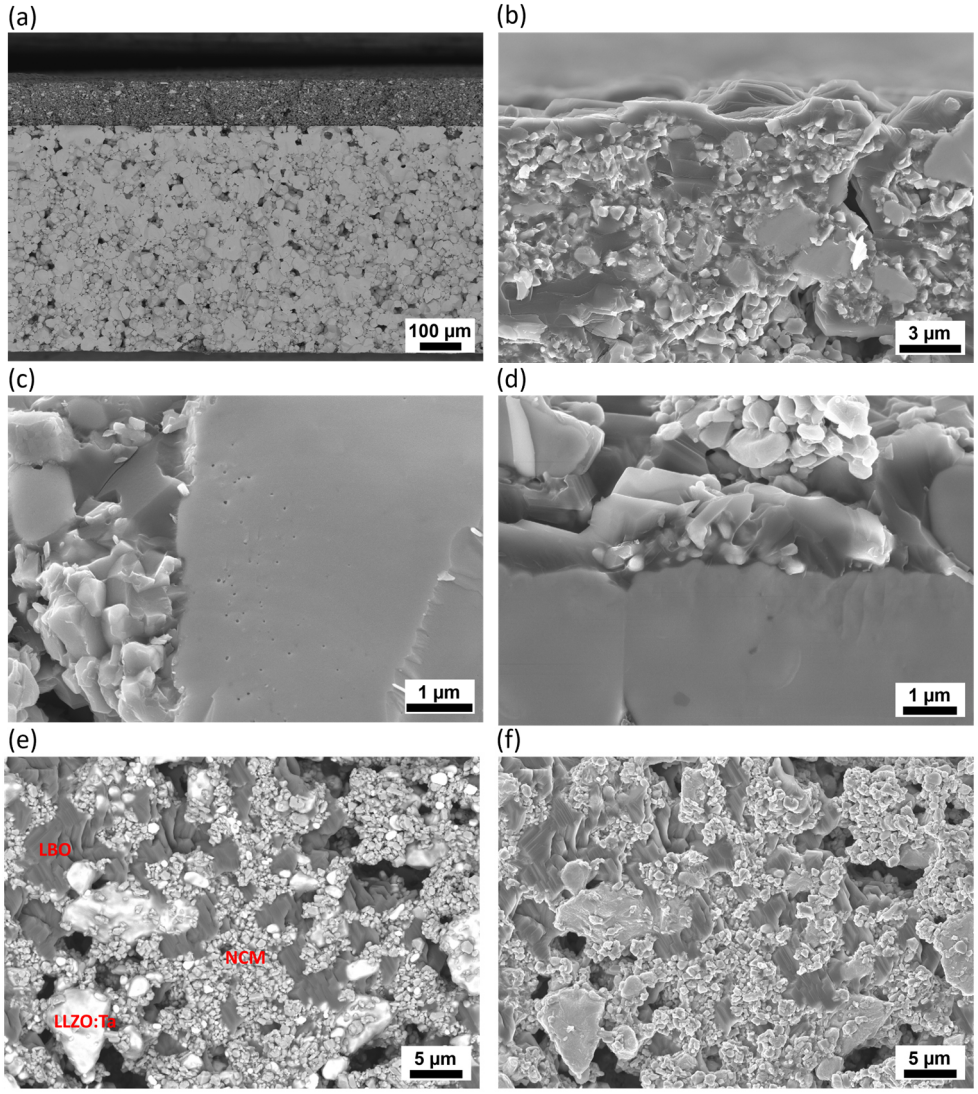

Figure S 16: SEM images (8 kV) of the fabricated half-cell. (a) Cross sectional, BSE-image of a fracture surface of the half-cell showing the composite cathode on top of the LLZO:Ta separator. (b) SE-image of the composite cathode showing the phase distribution. (c) Higher magnification SE image at the interface between NCM811, LBO, and LLZO:Ta within the composite cathode and (d) at the interface between composite cathode and separator. Surface (e) BSE- and (f) SE-images of the composite cathode (top view on (a)).

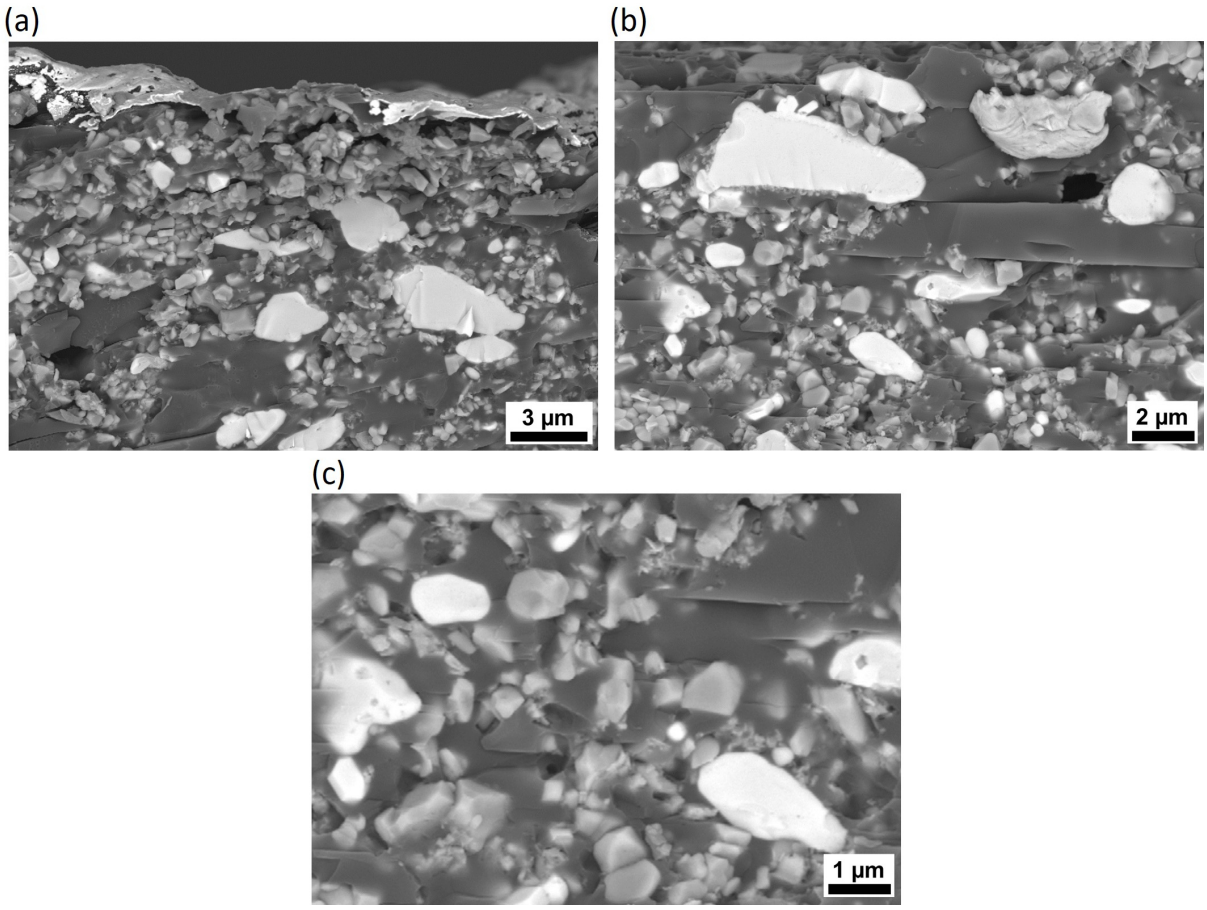

Figure S 17: Cross sectional BSE-SEM images of the composite cathode after 30 charge/discharge cycles with magnifications of (a) 5k, (b) 6k, and (c) 12k.

Supporting TEM analysis

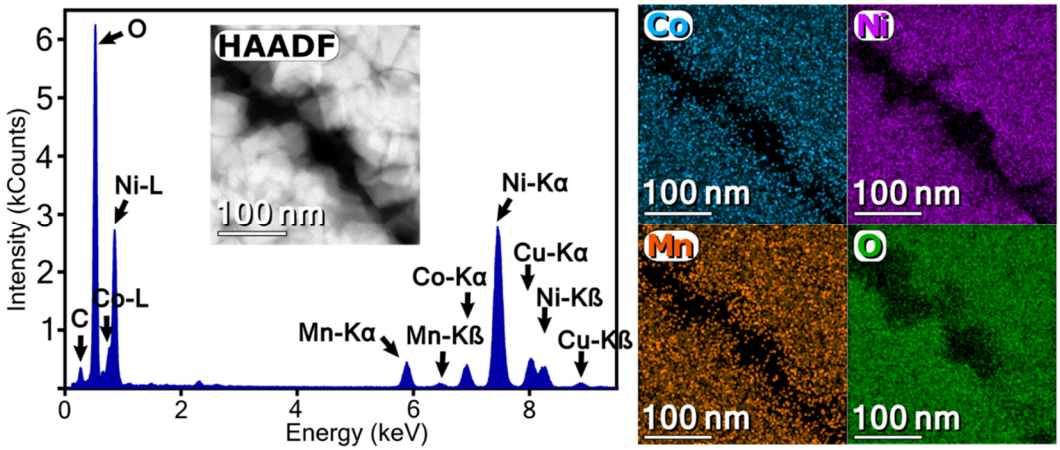

Figure S 18: HAADF-STEM image and an EDS spectrum taken from a cuboidal primary particle as well as elemental EDS mappings for Co, Ni, Mn, and O.

Supporting ion beam analysis data

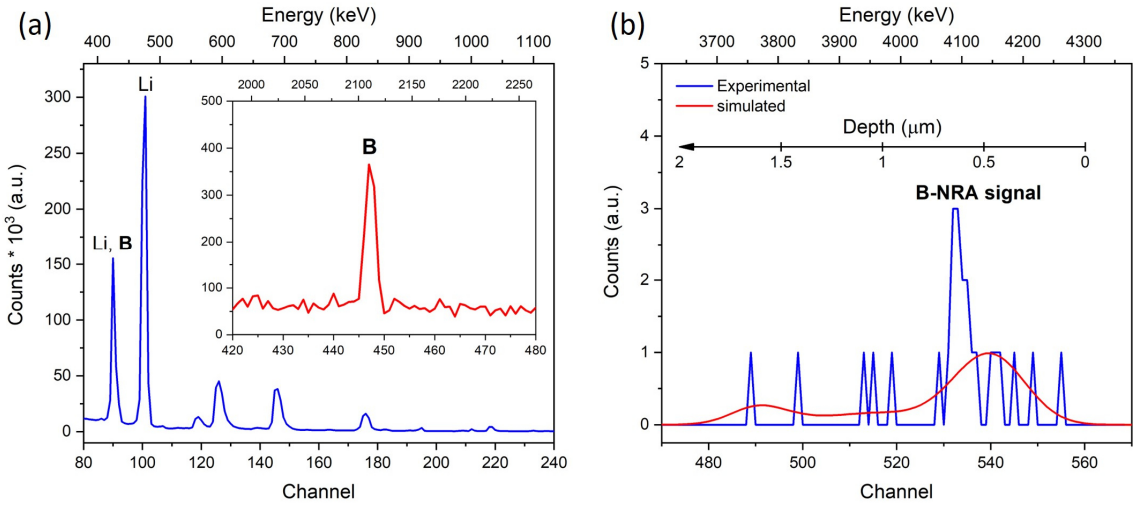

Figure S 19: Detection and localization of boron in NCM. (a) PIGE spectrum of 2B-NCM811 showing the Li- and B-signals. (b) NRA spectrum of 2B-NCM111 showing the B-signal.

Supporting DTA/TG/MS data

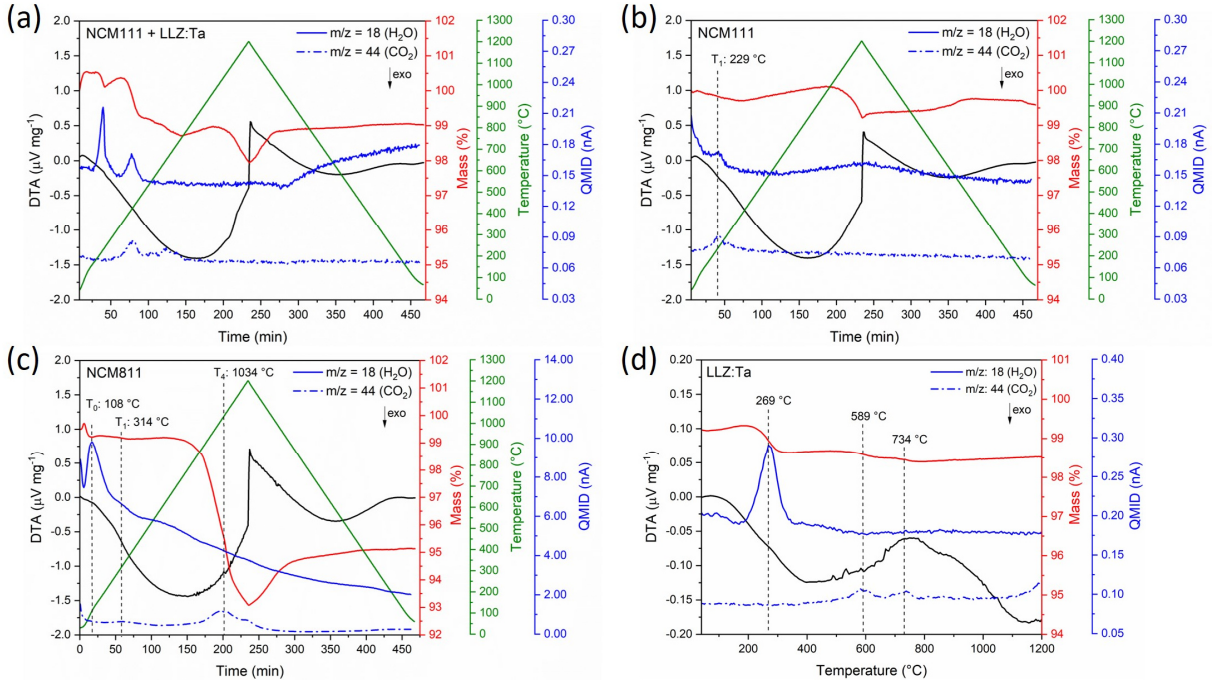

Figure S 20: DTA/TG/MS for (a) an 1:1 mixture of LLZO:Ta and NCM111, (b) pure NCM111, (c) pure NCM811, and (d) pure LLZO:Ta. The heating and cooling processes are visualized.

Supplementary data – Electrochemical characterization pristine and doped NCM

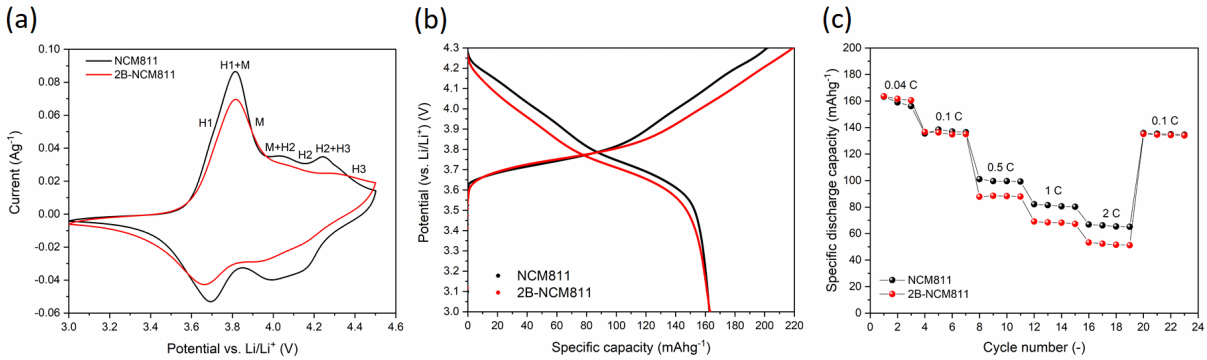

Figure S 21: Electrochemical performance of pristine and 2B-NCM811. (a) Cyclic voltammogram curves at a scan rate of 0.05 mV s^{-1} for the third cycle. (b) First galvanostatic charge-discharge cycle at 0.04 C and (c) rate capability tests at various C-rates.

Cyclic voltammetry (CV) (Figure S 21a) and galvanostatic charge/discharge analysis (Figure S 21b) confirm the electrochemical activity of NCM811 and 2B-NCM811. In the initial cycle at 0.04 C, 2B-NCM811 delivers a higher charge capacity than pristine NCM811, while similar discharge capacities of 163 and 164 mAh g^{-1} were obtained for pristine NCM811 and 2B-NCM811, respectively (Figure S 21b). The 2B-NCM811 delivers an initial Coulombic efficiency of only 75 %, while for pristine NCM811 82 % was obtained. The B-doped NCM811 cathode shows a higher charge capacity, while afterwards a similar discharge capacity was obtained. It is suggested that B doping and the resulting boron enrichment on the particle surface leads to a more intense SEI formation, resulting in a higher irreversible capacity in the initial cycle, but this phenomenon needs to be investigated further by future experiments. NCM811 and 2B-NCM811 are electrochemical active but the low discharge capacity of around 160 mAh g^{-1} is not satisfactory for Ni-rich NCM811. The reduced capacities can be attributed to the enhanced cation disorder discussed before.

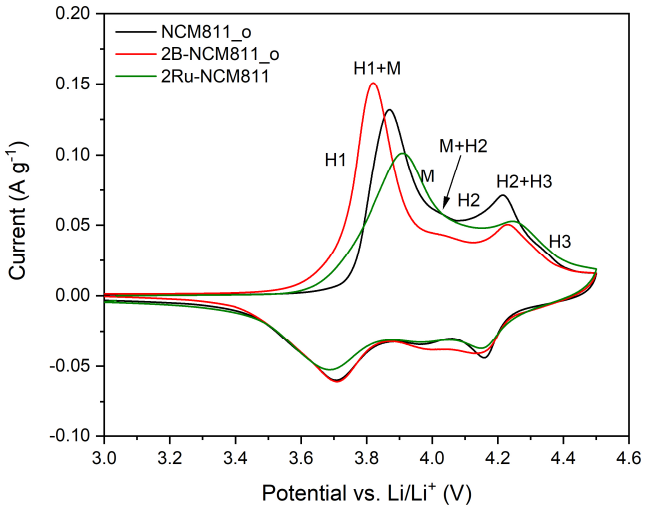

Figure S 22: Cyclic voltammogram curves of pristine NCM811_o, 2B-NCM811_o, and 2Ru-NCM811 at a scan rate of 0.05 mV s^{-1} for the first cycle.

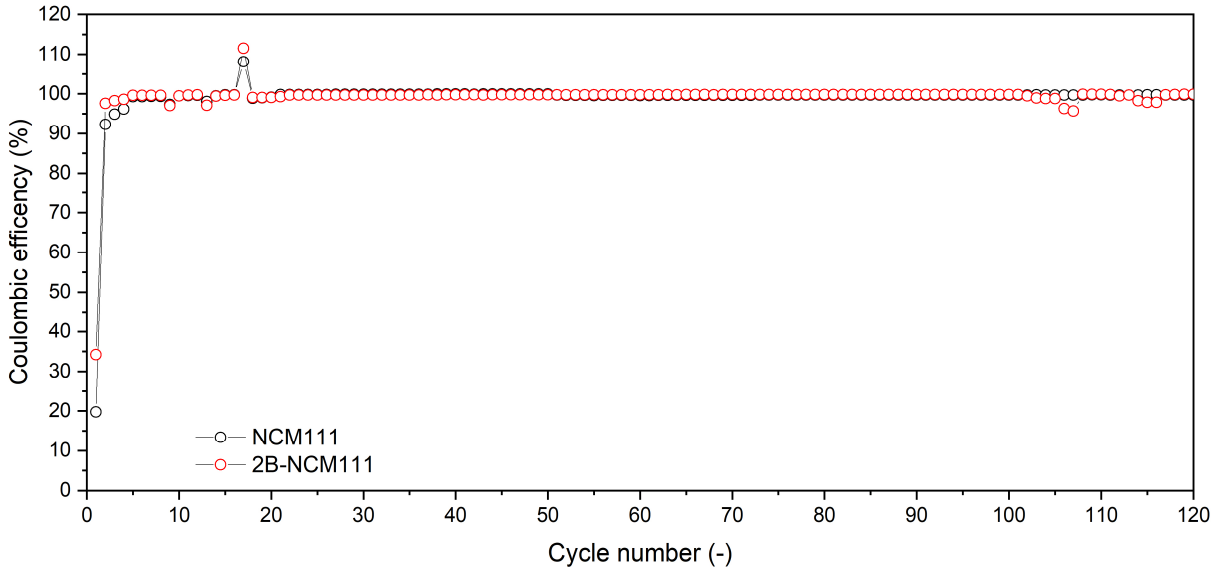

Figure S 23: Coulombic efficiencies for pristine NCM111 and 2B-NCM111 during rate capability tests and long-term cycling.

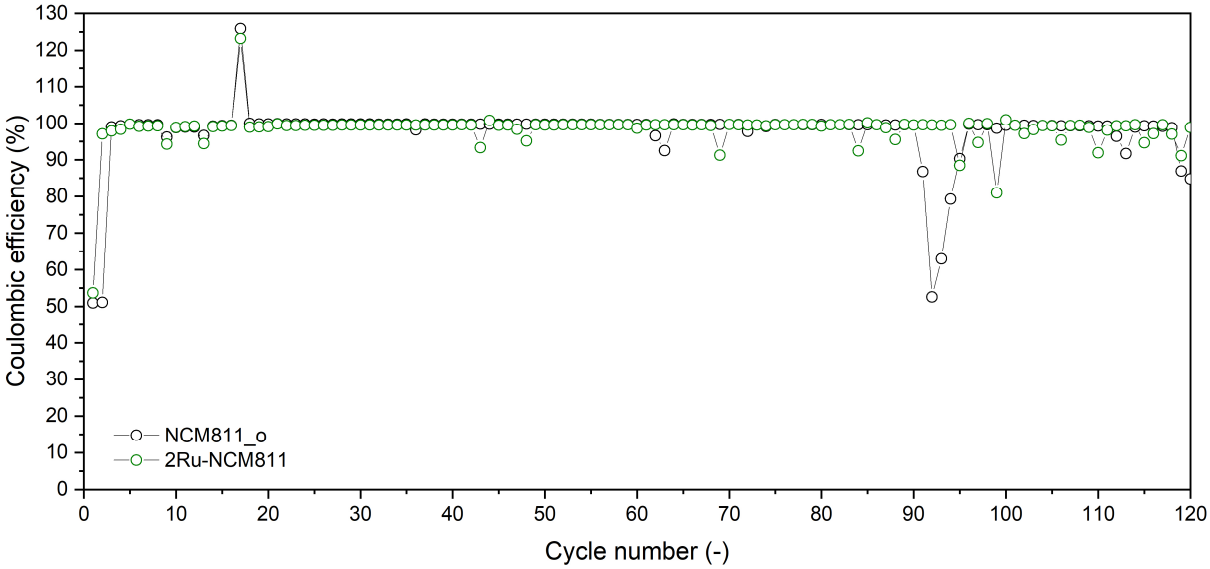

Figure S 24: Coulombic efficiencies for pristine NCM811_o and 2Ru-NCM811 during rate capability tests and long-term cycling.

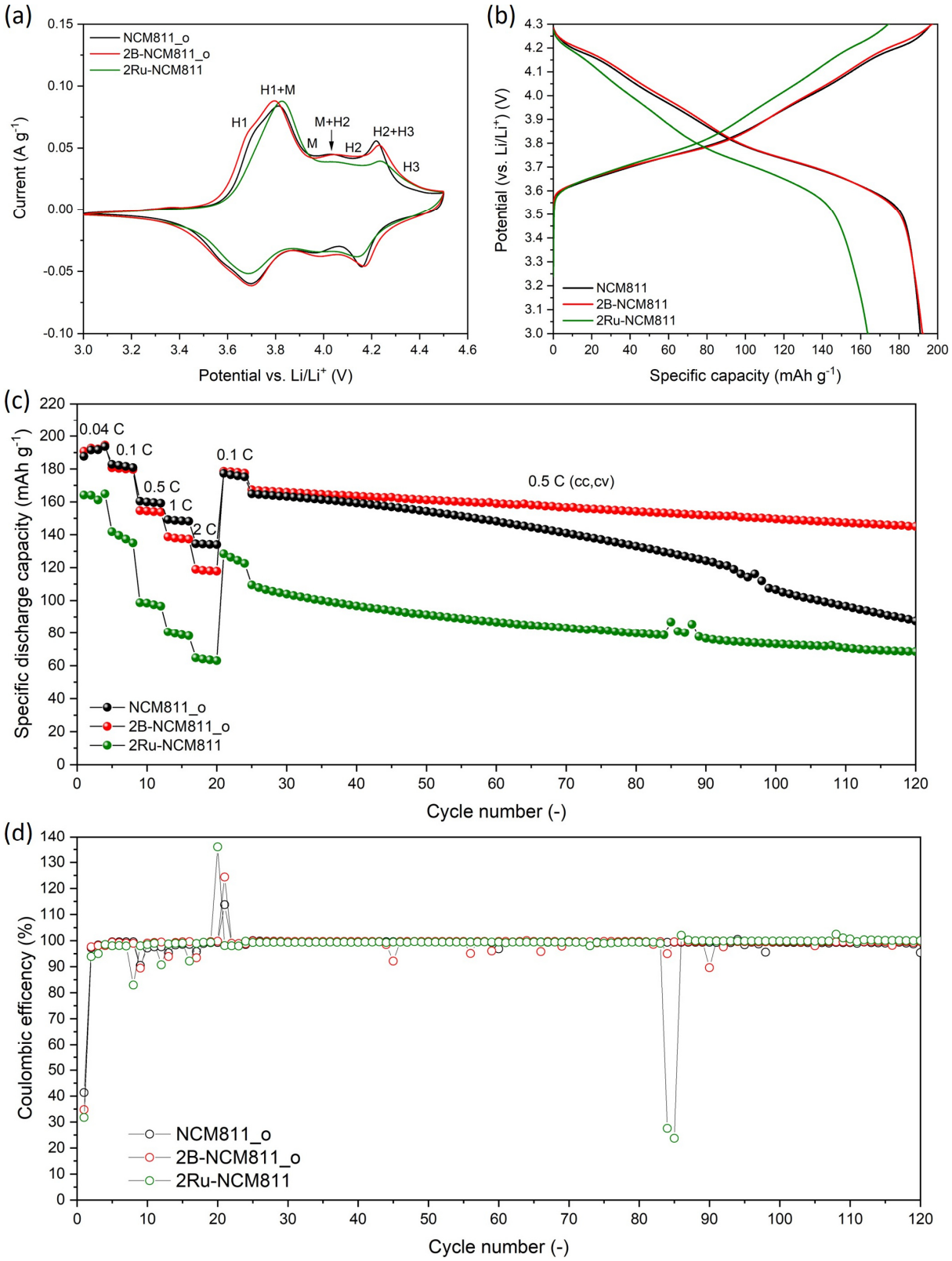

Figure S 25: Electrochemical performance of NCM811_o, 2B-NCM811_o, and 2Ru-NCM811. (a) Cyclic voltammogram curves at a scan rate of 0.05 mV s^{-1} for the second cycle. (b) Galvanostatic charge-discharge profiles at 0.04 C for the second cycle. (c) Rate capability tests at various C-rates with prolonged cycling at 0.5 C (cc, cv) and (d) Coulombic efficiencies for pristine NCM811_o, 2B-NCM811_o, and 2Ru-NCM811 during rate capability tests and long-term cycling.

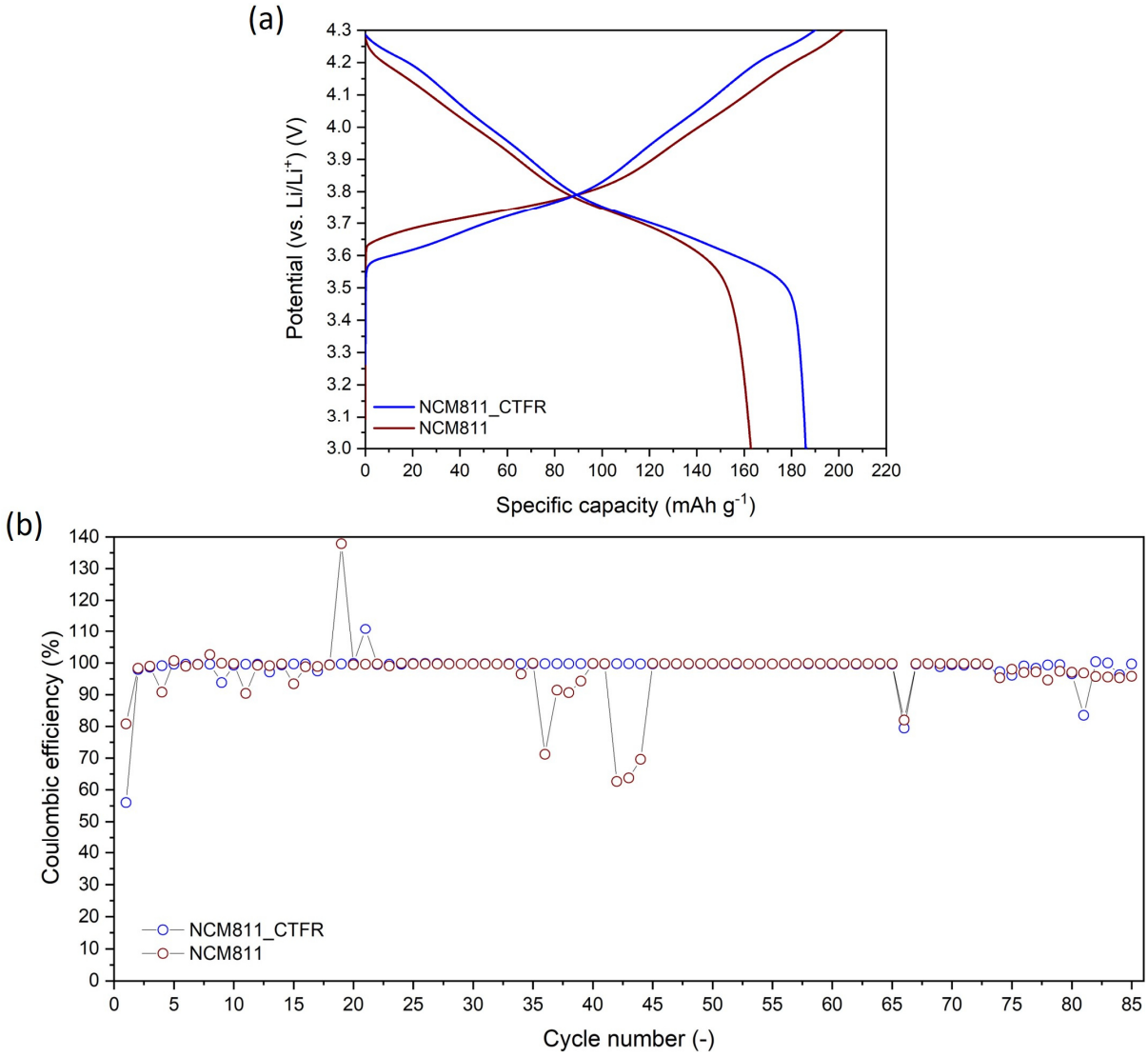

Figure S 26: (a) Galvanostatic charge-discharge profiles at 0.04 C for the second cycle and (b) Coulombic efficiencies for NCM811 and NCM811_CTFR during rate capability tests and long-term cycling.

Supplementary data – XPS

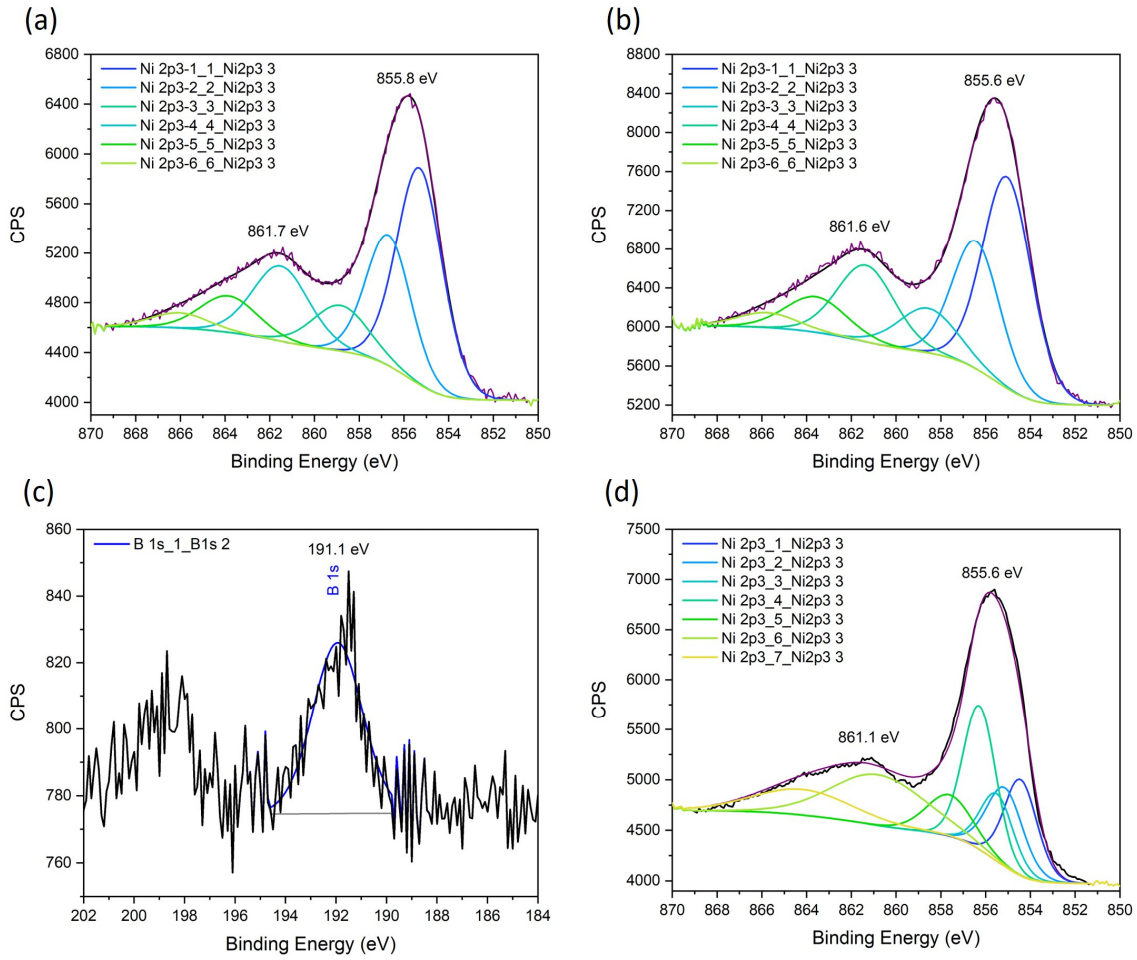

Figure S 27: Ni 2p3 XPS spectra collected from (a) NCM811, (b) 2B-NCM811, and (d) 2Ru-NCM811. (c) B 1s2 XPS spectrum collected from 2B-NCM811.

Supplementary data – Simulation

Table S 7: Lattice parameters for pristine NCM811 and 2Ru-NCM811 obtained by DFT calculation.

	a (Å)	*b* (Å)	*c* (Å)
$LiNi_{0.8}Co_{0.1}Mn_{0.1}O_2$	2.889	2.879	14.301
$LiNi_{0.8}Co_{0.1}Mn_{0.1}Ru_{0.02}O_2$	2.915	2.874	14.298
$Li_{0.98}Ni_{0.8}Co_{0.1}Mn_{0.1}Ru_{0.02}O_2$	2.915	2.895	14.366

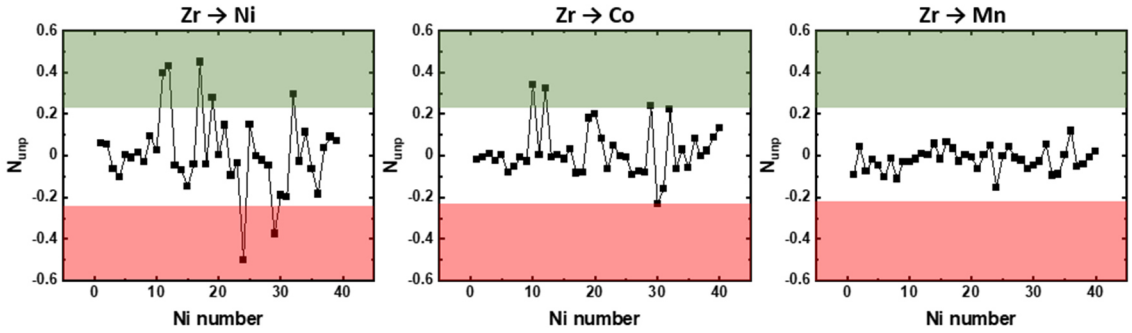

Figure S 28: Calculated change in magnetic moment of Ni cations in NCM811 after substitution of each TM with Zr. The positive values indicate that Ni cations undergo reduction, while the negative values indicate the oxidation of Ni cations. The green and red filled colors present regions where large reduction and oxidation, respectively occur.

Supplementary data – Characterization of NCM811, LLZO:Ta and LBO

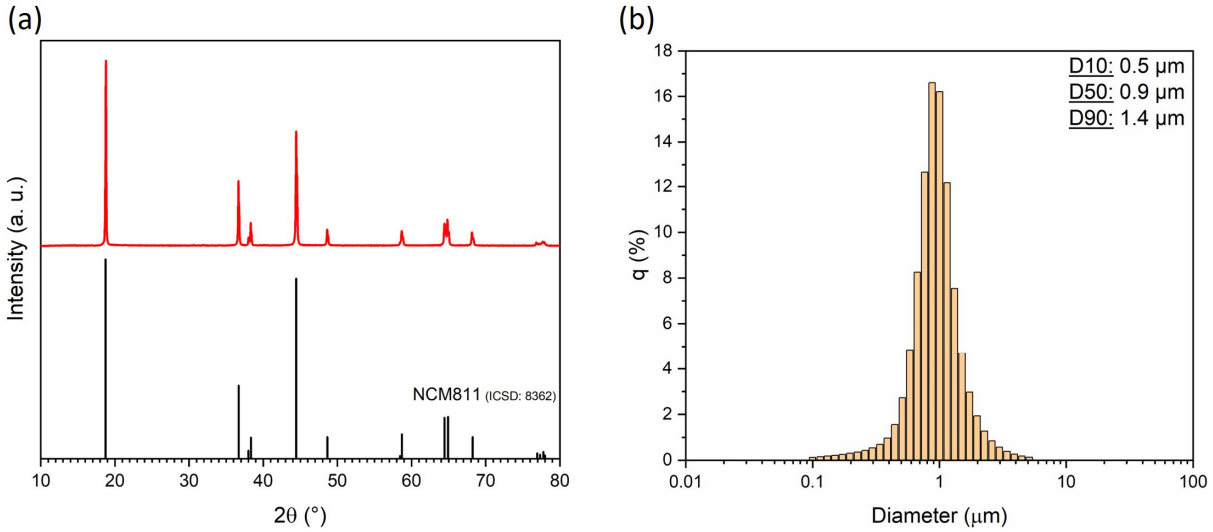

Figure S 29: Characterization of commercial NCM811 (MTI Corporation). (a) Powder XRD pattern and (b) particle size distribution (PSD) of the ball milled power.

The aimed composition of LLZO:Ta was $Li_{6.45}Al_{0.05}La_3Zr_{1.6}Ta_{0.4}O_{12}$. ICP-OES (Table S 8) shows a higher Li content which can be explained by the used Li excess during the synthesis. The enhanced Al content results from an aluminum uptake from the Al_2O_3 crucible during the calcination and sintering steps. Hafnium is an impurity of the ZrO_2 precursor which does not have a significant impact on the performance of the LLZO, as reported previously [255].

Table S 8: Chemical composition of LLZO:Ta determined by ICP-OES.

	Elementary composition [mol]					
	Li	**La**	**Zr**	**Ta**	**Al**	**Hf**
LLZO:Ta	7.40	3.23	1.58	0.42	0.17	0.02

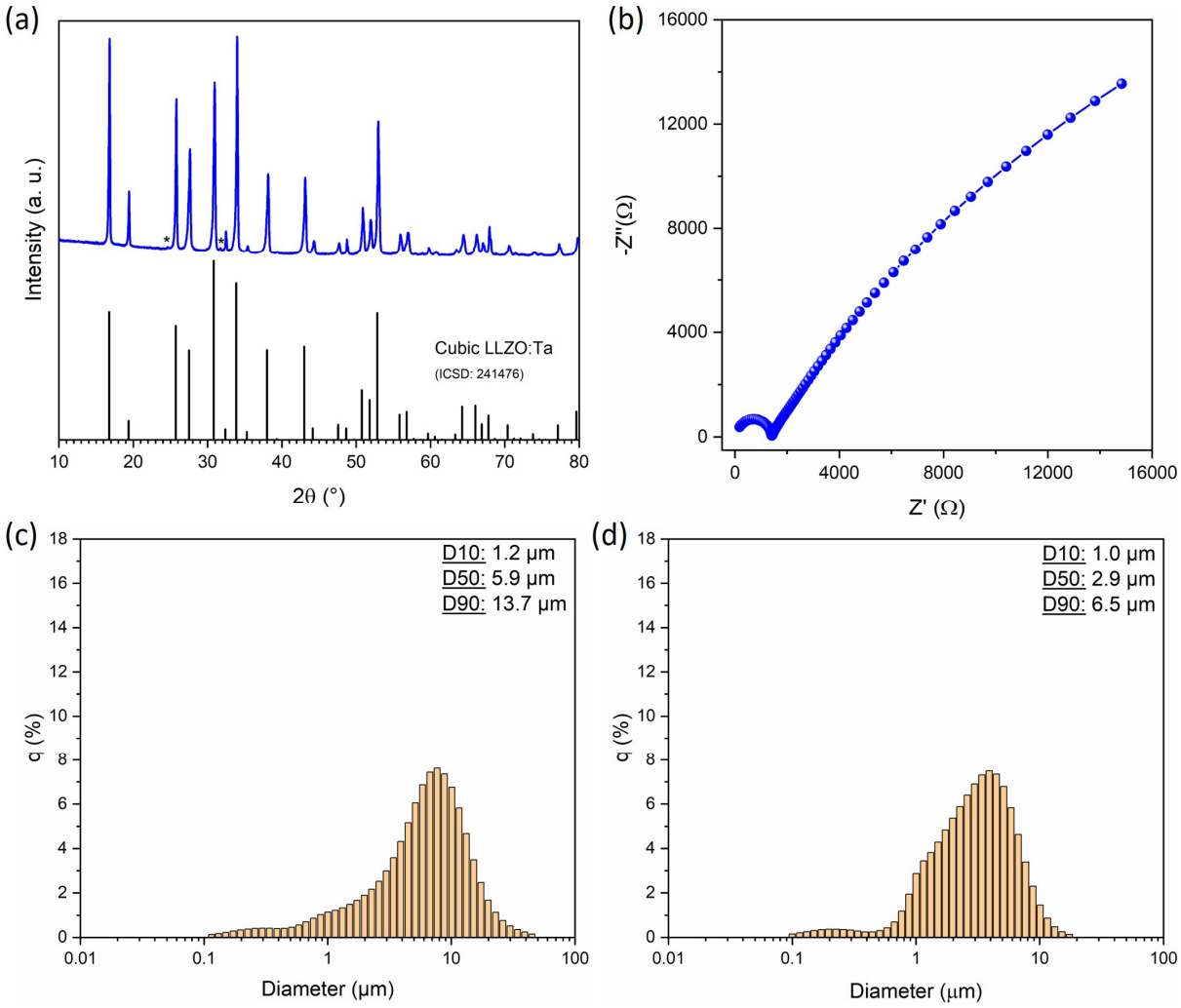

Figure S 30: (a) XRD pattern of a sintered LLZO:Ta pellet. The side phase $La_2Li_{0.5}Al_{0.5}O_4$ is marked with *. (b) Nyquist plot of the impedance measurement to determine the Li-ion conductivity of LLZO:Ta. Particle size distributions of (c) sintered and ground LLZO:Ta powder and (d) LLZO:Ta powder after planetary ball milling.

Sintered LLZO:Ta pellets had a geometrical density of 88 %. Based on the impedance measurement shown in Figure S 30d, a room temperature ionic conductivity of 0.8 mS cm^{-1} was determined.

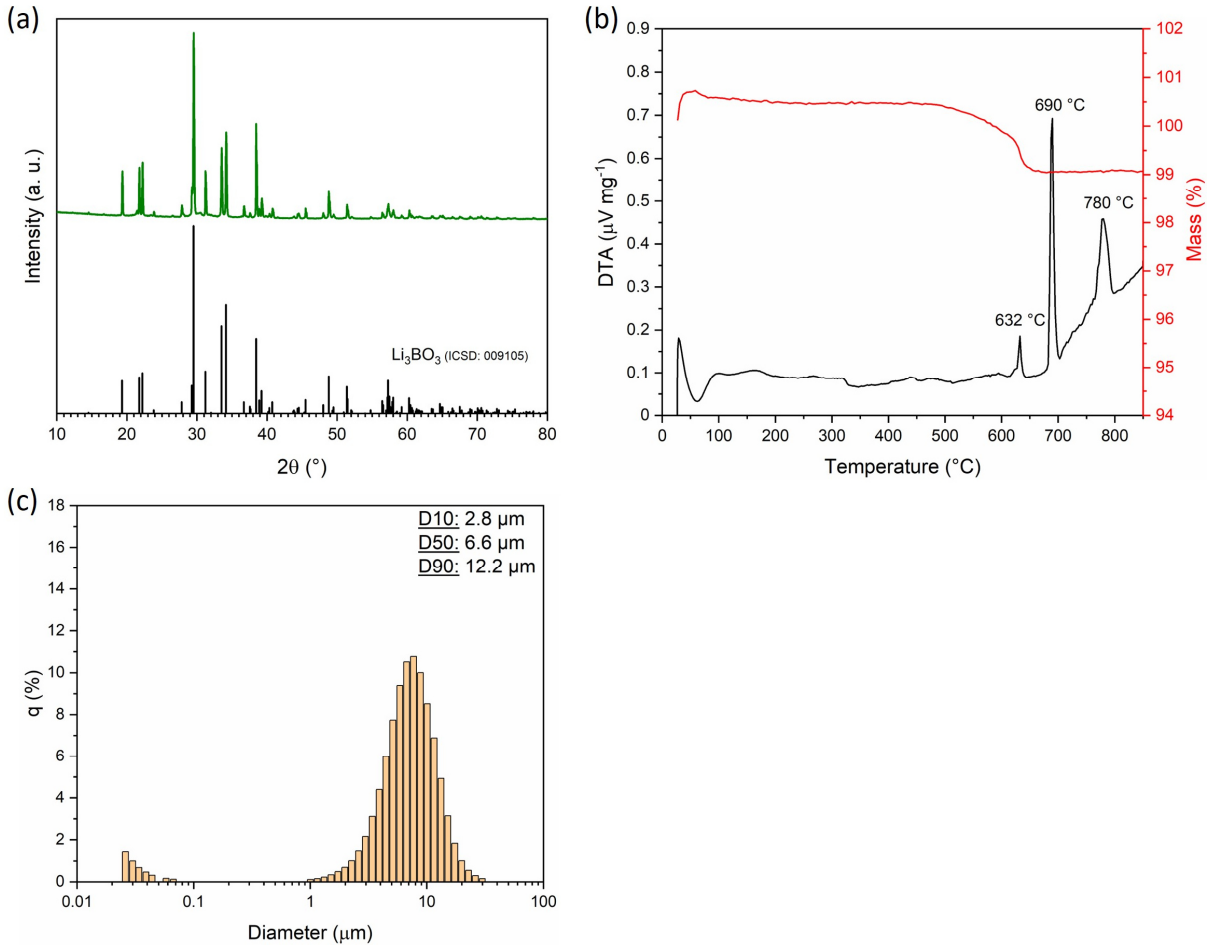

Figure S 31: (a) XRD pattern of synthesized Li_3BO_3 (LBO). (b) DTA-TG measurement to determine the melting point of LBO. (c) Particle size distribution of the ball milled LBO.

The sintering aid Li_3BO_3 (LBO), synthesized by a solid-state reaction, contains in addition to the desired monoclinic Li_3BO_3 phase a small amount of an unknown borate phase as shown in the powder XRD pattern (Figure S 31c). The presence of an additional borate phase with higher melting point was also observed by DTA (Figure S 31d). However, DTA furthermore indicates, that the desired Li_3BO_3 phase, which should serve as a sintering aid, melts at 690 °C. This is in agreement with the reported melting points in literature of around 700 °C [156, 256].

Publications and presentations

Publications

1. *Lattice doping or surface coating: a comparison between B and Ru doping*
   Christoph Roitzheim, Liang-Yin Kuo, Helen Valencia, Martin Finsterbusch, Olivier Guillon, Dina Fattakhova-Rohlfing, and Payam Kaghazchi, Manuscript in preparation.

2. *All-solid-state Li batteries with NCM-garnet based composite cathodes: the impact of NCM composition on material compatibility*
   Christoph Roitzheim, Yoo Jung Sohn, Liang-Yin Kuo, Grit Häuschen, Markus Mann, Doris Sebold, Martin Finsterbusch, Payam Kaghazchi, Olivier Guillon, and Dina Fattakhova-Rohlfing, *ACS Applied Energy Materials* **2022**, 5, (6), 6913-6926.

3. *Cold sintered $LiMn_2O_4$ for high-rate capability electrodes*
   Khushnuda Nur, **Christoph Roitzheim**, Martin Finsterbusch, Martin Bram, and Olivier Guillon, *Journal of The Electrochemical Society* **2022,** 169, (2), 020556.

4. *Boron in Ni-rich NCM811 cathode material: impact on atomic and microscale properties*
   Christoph Roitzheim, Liang-Yin Kuo, Yoo Jung Sohn, Martin Finsterbusch, Sören Möller, Doris Sebold, Helen Valencia, Maria Meledina, Joachim Mayer, Uwe Breuer, Payam Kaghazchi, Olivier Guillon, and Dina Fattakhova-Rohlfing, *ACS Applied Energy Materials* **2022,** 5, (1), 524-538.

5. *Analysis on discharge behavior and performance of As- and B-doped silicon anodes in non-aqueous Si–air batteries under pulsed discharge operation*
   Yasin Emre Durmus, **Christoph Roitzheim**, Hermann Tempel, Florian Hausen, Yair Ein-Eli, Hans Kungl, and Rüdiger-A. Eichel, *Journal of Applied Electrochemistry* **2020,** 50, (1), 93-109.

6. *Tuning a robust system: N,O zinc guanidine catalysts for the ROP of lactide*
   Pascal M. Schäfer, Paul McKeown, Martin Fuchs, Ruth D. Rittinghaus, Alina Hermann, Johanna Henkel, Sebastian Seidel, **Christoph Roitzheim**, Agnieszka N. Ksiazkiewicz, Alexander Hoffmann, Andrij Pich, Matthew D. Jones, and Sonja Herres-Pawlis, *Dalton Transactions* **2019,** 48, (18), 6071-6082.

Presentations

1. *Simulation supported localization of boron in B-doped $Li[Ni_{0.8}Co_{0.1}Mn_{0.1}]O_2$ as cathode material for Li-ion batteries*
   Christoph Roitzheim, Liang-Yin Kuo, Yoo Jung Sohn, Sören Möller, Martin Finsterbusch, Payam Kaghazchi, Olivier Guillon and Dina Fattakhova-Rohlfing

   International Society of Electrochemistry (ISE), 72nd Annual Meeting, **2021**, Jeju Island, Korea. (Oral presentation, on-site)

2. *Synthesis of modified cathode materials for ceramic All-Solid-State Lithium Batteries*
   Christoph Roitzheim, Sören Möller, Martin Finsterbusch, Payam Kaghazchi, Olivier Guillon and Dina Fattakhova-Rohlfing

   Deutsche Keramische Gesellschaft e.V. (DKG), CERAMICS 2021, **2021**, virtual. (Poster presentation)
   This poster received the 3rd place of the poster competition endowed with 250 € prize money and a certificate sponsored by DURAVIT AG.

3. *Modified Cathode Materials for garnet based All-Solid-State Lithium Batteries*
   Christoph Roitzheim, Martin Finsterbusch, Payam Kaghazchi and Dina Fattakhova-Rohlfing

   ECS Meeting Abstracts **2020,** MA2020-02, (5), 987-987.
   The Electrochemical Society, ECS PRiME, **2020**, Hawaii, USA, virtual. (Oral presentation)

4. *Synthesis of optimized Cathode materials for All-Solid-State Lithium-Ion Batteries*
   Christoph Roitzheim, Martin Finsterbusch, Payam Kaghazchi and Dina Fattakhova-Rohlfing

   International Battery Association (IBA), IBA 2020, **2020**, Bled, Slovenia. (Poster presentation; conference changed to virtual IBA 2020 without poster session)

Curriculum vitae

Aus datenschutzrechtlichen Gründen ist der Lebenslauf in der Online-Version nicht enthalten